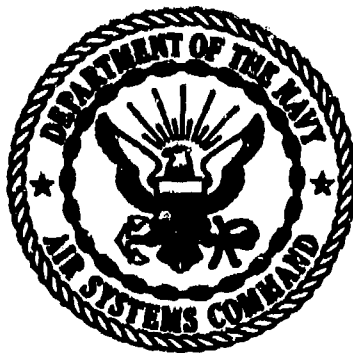LEVEL

INTERIM REPORT

ADVANCED COMPOSITE AIRCRAFT

ELECTROMAGNETIC DESIGN AND SYNTHESIS

CONTRACT N00019-79-C-0172

APRIL 1980

DTIC
ELECTE
S   MAR 13 1981   D

A

PREPARED FOR

OFFICE OF NAVAL RESEARCH

AND   81 3 12 018

NAVAL AIR SYSTEMS COMMAND

REPORT DOCUMENTATION PAGE

READ INSTRUCTIONS
BEFORE COMPLETING FORM

1. REPORT NUMBER	2. GOVT ACCESSION NO.	3. RECIPIENT'S CATALOG NUMBER
NAVAIR-518-1	AD-A096291	

4. TITLE (and Subtitle)
Advanced Composite Aircraft Electromagnetic Design and Synthesis, Interim Report

5. TYPE OF REPORT & PERIOD COVERED
Sep 1978 – May 1980

6. PERFORMING ORG. REPORT NUMBER

7. AUTHOR(s)
R. WALLENBERG, G. DIKE, J. BIRKEN, J. BARRETT
E. KURT, K. RUDOLPH, L. WIDMANN, R. HARRINGTON

8. CONTRACT OR GRANT NUMBER(s)
N00014-78-C-0673
N00019-79-C-0172

9. PERFORMING ORGANIZATION NAME AND ADDRESS
Syracuse Research Corporation
Merril Lane
Syracuse, New York 132101

10. PROGRAM ELEMENT, PROJECT, TASK AREA & WORK UNIT NUMBERS
63251N W0647-TW

11. CONTROLLING OFFICE NAME AND ADDRESS
Naval Air Systems Command
Advanced Electromagnetics
Washington, D. C. 20361

12. REPORT DATE
May 1980

13. NUMBER OF PAGES
280

14. MONITORING AGENCY NAME & ADDRESS(if different from Controlling Office)

15. SECURITY CLASS. (of this report)
Unclassified

15a. DECLASSIFICATION/DOWNGRADING SCHEDULE

16. DISTRIBUTION STATEMENT (of this Report)

APPROVED FOR PUBLIC RELEASE
DISTRIBUTION UNLIMITED

17. DISTRIBUTION STATEMENT (of the abstract entered in Block 20, if different from Report)

18. SUPPLEMENTARY NOTES

19. KEY WORDS (Continue on reverse side if necessary and identify by block number)
Composite Airframes, Composite Materials, Electromagnetic Coupling Lightning, Nuclear EMP, Radar Effects, Electromagnetic Shielding, Joint Coupling, Transfer Impedance, and Systems Trade-offs.

20. ABSTRACT (Continue on reverse side if necessary and identify by block number)
The construction of aircraft, missiles and helicopters with unprotected advanced composite materials increases their electromagnetic environment vulnerability. This is further aggravated by the diminishing susceptability of high density digital devices (LSI, VLSI and VHSIC) which are being utilized in the digital control systems. This study quantifies the threat to different devices in different composite airframes. It shows which composite material exhibit the least vulnerability and initiates trade-offs to compensate it. Thin metal coatings are shown to significantly improve

DD FORM 1473 EDITION OF 1 NOV 68 IS OBSOLETE
1 JAN 73
S/N 0102-LF-014-6601

20. (Continued)

this with very small weight penalties for aluminum coatings. The use of coatings offers other desirable spin-offs, one being simple design composite structural joints exhibiting low electromagnetic vulnerability.

AUTHORS

Syracuse Research Corporation

J. Barrett
E. Burt
G. Dike
R. Harrington
R. Rudolph
R. Wallenberg
L. Widmann

Naval Air Systems Command

J. Birken

TABLE OF CONTENTS

i

TABLE OF CONTENTS (Continued)

LIST OF ILLUSTRATIONS

LIST OF ILLUSTRATIONS (Continued)

LIST OF TABLES

SECTION 1

INTRODUCTION

A major concern with the increasing use of composite materials and low voltage electronics is the amount of electromagnetic (EM) coupling to the interior of an aircraft and to the cables and electronic devices within it. The introduction of boron/epoxy, graphite/epoxy, and Kevlar/epoxy composite materials as structural elements in modern airframes will result in a substantial reduction in airframe weight, due to the high strength-to-weight ratios of these materials. The use of these new composite materials has raised questions relative to the aircraft vulnerability resulting from the effects of lightning, high power radar, nuclear electromagnetic pulse (EMP), and precipitation static. The problems are further compounded by the fact that these materials are relatively easy to construct, and have resulted in a proliferation of available composite materials.

This report describes simple methods for determining the shielding provided by an aircraft's exterior surface and the coupling of the interior fields to cables and transmission lines within aircraft cavities. This data is used to determine whether devices commonly found on aircraft will be subject to upset or burnout. The results found in this volume can be used to perform trade-offs between EM shielding, weight, and cost.

Section 2 describes the waveforms and the associated spectrum for the natural threats of direct- and nearby-strike lightning as well as precipitation static and the friend/foe threats consisting of the nuclear EMP, low frequency communications, and shipboard microwave radars. A more detailed radio frequency (RF) threat has been published by the Syracuse Research Corporation (SRC) as a separate volume under this contract entitled "Threats to EM Integrity of Advanced Composite Aircraft" (SRC TN 78-395R).

A formulation starting from Maxwell's equations is presented in Section 3 for coupling to the interior of a composite shell. Approximations are

made which decouple the interior problem from the exterior by the use of the concept of transfer impedance. The transfer impedance concept is simply derived for shields which are locally planar; that is, for shields which are thin compared to their radius of curvature and for which the wavelength within the shield is much smaller than that external to the shield.

The surface transfer impedance relates the interior tangential electric field to the equivalent exterior surface skin current density induced by the incident EM radiation. For homogenous shields, including mixed-orientation graphite composite enclosures at low frequency, it is shown in Section 4 that one can approximately relate the magnitude of the surface transfer impedance to the magnetic or electric shielding effectiveness, SE, as

$$|Z_{ST}| \simeq Z/10^{SE/20} \tag{1}$$

over the open interval (f_{min}, ∞). The impedance-like quantity Z is dependent on the frequency of the incident field and the shield geometry expressed as a volume-to-surface ratio. The enclosure geometries for which this relation holds includes spheres, cylinders, and parallel plates under a uniform incident field. This section is described in more detail under a separate report entitled "Relationship of Material Properties to Electromagnetic (EM) Shielding" (SRC TN 79-037).

A brief definition and analytical model for joints is given in Section 5. Curves are presented for typical measured joint admittances and an analytical model is summarized.

Given an estimate of the interior field levels caused by diffusion or joint penetration, simple expressions are defined in Section 6 for upper bounds on the open-circuit voltage, short-circuit current, power, and energy at the terminals of a shielded or unshielded transmission line. Examples are illustrated for lightning and nuclear EMPs.

Section 7 describes the Wunsch model commonly used to describe damage levels as a function of pulse width for a general class of devices including resistors, diodes, and transistors. Section 8 summarizes a study on upset and burnout as applied to integrated circuits performed by McDonnell Douglas entitled "Integrated Circuit Electromagnetic (EM) Susceptibility Investigation". From it the power densities incident on a cable terminating in an integrated circuit which can cause device update can be obtained as a function of frequency.

Section 9 presents a trade-off study between EM shielding provided by covering graphite/epoxy composites with highly conducting coatings. Shielding properties and the weight penalties for various coatings are considered. In addition, the data is parameterized as a function of the thickness and extra weight required for a given amount of shielding.

A bibliography of pertinent documents reviewed in this study are grouped according to category in Section 10. The category grouping are Threat (including lightning, precipitation static, the nuclear EMP, and shipboard RF emitters), Shielding, Coupling, Transmission Line Coupling, Device Coupling and Susceptibility, and Miscellaneous.

Finally, Appendix A summarizes the work to date on shielding effectiveness of composites and joints on the Air Force-sponsored Grumman "Projection Optimization for Advanced Composite Structures". Appendix B summarizes the Culham Laboratory (United Kingdom) work on "Lightning Coupling to the General Dynamics Advanced Composite Forward Fuselage."

SECTION 2

THREAT LEVELS

2.0 INTRODUCTION

This section provides a brief description of the time waveforms and associated spectrum of the threats considered against a Navy advanced composite aircraft. The threats considered include nearby and direct strike lightning, the nuclear EMP, precipitation static, and the RF threat to US aircraft aboard US aircraft carriers caused by navigation aides, high frequency (HF) communications and carrier based radars. The RF threat shown in this report is only cursory.

A more detailed SECRET document has been published by the SRC under this contract entitled "Threats to EM Integrity of Advanced Composite Aircraft (U)," by R.B. Shields (SRC TN 78-395R1).

2.1 Direct Lightning Strike

A generalized wave shape for the current flowing from a typical negative cloud-to-ground flash is shown in Figure 2-1. Also indicated are the five main regions of a lightning flash: the leader, the initial return stroke, an intermediate current, a continuing current, and one or more restrikes.

When sufficient charge accumulates in the lower part of a cloud to cause an electric field which exceeds the ionization threshold of air, an electrical discharge is initiated toward the earth. Because the discharge requires a finite amount of charge and time for the channel resistance to lower to the arc phase, the discharge proceeds in a sequence of steps pausing periodically to allow the previous channel section to become fully conducting. This mechanism is known as the stepped leader process.

For an aircraft in an area where lightning is imminent, the highest electric field will occur near the extremities, typically the nose, wing, and tail sections. When the leader advances to a point where the field adjacent to the aircraft extremities has increased to about 30 kV/cm, the air will ionize and electric sparks will form at the extremities, extending in the direction of the oncoming leader. One of these so-called streamers will meet the nearest branch of the leader and form a continuous spark from the cloud charge center to the aircraft. The aircraft then becomes a part of the path taken by the leader. When the leader reaches its destination, a continuous ionized channel between charge centers is formed and a high amplitude return stroke current flows back up this channel.

After this initial discharge, many additional complete discharges can take place, including additional leader phases and return strokes.

It is the return stroke current which dominates the overall lightning flash current waveform, and which is often modeled when effects due to lightning are being analyzed. Among the parameters which determine the current waveform of the return stroke are the peak amplitude, the time to peak amplitude, and the time to half peak amplitude. These are often used to specify a current waveform model. Figures 2-2, 2-3, and 2-4 give the frequency of occurrence for values of these parameters. For a "worst-case" return stroke, typical values used for these parameters are:

> Peak Amplitude of 200 kA
> Time to Peak Amplitude of 2 μs
> Time to Half Peak Amplitude of 40 μs

Figure 2-2 shows that less than 1% of return strokes have a peak amplitude of more than 200 kA. Because of the infrequency of such high peak currents, there is a question as to the prudence of protecting against such a worst-case situation.

A peak amplitude of 200 kA translates roughly into an axial surface current density of

2-2
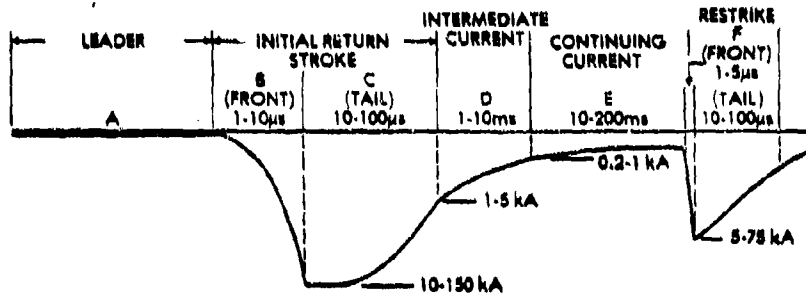
Figure 2-1. Generalized Waveshape of Current in Negative
Cloud-to-Ground Lightning (Note that the
drawing is not to scale)
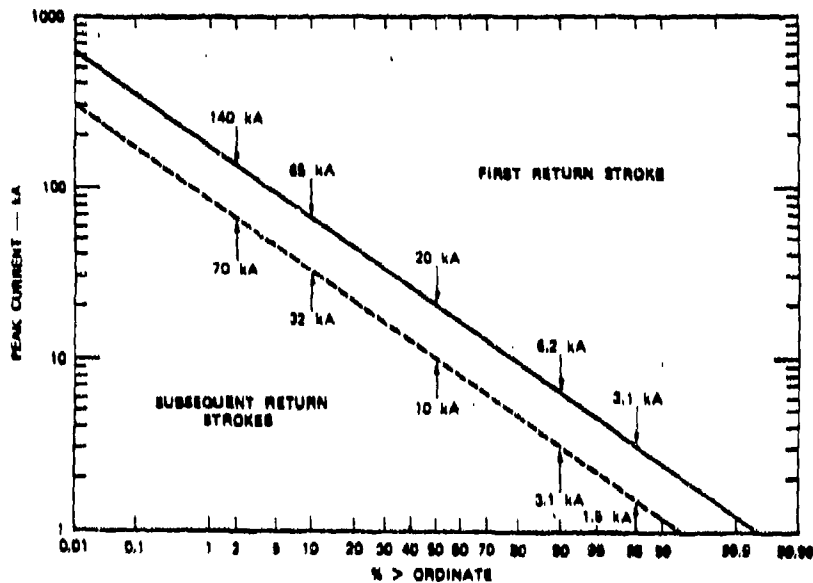
Figure 2-2. Distribution of Peak Currents for First
Return Stroke and Subsequent Strokes

2-3
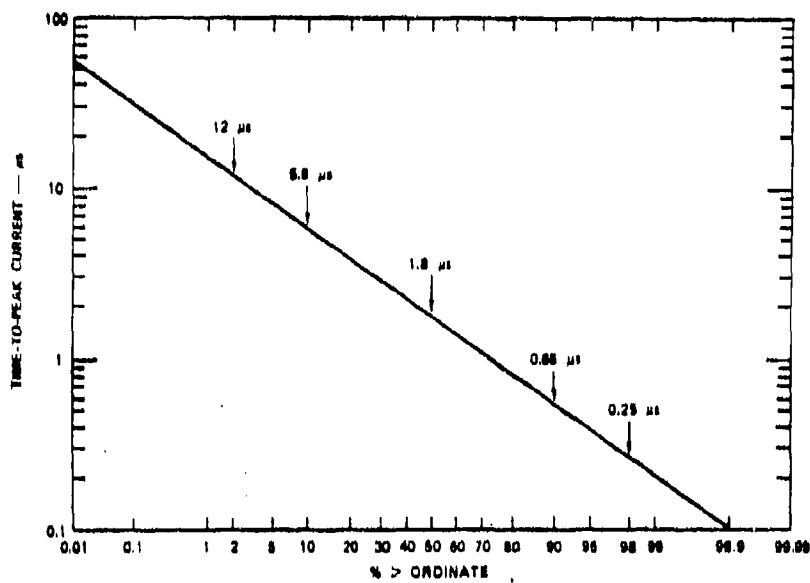
Figure 2-3. Distribution of Time to Peak Current
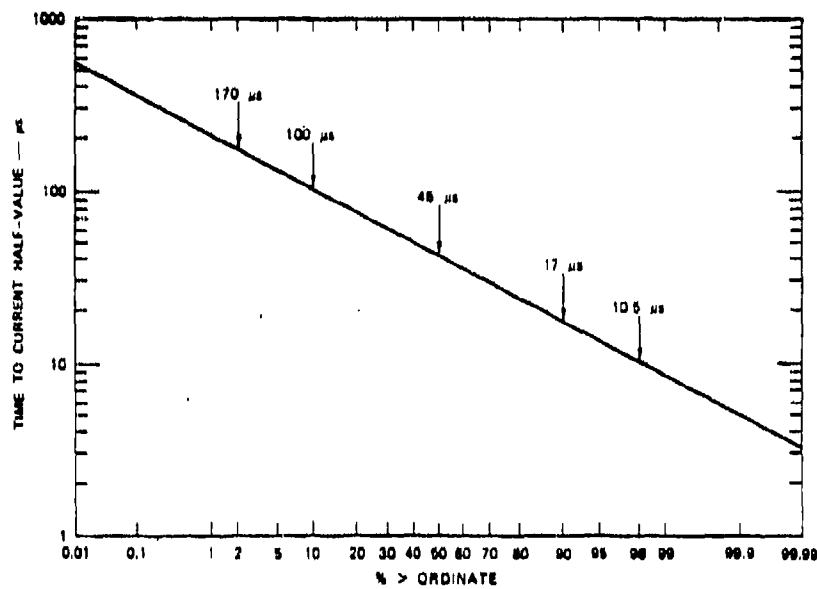
Figure 2-4. Distribution of Time to Current Half Value

2-4

$$J_s \approx \frac{I_{max}}{2\pi R} = \frac{200 \text{ kA}}{2\pi(0.5 \text{ m})} \approx 64 \text{ kA/m} \tag{1}$$

where R is the radius of the fuselage.[1]

Many models for the current waveform have been proposed. Five such models are described below. Then the spectrum of these current waveforms are shown and compared.

Figure 2-5 shows the triangular function used in Reference 1. This is perhaps the simplest function having the basic required characteristics of a quick rise to a maximum followed by a more gradual decay.

Figure 2-6 shows the Space Shuttle Lightning Protection Criteria waveform as given in Reference 2. This waveform includes the intermediate and continuing current phases of the lightning flash.

A double exponential function as shown in Figure 2-7 was used in Reference 3 as a model for the return stroke current. Analytically, this function is given by

$$I(t) = I_0(e^{-\alpha t} - e^{-\beta t}) \quad \begin{array}{l} I_0 = 206 \text{ kA} \\ \alpha = 1.7 \times 10^4 \text{ Hz} \\ \beta = 3.5 \times 10^6 \text{ Hz} \end{array} \tag{2}$$

A triple exponential function was used in Reference 4. This model has a peak amplitude of about 23 kA and is shown in Figure 2-8. The analytic form for this function is

$$I(t) = I_0(e^{-\alpha t} - e^{-\beta t}) + I_1 e^{-\gamma t} \quad \begin{array}{l} I_0 = 30 \text{ kA} \\ I_1 = 2.5 \text{ kA} \\ \alpha = 2 \times 10^4 \text{ Hz} \\ \beta = 2 \times 10^5 \text{ Hz} \\ \gamma = 2 \times 10^3 \text{ Hz} \end{array} \tag{3}$$
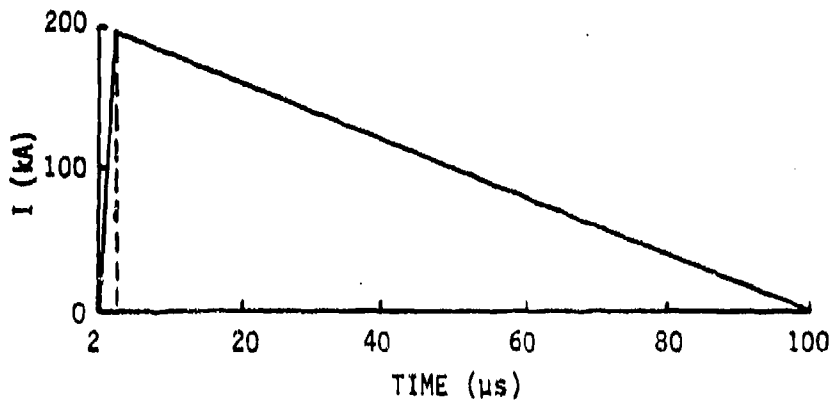
Figure 2-5. Worst-Case Triangular Current Waveform[5]
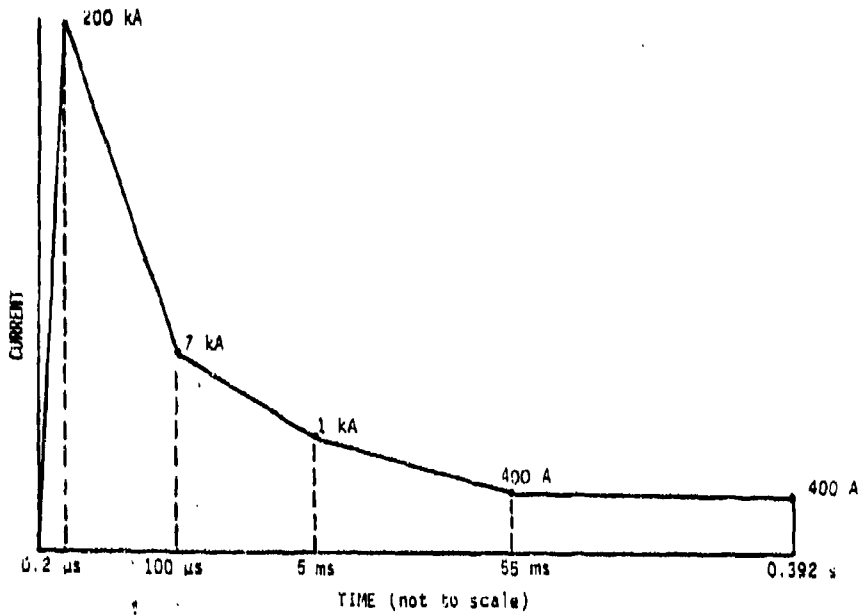
Figure 2-6. Worst-Case Space Shuttle Current Waveform[1]
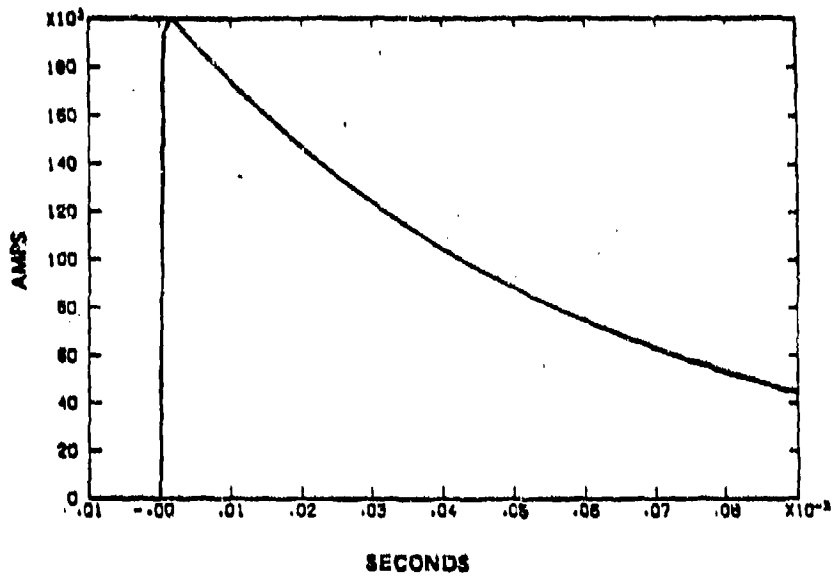
Figure 2-7. Worst-Case Double Exponential Current Waveform[2]
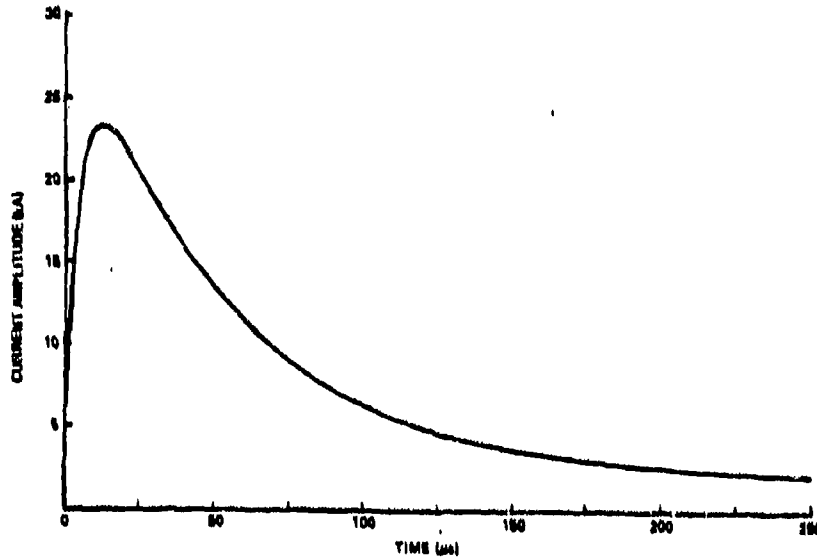
Figure 2-8. Triple Exponential Current Waveform[6]
(Discontinuos at t = 0)

2-7

The third term is included to account for the continuing current. One problem with this model is that the current is allowed to jump discontinuously from 0 to I_1 at $t = 0$.

Finally, Figure 2-9 shows a current waveform consisting of the sum of four exponentials. This waveform was proposed in Reference 5 as a modification of the previous model (Figure 2-8), in order to make the current continuous at $t = 0$. The function shown in Figure 2-9 is given by

$$I(t) = I_0(e^{-\alpha t} - e^{-\beta t}) + I_1(e^{-\gamma t} - e^{-\delta t}) \qquad I_0 = 30 \text{ kA} \qquad (4)$$

$$I_1 = 2.5 \text{ kA}$$
$$\alpha = 2 \times 10^4 \text{ Hz}$$
$$\beta = 2 \times 10^5 \text{ Hz}$$
$$\gamma = 1 \times 10^3 \text{ Hz}$$
$$\delta = 2 \times 10^4 \text{ Hz}$$

It is also of interest to examine these current waveforms in the frequency domain. Figures 2-10 through 2-14 show the Fourier transforms of the waveforms shown in Figures 2-5 through 2-9, respectively.

In order to better compare the spectrums of the waveforms in Figures 2-12, 2-13, and 2-14, Equations 3 and 4 can be modified so that they both have a peak current of 200 kA. This is accomplished by multiplying the right-hand side of Equation 3 by 8.7 and multiplying the right-hand side of Equation 4 by 9.1. The spectrums of the resultant functions are plotted together in Figure 2-15 along with the spectrum shown in Figure 2-12. Figure 2-16 combines Figures 2-10, 2-11, and 2-15.

It can be seen from Figure 2-16 that the first two models (Figures 2-5 and 2-6) have virtually identical spectrums. The spectrums of the triple exponential model has a higher amplitude at high frequencies than any of the other models. This may be due to the discontinuity that this model introduces at $t = 0$.
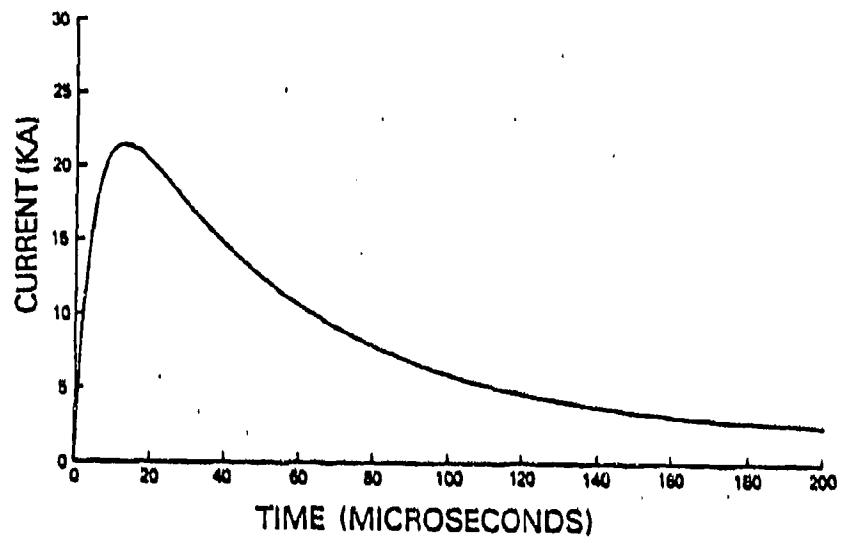
Figure 2-9. Four-Term Exponential Current Waveform [7]
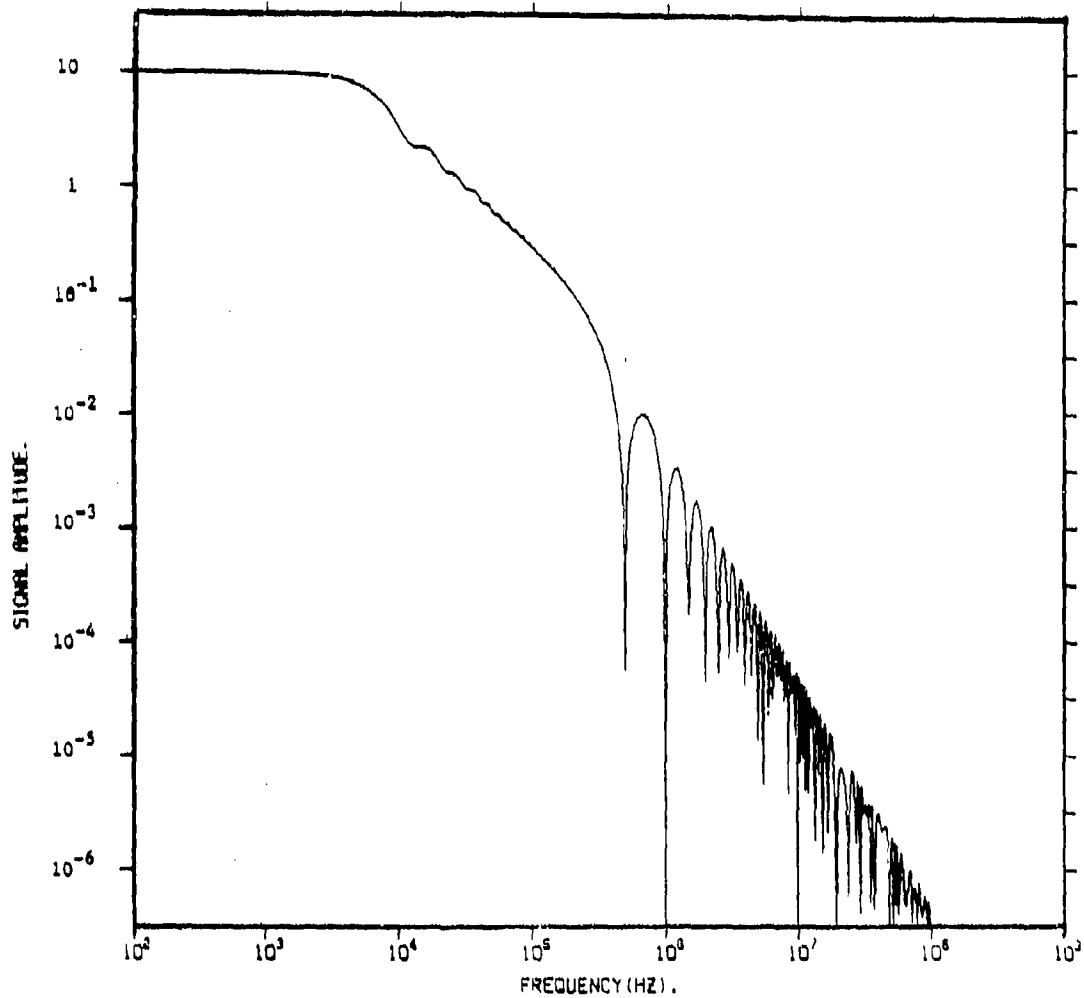
Figure 2-10. Spectrum of the Triangular Current Waveform
Shown in Figure 2-5
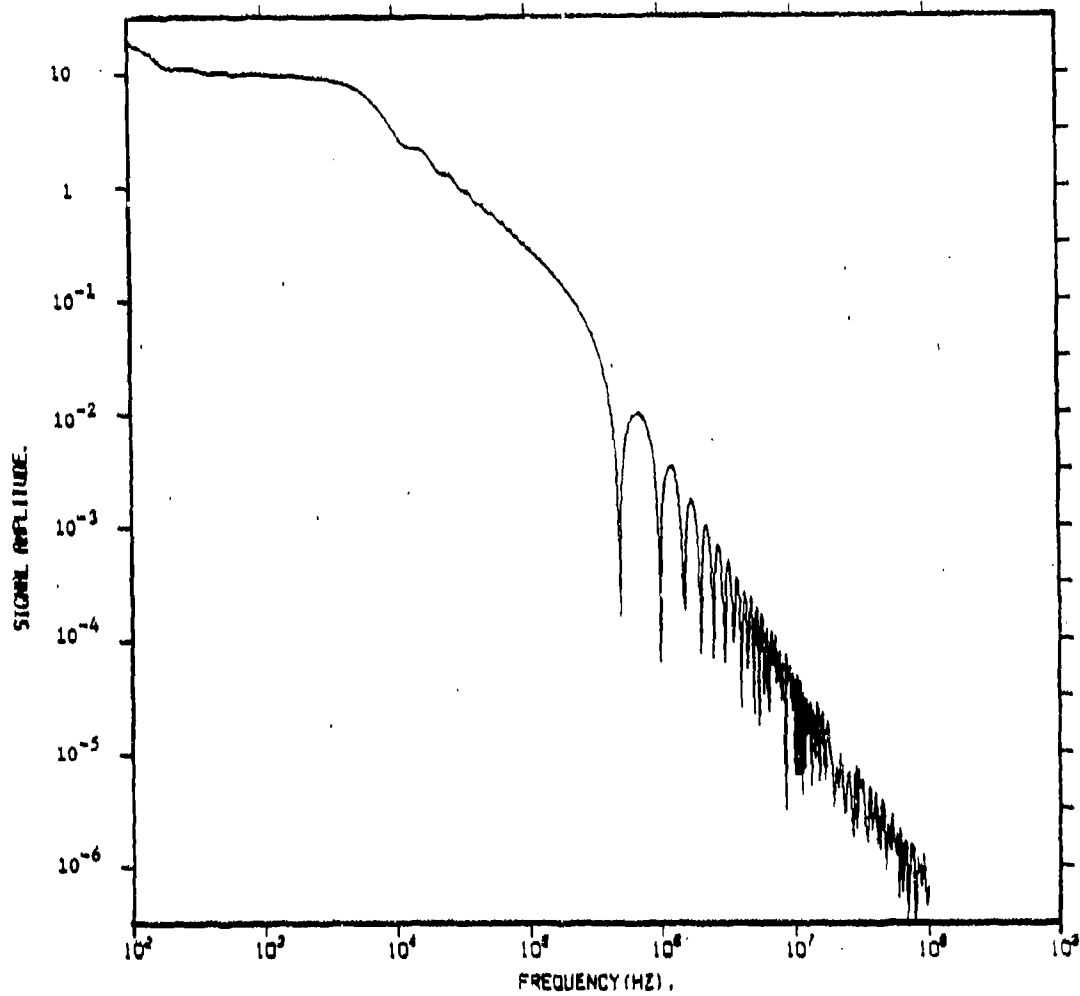
Figure 2-11. Spectrum of the Space Shuttle Current Waveform
Shown in Figure 2-6
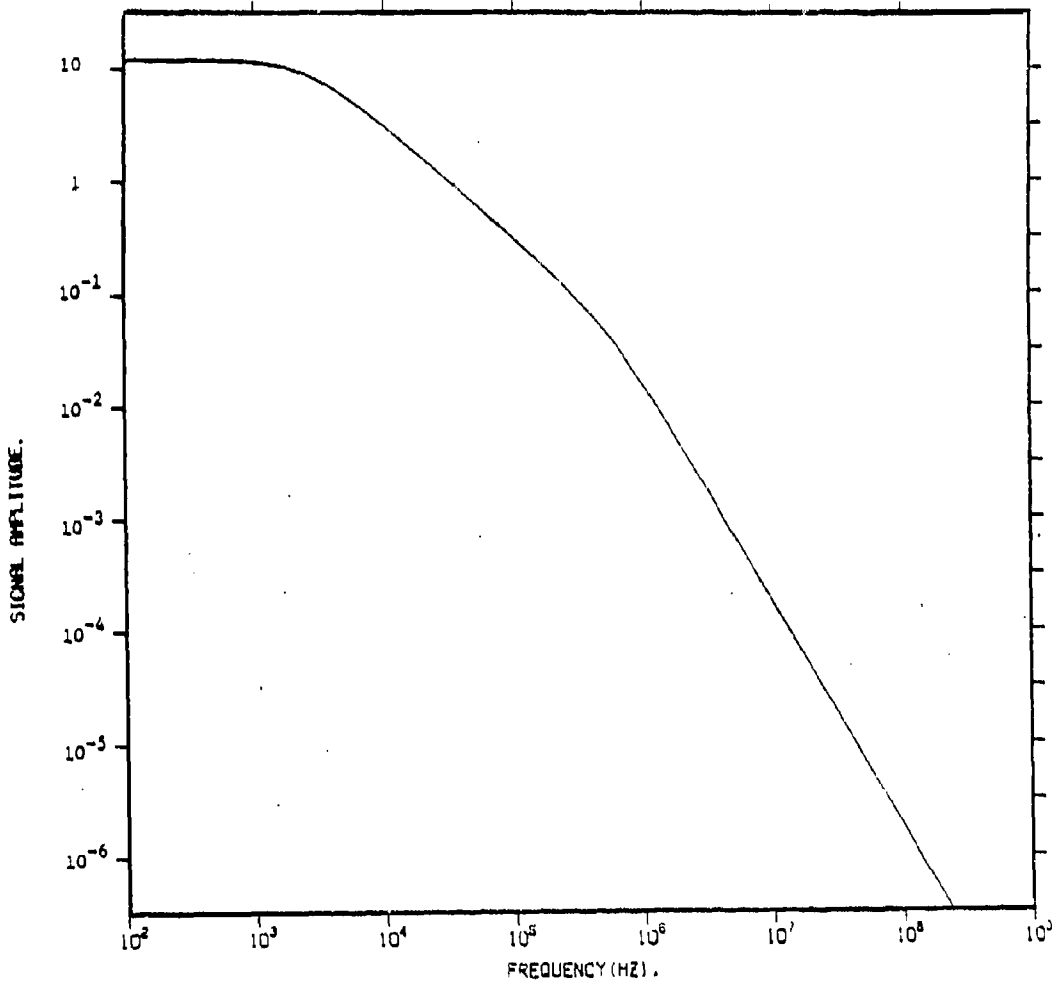
Figure 2-12. Spectrum of the Double Exponential Current Waveform Shown
in Figure 2-7

2-12
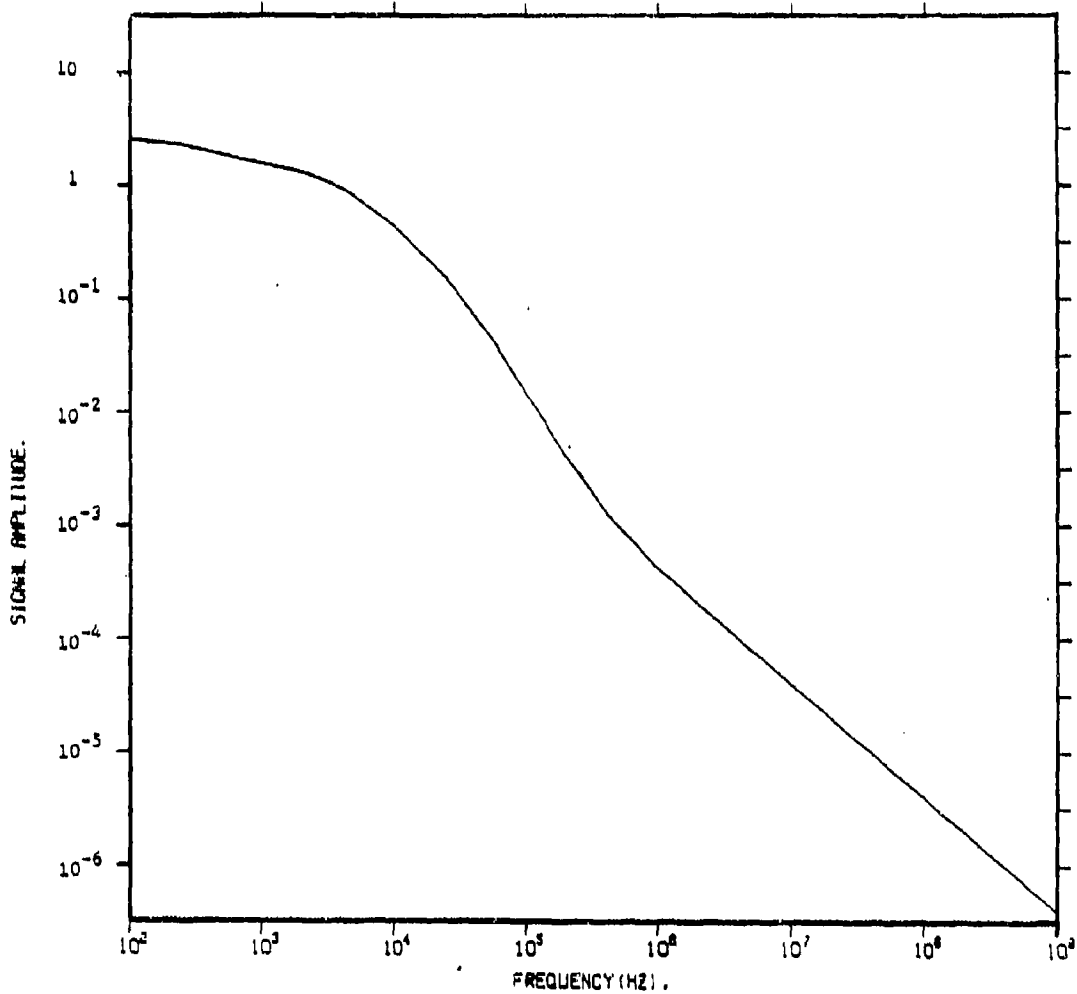
Figure 2-13.   Spectrum of the Triple Exponential Current Waveform Shown
in Figure 2-8

2-13
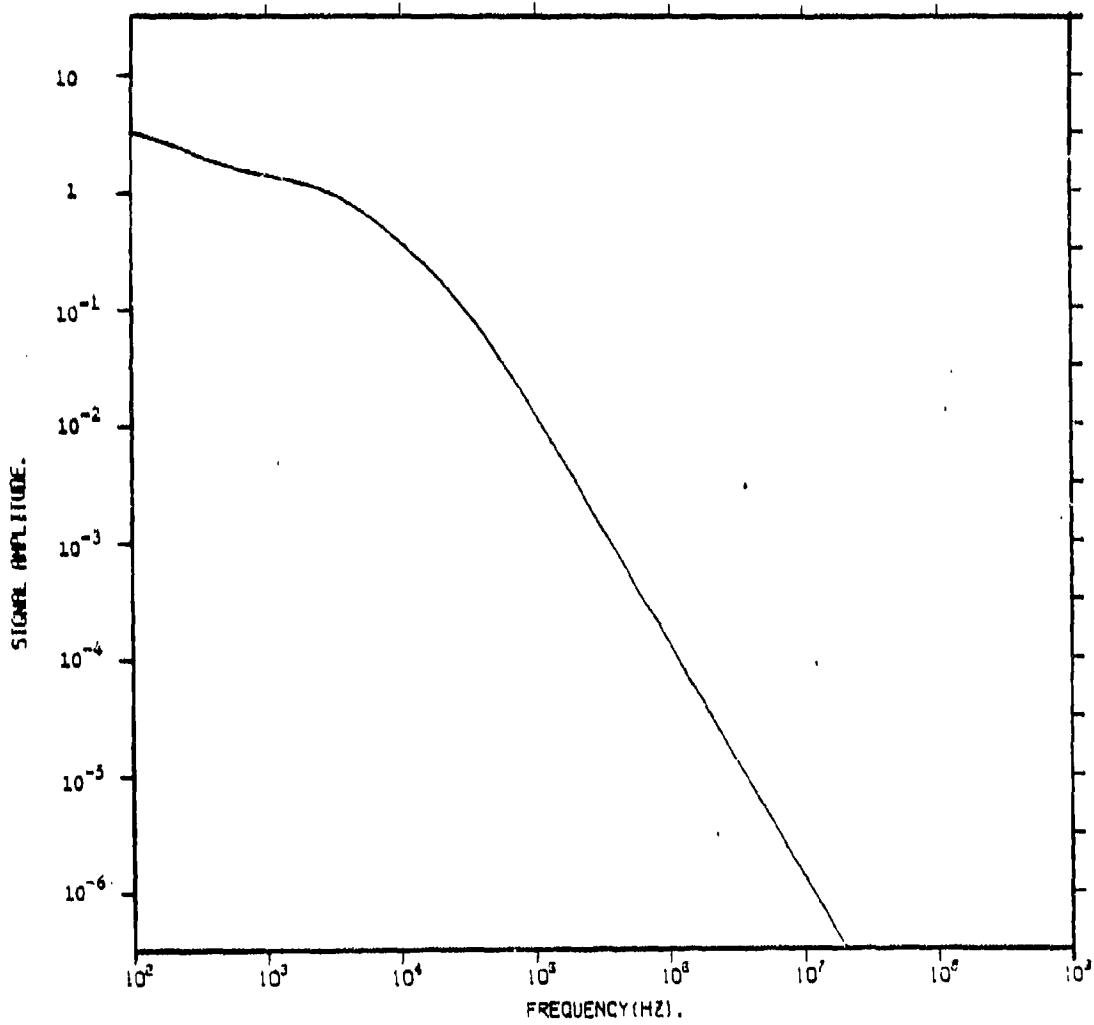
Figure 2-14. Spectrum of the Four-Termed Exponential Current Waveform
Shown in Figure 2-9
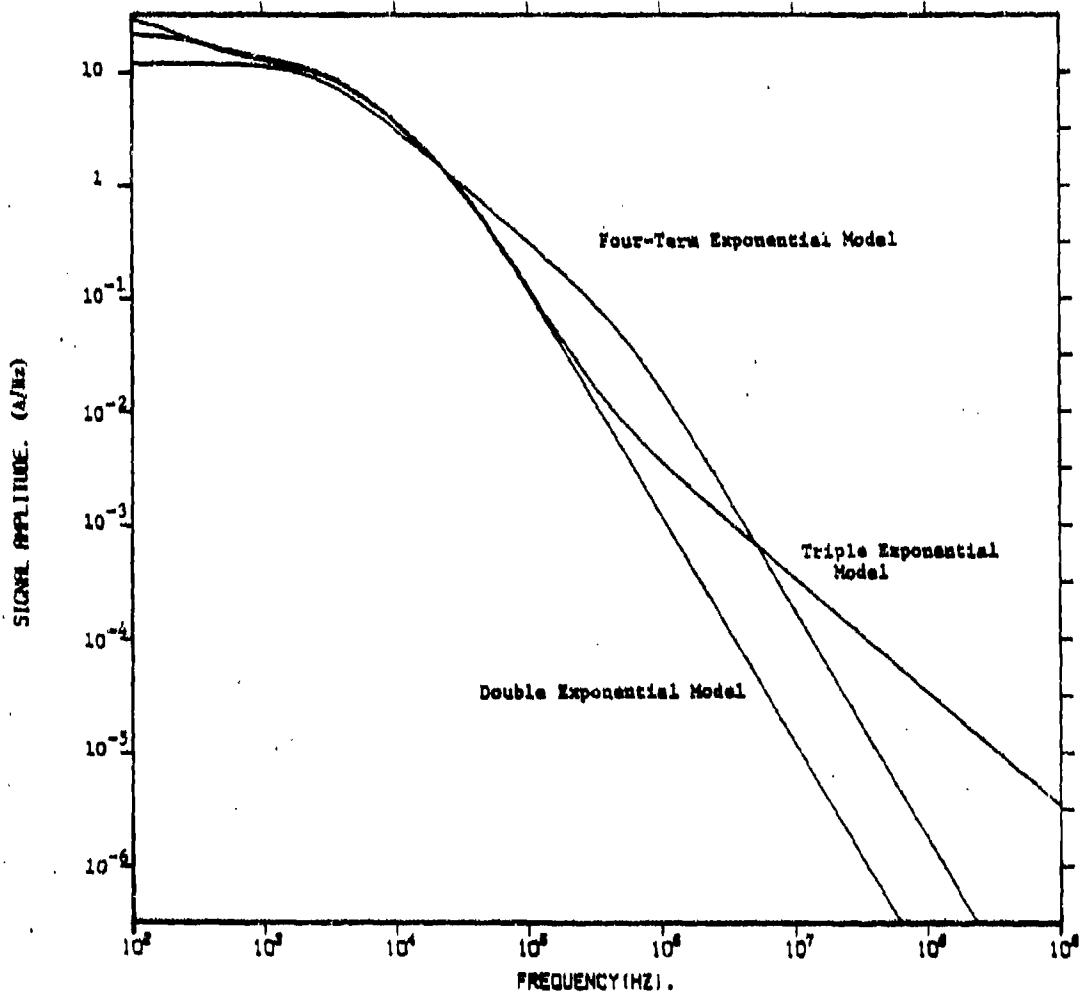
Figure 2-15. Spectrum of Double Exponential Current Waveform and Spectrums of Rescaled Triple and Four-Termed Exponential Current Waveforms
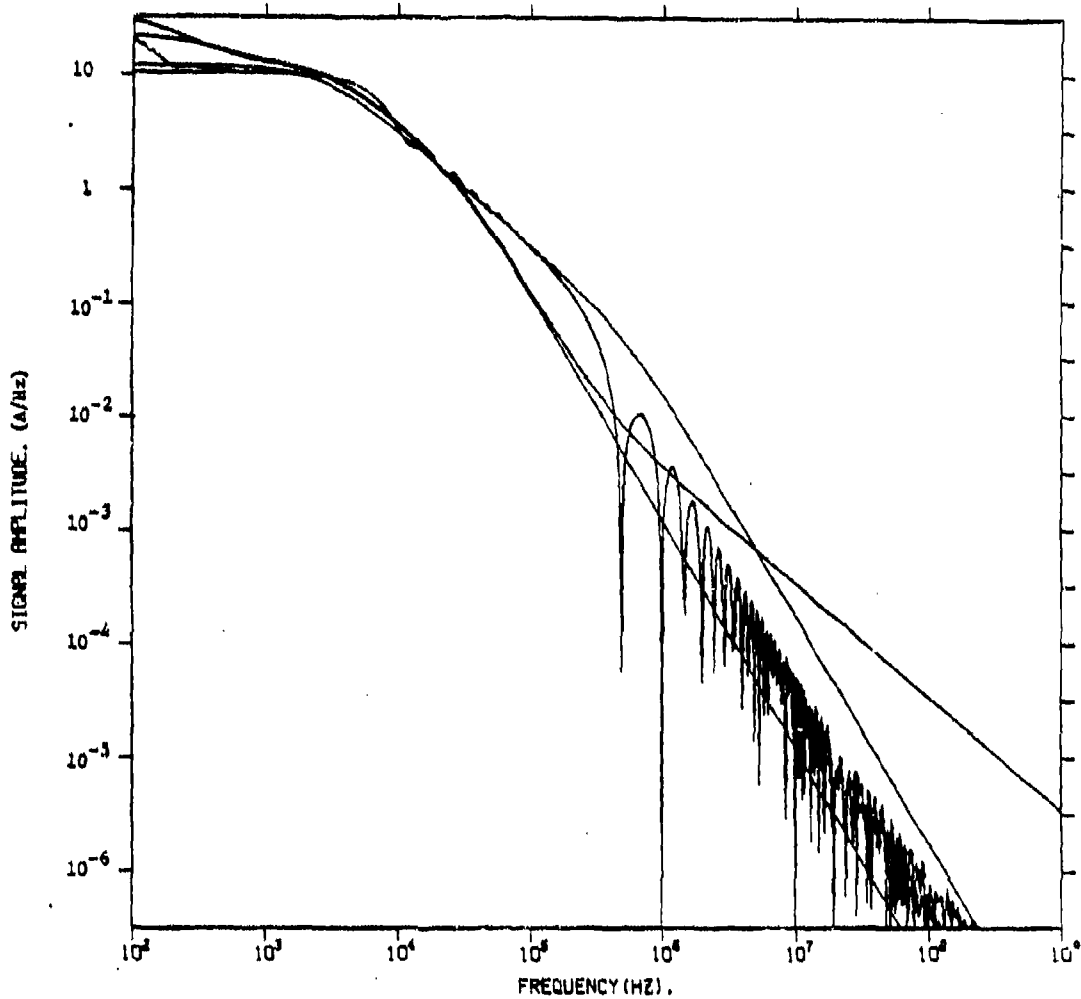
Figure 2-16.   Superposition of Figures 2-10, 2-11, and 2-15

It should be noted that it is not universally accepted that the current waveform can be accurately modeled by piece-wise linear or exponential type models. In Reference 6, the mechanism of the return stroke formulation is studied. That analysis suggest that the current waveform may differ substantially from the exponential type models.

2.2 Nearby Lightning Strike

The fields produced by a lightning strike near an aircraft can be approximated by those due to an infinite current column with the same current waveform as in the attached case. The magnetic field, H, is given by[3, p. 74]

$$H = I/2\pi R \qquad (5)$$

where I is the current waveform and R is the distance from the lightning strike to the aircraft.

In particular, if R = 100 m and I_{max} = 200 kA, we have

$$H_{max} \approx 320 \text{ A/m}$$

The induced surface current density would then be

$$J_{max} \approx 2 H_{max} = 640 \text{ A/m} = 0.64 \text{ kA/m} \qquad (6)$$

This is two orders of magnitude smaller than the surface current due to a direct strike, as calculated in Equation 5.

Generally, the currents induced by a nearby lightning strike can be expected to be quite small when compared to the currents due to a direct strike.

2.3 Precipitation Static

When an aircraft flies through dry precipitation such as sleet, hail or snow, the impact of particles on the aircraft will cause a charge to separate from some of the particles and join the aircraft, leaving the aircraft with an excess of positive or negative charges (depending on the form of precipitation)

(see Figure 2-17). The electric potential of regions of the aircraft can be increased to the point that corona discharges take place (see Figure 2-19). These discharges are in the form of a series of short pulses. The individual pulses associated with these discharges, according to Reference 1, can be modeled as

$$f(t) = Ae^{-\alpha t} \tag{7}$$

where A is the pulse amplitude and α is the pulse delay constant. Both A and α are functions of atmospheric pressure, and hence of altitude. The number of such pulses per minute, denoted by ν, is also a function of atmospheric pressure. A good fit to observed values of A, α and ν can be obtained by using:

$$A = 7.90569 \times 10^5 \ p^{0.25}$$
$$\alpha = 2.7777 \times 10^{-2} \ p \tag{8}$$
$$\nu = 3.83767 \times 10^3 \ p^{0.48}$$

where p is atmospheric pressure, measured in torrs.

Pressure and altitude can be related by

$$p = 760 \ \exp - (\frac{h + 0.002 \ h^2}{25}) \tag{9}$$

where h is altitude given in kilofeet and p is again in torrs. The noise spectrum produced by ν pulses per second is given by

$$P = A(\frac{\nu}{\pi})^{1/2} \ (\omega^2 + \alpha^2)^{-1/2} \tag{10}$$

Figures 2-19a and 2-19b show some characteristics of this spectrum.

When charge is deposited on dielectric surfaces such as radomes, windshields or composite material structures, it cannot flow freely to other parts of the aircraft because of the insulating character of these surfaces. If the potential between these surfaces and the main body of the aircraft becomes too great a surface streamer discharge will occur.

2-18

SA-2919-5
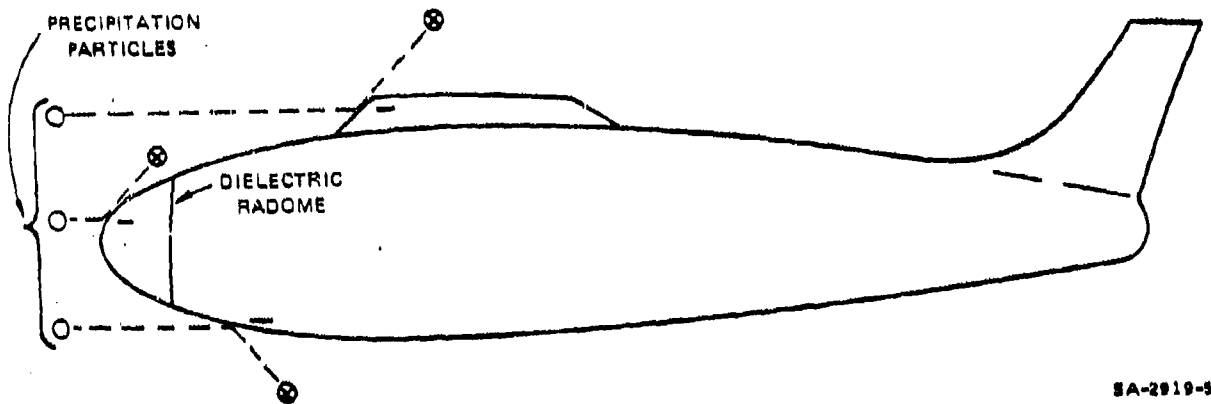
Figure 2-17. Frictional Charging of Aircraft by Impinging Particles
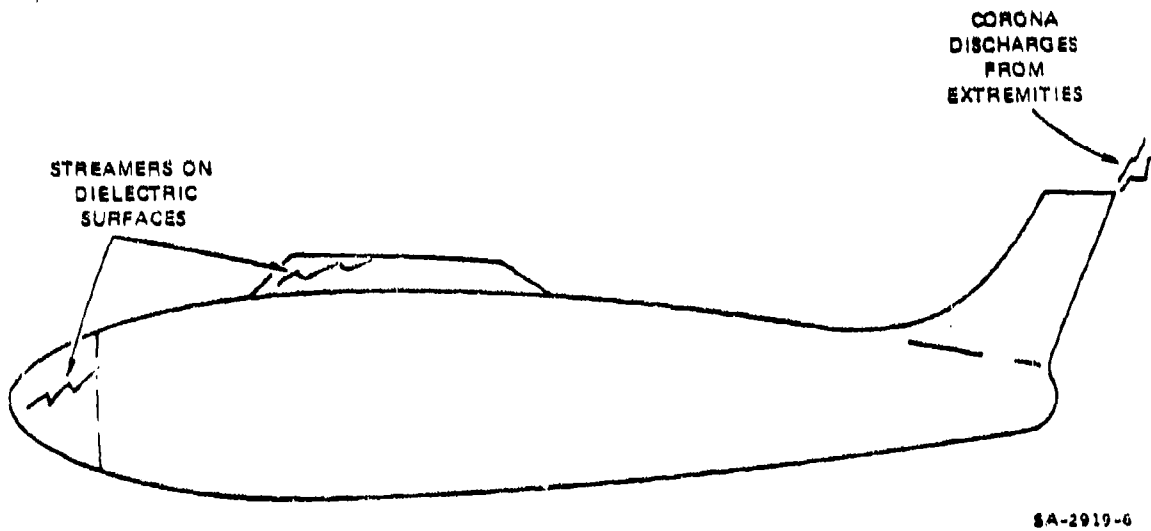
SA-2919-6

Figure 2-18. Noise Sources Associated with Static Electrification

2-19
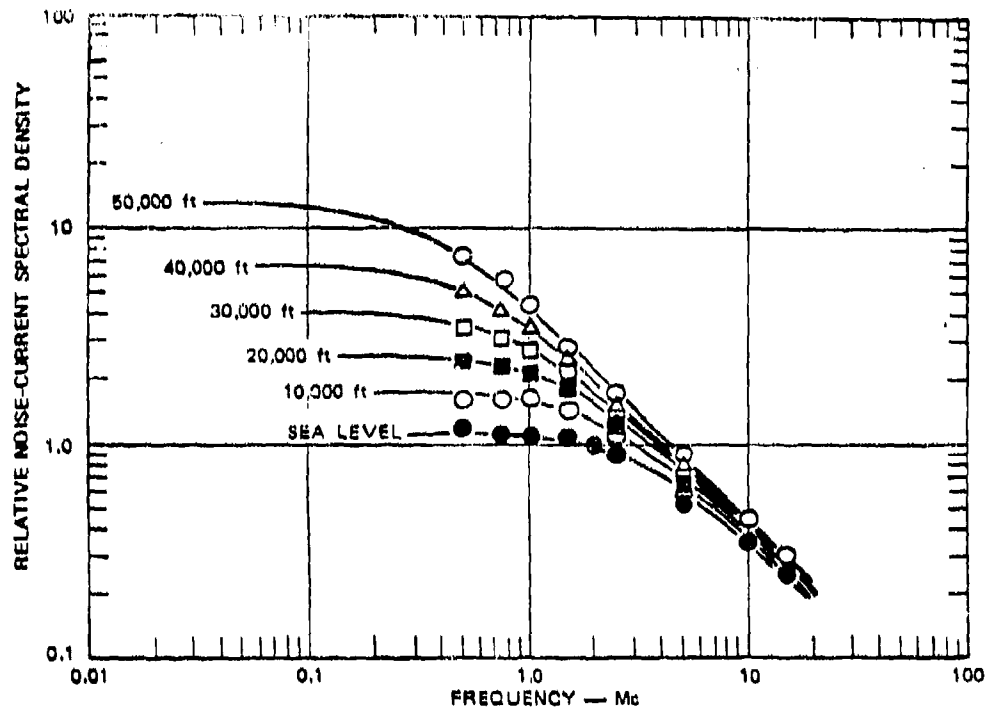
(a) NORMALIZED SPECTRUM SHOWING ALTITUDE EFFECTS
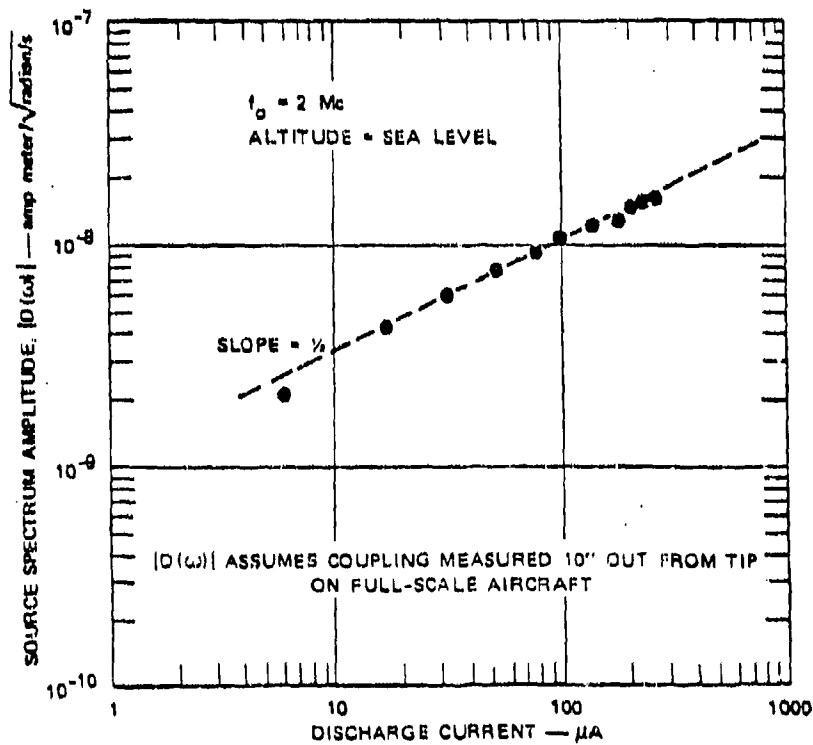
(b) RELATIONSHIP OF ABSOLUTE NOISE LEVEL TO DISCHARGE CURRENT   SA-2919-7

Figure 2-19. Corona-Noise-Source Spectrum Characteristics

2-20

The current flow from a single pulse of a streamer discharge can be approximated by

$$I(t) = I_{max} (ae^{-\alpha t} + be^{-\beta t}) \tag{11}$$

where, for a typical streamer,

$$a = 0.597 \qquad \alpha = 1.67 \times 10^7 \text{ Hz}$$
$$b = 0.403 \qquad \beta = 3.47 \times 10^6 \text{ Hz}$$
$$I_{max} = 0.01 \text{ A}$$

Clearly, this current is many orders of magnitude smaller than that due to lightning.

This waveform has been used with a typical coupling factor of $\psi = 3 \text{ m}^{-1}$ for several streamer lengths to compute the induced current in a wire located immediately below the streamer. The results of these calculations are shown in Figure 2-20.
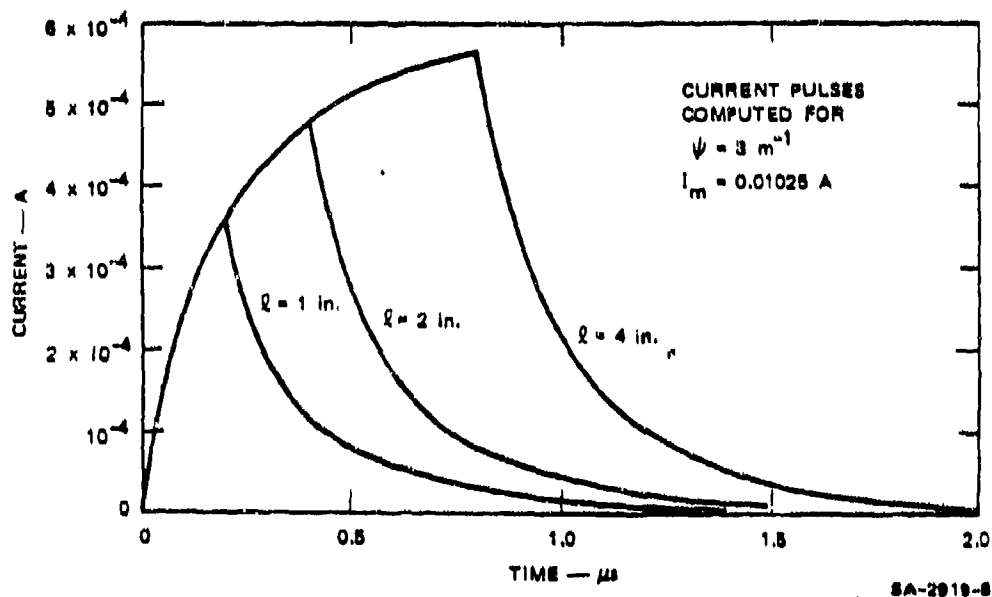
Figure 2-20. Typical Current Pulses Induced by Streamer Discharges

2-21

To aid in understanding streamer-noise source characteristics, source spectrum calculations have been carried out in Reference 1 for various dielectric regions. The results indicate that as the size of the region increased so does the low frequency content of the streamer-noise source spectrum.

2.4 EMP Threat

A nuclear detonation is accompanied by an EM pulse, generally referred to as EMP or nuclear EMP. This EMP should be distinguished from other nuclear, shorter wavelength, EM radiation associated with a nuclear detonation such as visible light, X-rays, or gamma rays.

The EMP threat studied here is the high altitude burst threat which is commonly used in the open literature[2,7]. The incident field is assumed to be a plane wave with an electric field waveform given by a double exponential function as shown in Figure 2-21. Analytically, this waveform is given by·

$$E(t) = V_o(exp^{-\alpha t} - exp^{-\beta t}) \qquad (12)$$

where we will use the following typical values for the parameters:

$$\begin{aligned} V_o &= 58.15 \text{ kV/m} \\ \alpha &= 6.3 \text{ MHz} \\ \beta &= 189 \text{ MHz} \end{aligned} \qquad (13)$$

This waveform has a peak value of 50 kV/m with a rise to peak time of 0.019 µs and a time to half peak amplitude of 0.185 µs. The H-field is assumed to be given by $H = E/\eta_o$ where $\eta_o = 377 \Omega$ is the impedance of free space. It is interesting to note the difference between this threat and the double exponential lightning EMP threat shown in Figure 2-7. The time scale of the lightning EMP is about 100 times that of the EMP. It is really this difference in time scaling that makes the two threats appear so different with regard to threat analysis. This difference shows up clearly in the frequency domain.

The Fourier transform of the EMP threat as given in Equation 12 can be easily computed to give
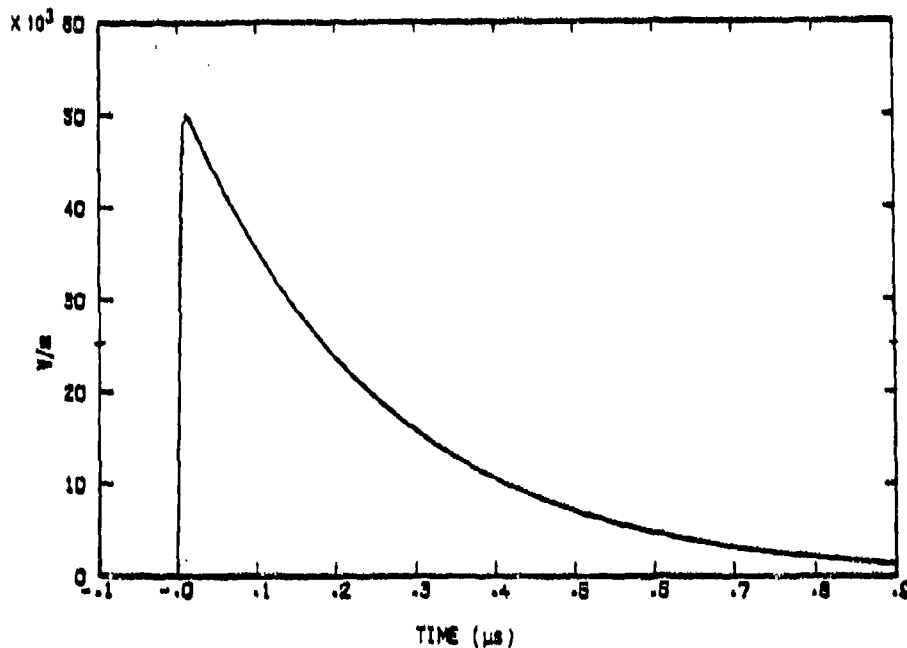
Figure 2-21. EMP Waveform

$$E(\omega) = \frac{V_o(\beta - \alpha)}{(\alpha + j\omega)(\beta + j\omega)} \tag{14}$$

where $\omega = 2\pi f$ and f is frequency.

Figure 2-22 presents a plot of the amplitude of E as a function of frequency. Compare this to Figure 2-12 which shows the spectrum of the double exponential lightning EMP waveform. The EMP waveform has a much higher frequency content than the lightning EMP waveform.

These results tend to verify that for an aircraft size target, the lightning EMP can be treated fairly accurately using low frequency techniques whereas the EMP threat cannot. For example, at 100 MHz (corresponding to a wavelength of ~10 ft) the amplitude of the EMP is about $10^{-2.5}$ times its peak value. The lightning amplitude of this frequency is down from its peak by a factor of 10^{-7}.

2-23
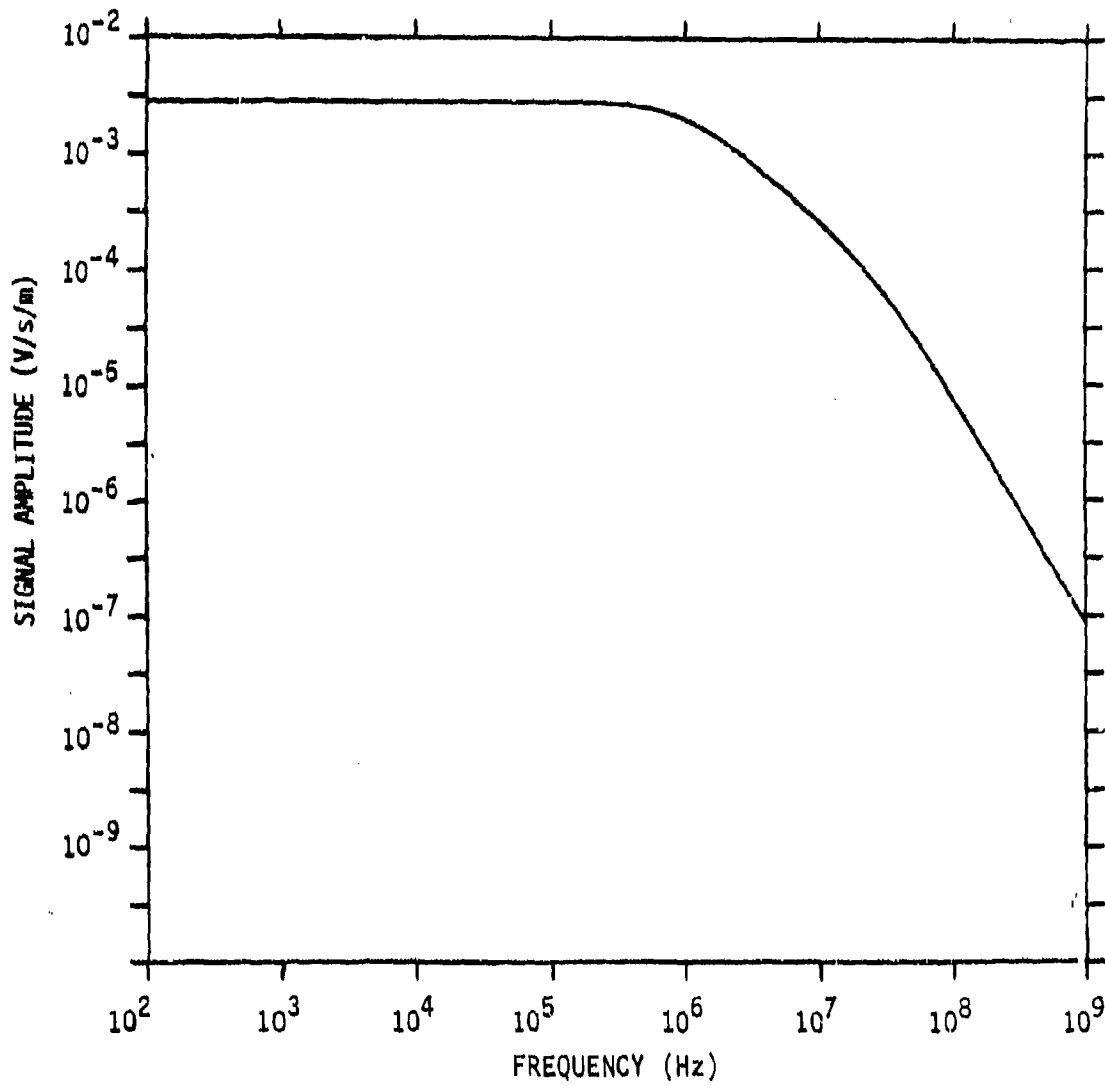
Figure 2-22.   Spectrum of the Double Exponential EMP Waveform
Shown in Figure 2-21

2.5 Shipborne RF Threat

A detailed RF threat document has been generated under separate cover entitled "Threats to the Electromagnetic Integrity of Advanced Composite Aircraft."[8] Sources of the information are included in the document. An unclassified threat level is shown in Figure 2-23. It shows the peak values of the carrier deck environment expressed in V/m. Only the more powerful aircraft carrier transmitters are shown: a navigation aid at 300 to 500 kHz, HF communications at 2 to 30 MHz, and radars at UHF (200 and 450 MHz) and microwave frequencies (greater than 1 GHz). Many other emitters of lower power are not shown.

This information was presented by G. Weinstock of McDonnell-Douglas Corporation, St. Louis, Missouri at the Naval Air Systems Command on 5 March 1979. It correlated well with the threat described in Reference 8.

Radar and communication sources are specified in terms of their effective radiated power (ERP). The peak ERP is available on many emitters. This quantity can be measured on noncooperative emitters and it can also be estimated fairly accurately from knowledge of transmitter output, line losses, and antenna gain. The peak ERP represents the peak power in a pulse or continuous wave/amplitude modulation waveform and the average power in a continuous wave/frequency modulation waveform. The average ERP is calculated by multiplying the peak ERP by the duty cycle for a pulsed radar. Both peak and average ERP are useful for studying electromagnetic interferences, with the peak being used to estimate the voltage spikes induced in the electronics and the average being used to determine heating or burn out levels. ERP has the units of power (watts, kilowatts, etc.) and is frequently expressed in dB referred to a milliwatt (dBm) so $1 \text{ W} = 10^3 \text{ mW} = +30 \text{ dBm}$.

Power density and field intensity generated by a radiating source depend on the distance from the source. Assuming that one is in the far field, the power density is given by:

$$\text{Power Density} = \frac{\text{ERP}}{4\pi \, r^2}$$

2-25
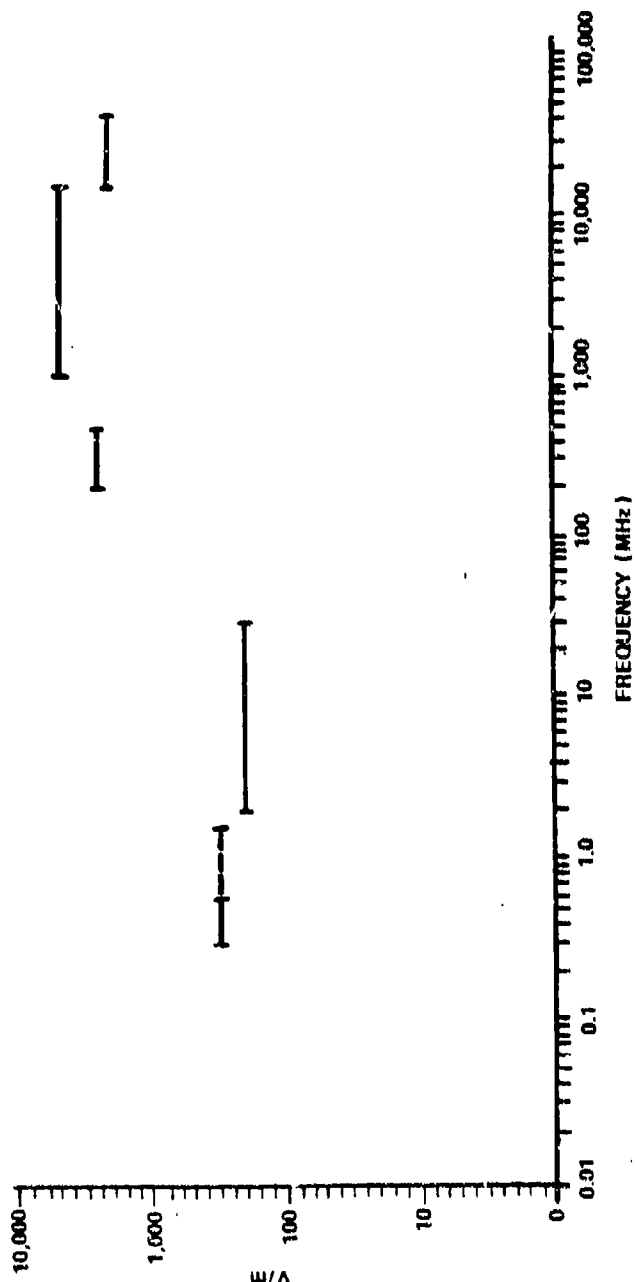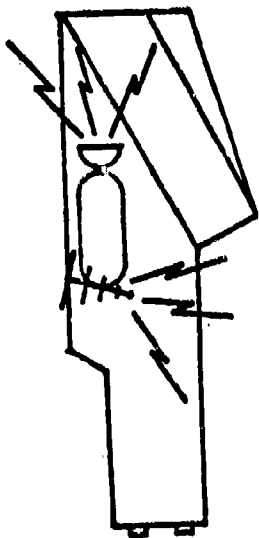
Figure 2-23. Transmitter Field Strength on Carrier Flight Deck

2-26

where r is the distance from the radiator. Power density is commonly expressed in mW/cm^2.

Field intensity is given by:

$$E = \sqrt{\frac{ERP}{4\pi \; r^2}} \; 376.7 \; \Omega$$

If ERP is in W and r is in m, the units of E are V/m which is common usage.

Damage mechanisms for devices are thermal in nature. For worst-case analysis, the heat is assumed to be produced by the absorbed RF signal, and there is no frequency dependence. At pulse durations in excess of about 10 µs, as discussed in Section 7, the amount of power required for damage is set by the rate at which heat can be conducted away from the hot spot. For pulse durations in excess of 30 µs., the average power is

$$P_{avg} = P_{peak} \; x \; PW \; x \; PRF \tag{15}$$

where:

$$P_{avg} = \text{average power}$$
$$P_{peak} = \text{pulse peak power}$$
$$PW = \text{pulse width}$$
$$PRF = \text{pulse repetition frequency}$$

Typical pulse widths are around 0.4 µs and PRFs can vary between 10 to 100 pulse/s up to thousands depending on the application.

In addition, a typical scanning radar typically revolves at 0 to 12 revolution/min with a 1° beamwidth. An aircraft on a carrier deck is then in the main beam of the scanning radar for

$$T_D = \frac{\theta_B}{\frac{RPM \; x \; 360}{60}} \; \text{second/beamwidth}$$

where θ_B is the radar antenna beamwidth and RPM is the revolution/min scan rate of the radar antenna. Antenna dwell times due to scan can thus be roughly on

the order of 50 us. This information is useful in obtaining equivalent rectangular pulse lengths for use in damage power evaluation using a Wunsel model as described in Section 6.

2.6 REFERENCES

1. R.B. Cook and R.A. Peralla, <u>Coupling of Lightning Stroke Currents to F-18 Balanced Twisted Shielded Pair Cables</u>, prepared by Electro Magnetic Applications, Inc., for the Naval Air Systems Command, March 1979.

2. F.A. Fisher and J.A. Plumer, <u>Lightning Protection of Aircraft</u>, prepared by the General Electric Company for NASA Lewis Research Center, NASA Reference Publication 1008, October 1977.

3. R. Force, P. Geren, D. Strawe, and A. Schmidt, <u>Investigation of Effects of Electromagnetic Energy on Advanced Composite Aircraft Structures and Their Associated Avionic/Electrical Equipment</u>, Phase II, Vol. 1, prepared by the Boeing Company for Naval Air Systems Command, Final Report, September 1977.

4. D.M. LeVine and R. Meneghini, <u>Radiation from a Current Filament Driven by A Traveling Wave</u>, prepared by NASA, NASA TN D-8309, October 1976.

5. D.M. LeVine and R. Meneghini, "Simulation of Radiation from Lightning Return Strokes", <u>Radio Science</u>, Vol. 13, No. 5, pp. 801-809, October 1978.

6. Price and Pierce, "The Modeling of Channel Current in the Lightning Return Stroke", <u>Radio Science</u>, Vol. 12, No. 3, pp. 381-388, May-June 1977.

7. L.W. Rickett, J.E. Bridges, and J. Miletta, <u>EMP Radiation and Protective Techniques</u>, John Wiley and Sons, 1976.

8. R.B. Shields, "Threats to the Electromagnetic Integrity of Advanced Composite Aircraft (U)", prepared by the Syracuse Research Corporation under Contract N00014-78-C-0673 for the Naval Air Systems Command and the Office of Naval Research, SRC TN 78-395R1, November 1978 (Secret).

SECTION 3

PENETRATION OF ELECTROMAGNETIC WAVES
THROUGH LOSSY SHELLS

The penetration of electromagnetic waves through lossy shells
is of interest in the general problem of determining electromagnetic
interference of electrical equipment interior to aircraft, missiles, and
other vehicles. The problem we consider here is that of field penetra-
tion into an interior region completely enclosed by a sheet of lossy
matter. For simplicity, we will consider the lossy matter to be linear,
homogeneous, and isotropic. The relaxation of any one of these three
restrictions greatly complicates the problem.

3.1 FORMULATION OF THE PROBLEM

Figure 3-1 illustrates the general problem to be considered. A
time-harmonic electromagnetic wave $\underline{E}^i$, $\underline{H}^i$ is incident on a body defined
by the external surface S_1 and the internal surface S_2. Unit outward
normals to the surfaces S_1 and S_2 are denoted by $\underline{n}_1$ and $\underline{n}_2$, respec-
tively. The two surfaces divide all space into three regions, region
"a" external to S_1, region "b" between S_1 and S_2, and region "c" internal
to S_2. The constitutive parameters of region "a" are denoted by ε_a, μ_a,
of region "b" by ε_b, μ_b, and of region "c" by ε_c, μ_c. Loss is taken into
account by letting ε and/or μ be complex. The total field in region "a"
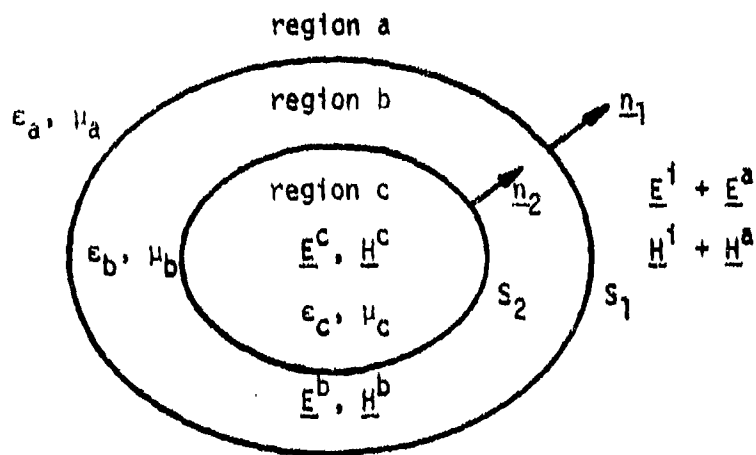
Figure 3-1. A Material Shell excited by an Incident Wave $\underline{E}^i$, $\underline{H}^i$

is denoted by $\underline{E}^i + \underline{E}^a$, $\underline{H}^i + \underline{H}^a$, that in region "b" by $\underline{E}^b$, $\underline{H}^b$, and that in region "c" by $\underline{E}^c$, $\underline{H}^c$.

We next divide the problem into three equivalent problems, one for each region.[1] Figure 3-2 shows the equivalent problem for region "a". It consists of equivalent electric and magnetic currents

$$\underline{J}_1 = \underline{n}_1 \times (\underline{H}^i + \underline{H}^a) \tag{1}$$

$$\underline{M}_1 = (\underline{E}^i + \underline{E}^a) \times \underline{n}_1$$

on S_1, radiating into an infinite medium of constitutive parameters ε_a, μ_a everywhere. The field $\underline{E}^a$, $\underline{H}^a$ is that produced by $\underline{J}_1$, $\underline{M}_1$, which
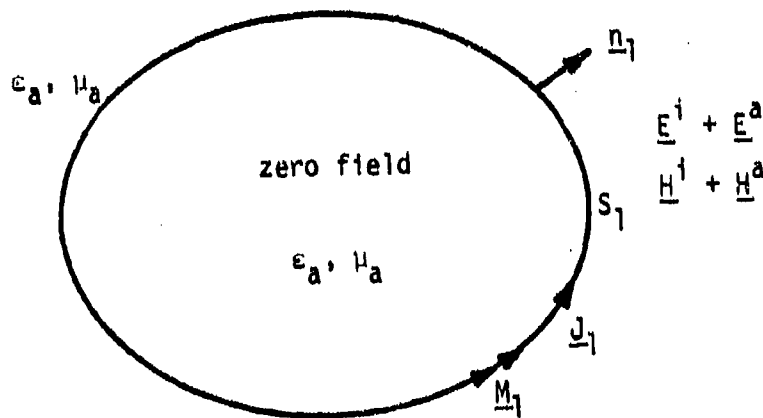
Figure 3-2. Equivalent Problem for Region "a"

can be calculated using the potential integrals and the "infinite region" Green's function

$$G^a = \frac{e^{-jk_a|\underline{r} - \underline{r}'|}}{4\pi |\underline{r} - \underline{r}'|} \qquad (2)$$

where $k_a = \omega\sqrt{\epsilon_a\mu_a}$, and $\underline{r}$, $\underline{r}'$ are the radius vectors to the source point, field point, respectively. We represent this field computation by

$$\underline{E}^a = \underline{E}^a(\underline{J}_1, \underline{M}_1)$$

$$\underline{H}^a = \underline{H}^a(\underline{J}_1, \underline{M}_1) \qquad (3)$$

Note that the $\underline{E}^a$ and $\underline{H}^a$ operators are linear, that is, $\underline{E}^a(\underline{J}, \underline{M}) = \underline{E}^a(\underline{J}, \underline{0}) + \underline{E}^a(\underline{0}, \underline{M})$.

Figure 3-3 shows the equivalent problem for region "b". It consists of the currents $-\underline{J}_1$, $-\underline{M}_1$ on S_1, plus the currents
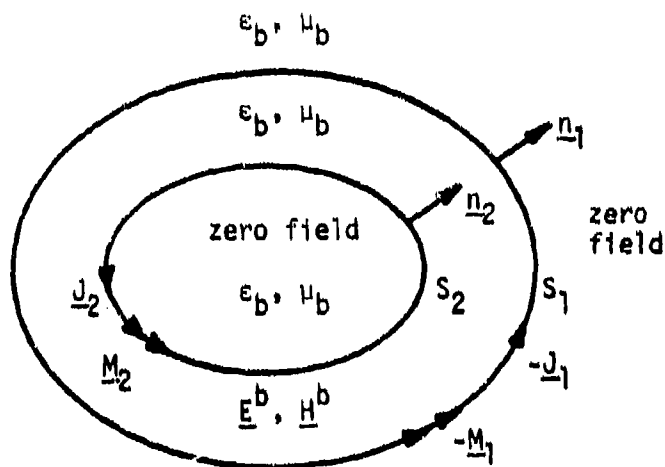
Figure 3-3. Equivalent Problem for Region "b"

$$\underline{J}_2 = \underline{n}_2 \times \underline{H}^b$$

(4)

$$\underline{M}_2 = \underline{E}^b \times \underline{n}_2$$

on S_2, all radiating into an infinite medium with constitutive parameters ε_b, μ_b everywhere. The field $\underline{E}^b$, $\underline{H}^b$ is that produced by $-\underline{J}_1$, $-\underline{M}_1$ and $\underline{J}_2$, $\underline{M}_2$, which can be calculated using the potential integrals and the "infinite region" Green's function

$$G^b = \frac{e^{-jk_b |\underline{r} - \underline{r}'|}}{4\pi |\underline{r} - \underline{r}'|}$$

(5)

where $k_b = \omega\sqrt{\varepsilon_b \mu_b}$. We represent this field computation by

$$\underline{E}^b = -\underline{E}^b(\underline{J}_1, \underline{M}_1) + \underline{E}^b(\underline{J}_2, \underline{M}_2)$$

(6)

$$\underline{H}^b = -\underline{H}^b(\underline{J}_1, \underline{M}_1) + \underline{H}^b(\underline{J}_2, \underline{M}_2)$$

3-4

Here we have used the linearity relationship to replace $\underline{E}^b(-\underline{J}, -\underline{M})$ by $-\underline{E}^b(\underline{J}, \underline{M})$, and similarly for $\underline{H}^b$.

Figure 3-4 shows the equivalent problem for region "c". It consists of the currents $-\underline{J}_2$, $-\underline{M}_2$ on S_2, radiating into an infinite medium with constitutive parameters ϵ_c, μ_c everywhere. The field $\underline{E}^c$, $\underline{H}^c$ is that produced by $-\underline{J}_2$, $-\underline{M}_2$, which can be calculated from the potential integrals and the "infinite region" Green's function

$$G^c = \frac{e^{-jk_c |\underline{r} - \underline{r}'|}}{4\pi |\underline{r} - \underline{r}'|} \tag{7}$$

where $k_c = \omega\sqrt{\epsilon_c \mu_c}$. We represent this field computation by
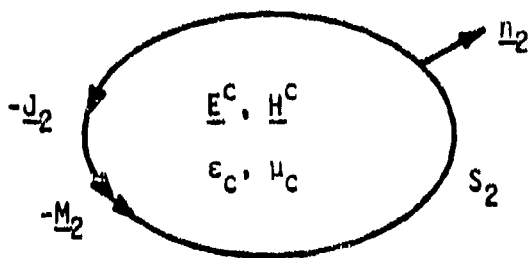
Figure 3-4. Equivalent Problem for Region "c"

$$\underline{E}^c = - \underline{E}^c(\underline{J}_2, \underline{M}_2)$$

$$\tag{8}$$

$$\underline{H}^c = - \underline{H}^c(\underline{J}_2, \underline{M}_2)$$

where we have again used the relationship $\underline{E}^c(-\underline{J}, -\underline{M}) = - \underline{E}^c(\underline{J}, \underline{M})$, and similarly for $\underline{H}^c$.

Finally, we must apply the boundary conditions that tangential components of $\underline{E}$ and $\underline{H}$ in the original problem are continuous across S_1 and S_2. In terms of the equivalent problem "a", $\underline{E}^a_{tan}$ and $\underline{H}^a_{tan}$ must be evaluated just outside S_1, denoted S_1^+, since they are discontinuous across $\underline{J}_1$, $\underline{M}_1$ on S_1. Similarly, in terms of the equivalent problem "b", $\underline{E}^b_{tan}$ and $\underline{H}^b_{tan}$ must be evaluated just inside S_1, denoted S_1^-, since they are discontinuous across $-\underline{J}_1$, $-\underline{M}_1$ on S_1. We therefore have for the continuity conditions on S_1

$$(\underline{E}^a + \underline{E}^i)_{tan\ S_1^+} = \underline{E}^b_{tan\ S_1^-}$$

$$\tag{9}$$

$$(\underline{H}^a + \underline{H}^i)_{tan\ S_1^+} = \underline{H}^b_{tan\ S_1^-}$$

Similar reasoning and notation leads to the continuity conditions for S_2

$$\underline{E}^b_{tan\ S_2^+} = \underline{E}^c_{tan\ S_2^-}.$$

$$\tag{10}$$

$$\underline{H}^b_{tan\ S_2^+} = \underline{H}^b_{tan\ S_2^-}$$

The four equations resulting from substituting Equations 3, 6, and 8 into

Equations 9 and 10 are sufficient to determine the four unknowns $\underline{J}_1$, $\underline{M}_1$, $\underline{J}_2$, and $\underline{M}_2$.

To express these four equations in operator notation, we define the following linear operators:

$$\underline{E}^a_{tan\ S_1^+} = -\mathcal{L}^a_{11}(\underline{J}_1, \underline{M}_1)$$

$$\underline{H}^a_{tan\ S_1^+} = -\mathcal{M}^a_{11}(\underline{J}_1, \underline{M}_1)$$

$$\underline{E}^b_{tan\ S_1^-} = \mathcal{L}^b_{11}(\underline{J}_1, \underline{M}_1) - \mathcal{L}^b_{21}(\underline{J}_2, \underline{M}_2)$$

$$\underline{H}^b_{tan\ S_1^-} = \mathcal{M}^b_{11}(\underline{J}_1, \underline{M}_1) - \mathcal{M}^b_{12}(\underline{J}_2, \underline{M}_2) \qquad (11)$$

$$\underline{E}^b_{tan\ S_2^+} = \mathcal{L}^b_{12}(\underline{J}_1, \underline{M}_1) - \mathcal{L}^b_{22}(\underline{J}_2, \underline{M}_2)$$

$$\underline{H}^b_{tan\ S_2^+} = \mathcal{M}^b_{12}(\underline{J}_1, \underline{M}_1) - \mathcal{M}^b_{22}(\underline{J}_2, \underline{M}_2)$$

$$\underline{E}^c_{tan\ S_2^-} = \mathcal{L}^c_{22}(\underline{J}_2, \underline{M}_2)$$

$$\underline{H}^c_{tan\ S_2^-} = \mathcal{M}^c_{22}(\underline{J}_2, \underline{M}_2)$$

It should be apparent that, in the notation $\mathcal{L}^x_{pq}$, x denotes the constitutive parameters ϵ_x, μ_x, p denotes the surface S_p on which the currents reside, and q denotes the surface S_q on which the tangential components of $\underline{E}$ are evaluated. Similar notation applies to the $\mathcal{M}^x_{pq}$ operator for

the tangential components of $\underline{H}$. $\mathcal{L}$ denotes an electric-field operator and $\mathcal{M}$ denotes a magnetic-field operator. We can now write the equations resulting from Equation 10 as

$$\mathcal{L}^a_{11}(\underline{J}_1, \underline{M}_1) + \mathcal{L}^b_{11}(\underline{J}_1, \underline{M}_1) - \mathcal{L}^b_{21}(\underline{J}_2, \underline{M}_2) = \underline{E}^i_{tan} \, S_1$$

$$\mathcal{M}^a_{11}(\underline{J}_1, \underline{M}_1) + \mathcal{M}^b_{11}(\underline{J}_1, \underline{M}_1) - \mathcal{M}^b_{21}(\underline{J}_2, \underline{M}_2) = \underline{H}^i_{tan} \, S_1$$

$$\quad (12)$$

$$-\mathcal{L}^b_{12}(\underline{J}_1, \underline{M}_1) + \mathcal{L}^b_{22}(\underline{J}_2, \underline{M}_2) + \mathcal{L}^c_{22}(\underline{J}_2, \underline{M}_2) = 0$$

$$-\mathcal{M}^b_{12}(\underline{J}_1, \underline{M}_1) + \mathcal{M}^b_{22}(\underline{J}_2, \underline{M}_2) + \mathcal{M}^c_{22}(\underline{J}_2, \underline{M}_2) = 0$$

The $\underline{E}^i$, $\underline{H}^i$ are continuous across S_1, hence we have dropped the superscript on S_1 in the right hand terms of the first two equations. The operators $\mathcal{L}$ and $\mathcal{M}$ are known, but complicated. Equation 12 are general in that they apply to any shell of linear, homogeneous, and isotropic matter. It should be pointed out that there are other surface formulations for the problem[2] equivalent to the one we have discussed in detail above.

3.2 THIN HIGHLY CONDUCTING SHELLS

Composite materials which have a high conductivity ($\sigma \sim 10^4$) are used extensively in military aircraft construction. We have considered some approximate formulations for thin highly conducting shells.

For very low frequencies, that is, when the wavelength in the shell is large compared to shell thickness t, we can use the impedance sheet approximation of Reference 3. In this case, the problem reduces to that of a loaded body, for which the operator equation is[4]

$$\mathcal{L}(\underline{J}) + \mathcal{Y}_L \underline{J} = \underline{E}^i_{\tan} \ S \tag{13}$$

Here we have considered S_1 and S_2 to be approximately the same surface S, supporting an electric current $\underline{J}$. The effect of the equivalent magnetic current is negligible compared to that of $\underline{J}$. The load impedance for this case is obtained by substituting σ_b for $j\omega\Delta\epsilon$ in Reference 3, or

$$\mathcal{Y}_L = \frac{1}{\sigma_b d} \tag{14}$$

Since the shell is highly conducting, this solution is valid only at very low frequencies.

For higher frequencies we can consider region "b" to support traveling waves, and use a transmission line analogy[5]. Figure 3-5 shows a section of the shell between surfaces S_1 and S_2, assumed to be locally plane. The intrinsic impedance of the shell

$$\eta_b \approx (1 + j)\sqrt{\frac{\omega\mu_b}{2\sigma_b}} \tag{15}$$

is normally much smaller in magnitude than η_a and η_c (usually free space). Hence, region "a" sees almost a short circuit at S_1, and region "b" sees almost an open circuit at S_2. Thus, in region "b", we have
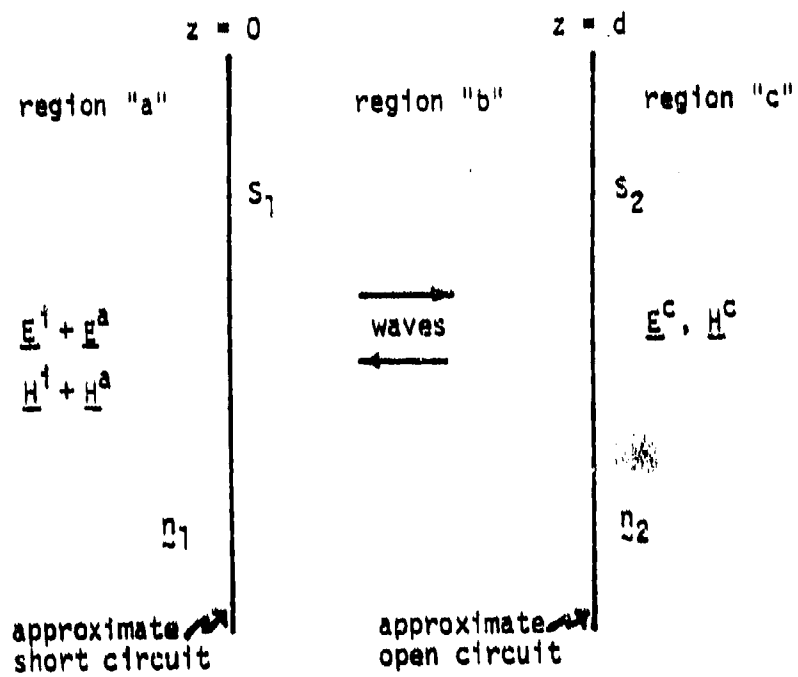
Figure 3-5. Wave Approximation for the Thin Highly Conducting
Shell Problem

$$H_t = A \sinh \gamma_b(t - z)$$

$$(16)$$

$$E_t = \eta_b A \cosh \gamma_b(t - z)$$

where γ_b is the intrinsic propagation constant in the shell,

$$\gamma_b = (1 + j) \sqrt{\frac{\omega \mu_b \sigma_b}{2}}$$

$$(17)$$

and z is the distance from S_1 in region "b". The impedance seen at S_1 is

$$\eta_L = \left.\frac{E_t}{H_t}\right|_{z=0} = \eta_b \coth \gamma_b t$$

$$(18)$$

Insofar as the external problem is concerned, we still use Equation 13 for the external problem with η_L given by Equation 18. Note that

$$\eta_L \xrightarrow[t \to 0]{} \frac{1}{\sigma_b t}$$

$$(19)$$

which is the very low frequency approximation, and

$$\eta_L \xrightarrow[t \to \infty]{} \eta_b$$

$$(20)$$

which is the high frequency approximation; i.e., the shell looks infinitely thick to the exterior field.

It still remains to determine the interior field. For this, evaluate A in Equation 16 by letting $z = 0$.

$$J_1 = H_t = A \sinh \gamma_b t$$

$$(21)$$

$$M_1 = E_t = \eta_b A \cosh \gamma_b t$$

3-11

The first equation gives

$$A = \frac{J}{\sinh \gamma_b t} \tag{22}$$

where we have set $J_1 = J$ of Equation 13. The second equation of Equation 21 gives an approximate solution for M_1, which is not needed for the internal problem. (The M_1 insures that the wave in the equivalent problem of Figure 3-3 travels only inward; i.e., there is zero field external to region "b".) Using Equation 22 and setting $z = t$ in Equation 16, we have

$$H_t \Big|_{z=t} \approx 0$$

$$E_t \Big|_{z=t} \approx \eta_b \frac{J}{\sinh \gamma_b t} \tag{23}$$

We use approximate equalities in Equation 23 because we have used the approximation that region "b" sees an open circuit at S_2. From Equation 23 we have

$$\underline{J}_2 \approx 0$$

$$\underline{M}_2 \approx \frac{-\eta_b}{\sinh \gamma_b t} \, \underline{n} \times \underline{J} \tag{24}$$

For a better approximation to $\underline{J}_2$ in Equation 24 we could use the wave impedance looking into region "c" to relate $\underline{J}_2$ to $\underline{M}_2$. For this, we could use $\underline{M}_2$ as known in the third equation of Equation 12 with $\mathcal{L}_{12}^b = 0$ to determine $\underline{J}_2$. Alternatively, we could use $\underline{M}_2$ as known in the fourth equation of (12) with $\mathcal{m}_{12}^b = 0$ to determine $\underline{J}_2$. If necessary, we could also take $\underline{J}_1$ and $\underline{M}_1$ as known quantities in either of these two equations. For a cruder,

but easier approximation, we could assume plane waves at S_2 in region "c", and obtain

$$\underline{J}_2 \approx \frac{\eta_b}{\eta_c \sinh \gamma_b t} \ \underline{J}$$ (25)

Since $1/\eta_c \ll 1$ usually, $\underline{J}_2$ is small compared to $\underline{M}_2$, but not zero as implied by the first of equation of Equation 24.

Once whe have $\underline{M}_2$ and $\underline{J}_2$, we can calculate $\underline{E}^c$ and $\underline{H}^c$ in region "c" by solving the "homogeneous region" problem of Figure 3-4. This involves the potential integrals with constitutive parameters those of region "c". Note that, insofar as the field in region "c" is concerned, the equivalent magnetic current $\underline{M}_2$ contributes more than the equivalent electric current $\underline{J}_2$.

3.3 DISCUSSION

The general three region problem, presented by Figure 3-1, is basically very complicated. The solution of the three equivalent problems, Figures 3-2, 3-3, and 3-4, could in principle be obtained by solving Equation 3-12 by the moment method[5,6]. For shells of revolution, the required computer programs could be obtained from those used ̄ a homogeneous material body of revolution[2]. However, this would require considerable effort. A combination of these programs plus the thin shell approximations of Subsection 3.2 could be used for an approximate solution to that problem. However, this again represents a considerable effort. In any event, a careful study should be made to determine the ranges of parameters for which the thin conducting shell approximations are valid.

3.4 REFERENCES

1. R. F. Harrington, "Time-Harmonic Electromagnetic Fields," McGraw-Hill Book Co., 1961, pp. 106-110.

2. J. R. Mautz and R. F. Harrington, "Electromagnetic Scattering from a Homogeneous Material Body of Revolution," A.E.Ü. (Germany), vol. 33, No. 2, February 1979, pp. 71-80. See also Report RADC-TR-78-16, January 1978.

3. R. F. Harrington and J. R. Mautz, "An Impedance Sheet Approximation for Thin Dielectric Shells," IEEE Trans., vol. AP-23, No. 4, July 1975, pp. 531-534.

4. R. F. Harrington and J. R. Mautz, "Radiation and Scattering from Loaded Bodies of Revolution," Appl. Sci. Res., vol. 26, June 1971, pp. 209-217. See also Report AFCRL-70-0046, D.D.C. No. 701744, January 1970.

5. S. Ramo and J. R. Whinnery, "Fields and Waves in Modern Radio," second edition, John Wiley and Sons, 1953, Chap. 7.

6. R. F. Harrington, "Field Computation by Moment Methods," Macmillan Co., 1968, Chap. 5.

7. A. J. Poggio and E. K. Miller, "Integral Equation Solutions of Three-dimensional Scattering Problems," in R. Mittra (Ed.), "Computer Techniques for Electromagnetics," Pergamon Press, 1973, Chap. 4.

SECTION 4

RELATIONSHIP OF MATERIAL PROPERTIES AND
TRANSFER IMPEDANCE TO EM SHIELDING

The EM protection offered by a shield is generally specified in terms
of the electric and magnetic shielding effectiveness of the shield, which is
defined by

$$MSE = 20 \log_{10} |MSR^{-1}| \tag{1}$$

where

$$MSR^{-1} = \frac{H_{INCIDENT}}{H_{INTERNAL}} \tag{1a}$$

and

$$ESE = 20 \log_{10} |ESR^{-1}| \tag{2}$$

where

$$ESR^{-1} = \frac{E_{INCIDENT}}{E_{INTERNAL}} \tag{2a}$$

The quotients of the interior and incident fields are referred to as the magne-
tic and electric shielding ratios. In the literature that is available, some
authors (e.g., Bedrosian and Lee with respect to uniform incident fields) de-
fine the magnetic shielding ratio to be the ratio of the internal magnetic field
to the uniform portion of the external magnetic field. One must be careful when
using this definition since the "definition" can change with shield geometry:
for a flat shield the scattered field is uniform so the entire external field
is uniform, while for a curved shield only the incident field will be uniform.
The inclusion of the scattered field in the magnetic shielding ratio introduces
a 6 dB gain in the magnetic shielding effectiveness of the shield.

The basic problem with such shielding specification is one of unique-
ness. In general, the interior fields are not spacially uniform even when those

external to the shield   In this case, the shielding effectiveness becomes dependent upon the choice of the interior field to use in the shielding effectiveness definition. Although the shielding effectiveness specification can be ambiguous, there, are certain geometries for which a spacially uniform incident field will produce a uniform interior field. These geometries are shown in Figure 4-1. For these cases, the shielding effectiveness definitions are unique. The indicated dimensions are assumed to be small in free space wavelengths.

The interrelationships between electric shielding effectiveness, magnetic shielding effectiveness, and surface transfer impedance for these geometries under an incident uniform magnetic/electric field and their dependence upon the incident frequency and the shield material parameters have been investigated. Included in the investigation was a study of the magnetic shielding effectiveness of an infinite flat plate with an incident nonuniform magnetic field generated by a nearby loop antenna. A complete detailed report of this study is contained in Reference 6.

4.1 SHIELD EFFECTIVENESS FOR A UNIFORM MAGNETIC FIELD

For a uniform magnetic field, the magnetic shielding effectiveness is a function of the shield material parameters (σ, μ, ε, d), the frequency of the impinging wave, and the shield geometry. The shielding effectiveness formulas are summarized in Table 4-1.

For low frequencies, $\omega < \dfrac{0.1}{\mu \varepsilon d^2}$[*], the inverse magnetic shielding ratio of a flat plate is given by

$$MSR^{-1} \simeq 1 + Z_o \, \sigma \, d \tag{3}$$

and hence is completely determined by the conductivity and the thickness of the shield. Figure 4-2 illustrates the low frequency magnetic shielding effectiveness available for aluminum, titanium, mixed-orientation graphite/epoxy, and

---

[*] $\omega < \dfrac{0.1}{\mu \sigma d^2}$ => $\cosh(\gamma d) \simeq 1$, $\sinh(\gamma d) \simeq \gamma d$.

4-2
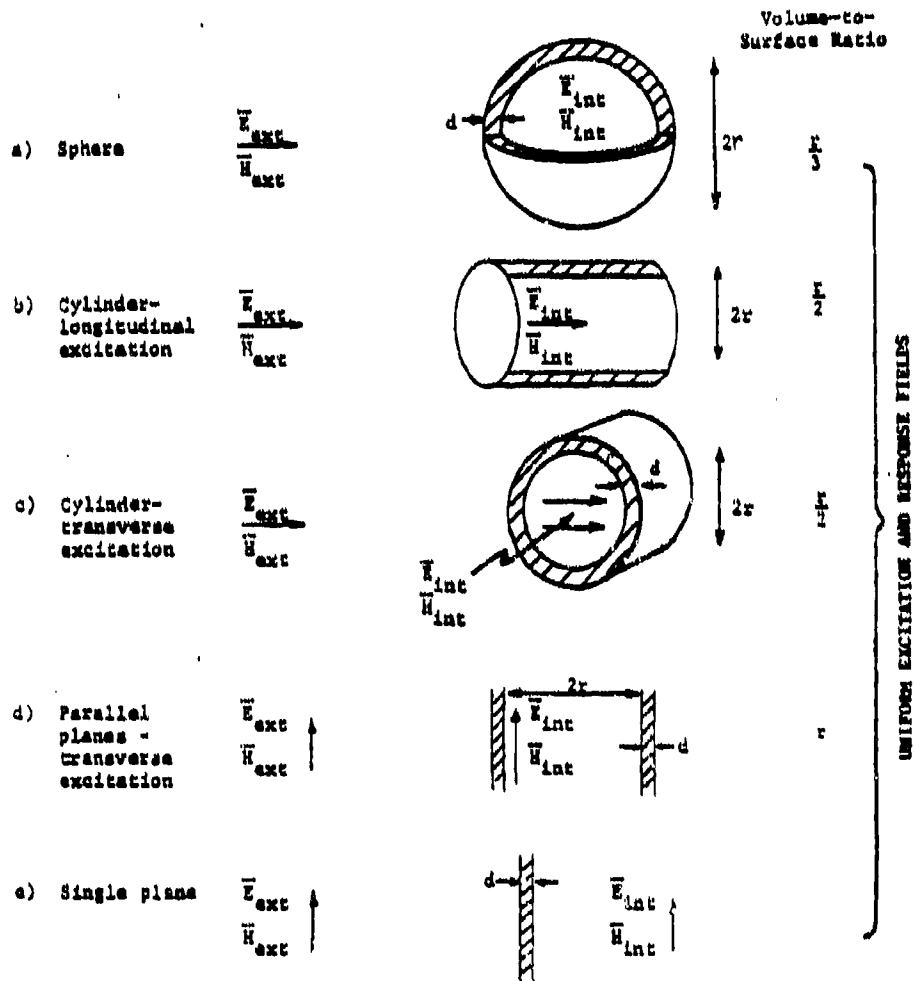
Figure 4-1.   Shield Geometries for which Spacially Uniform Exterior
               Fields Produce Uniform Interior Fields

PLATE THICKNESS CORRESPONDS TO 8 PLY COMPOSITE MATERIAL
AT 0.00525 IN/PLY

SHIELD CONDUCTIVITY, σ, IN UNITS OF mhos/m
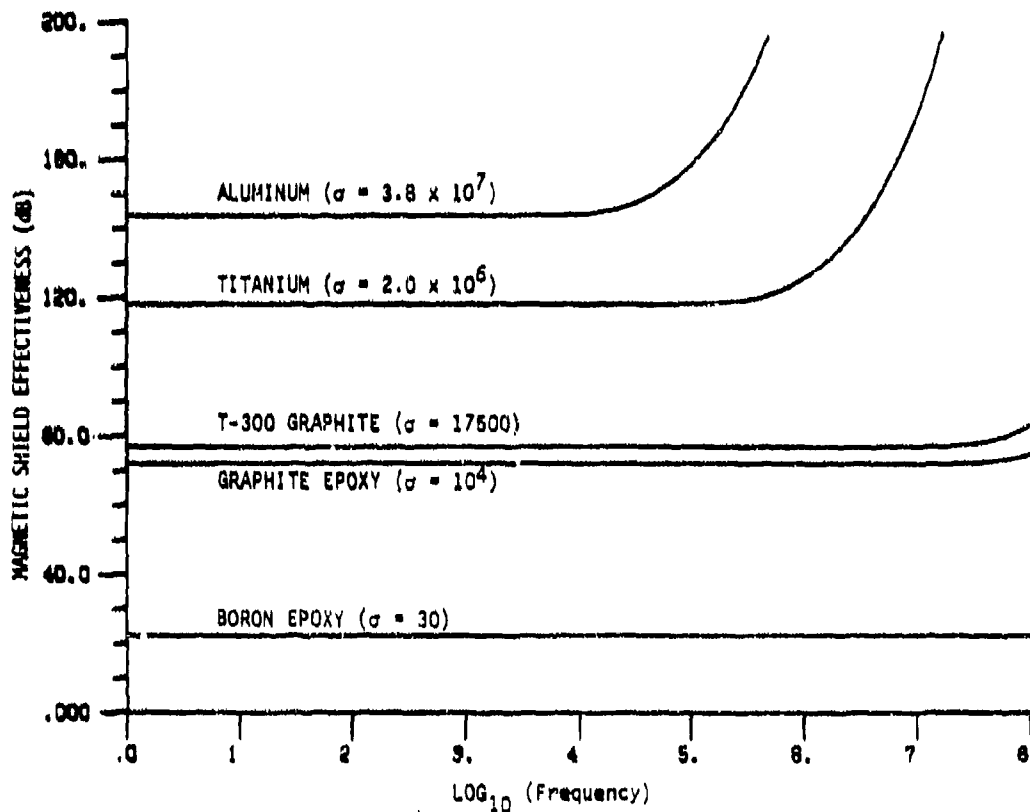
Figure 4-2. Magnetic Shielding Effectiveness of a Flat Plate under
a Uniform Magnetic Field

4-4

**Table 4-1. Magnetic Shielding Effectiveness Formulas
for Incident Uniform Magnetic Fields**

Geometry	Inverse Magnetic Shielding Ratio $(MSR^{-1} = \dfrac{H_{INCIDENT}}{H_{INTERNAL}})$
flat plate	$\cosh(\gamma d) + Z_o/2\eta \ \sinh(\gamma d)$
parallel plates (separation 2r)	$\cosh(\gamma d) + Z/\eta \ \ \sinh(\gamma d)$
cylindrical shell (radius r)	$\cosh(\gamma d) + Z/2\eta \ \ \sinh(\gamma d)$*
spherical shell (radius r)	$\cosh(\gamma d) + \frac{1}{3} [Z/\eta + 2\eta/Z] \ \sinh(\gamma d)$

where $Z = j\omega\mu r$, $\eta = [j\omega\mu/\sigma]^{1/2}$, $\gamma = [j\omega\mu\sigma]^{1/2}$, $Z_o = 377$, and $d =$ the shield thickness

mixed-orientation boron/epoxy flat plates of 0.00107 m (corresponding to 8-ply composite material at 0.00525 in/ply) thickness.

The remaining geometries, referred to as enclosure geometries, are frequency dependent at low frequencies. The inverse magnetic shielding ratios for enclosures can be written as

$$MSR^{-1} = \cosh(\gamma d) + \frac{V}{S} \ \gamma\sinh(\gamma d) \qquad (4)$$

where $\frac{V}{S}$ is the volume-to-surface ratio in MSK units of the enclosure. For spherical geometries this representation is valid only for

$$f > [9\pi \ \mu\sigma \ (\frac{V}{S})^2]^{-1}. \qquad (5)$$

For low frequencies, $\omega < 0.1/\mu\sigma d^2$, the inverse magnetic shielding ratio for an enclosure can be approximated by

$$MSR^{-1} = 1 + (\frac{V}{S}) \gamma^2 d . \qquad (6)$$

---

*King (Reference 1) has shown that this formula is valid for all angles of incidence of the external field relative to the cylinder axis for $r \ll d$.

Hence, at low frequencies, the magnetic shielding effectiveness of an enclosure in a uniform incident magnetic field is dependent upon the field frequency as well as on the shield geometry (expressed in $\frac{V}{S}$) and the material parameters (σ and d) of the shield.

The magnetic shielding effectiveness of an enclosure exhibits a "break point" at

$$f_b = [2\pi \left(\frac{V}{S}\right) \mu\sigma d]^{-1} \qquad (7)$$

below which the magnetic shielding effectiveness is approximately zero. Above the breakpoint the magnetic shielding effectiveness increases with frequency as $20 \log_{10}(f/f_b)$. This behavior is illustrated in Figure 4-3 for aluminum, titanium, and mixed-orientation graphite/epoxy composite enclosures with unit volume-to-surface ratio and a shield thickness of 0.005 m. Since the volume-to-surface ratio is proportional to the radius (plate separation) of the enclosure, the breakpoint frequency is inversely proportional to the enclosure radius (plate separation), the shield conductivity and the shield thickness.

Figure 4-4 illustrates the dependence of magnetic shielding effectiveness of an enclosure on the volume-to-surface ratio. The graph is for an 8-ply mixed-orientation graphite/epoxy composite ($\sigma = 10^4$ mhos/m). As can be seen from Equation 6, the magnetic shielding effectiveness of an enclosure increases as $20 \log \frac{V}{S}$.

Figure 4-5 is included to emphasize the differences in magnetic shielding effectiveness as one changes the shield geometry. It is very important in discussing the magnetic shielding effectiveness of a shield that one must not only identify the shield's material parameters but also the shield geometry. The data shown is for an 8-ply mixed-orientation graphite/epoxy shield ($\sigma = 10^4$ mhos/m).

It should be stressed that these shielding results are valid for the enclosures described only when the incident field is a uniform magnetic field.

4-6
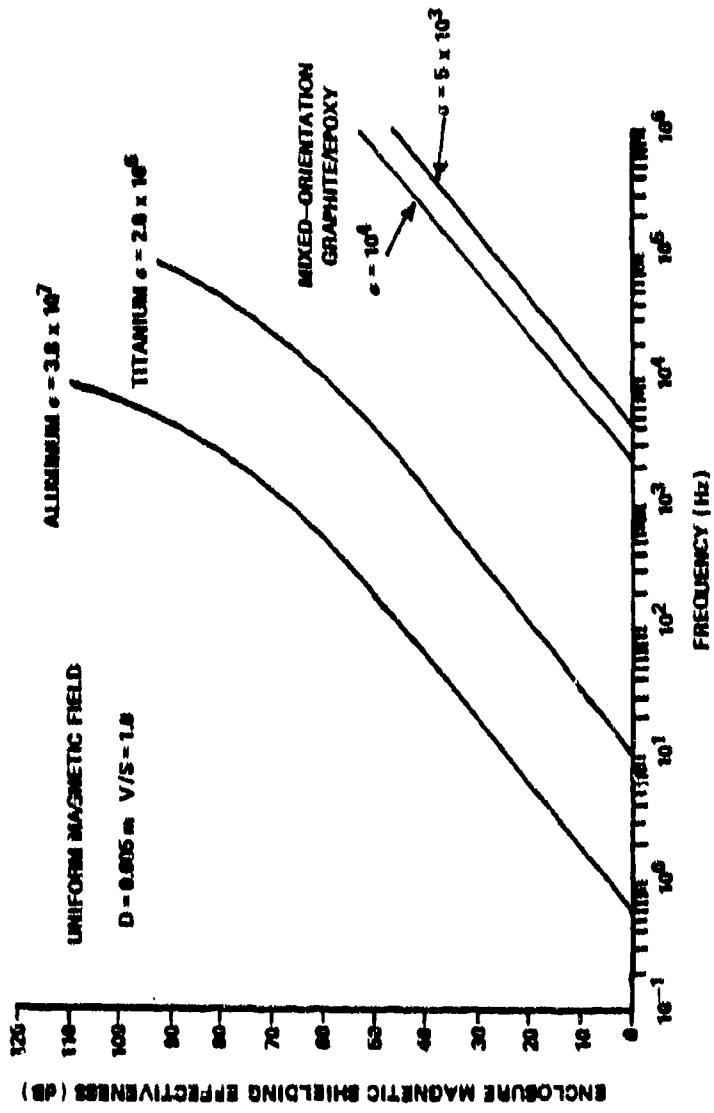
Figure 4-3. Magnetic Shielding Effectiveness Breakpoint Behavior for Enclosures

4-7

SHIELD THICKNESS CORRESPONDS TO 8 PLY COMPOSITE
MATERIAL AT 0.00525 IN/PLY

SHIELD CONDUCTIVITY = 10^4 mhos/m
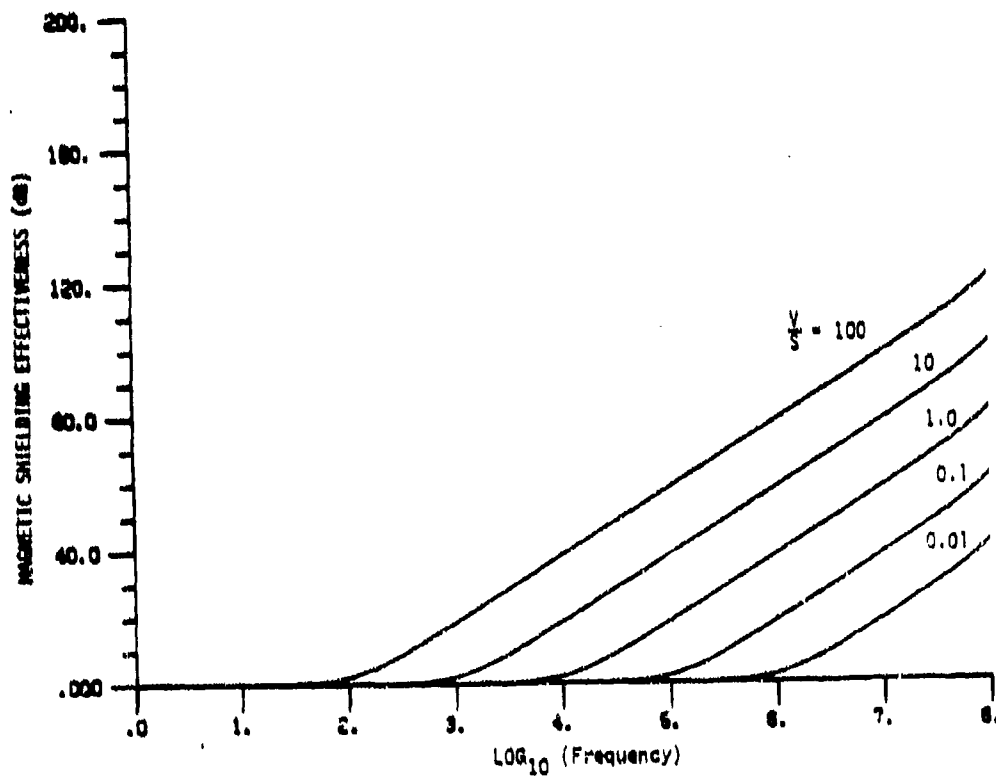
Figure 4-4. Magnetic Shielding Effectiveness of an Enclosure under a
Uniform Magnetic Field as a Function of Volume-to-Surface
Ratio

SHIELD THICKNESS CORRESPONDS TO 8 PLY COMPOSITE
MATERIAL AT 0.00525 IN/PLY

SHIELD CONDUCTIVITY = 10^4 mohs/m
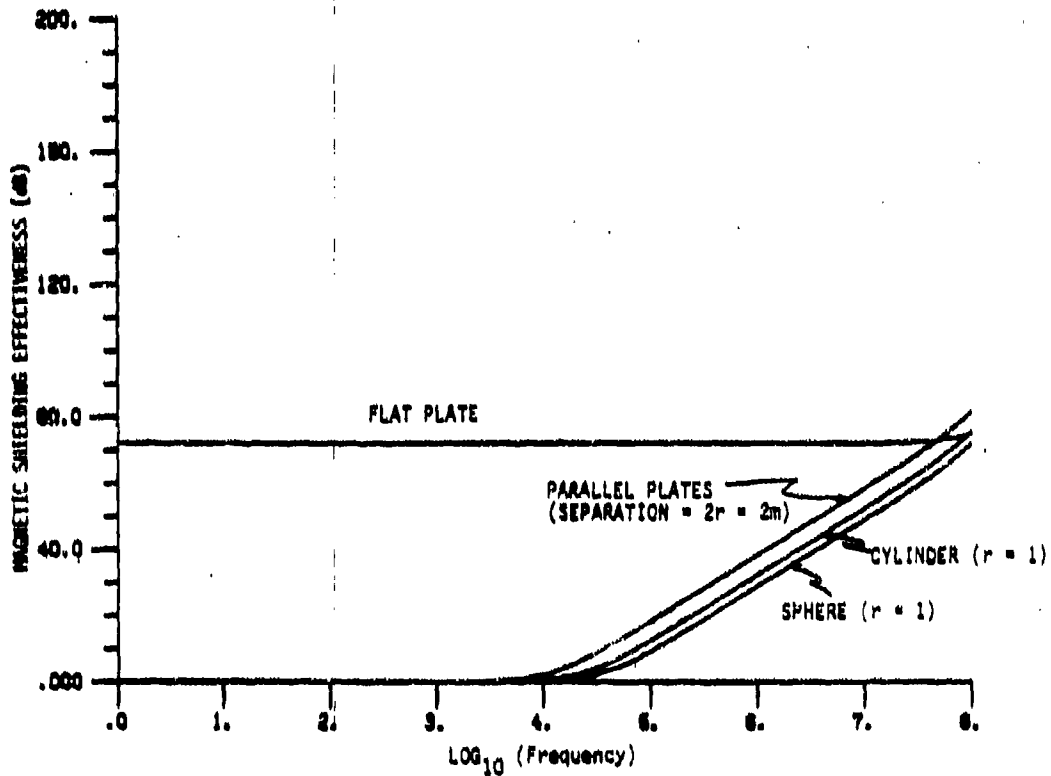
Figure 4-5. Magnetic Shielding Effectiveness on the Uniform Incident
Magnetic Field

To illustrate that the shielding effectiveness of a shield is dependent upon the type of field incident upon the shield, we consider a nonuniform magnetic field incident on an infinite flat plate.

4.2 FLAT PLATE SHIELDING FOR A NONUNIFORM MAGNETIC FIELD

The geometry for studying the magnetic shielding effectiveness of an infinite flat plate with an incident nonuniform magnetic field generated by a loop antenna parallel to the shield is given in Figure 4-6. An integral expression for the magnetic shielding effectiveness has been derived by Bannister[1], for which quite managable low frequency approximations exist with the appropriate frequency restrictions. The expressions presented are valid only for those materials which are essentially isotropic in the plane of the flat plate; e.g., for multilayer mixed-orientation graphite laminates but not for unidirectional samples. This restriction is a consequence of the need for roughly circular currents to flow in the plane of the flat plate if the incident magnetic field is to be terminated.
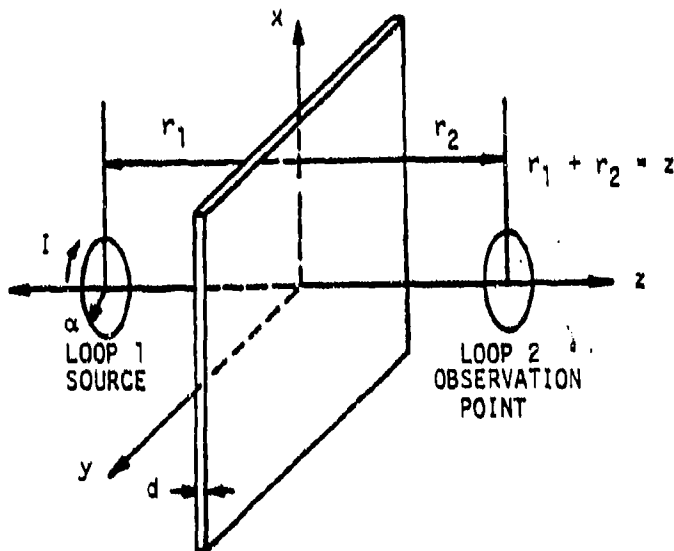
Figure 4-6.   Geometry for Magnetic Shielding Effectiveness of an
Infinite Flat Plate under a Nonuniform Magnetic Field

For $\dfrac{0.5}{\mu\sigma d^2} < \omega < 2\pi c/(20[a^2 + (r_1 + r_2 - d)^2]^{1/2})$

$$MSE = 8.686 \ [\omega\mu\sigma/2]^{1/2} \ d + 20 \ \log_{10} \ [(\omega\mu\sigma/2)^{1/2}(r_1 + r_2)/8.485]^{(1)} \qquad (8)$$

For $\dfrac{200}{\mu\sigma \ (a^2 + (r_1 + r_2))^2} < \omega < \min \begin{cases} 4/(\mu\sigma d^2) \\ 2\pi c/(20[a^2 + (r_1 + r_2 - d)^2]^{1/2}) \end{cases}$

$$MSE = 10 \ \log_{10} \ [1 + [(\frac{\omega\mu\sigma d}{6})(\frac{a^2 + (r_1 + r_2)^2}{r_1 + r_2})]^2 \ . \qquad \overset{(2)}{\qquad} \qquad (9)$$

Both of these approximations are made under the assumption that $(r_1 + r_2) \gg d$.

Note that in the case of a nonuniform field generated by a loop anten-na, the magnetic shielding effectiveness is dependent not only upon the shield parameters (σ, d) and frequency but also on the source-shield geometry (a, r_1, r_2). For $(r_1 + r_2) \gg a$, $(r_1 + r_2) \ (\frac{\omega\mu\sigma d}{6}) > 1$, the dependence of the magnetic shielding effectiveness on the source-shield geometry (a, r_1, r_2) can be ex-pressed as

$$MSE = \zeta(f, \ \sigma, \ d) + 20 \ \log_{10} \ (r_1 + r_2) \ . \qquad (10)$$

Figure 4-7 gives the magnetic shielding effectiveness as a function of conduc-tivity and shield thickness for conductivities of 3.8×10^7 mhos/m (aluminum) and 17500 mhos/m, 1.0×10^4 mhos/m, 5×10^3 mhos/m (conductivities associated with mixed-orientation graphite/epoxy composite) and shield thickness of 0.0032 m, 0.00214 m, and 0.00107 m (corresponding to the thickness of 24, 16, and 8 ply graphite/epoxy laminates at 0.0525 in/ply). The source-shield geometry was chosen in accordance with the flat plate test facility described in Boeing D180-18879-1[6] with the loop radii equal to 0.013 m (1/2 in.) and a source to detec-tor loop center to center separation of 0.0509 m (2 in.). The theoretical results shown for the mixed-orientation graphite/epoxy composite compare very closely to Boeing test results for 24 ply, 16 ply, and 8 ply T300 graphite/epoxy laminate with 0°/45°/90° and 0°/90° layups. These test results are shown in Figures 4-8a and 4-8b, respectively.

LOOP DIAMETER = 1 in.

ANTENNA-PLATE SEPARATION = 1 in.

PLATE THICKNESS CORRESPONDS TO 8 PLY COMPOSITE
MATERIAL AT 0.00525 IN/PLY
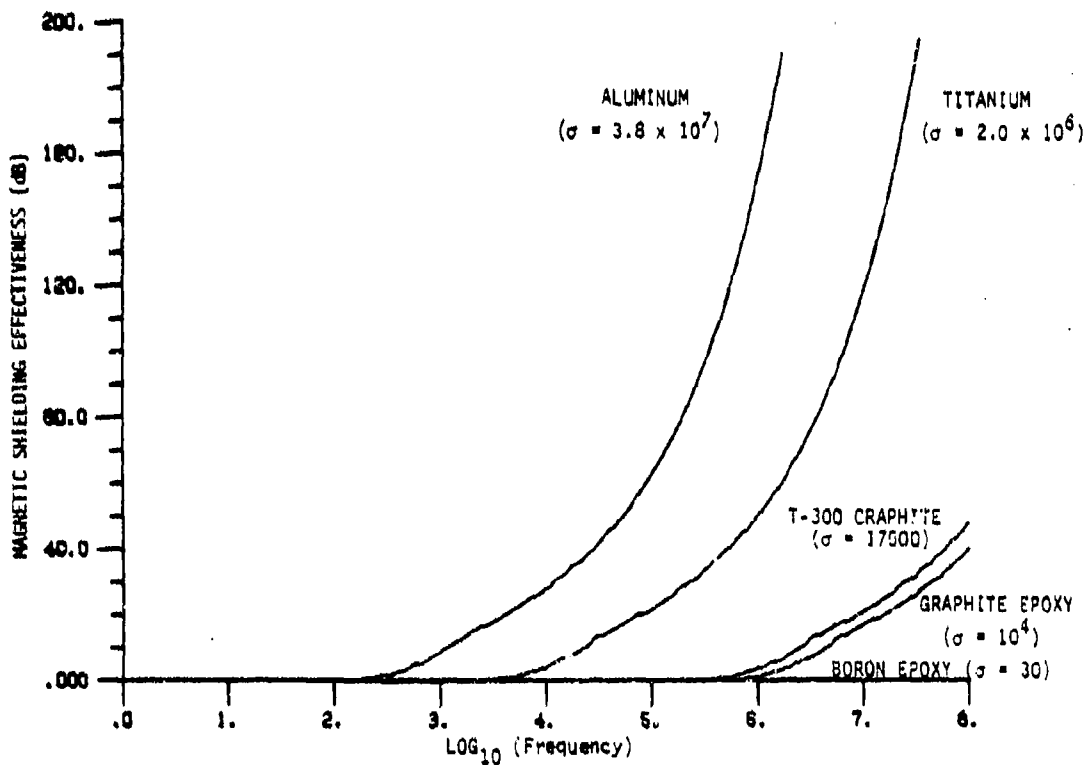
(a) Plate Thickness = 0.0032 m

Figure 4-7. Magnetic Shielding Effectiveness of a Flat Plate under a Non-
uniform Magnetic Field generated by a Loop Antenna Parallel
to the Plate (Sheet 1 of 3)

4-12

LOOP DIAMETER = 1 in.

ANTENNA-PLATE SEPARATION = 1 in.

PLATE THICKNESS CORRESPONDS TO 12 PLY COMPOSITE
MATERIAL AT 0.00525 IN/PLY
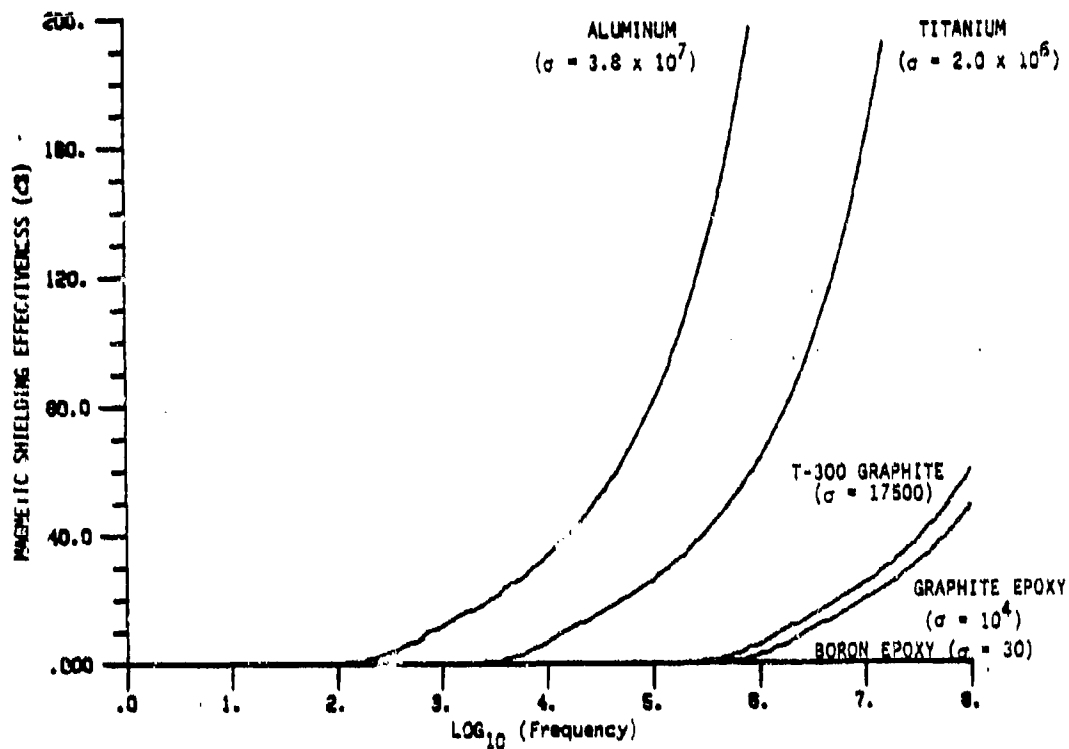
(b) Plate Thickness = 0.00214 m

Figure 4-7. Magnetic Shielding Effectiveness of a Flat Plate under a Non-
uniform Magnetic Field generated by a Loop Antenna Parallel
to the Plate (Sheet 2 of 3)

4-13

LOOP DIAMETER   = 1 in.

ANTENNA-PLATE SEPARATION = 1 in.

PLATE THICKNESS CORRESPONDS TO 24 PLY COMPOSITE
MATERIAL AT 0.00525 IN/PLY
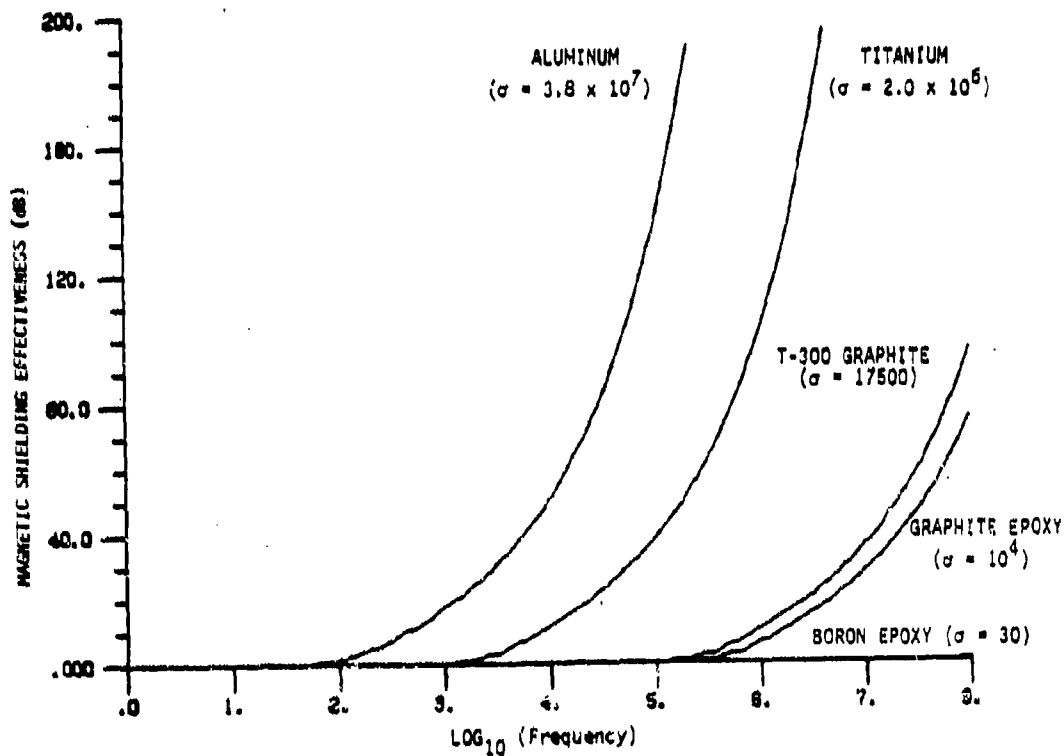
(c) Plate Thickness = 0.00107 m

Figure 4-7. Magnetic Shielding Effectiveness of a Flat Plate under a Non-
uniform Magnetic Field generated by a Loop Antenna Parallel
to the Plate (Sheet 3 of 3)
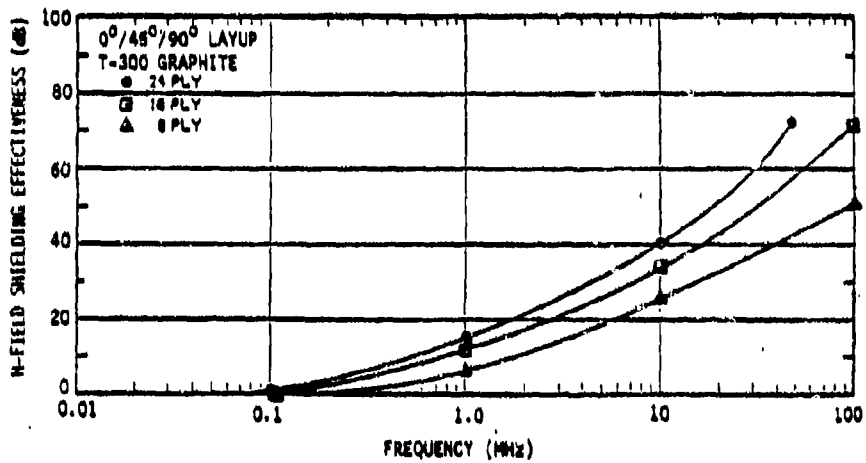
(a) 0°/45°/90° Layup
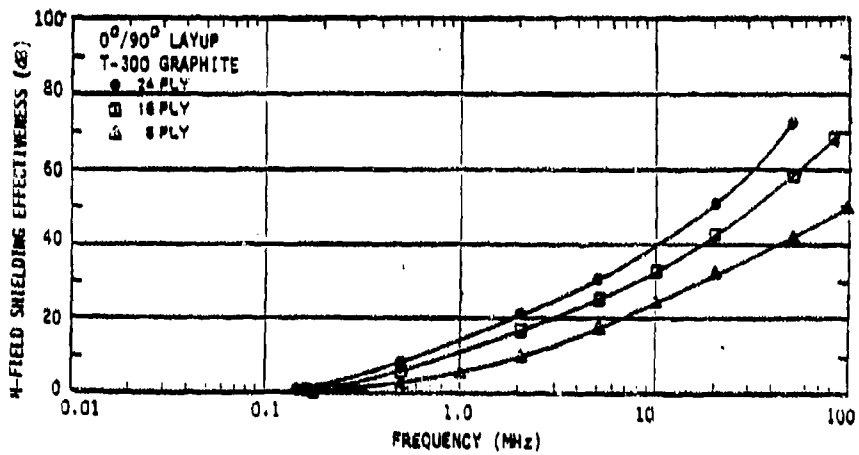
(b) 0°/90° Layup

Figure 4-8. Infinite Flat Plate with a Nonuniform Incident Magnetic
Field Test Results

To illustrate the dependence of the magnetic shielding effectiveness on the type of incident field, Figure 4-9 shows the shielding effectiveness of a 0.0032 m thick flat mixed-orientation graphite/epoxy plate (conductivity = 10^4 mhos/m) with a uniform incident magnetic field and, with a nonuniform incident magnetic field generated by a 1 in. diameter loop antenna parallel to the plate at a range of 1 in. (geometry of Figure 4-6).

Table 4-2 attempts to characterize the significant properties of magnetic shielding effectiveness for the situations described in this report.

4.3 ELECTRIC SHIELDING EFFECTIVENESS FOR ENCLOSURES UNDER A UNIFORM MAGNETIC FIELD

Following Schelkunoff's[7] approach to EM shielding, the electric shielding effectiveness of a material is primarily the result of loss due to absorption and reflection.

Absorption Loss: When an EM wave passes through a medium, its amplitude decreases exponentially due to currents induced in the medium producing ohmic losses and heating of the material. The electric field can therefore be written as

$$E_1 = E_o \exp^{[-t/\delta]} \tag{11}$$

where E_1 is the electric field intensity at a distance, t, within the media and E_o is the incident field strength. The distance required for the wave to be attenuated to 1/e (37%) of its original value is defined as the skin depth, which is equal to

$$\delta = \sqrt{\frac{2}{\omega\mu\sigma}} \quad m \quad . \tag{12}$$

The loss due to absorption for a shield d meters thick can be written as

$$ESE(Absorption) = -20 \log_{10}(\exp^{[-d/\delta]}) = 8.686 \, d/\delta$$

$$= 8.686d\sqrt{\frac{\omega\mu\sigma}{2}} \, , \tag{13}$$

giving the absorption loss at 8.686 dB/skin depth.

4-16
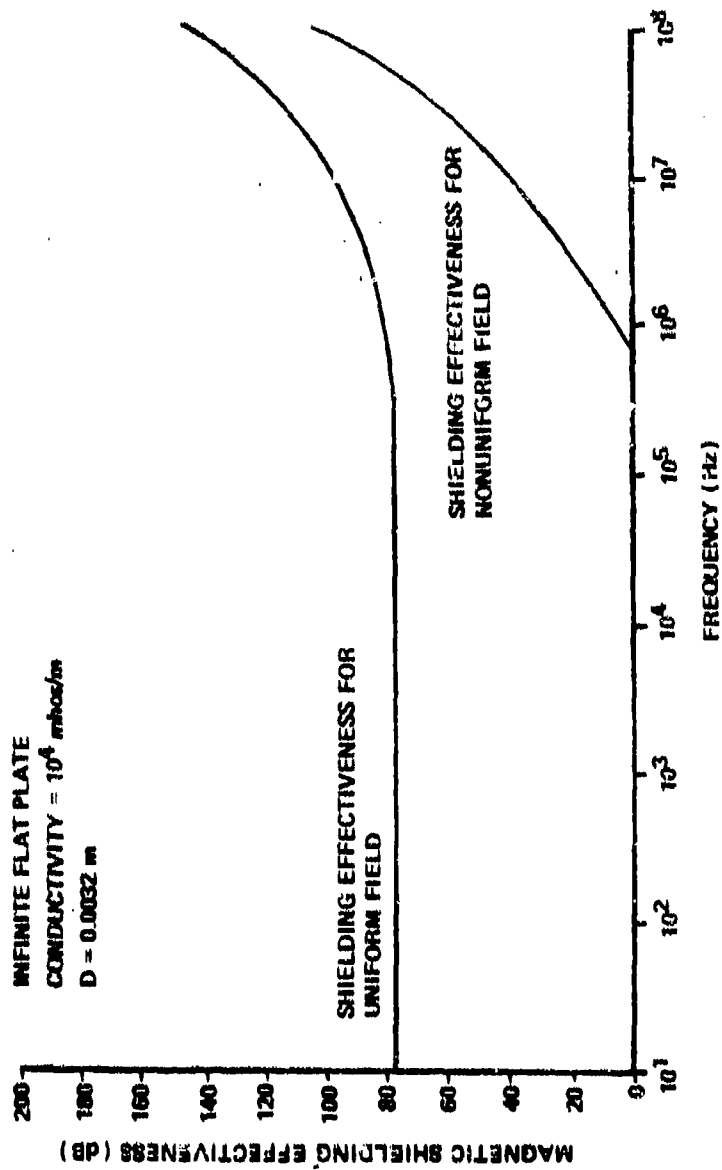
Figure 4-9. Magnetic Shielding Effectiveness for a Mixed-Orientation Graphite/Epoxy Composite Enclosure under a Uniform Field as a Function of Volume-to-Surface. Conductivity = 10^4. Shield Thickness = 0.003 m

Table 4-2. Summary of Properties of Magnetic Shielding (Sheet 1 of 3)

Uniform Incident Magnetic Field

Flat Plate Geometry:

Exact expression for the magnetic shielding effectiveness is given by

$$MSE = 20 \log_{10}\left|\cosh(\gamma d) + \frac{377}{\eta} \sinh(\gamma d)\right|$$

The low frequency limit of the magnetic shielding effectiveness is given by $\lim_{f \to 0} MSE(\text{flat plate}) = 20 \log_{10}|1 + 377\sigma d|$.

For $f < \dfrac{0.1}{2\pi\mu\sigma d^2}$, $MSE \cong 20 \log_{10}|1 + 377 \sigma d|$ showing the low frequency magnetic shielding effectiveness is dependent only upon the conductivity and shield thickness.

For $f > \dfrac{0.1}{2\pi\mu\sigma d^2}$, the magnetic shielding effectiveness increases exponentially with frequency.

Enclosure Geometry (parallel plates, cylinders, spheres):

Exact expression for the magnetic shielding effectiveness is given by $MSE = 20 \log_{10}\left|\cosh(\gamma d) + \frac{V}{S}\gamma\sinh(\gamma d)\right|$ where $\frac{V}{S}$ is the volume-to-surface ratio of the enclosure.

For spherical geometries, this expression is valid only for frequencies greater than $0.1/[9\pi\,\mu\sigma\,(\frac{V}{S})^2]$.

For frequencies less than $0.1/[9\pi\,\mu\sigma\,(\frac{V}{S})^2]$ the magnetic shielding effectiveness for a spherical geometry is given by $MSE = 20 \log_{10}\left|\cosh(\gamma d) + \frac{1}{3}\left[\frac{j\omega\mu r}{\eta} + \frac{2\eta}{j\omega\mu r}\right]\sinh(\gamma d)\right|$.

For $f < \dfrac{0.1}{2\pi\mu\sigma d^2}$ $MSE \cong 20 \log_{10}\left|1 + \frac{V}{S}\gamma^2 d\right|$ showing the low frequency magnetic shielding effectiveness is dependent upon the conductivity, shield thickness, enclosure geometry ($\frac{V}{S}$) and frequency.

Enclosure magnetic shielding effectiveness exhibits a break-point $f_b = \dfrac{1}{2\pi\,(\frac{V}{S})\,\mu\sigma d}$. Below f_b, $MSE \cong 0$. Above f_b, the MSE grows approximately as $20 \log_{10}|f/f_b|$.

Table 4-2. Summary of Properties of Magnetic Shielding (Sheet 2 of 3)

Enclosure Geometry (continued):	For fixed σ, f, d; the dependence of the magnetic shielding effectiveness is approximately MSE ($\frac{V}{S}$) = C(σ, f, d) + 20 $\log_{10}$ ($\frac{V}{S}$). The magnetic shielding effectiveness increases with frequency.

Nonuniform incident magnetic field generated by a nearby loop antenna

Flat Plate Geometry:

An exact integral expression for the magnetic shielding effectiveness has been derived by Bannister.(1)

For $\dfrac{0.5}{2\pi\mu\sigma d^2} < f < c/[20(a^2 + (r_1 + r_2 - d)^2)^{1/2})$ the magnetic shielding effectiveness can be approximated as

$$MSE = 8.686 \ [\omega\mu\sigma]^{1/2}d + 20 \ \log_{10}\left\{[\tfrac{\omega\mu\sigma}{2}]^{1/2}(r_1 + r_2)/8.485\right\}.$$

For $\dfrac{200}{2\pi\mu\sigma(a^2 + (r_1 + r_2)^2)} < f < \min \begin{cases} 4/(2\pi\mu\sigma d^2) \\ c/[20(a^2+(r_1+r_2-d)^2)^{1/2}) \end{cases}$

the magnetic shielding effectiveness can be approximated as

$$MSE = 10 \ \log_{10} \ (1 + (\tfrac{\omega\mu\sigma d}{6})(\tfrac{a^2 + (r_1 + r_2)^2}{r_1 + r_2})^2)$$

[Both of these approximations require $r_1 + r_2 >> d$]

The magnetic shielding effectiveness is dependent upon the shield parameters (σ and d), frequency, and the source-shield geometry (a, r_1, r_2).

For $[a^2 + (r_1 + r_2)^2]^{1/2} < 10$, the low frequency limit of the magnetic shielding effectiveness; limit MSE (flat plate-field generated by nearby loop) = 0. $\quad f \to 0$

For $(r_1 + r_2) >> a$, the dependence of the magnetic shielding effectiveness on the source to detector loop distance, $[(r_1 + r_2)^2 + a^2]^{1/2}$, for constant f, σ, and d is approximately MSE = C(f, σ, d) + 20 $\log_{10}(r_1 + r_2)$.

For materials of lower conductivity, such as graphite/epoxy composites, no magnetic shielding is offered for frequencies

below $\min \begin{cases} \dfrac{0.5}{(2\pi\mu\sigma d^2)} \\ \\ \dfrac{200}{2\pi\mu\sigma(a^2 + (r_1 + r_2)^2)} \end{cases}$. Above this minimum

frequency, the shielding effectiveness grows "exponentially" with frequency - the rate of growth increases with increasing conductivity and shield thickness.

Reflection Loss: The reflection loss at the interface between two media is related to the difference in characteristic impedances between the media. The intensity of the transmitted wave from a medium with impedance, Z_1, to a medium with impedance, Z_2, is

$$E_1 = \frac{2Z_2}{Z_1 + Z_2} E_o \qquad (14)$$

where E_o is the intensity of the incident wave and E_1 is the intensity of the transmitted wave.

When a wave passes through a shield, it encounters two boundaries - the second boundary being that between the medium with impedance Z_2 and the medium with impedance Z_1. The transmitted wave, E_t, through this boundary is given by

$$E_t = \frac{2Z_1}{Z_1 + Z_2} E_1 . \qquad (15)$$

If the shield is thick compared to the skin depth, there is high absorption loss and the effect of multiple reflections between the two boundaries is negligible. The total transmitted wave is then

$$E_t = \frac{4Z_1 Z_2}{(Z_1 + Z_2)^2} E_o . \qquad (16)$$

If the shield is not thick, multiple reflections occur between the two boundaries since the absorption loss in the shield is small. However for electric fields, since $Z_1 \gg Z_2$*, most of the incident wave is reflected at the first boundary and only a small percentage enters the shield. Therefore, multiple reflections within the shield can be neglected for electric fields and so the total transmitted wave is the same as that for a thick shield.

For $Z_1 \gg Z_2$

$$E_t \simeq \frac{4 Z_2}{Z_1} E_o . \qquad (17)$$

---

*Since $Z_1 = E/H = \sqrt{\mu/\varepsilon}$ and $Z_2 =$ shield impedance, in the case of an electric field $Z_1 \gg Z_2$.

For wave impedance and shield impedance $\eta = \sqrt{\dfrac{j\omega\mu}{\sigma}} = Z_2$, the reflection loss for an incident E field is

$$\text{ESE(reflection)} = 20 \log_{10} \frac{4|Z_1|}{|\eta|} \text{ dB} . \qquad (18)$$

For an enclosure, the inverse electric shielding ratio is

$$\text{ESR}^{-1} = \frac{\gamma b \sinh(\gamma d)}{2(2\pi \, b/\lambda)^2} \qquad (6) \qquad\qquad (19)$$

where

$$b = \begin{cases} \text{radius of cylinder for cylindrical enclosures} \\ 1/2 \text{ plate separation for parallel plate enclosures} \\ 2/3 \text{ radius of the sphere for spherical enclosures} \end{cases}$$

Noting $b = \dfrac{2V}{S}$, where $\dfrac{V}{S}$ is the volume-to-surface ratio of the enclosure,

$$\text{ESR}^{-1} = \frac{\gamma \sinh(\gamma d)}{(4\pi/\lambda)^2 \, \frac{V}{S}} \qquad (20)$$

For frequencies such that the skin depth is greater than $\sqrt{20}\, d$, where d is the shield thickness, the electric shielding effectiveness due to absorption is less than 2 dB so that the electric shielding effectiveness is primarily due to reflective losses; i.e.,

$$\text{ESE(reflective loss)} = 20 \log_{10} \left| \text{ESR}^{-1} \right|. \qquad (21)$$

$$\delta > \sqrt{20}\, d \iff \omega < \frac{0.1}{\mu\sigma d^2}$$

$$\Rightarrow \text{ESE(reflective loss)} = 20 \log_{10}(\sigma d/8\pi\varepsilon \, \tfrac{V}{S}) - 20 \log_{10}(f) \qquad (22)$$

Therefore, for radian frequencies less than $\dfrac{0.1}{\mu\sigma d^2}$, the electric shielding effectiveness decreases as $-20 \log_{10}(f)$.

As the skin depth approaches $\sqrt{20}\,d$, contributions in shielding effectiveness due to absorption losses become significant. The exponential nature of electric shielding due to absorption losses causes a minimum to exist in the total electric shielding effectiveness of the shield. Employing Newton's method, the electric shielding effectiveness attains its minimum when $\sqrt{\frac{\omega\mu\sigma}{2}}\,d = 2.99008$ or $f = \frac{(2.99008)^2}{\pi\mu\sigma d^2}$.

Note that $\sqrt{\frac{\omega\mu\sigma}{2}}\,d = \frac{d}{\delta}$, where δ is the skin depth, so the minimum electric shielding effectiveness occurs when the frequency is such that the skin depth is approximately one third (1/2.99008) the shield thickness.

Table 4-3 gives the frequency at which minimum electric shielding effectiveness occurs for aluminum ($\sigma = 3.8 \times 10^7$ mhos/m), titanium ($\sigma = 2.0 \times 10^6$ mhos/m), and mixed-orientation graphite/epoxy composite ($\sigma = 10^4$ mhos/m and $\sigma = 5 \times 10^3$ mhos/m) enclosures for shield thickness from 0.0011 m to 0.025 m. Tables 4-4 through 4-7 give the electric shielding effectiveness associated with these frequencies (the minimum electric shielding offered by the enclosure). Since the electric shielding effectiveness is dependent on the volume-to-surface ratio as well as the shield thickness and conductivity, the electric shielding effectiveness at the frequency at which shielding is at a minimum are given as a function of volume-to-surface ratio.

Figure 4-9 illustrates the typical form of the frequency dependence of electric shielding effectiveness for an 8-ply mixed-orientation graphite/epoxy enclosure ($\sigma = 10^4$ mhos/m) and a similar aluminum enclosure of the same thickness.

Writing the inverse electric shielding ratio as

$$ESR^{-1} = \frac{\gamma \sinh(\gamma d)}{(4\pi/\lambda)^2} \left(\frac{V}{S} \right)^{-1}, \tag{23}$$

the electric shielding effectiveness can be written as

$$ESE = k(f, \sigma, d) - 20 \log_{10}\left(\frac{V}{S} \right) \tag{24}$$

4-22

Table 4-3. Frequency (Hz) at which the Electric Shielding Effectiveness of an Enclosure under an Incident Uniform Electric Field is at a Minimum

SHIELD THICKNESS (m)	SHIELD CONDUCTIVITY (mhos/m)			
	3.5E7	2E6	1E4	5E3
.0011	.49E 05	.94E 06	.19E 09	.37E 09
.0021	.14E 05	.26E 06	.51E 08	.10E 09
.0032	.58E 04	.11E 06	.22E 08	.44E 08
.0050	.24E 04	.45E 05	.91E 07	.18E 08
.0100	.60E 03	.11E 05	.23E 07	.45E 07
.0150	.26E 03	.50E 04	.10E 07	.20E 07
.0200	.15E 03	.28E 04	.57E 06	.11E 07
.0250	.95E 02	.18E 04	.36E 06	.72E 06

Table 4-4. Minimum Electric Shielding Effectiveness (dB) for an Aluminum Enclosure

MATERIAL: ALUMINUM   CONDUCTIVITY: .350E 08

SHIELD THICKNESS (m)	VOLUME-TO-SURFACE				
	.01	.1	1.	10.	100.
.0011	239	219	199	179	159
.0021	255	235	215	195	175
.0032	256	246	226	206	186
.0050	278	258	233	218	198
.0100	296	276	256	236	216
.0150	307	287	267	247	227
.0200	314	294	274	254	234
.0250	320	300	280	260	240

Table 4-5. Minimum Electric Shielding Effectiveness (dB) for a Titanium Enclosure

MATERIAL: TITANIUM   CONDUCTIVITY: .200E 07

SHIELD THICKNESS (m)	VOLUME-TO-SURFACE				
	.01	.1	1.	10.	100.
.0011	147	167	147	127	107
.0021	204	184	164	144	124
.0042	215	195	175	155	135
.0050	227	207	187	167	147
.0100	245	225	205	185	165
.0150	255	235	215	195	175
.0200	263	243	223	203	183
.0250	269	249	229	209	189

Table 4-6. Minimum Electric Shielding Effectiveness (dB) for a Graphite/Epoxy Enclosure ($\sigma = 10^4$ mhos/m)

MATERIAL: GRAPHITE EPOXY COMPOSITE   CONDUCTIVITY: .100E 05

SHIELD THICKNESS (m)	VOLUME-TO-SURFACE				
	.01	.1	1.	10.	100.
.0011	95	75	55	35	15
.0021	112	92	72	52	32
.0042	123	103	83	63	43
.0050	135	115	95	75	55
.0100	153	133	113	93	73
.0150	163	143	123	103	83
.0200	171	151	131	111	91
.0250	177	157	137	117	97

Table 4-7. Minimum Electric Shielding Effectiveness (dB) for
a Graphite/Epoxy Enclosure ($\sigma = 5 \times 10^3$ mhos/m)

MATERIAL: GRAPHITE EPOXY COMPOSITE   CONDUCTIVITY: .500E 04

SHIELD THICKNESS (m)	VOLUME-TO-SURFACE				
	.01	.1	1.	10.	100.
.0011	83	63	43	23	3
.0021	100	80	60	40	20
.0032	111	91	71	51	31
.0050	123	103	83	63	43
.0100	141	121	101	81	61
.0150	151	131	111	91	71
.0200	159	139	119	99	79
.0250	165	145	125	105	85

VOLUME-TO-SURFACE RATIO = 1

SHIELD THICKNESS CORRESPONDS TO 8 PLY COMPOSITE
MATERIAL OF 0.00525 IN/PLY
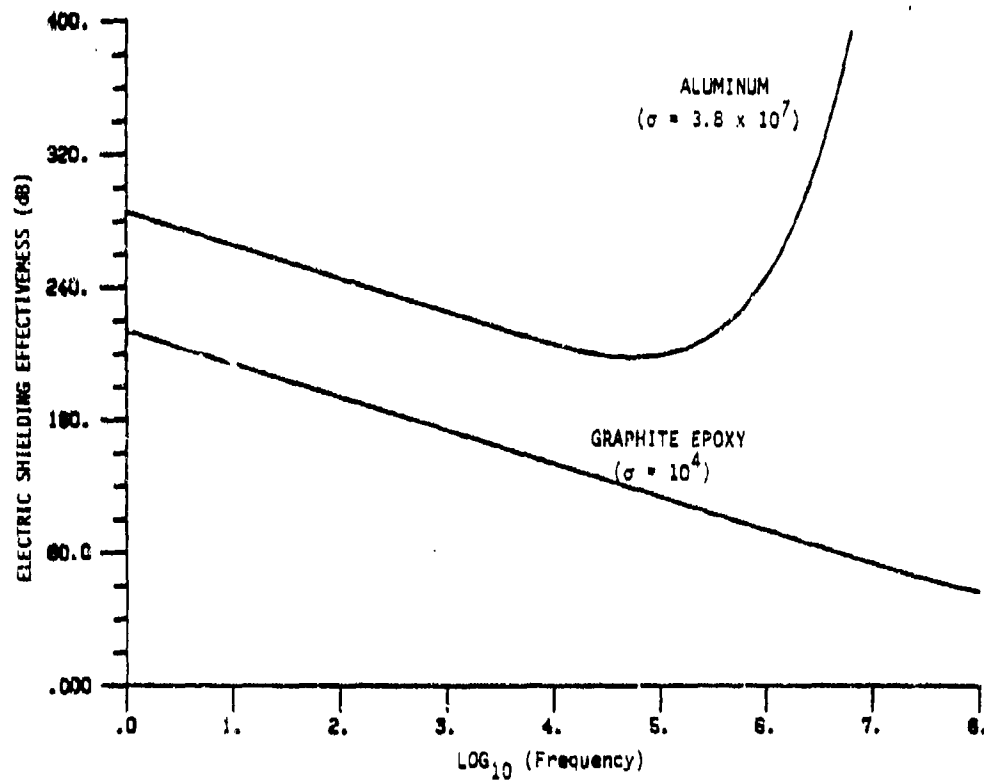
Figure 4-9.   Electric Shielding Effectiveness of an Enclosure under a
Uniform Electric Field

Hence, for fixed frequency, conductivity, and shield thickness, the electric shielding effectiveness decreases with increasing volume-to-surface ratio in contrast to the magnetic shielding effectiveness which increases with increasing volume-to-surface ratio at approximately $20 \log_{10}(\frac{V}{S})$. Figure 4-10 illustrates the dependence of an 8-ply mixed-orientation graphite/epoxy enclosure ($\sigma = 10^4$ mhos/m) on the volume-to-surface ratio of the enclosure.

Table 4-8 summarizes the major properties of the electric shielding effectiveness of an enclosure under a uniform electric field.

Shield Conductivity = 10^4 mhos/m

Shield Thickness corresponds to 8-ply composite material at 0.00525 in/ply

Volume-to-Surface (V/S) Ratio	Minimum ESE (dB)
0.01	95
0.1	75
1.0	55
10.0	35
100.0	15
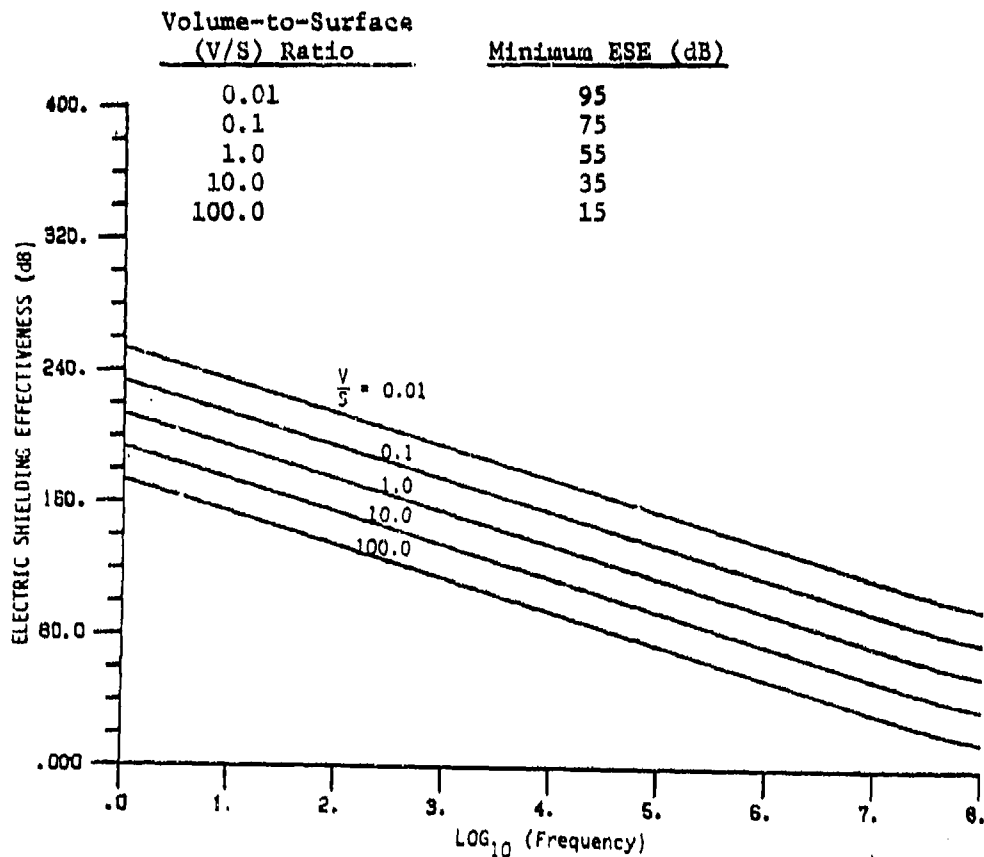
Figure 4-10. Electric Shielding Effectiveness of an Enclosure under a Uniform Electric Field as a Function of Enclosure Volume-to-Surface Ratio

4-27

Table 4-8. Properties of Electric Shielding for Enclosures Under a Uniform Incident Electric Field

---

: ESE = shielding due to reflection and shielding due to absorption losses

: For enclosures, the inverse electric shielding ratio is $\dfrac{\gamma \sinh(\gamma d)}{(4\pi/\gamma)^2 \frac{V}{S}}$ where $\frac{V}{S}$ is the volume-to-surface ratio of the enclosure

: For $\omega < 0.1/\mu\sigma d^2$, corresponding to a skin depth of $\sqrt{20}\, d$ (where d is the shield thickness), the electric shielding is primarily due to reflective losses

: For $\omega < 0.1/\mu\sigma d^2$, the electric shielding effectiveness decreases as $-20 \log_{10}(f)$ (ESE = $20 \log_{10}[\sigma d/(8\pi\epsilon \frac{V}{S})] - 20 \log_{10}(f)]$)

: For $\omega > 0.1\mu\sigma d^2$, shielding due to absorption becomes significant and grows exponentially, dominating shielding due to reflection losses

: A minimum electric shielding effectiveness exists at $f = (2.99008)^2/ (\pi\mu\sigma d^2)$, the frequency at which the skin depth is approximately one-third the shield thickness

: The dependence of electric shielding effectiveness on the volume-to-surface ratio is ESE = $K(\sigma, f, d) - 20 \log_{10}(\frac{V}{S})$, in contrast to the magnetic shielding effectiveness which is approximately $C(\sigma, f, d) + 20 \log_{10}(\frac{V}{S})$

4.4 EM RELATIONSHIPS BETWEEN SHIELDING
EFFECTIVENESS AND TRANSFER IMPEDANCE

The difficulty with expressions for electric and magnetic shielding effectiveness is the extreme dependence of the shielding effectiveness on the nature of the exciting field and on the geometry of the shield (i.e., they must be used only for those basic geometries for which they were derived). Similarly, the extensive laboratory measurements of electric and magnetic shielding effectiveness that have been made over the spectrum of composite materials of current interest are valid only for the geometry of the test; the results cannot be extended directly to more difficult geometries.

Shields which are thin compared to their radii of curvature and for which the wavelength of the incident EM field within the shield is much smaller than that external to the shield are called locally planar since their EM behavior is essentially a local phenomena. For a locally planar shield, a measurement of the degree of EM protection offered by the shield, independent of geometry and incident field type, is the surface transfer impedance of the shield material. This impedance is defined to be the ratio of the interior tangential electric field to the surface current density of the current induced by the incident EM field. The surface transfer impedance, Z_{st}, of a homogeneous conducting shield (including mixed-orientation graphite/epoxy composites) is determined by the material conductivity and thickness, and the frequency of the incident field:

$$Z_{st} = E_t/J = \eta \operatorname{csch}(\gamma d) \tag{25}$$

where $\approx \sqrt{\frac{j\omega\mu}{\sigma}}$ is the intrinsic impedance of the shield, $\approx \sqrt{j\mu\sigma}$ is the propagation factor, and d is the shield thickness.

Figure 4-11 illustrates the dependence of the surface transfer impedance on the material thickness and material conductivity, respectively, as a function of frequency. The low frequency asymptote to the surface transfer impedance is

$$Z_{st} = 1/\sigma d \tag{26}$$

4-29

MATERIAL THICKNESS CORRESPONDS TO 8 PLY COMPOSITE
MATERIAL AT 0.00525 IN/PLY
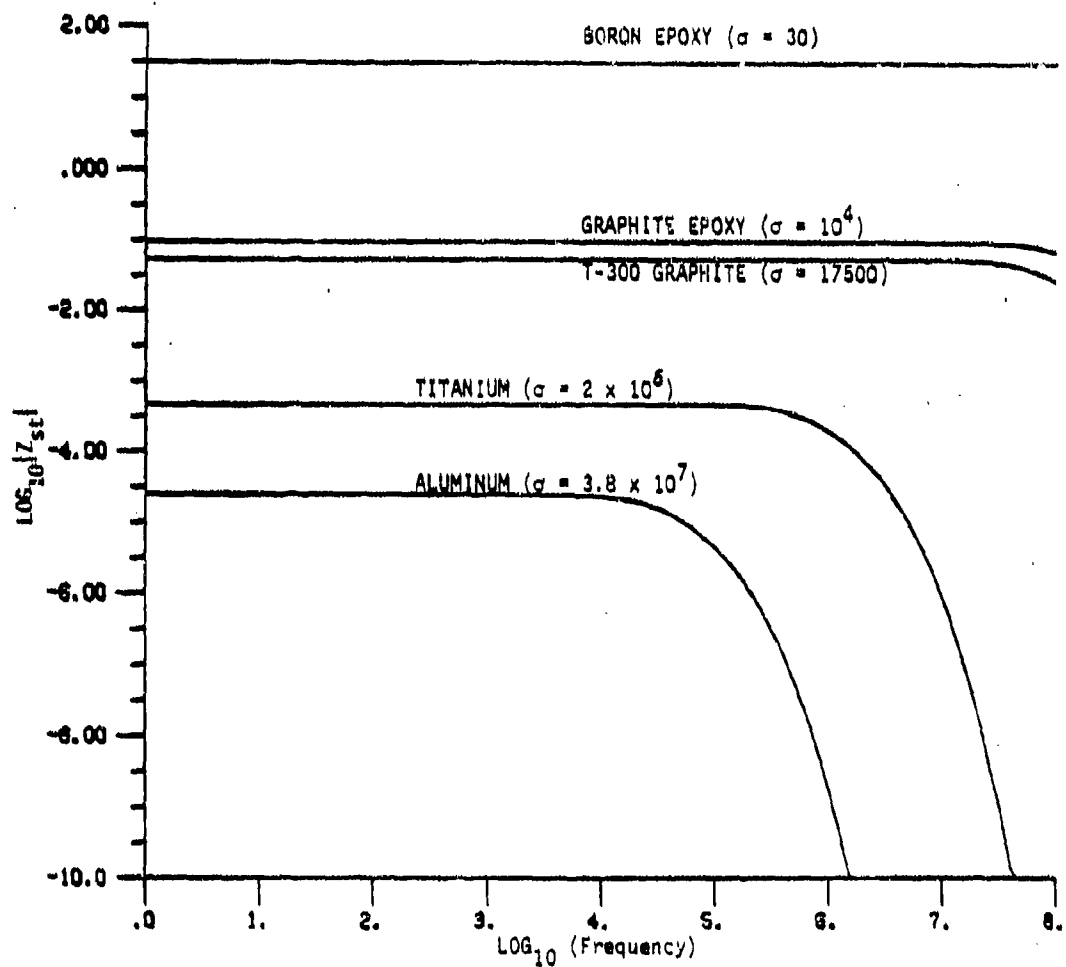
Figure 4-11.   Surface Transfer Impedance as a Function of Frequency

For homogeneous conducting shields with a geometry of the type shown in Figure 4-11 under a uniform magnetic field and for a homogeneous conducting infinite flat plate with a nonuniform magnetic field produced as shown in Figure 4-6, the surface transfer impedance can be related to the magnetic shielding effectiveness as

$$MSE \simeq 20 \ \log_{10} |Z/Z_{st}| \tag{27}$$

over a frequency interval dependent upon the shield geometry, conductivity, and thickness where:

- $Z = \sqrt{\dfrac{\mu o}{\epsilon}} \simeq Z_0 = \sqrt{\dfrac{\mu o}{\epsilon_o}} \simeq 377$ for a flat plate under a magnetic field

- $Z = (\dfrac{V}{S})j\omega\mu$ for a cylindrical, spherical, or parallel plate enclosure with volume-to-surface ratio ($\dfrac{V}{S}$) under a uniform magnetic field, as illustrated in Figure 4-11.

- $Z = \omega\mu(r_1 + r_2)/6$ for an infinite flat plate with a nonuniform magnetic field generated as shown in Figure 4-6 under the assumptions $r_1 + r_2 \gg a$ and $d(r_1 + r_2) \gg 0.03$.

Similarly, for a homogeneous conducting enclosure of the type shown in Figure 4-1, the electric shielding effectiveness can be related to the surface transfer impedance as

$$ESE \simeq 20 \ \log_{10} |Z/Z_{st}| \tag{28}$$

over a frequency interval dependent upon the shield geometry, conductivity, and thickness, where $Z = j[8\pi\epsilon f(\dfrac{V}{S})]^{-1}$.

These relationships provide a means for extending the application of laboratory measurements of the magnetic shielding effectiveness of a homogeneous conducting material to locally planar homogeneous conducting shields, in general, through the concept of surface transfer imepdance. Conversely, laboratory measurements of the surface transfer impedance of a homogeneous conducting shield of arbitrary locally planar geometry can be used to determine the associated magnetic shielding effectiveness for shields of the basic geometries and

4-31

associated incident field types discussed. These relationships are valid over a frequency interval dependent on the shield geometry, conductivity, and thickness. As an example, quadraxial measurements performed by Boeing[5] of the surface transfer impedance of 24 ply T-300 graphite (Figure 4-12) were used to compute the magnetic shielding effectiveness for a flat plate with a uniform magnetic field, an enclosure of the type shown in Figure 4-1 with a volume-to-surface ratio of one under a uniform magnetic field generated as shown in Figure 4-6. The results ar shown in Figures 4-13a, 4-13b, and 4-13c, respectively. Measured magnetic shielding effectiveness data is included in Figure 4-13c for comparison. Theoretical magnetic shielding effectiveness values were provided for comparison in Figures 4-13a and 4-13b due to the lack of real measurements under the equivalent situations.

An immediate corollary to the relationship $MSE \simeq 20 \log_{10}|Z/Z_{st}|$, valid for the frequency intervals over which the relationships hold is as follows:

For two shields of the same geometry with conductivities and shield thickness (σ_i, d_i), respectively, with $i = 1, 2$, the difference in the magnetic shielding effectiveness offered by the shields is

$$MSE(\sigma_1, d_1) - MSE(\sigma_2, d_2) = 20 \log_{10} \left| \frac{Z_{st}(\sigma_2, d_2)}{Z_{st}(\sigma_1, d_1)} \right| \qquad (29)$$

(The shield geometries and associated field types for which this relationship holds are those in Figures 4-1 and 4-6.) This relationship provides a "back-of-the-envelope" solution to the gain or loss in magnetic shielding effectiveness when conducting films are added to shields or when different materials are used for the shield. Figure 4-14 shows the gain in magnetic shielding when 24 ply T-300 graphite is coated with one mil aluminum foil, two mil aluminum foil, 120 mesh aluminum screen, and 120 mesh phosphor bronze screen.
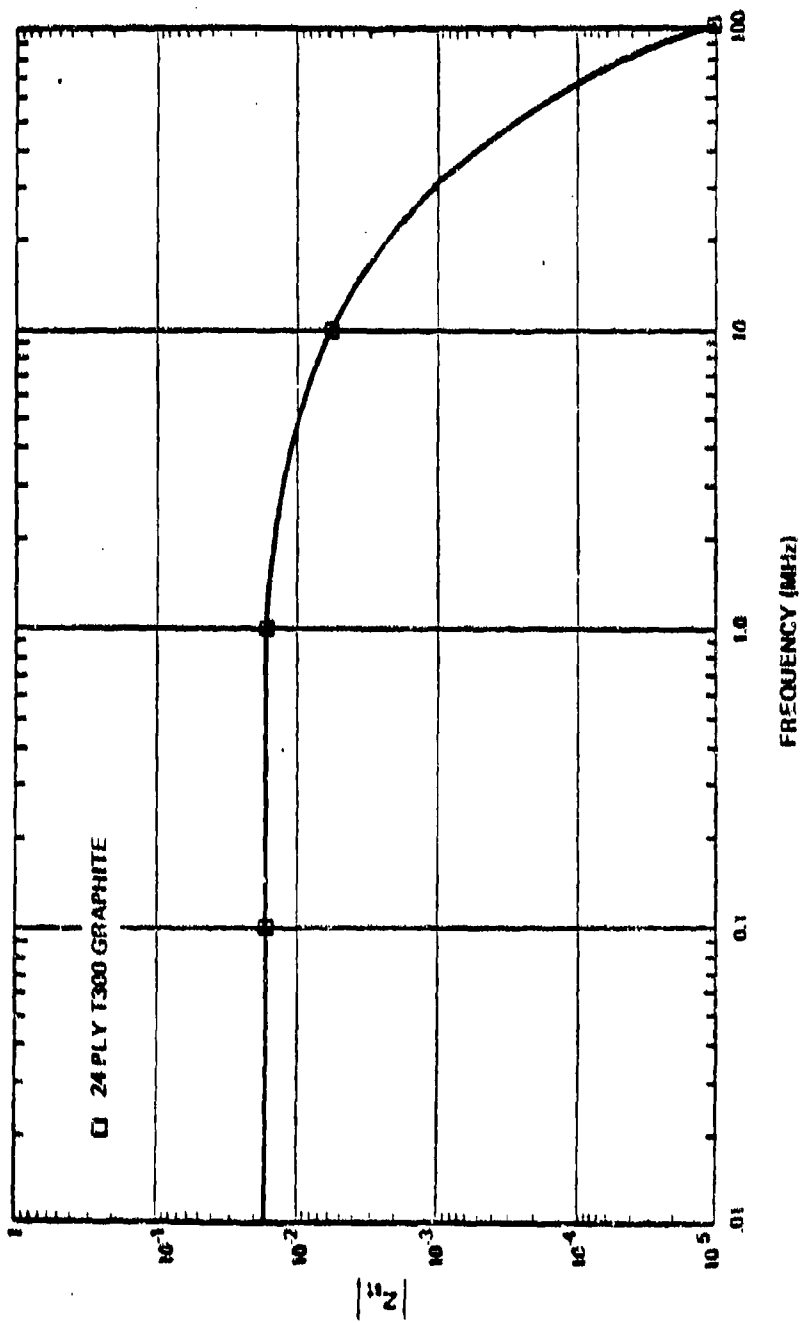
Figure 4-12. Measured Surface Transfer Impedance of 24 Ply T-300 Graphite/Epoxy[5]

SHIELD THICKNESS = 0.0032 m
CONDUCTIVITY · 17500 ⍵/m
MATERIAL · 24 PLY T-300 GRAPHITE

(a)   Flat Plate under a Uniform Magnetic Field

SHIELD THICKNESS · 0.0032 m
VOLUME-TO-SURFACE RATIO · 17500 ⍵/m
MATERIAL · 24 PLY T-300 GRAPHITE
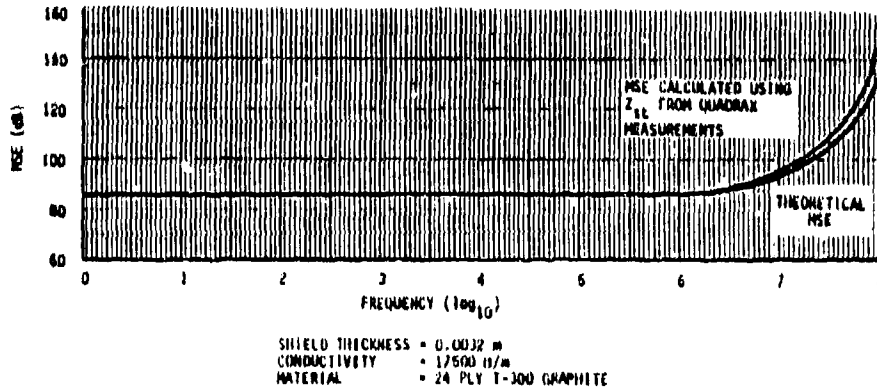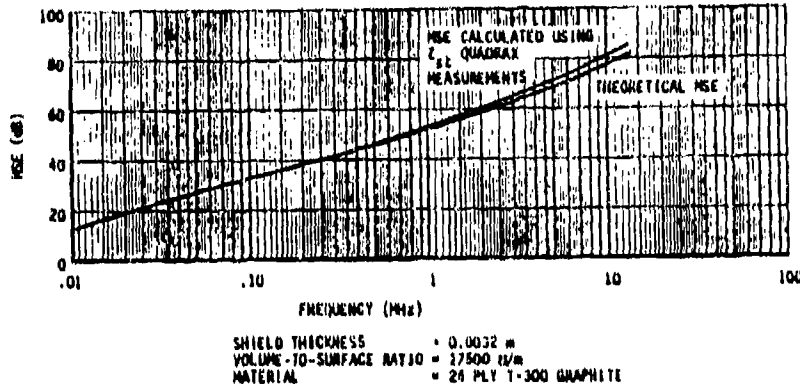
(b)   Volume under a Uniform Magnetic Field

SOURCE-DETECTOR LOOP SEPARATION · 0.0609 m
SHIELD THICKNESS · 0.0032 m
LOOP RADII · 0.0127 m
MATERIAL · 24 PLY T-300 GRAPHITE
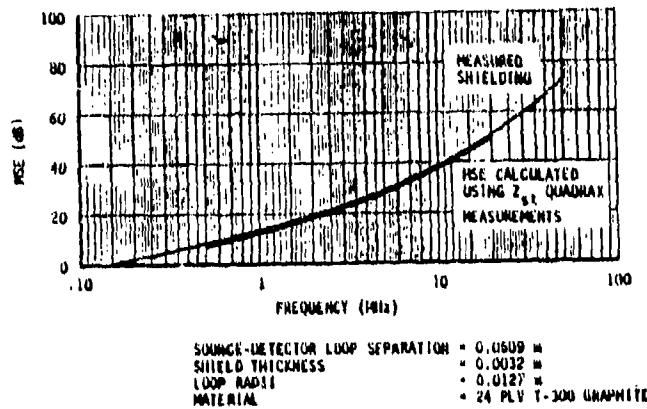
(c)   Flat Plate under a Nonuniform Magnetic Field

Figure 4-13.   Shielding Effectiveness

4-34
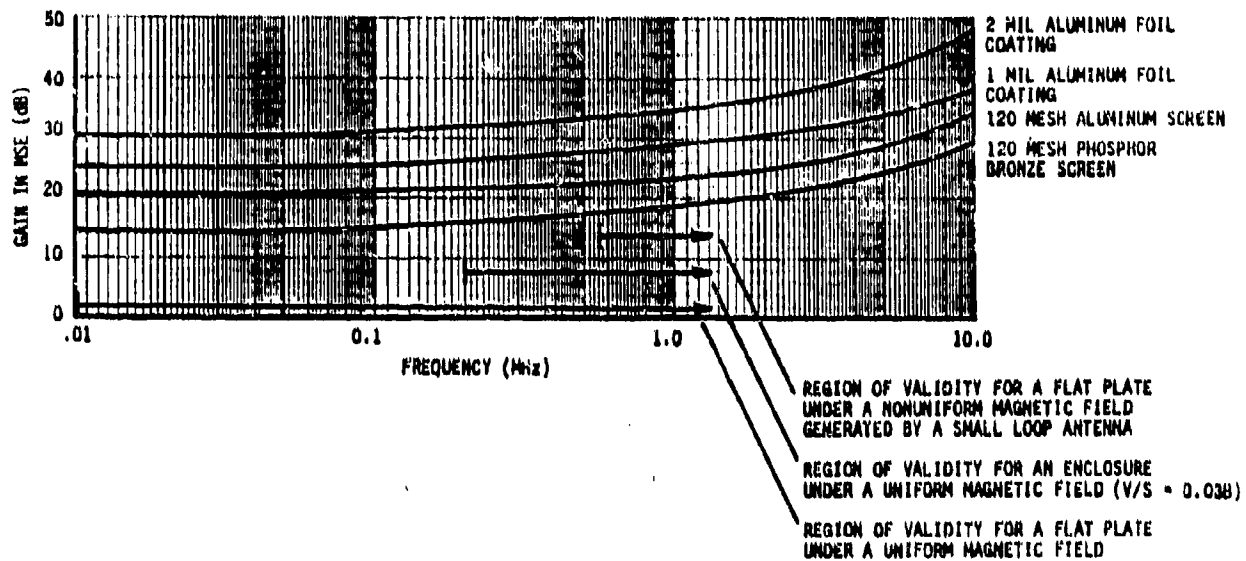
Figure 4-14. Gain in Magnetic Shielding Effectiveness of 24 Ply T300 Graphite Composite through Applications of Aluminum Foil, Aluminum Screen, and Phosphor Bronze Screen

4.5 REFERENCES

1. L.V. King, "Electromagnetic Shielding at Radio Frequencies," _Philosophical Magazine and Journal of Science_, Series 7, Vol. 15, No. 97, Febraury 1933.

2. P.R. Bannister, "Further Notes for Predicting Shielding," _IEEE Transactions On Electromagnetic Compatibility_, Vol. EMC-11, No. 2, May 1969.

3. P.R. Bannister, "New Theoretical Expression, for Predicting Shielding Effectiveness for the Plane Shield Case," _IEEE Transactions on Electromagnetic Compatibility_, Vol. EMC-10, No. 1, March 1968.

4. G. Bedrosian and K.S.H. Lee, "EMP Penetration Through Metal Skin Panels and Into Aircraft Cavities," _Air Force Weapons Laboratory Interaction Note 314_, Kirtland Air Force Base, New Mexico, August 1976.

5. D. Strawe and L. Piszker, _Interaction of Advanced Composites with Electromagnetic Pulse (EMP) Environment_, Final Report prepared by Boeing Aerospace Company for Wright-Patterson Air Force Base under Contract F33615-74-C-5158, AFML-TR-75-141, September 1975.

6. G. Dike, _Relationship of Material Properties to Electromagnetic Shielding_, prepared by the Syracuse Research Corporation for the Office of Naval Research and the Naval Air Systems Command under Contract N00014-78-C-0673, SRC TN 79-037, January 1979 (Unclassified).

7. _Electromagnetic Properties and Effects of Advanced Composite Materials: Measurement and Modeling_, prepared by Georgia Institute of Technology, Syracuse University, State University of New York and the US Air Force Acadamey for the Rome Air Development Center, RADC TR 78-156, Phase Report, June 1978.

8. H.W. Ott, _Noise Reduction Techniques in Electronic Systems_, Wiley-Interscience, 1976.

SECTION 5

JOINT COUPLING

5.1 DEFINITION OF JOINT ADMITTANCE

Skin currents flowing across a join in the aircraft skin induce electric fields in the aircraft interior. These fields in turn induce transients on interior wiring. The maximum voltage which can be induced on an interior wire is the voltage drop across the joint, namely, $V_J = J_S/Y_J$ where J_S is the surface current density at the joint and Y_J is the joint admittance/unit length.

Well-formed joints in shield material (those of uniform construction and good electrical contact and without cracks or apertures) can be described in terms of a distributed joint transfer admittance per unit of joint width. A section of shield surface containing such a joint is shown in Figure 5-1. The exterior surface current density J_S flowing across the joint produces a voltage V_j across the joint on the inside. For a linear joint contact impedance, the interior joint voltage is proportional to exterior surface current $I_{tot} = J_S W$ and inversely proportional to joint width W. The proportionality factor between V_j and J_S is Y_j, the joint admittance per unit of joint width; i.e., $J_S = Y_j V_j$.

Typical joint construction is shown in Figure 5-2 for three different joints. Corresponding measured joint admittances are shown in Figure 5-3. Joint 2 is common practice and has a joint admittance of about 15 mhos/m over a large frequency range.

5.2 JOINT MODEL

Harrington[3] defines the joint admittance in a similar manner but identifies it as a transfer admittance. For the simple butt joint of Figure 5-4, transmission line theory and circuit theory applied to the equivalent circuit of Figure 5-5 yield

$$Y_J = (Y^a + Y^c)\cosh \gamma_b d + (Y_o + \frac{Y^a Y^c}{Y_o})\sinh \gamma_b d \qquad (1)$$
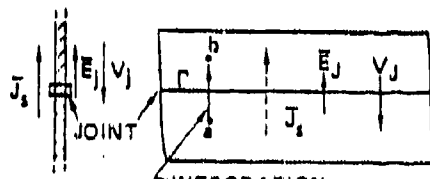
Joint voltage:

$$V_J = \int_a^b E_J \cdot dl = \frac{J_s}{Y_J}$$

Y_J (joint coupling admittance per unit joint width):

$$Y_J = \frac{J_s}{V_J} \quad \text{(mhos/meter)}$$

Example: Perfect sheets with joint
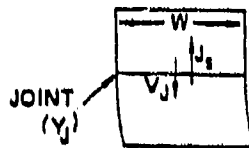
1. Total joint admittance:
$$Y_{tot} = Y_J W$$

2. Total joint current:
$$I_{tot} = J_s W$$

3. Joint voltage:
$$V_J = \frac{I_{tot}}{Y_{tot}} = \frac{J_s W}{Y_J W} = \frac{J_s}{Y_J}$$

Figure 5-1.   Joint Coupling[1]

1

C   C

|← 0.5" →|
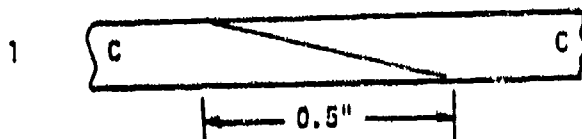
CYLINDER WAS FABRICATED EXTRA
LONG, CUT, MACHINED AND SECON-
DARILY BONDED WITH EA-934
ADHESIVE.

2

|← 1.0" →|

M   C

|← 1.0" →|
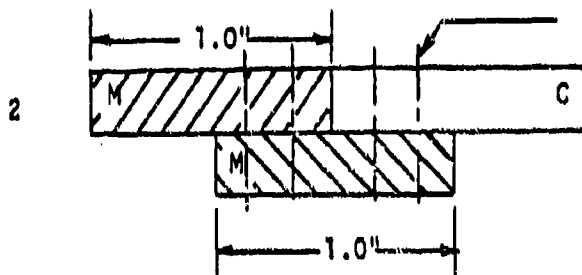
1/8 DIA RD.HD. RIVET C TO M
1/8 DIA BOLT M. TO M.

CYLINDER CENTER TOWARDS BOTTOM
OF PAGE. METAL RINGS FABRICATED
FROM ALUMINUM SHEET, CUT, ROLLED
AND WELDED. THE RIVETS OR BOLTS
WERE PLACED IN A CIRCUMFERENTIAL
ROW APPROXIMATELY ONE INCH APART
AND ALTERNATING 1/8 INCH TO EITHER
SIDE OF THE CIRC. CTR LINE.

3

M   C

|← 1.0" →| |← 0.5" →|
                     (TYP)
|←──────── 2.5" ────────→|
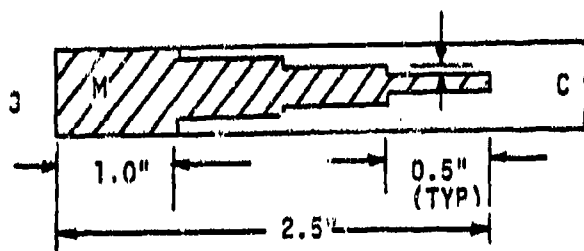
FIRST THREE STEPS (4 PLY PER
STEP) WERE PRECURED (COMPACTED),
EA-934 APPLIED TO SANDED COMPOSITE
STEPS, AND THEN LONGITUDINALLY
SLIT METAL RING MANEUVERED INTO
PLACE. REMAINING COMPOSITE STEPS
WERE APPLIED TO EA-934 COATED
METAL RING IN PLACE. METAL RING
WAS FABRICATED FROM 2024 ALUMINUM.

Figure 5-2. Structural Joints[1]

(a) Joint No. 2

(b) Joint Nos. 1 and 3
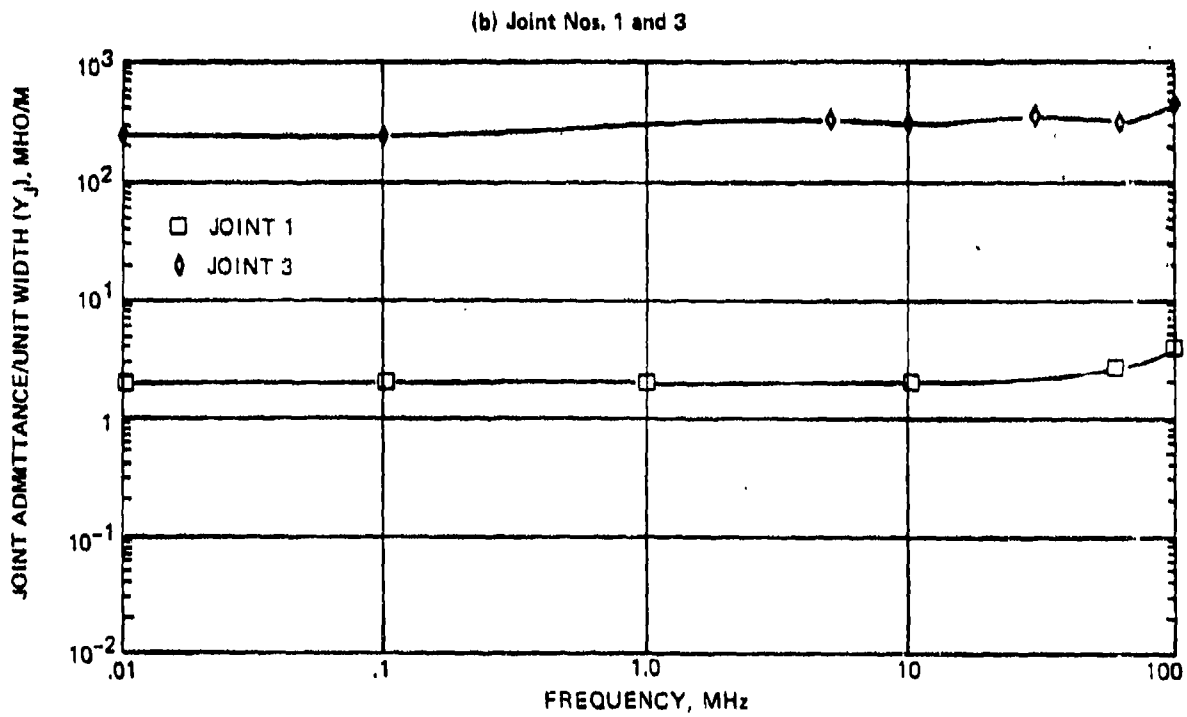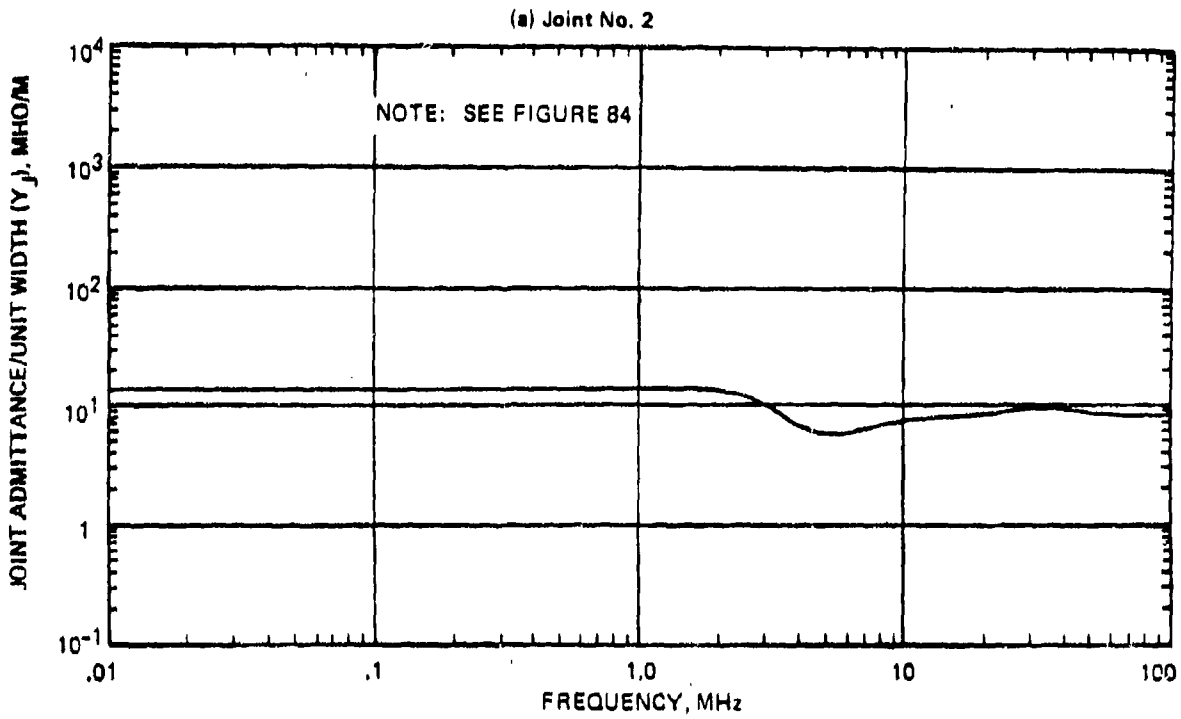
Figure 5-3. Measured Joint Admittance[1]

5-4
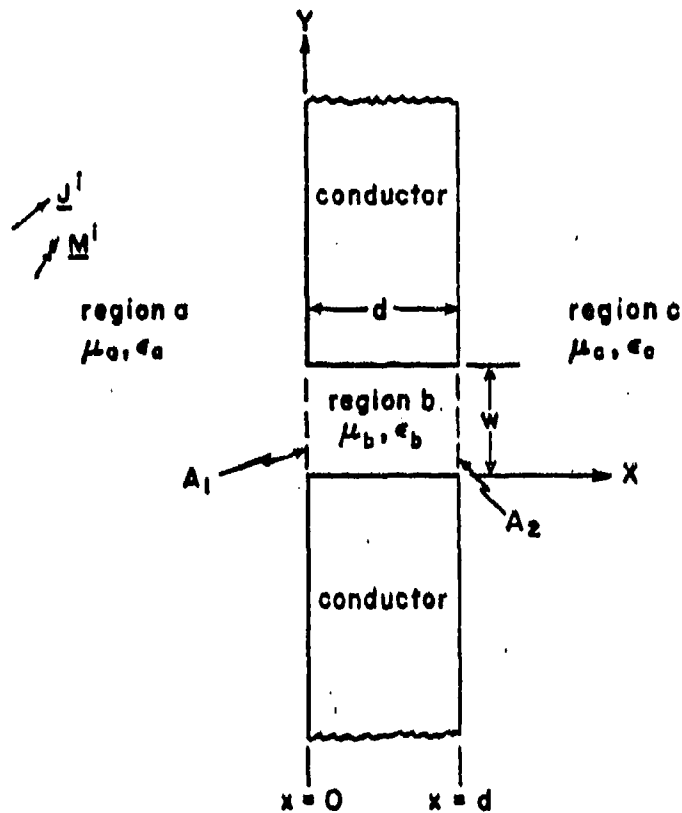
Figure 5-4. Uniform Slot of Width w in a Perfectly Conducting Screen of Thickness d
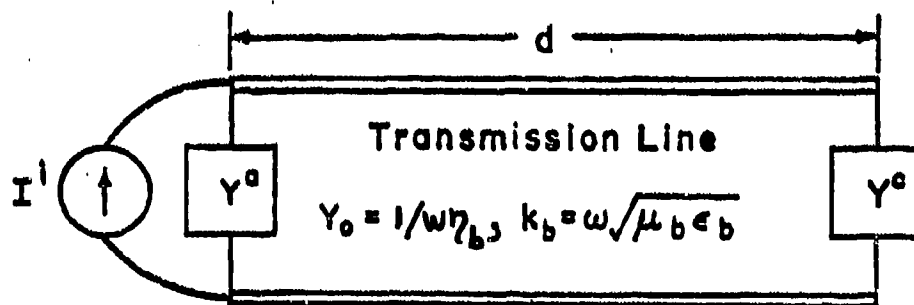
Figure 5-5. Equivalent Circuit for a Narrow Slot in a Thick Conducting Screen

Here Y^a is the aperture admittance of a thin slot opening into half space of region a. That for region c has the same form with all a's replaced by c's for region c. The aperture admittance has th form

$$Y^a = \frac{w}{\eta_a \lambda_a} [\pi - 2j \ln(C \, k_a \, w)] \qquad (2)$$

for region a. In Equation 2, η_a, λ_a, and k_a are the intrinsic impedance, wavelength, and wave number of medium a, respectively, and C is the constant depending on the choice of the assumed variation of the tangential electric field in the slot. It is well known that the aperture admittance of a thin slot opening into half space is insensitive to small variations in the tangential electric field in the slot about its true value. If the tangential electric field is assumed to be the quasi-static solution for a slot in a zero thickness screen, then

$$C = \gamma/8 \simeq 0.2226 \qquad (3)$$

Here $\gamma = 1.781...$. Since C is in a logarithmic term in Equation 2, it makes little difference which value is chosen. However, the solution remains strictly valid as the thickness $d \to 0$ when Equation 3 is chosen.

For a highly lossy slot, Equation 1 becomes

$$Y_j = \sigma d/w \qquad (4)$$

independent of frequency. This is the behavior shown over low frequency for the joints shown in Figure 5-3.

5.3 REFERENCES

1. F. Force, P. Geren, D. Strawe, and A. Schmidt, <u>Investigation of Effects of Electromagnetic Energy on Advanced Composite Aircraft Structures and Their Associated Avionic Electrical Equipment</u>, Phase II, Vol. 1, prepared by the Boeing Company for Naval Air Systems Command, Final Report D18-20186-4 under Contract N00019-76-C-0497, September 1977.

2. D.T. Auckland, "Electromagnetic Transmission through a Filled Slit of Arbitrary Cross Section in a Conducting Plane of Finite Thickness," Ph.D. Dissertation, Syracuse University, June 1979. Also available as Report TR 79-7, Department of Electrical and Computer Engineering, Syracuse University, June 1979.

3. R.F. Harrington, <u>Time-Harmonic Electromagnetic Fields</u>, McGraw-Hill Book Co., New York, Sec. 4-11, 1968.

SECTION 6

COUPLING OF EM FIELDS TO TRANSMISSION LINES

This section summarizes the coupling of an EM field to a transmission line. Expressions for the open-circuit voltage and short-circuit current are derived for a transmission line illuminated by a uniform EM field and a nonuniform field that can be modeled by a uniform field incident on a portion of the line. In either case, the Thevinin and Norton equivalent circuits can be used to aid analysis.

In Subsection 6.1, the open-circuit voltage and short-circuit current are first given as functions of frequency which are then Fourier transformed to the time domain. Subsection 6.2 gives a closer analysis of the open-circuit voltage as a function of frequency. Various graphs are presented for the special case of a uniform electric field. The case of a single wire over a ground plane is then shown to be equivalent to a two-wire transmission line, using imaging. Low frequency approximations are derived, followed by a discussion of coupling to a shielded cable.

Using the expressions derived in Subsection 6.1 for the open-circuit voltage and closed-circuit current as functions of time, upper bounds are computed for various quantities. The open-circuit voltage, closed-circuit current, power, and energy as seen across the end of a transmission line are given upper bound estimates.

The special cases of lightning EMP and nuclear EMP are discussed. Curves are presented giving the predicted open-circuit voltages and short-circuit currents for both threats for a model of a wire interior to an F-18. These results are compared to similar plots, obtained using an elaborate moment method scheme, presented in a report by the Boeing Aerospace Company.[1] Using these curves comparisons are made with the various upper bound estimates previously derived.

Finally, there is a discussion relating the Wunsch damage constant
for semiconducting devices, which assumes a square-wave power pulse, to more
general power waveforms. Two "equivalent" square-wave power pulses are de-
fined for a general waveform. One is equivalent in that it has the same dam-
age constant as the original pulse. The other is equivalent in that it has
the same energy content. The latter of these is much easier to compute and
yields results which err toward safety.

The results of this section are then use to estimate the total energy
across the ends of a transmission line from tabulated values of the peak open-
circuit voltage and short-circuit current.

6.1 DERIVATION OF $V_{OC}(t)$ AND $I_{SC}(t)$

An isolated two-wire transmission line illuminated by a uniform EM
field is shown in Figure 6-1. The lines lie in the x-z plane, parallel to the
z-axis with terminations parallel to the x-axis. The wires, of diameter a,
are a distance b apart and are of length L. The incident field propagates in
the -x direction with the E-field parallel to the z-axis. An expression for
the differential mode load current across the left-hand termination is given by:[2]

$$I(\omega) = \int_0^L (E^1(b, \omega) - E^1(0, \omega)) G(z, \omega) \, dz \qquad (1)$$

where

$$G(z, \omega) = \frac{Z_0 \cosh \gamma(L - z) + Z_2 \sinh \gamma(L - z)}{(Z_0 Z_1 + Z_0 Z_2) \cosh \gamma L + (Z_0^2 + Z_1 Z_2) \sinh \gamma L} \qquad (2)$$

and:

$E^1(b, \omega)$ = incident field evaluated at x = b

$E^1(0, \omega)$ = incident field evaluated at x = 0

Z_0 = characteristic impedance of the line

Z_1 = left-hand terminating impedance

Z_2 = right-hand terminating impedance
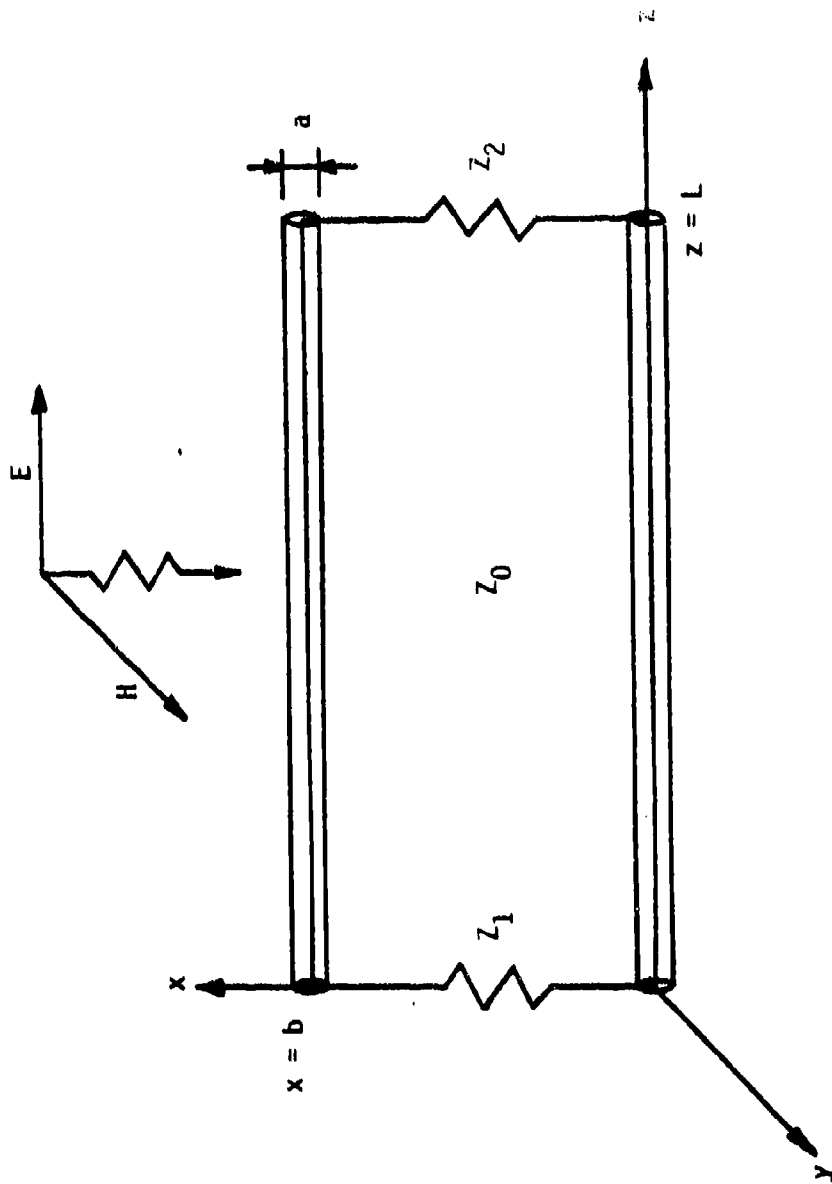
Figure 6-1. Two-Wire Line Illuminated by a Uniform EM Field

$$\gamma \quad = \alpha + j\beta = \text{propagation constant of line}$$

$\gamma \qquad = \alpha + j\beta =$ propagation constant of line

$\alpha \qquad =$ attenuation constant of the line

$\beta \qquad = \omega/v =$ phase constant of the line

$v \qquad =$ the velocity of propagation on the line

$\omega \qquad = 2\pi f$ where f is frequency

From Equation 1 expressions can be derived for the open-circuit voltage, V_{oc}, and the short-circuit current, I_{sc}, across the left-hand termination.

Letting,

$$G_{oc}(z,\omega) = \lim_{z_1 \to \infty} Z_1 G(z,\omega) = \frac{Z_0 \cosh \gamma(L-z) + Z_\ell \sinh \gamma(L-z)}{Z_0 \cosh \gamma L + Z_\ell \sinh \gamma L} \quad (3)$$

and

$$G_{sc}(z,\omega) = \lim_{z_1 \to \infty} G(z,\omega) = \frac{Z_0 \cosh \gamma(L-z) + Z_\ell \sinh \gamma(L-z)}{Z_0 (Z_\ell \cosh \gamma L + Z_0 \sinh \gamma L)} \quad (4)$$

we have

$$V_{oc}(\omega) = \int_0^L \left[E^i(b,\omega) - E^i(0,\omega) \right] G_{oc}(z,\omega) \, dz \quad (5)$$

and

$$I_{sc}(\omega) = \int_0^L \left[E^i(b,\omega) - E^i(0,\omega) \right] G_{sc}(z,\omega) \, dz \quad (6)$$

Consider the factor $E^1(b, \omega) - E^1(0, \omega)$ which appears in the above equations. If we assume zero phase for the incident field at $x = b/2$, this expression can be written as:

$$E^i(b,\omega) - E^i(0,\omega) = E_0(\omega) \left[e^{j k \frac{b}{2}} - e^{-j k \frac{b}{2}} \right] = 2j \, E_0(\omega) \sin\left(\frac{kb}{2}\right) \quad (7)$$

6-4

where k is the wave number for incident field in free space and $E_0(\omega)$ is the incident electric field.

In what follows we will use $E_0(\omega)$ instead of the more complicated expression in Equation 7. It is an easy matter to modify the results obtained to include the phase difference between the two lines. Our basic equations for V_{oc} and I_{sc} then become:

$$V_{oc}(\omega) = \int_0^L E_0(\omega)\, G_{oc}(z,\omega)\, dz \qquad (8)$$

and

$$I_{sc}(\omega) = \int_0^L E_0(\omega)\, G_{sc}(z,\omega)\, dz \qquad (9)$$

Equations 3 and 4 can be rewritten as

$$G_{oc} = \left[e^{-\gamma z} - 2 \sinh \gamma z \left(\sum_{n=1}^{\infty} \left(\Gamma e^{-2\gamma L} \right)^n \right) \right] \qquad (10)$$

and

$$G_{sc} = \left[e^{-\gamma z} + 2 \cosh \gamma z \left(\sum_{n=1}^{\infty} \left(-\Gamma e^{-2\gamma L} \right)^n \right) \right] \qquad (11)$$

where Γ is the reflection coefficient at the right-hand termination, given by

$$\Gamma = \frac{Z_2 - Z_0}{Z_2 + Z_0} \qquad (12)$$

This allows V_{oc} and I_{sc} to be expressed by:

$$V_{oc}(\omega) = \frac{E_0(\omega)}{\gamma} \left[2 e^{-\frac{\gamma L}{2}} \sinh\left(\frac{\gamma L}{2}\right) - 4 \sinh^2\left(\frac{\gamma L}{2}\right) \left(\sum_{n=1}^{\infty} \left(\Gamma e^{-2\gamma L} \right)^n \right) \right] \qquad (13)$$

and

$$I_{sc}(\omega) = \frac{E_o(\omega)}{Z_o \gamma} \left[2 e^{-\gamma \frac{L}{2}} \sinh\left(\frac{\gamma L}{2}\right) + 2 \sinh(\gamma L)\left(\sum_{n=1}^{\infty} (-\Gamma e^{-2\gamma L})^n \right) \right] \qquad (14)$$

V_{oc} and I_{sc} can be found as functions of time by applying the inverse Fourier transform to the above expressions. We will make the assumption at this point that the lines are lossless, so that $\gamma = j\beta$.

$$V_{oc}(t) = v \int_0^{T_o} E_o(t-\tau)d\tau + \sum_{n=1}^{\infty} v\Gamma \left\{ \int_{2nT_o}^{(2n+1)T_o} E_o(t-\tau)d\tau - \int_{(2n-1)T_o}^{2nT_o} E_o(t-\tau)d\tau \right\} \qquad (15)$$

and

$$Z_o I_{sc}(t) = v \int_0^{T_o} E_o(t-\tau)d\tau + \sum_{n=1}^{\infty} v(-\Gamma)^n \left\{ \int_{(2n-1)T_o}^{(2n+1)T_o} E_o(t-\tau)d\tau \right\} \qquad (16)$$

Here, $T_o = L/v$.

If we introduce the notation

$$I_n(t) = v \int_{nT_o}^{(n+1)T_o} E_o(t-\tau)d\tau \qquad (17)$$

then

$$V_{oc}(t) = I_o(t) + \sum_{n=1}^{\infty} \Gamma^n (I_{2n} - I_{2n-1}) \qquad (18)$$

$$Z_o I_{sc}(t) = I_o(t) + \sum_{n=1}^{\infty} (-\Gamma)^n (I_{2n} + I_{2n-1}) \qquad (19)$$

Each of the terms in these expressions can be interpreted as a (multiple) re-flection of an excitation arising from the incident field at some past time.

Similar expressions can be derived where the field is incident on only a portion of the line. (This allows for approximating the case of a non-uniform field, due to coupling through an aperture, for example.)[3] In particular, if we assume as before that the incident field is parallel to the line, with no z-dependence, and only effects the line between z_1 and z_2, $0 \leq z_1 < z_2 \leq L$, then

$$V_{oc}(t) = I_o^s(t) + \sum_{n=1}^{\infty} \Gamma^n (I_{2n}^s - I_{2n-1}^s) \tag{20}$$

$$Z_o I_{sc}(t) = I_o^s(t) + \sum_{n=1}^{\infty} (-\Gamma)^n (I_{2n}^s + I_{2n+1}^s) \tag{21}$$

where

$$I_{2n}^s(t) = v \int_{2nT_o+t_1}^{2nT_o+t_2} E_o(t-\tau) \, d\tau \tag{22}$$

and

$$I_{2n-1}^s(t) = v \int_{2nT_o-t_2}^{2nT_o-t_1} E_o(t-\tau) \, d\tau \tag{23}$$

6.2 OPEN-CIRCUIT VOLTAGE AS A FUNCTION OF FREQUENCY

From Equation 8, we have the open-circuit voltage defined as a function of frequency

$$V_{oc}(\omega) = \int_0^L E_o(\omega) G_{oc}(z,\omega) \, dz \tag{24}$$

For the special case where $E_o(\omega)$ is constant, the integral can be evaluated to yield

$$V_{oc}(\omega) = E_o \left[\frac{\frac{(Z_o^2 - Z_\ell^2)\lambda}{4\pi} \sin 4\pi \left(\frac{L}{\lambda}\right) + \frac{Z_\ell^2 \lambda}{2\pi} \sin 2\pi \left(\frac{L}{\lambda}\right) - j \frac{Z_\ell Z_o \lambda}{2\pi} \left(1 - \cos \frac{2\pi L}{\lambda}\right)}{Z_o^2 \cos^2 2\pi \left(\frac{L}{\lambda}\right) + Z_\ell^2 \sin^2 2\pi \left(\frac{L}{\lambda}\right)} \right] \tag{25}$$

Plots of this expression were made for values of L from zero to five wavelengths. The expressions were normalized so that choosing specific values of E_o and λ was unnecessary. Plots of the quantity $|V_{oc}|/E_o\lambda$ appear in Figure 6-2, for $Z_o = 100$ and $Z_2 = 30$. The open-circuit voltage is seen to have extrema for values of line length L approximately equal to multiples of one quarter wavelength. The approximation is much better for longer lines $(L > 2\lambda)$ than shorter ones. Figure 6-3 shows similar plots with the impedance values reversed. The positions of the maxima and minima are also seen to be reversed.

Figure 6-4 shows plots of open-circuit voltage normalized in a different manner. The line length was fixed at ten meters, and the frequency was varied from 100 kHz to 10 GHz. The quantity $|V_{oc}|/E_o$ was plotted, for $Z_o = 100$ and $Z_2 = 30$. The frequency for which the line length of 10 m equals one-quarter wavelength is 7.5 MHz (log = 6.88), which gives a maximum in the open-circuit voltage, in agreement with Figure 6-2. For significantly lower frequencies, the open-circuit voltage is seen to conform to the approximation $|V_{oc}| \approx E_o L$. For significantly higher frequencies, the open-circuit voltage experiences an ever-increasing number of excursions due to the log frequency scale. The plots do not show all of the excursions in the higher-frequency region because it would be impractical to raise the sampling rate to the required level.

Figure 6-5 is similar to Figure 6-4, except that the impedance values are reversed. The first maximum is seen to occur at 15 MHz (log = 7.18), corresponding to $L = \lambda/2$, in agreement with Figure 6-3.

Bounds for the open-circuit voltage can be computed for the higher-frequency region by using the observation that extrema occur when $d = n\lambda/4$. This substitution greatly simplifies the expression for open-circuit voltage, as follows:

$$\frac{|V_{oc}|}{E_o} = \begin{cases} \dfrac{\lambda}{2\pi}\sqrt{1 + \dfrac{Z_o^2}{Z_L^2}} & n = 1, 3, 5, 7, \ldots \\[4mm] \dfrac{\lambda}{\pi}\left(\dfrac{Z_L}{Z_o}\right) & n = 2, 6, 10, \ldots \\[4mm] 0 & n = 4, 8, 12, \ldots \end{cases} \tag{26}$$

6-8
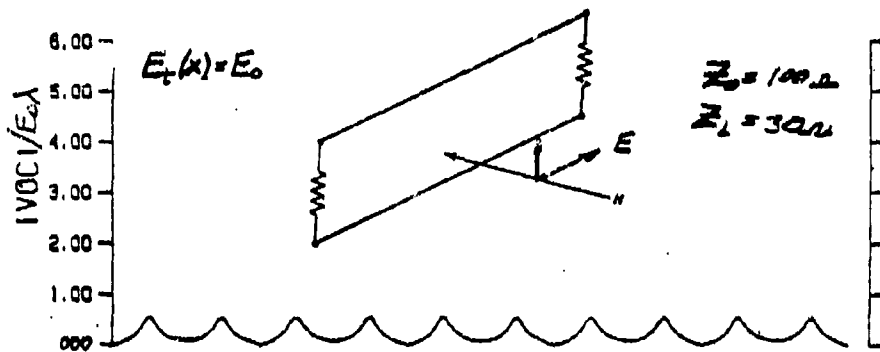
Figure 6-2. Normalized Plots of Open-Circuit Voltage
(Z_O = 100, Z_L = 30)
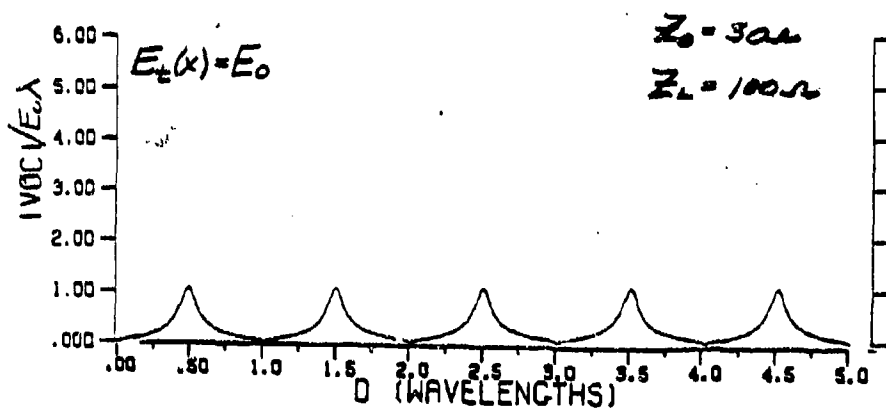
Figure 6-3. Normalized Plots of Open-Circuit Voltage
(Z_O = 30, Z_L = 100)
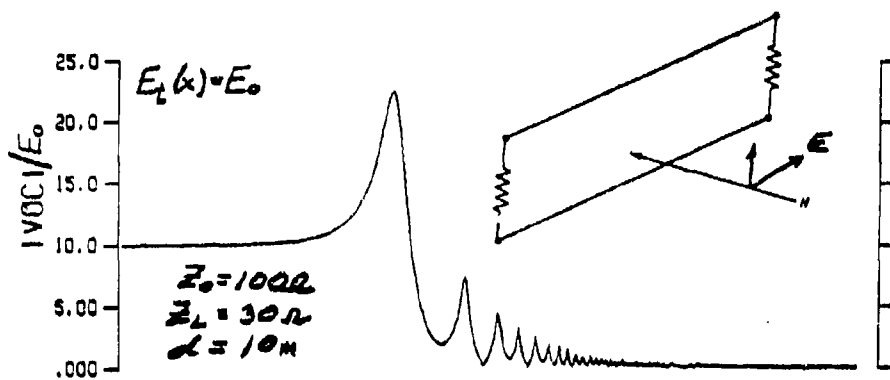
Figure 6-4. Normalized Open-Circuit Voltage as a Function of Frequency (Z_0 = 100, Z_L = 30, and L = 10 m)
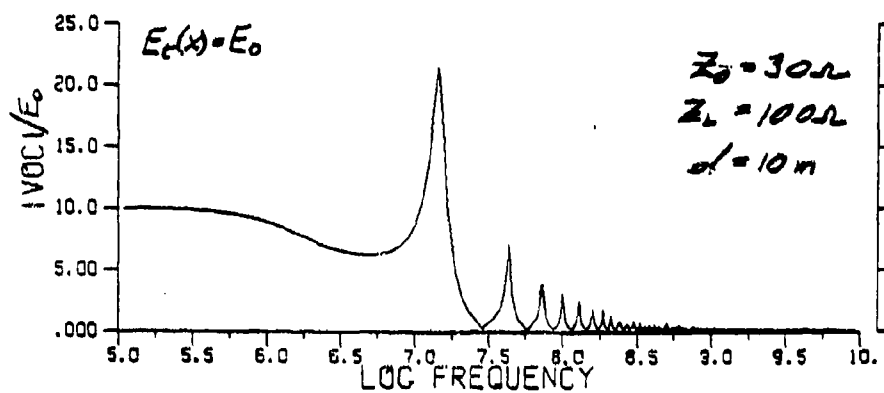
Figure 6-5. Normalized Open-Circuit Voltage as a Function of Frequency (Z_0 = 30, Z_L = 100, and L = 10 m)

6-10

Figures 6-6 and 6-7 show these bounds plotted over the open-circuit voltage for the same conditions as Figures 6-4 and 6-5. The bounds are violated at lower frequencies due to failure in the quarter-wavelength approximation for extrema location. If $Z_o > Z_2$, maxima occur for N odd and minima for n even. If $Z_2 > Z_0$ the reverse occurs.

6.3 WIRE OVER A GROUND PLANE

A single-wire transmission line terminated at both ends to a perfectly conducting ground plane is shown in Figure 6-8a. The distance between the wire and ground plane is b/2 and the terminating impedances are $Z_1/2$ and $Z_2/2$. The length of the wire is L, with diameter a. The incident field is denoted by $E^1(x, \omega)$ and is assumed as before to be parallel to the z-axis, propagating in the -x direction.

Using image theory, the ground plane can be replaced by the image of the wire and its terminations, together with the image field. This is shown in Figure 6-8b. Except for the presence of the image field, the image problem is equivalent to the two-wire transmission line problem discussed earlier.[2]

Two observations can be made when both the incident and image fields are considered. First, the differential mode current for a wire over a ground plane is twice that for an isolated two-wire system. Second, the common mode, or antenna mode current is zero.

Using the notation of Subsection 6-1 and this subsection, the single wire over a ground plane can be analyzed using the results of Subsection 6-1 simply by multiplying the incident field by a factor of 2.

6.4 LOW FREQUENCY APPROXIMATION

If the length, L, of the wires is assumed to be short compared to wavelength, then for lossless lines, Equations 8 and 9 can be approximated by:

$$V_{oc}(\omega) \approx \int_o^L E_o(\omega) \left(\frac{Z_o + j Z_2 \beta (L-z)}{Z_o + j Z_2 \beta L} \right) dz \approx L E_o(\omega) \qquad (27)$$

6-11
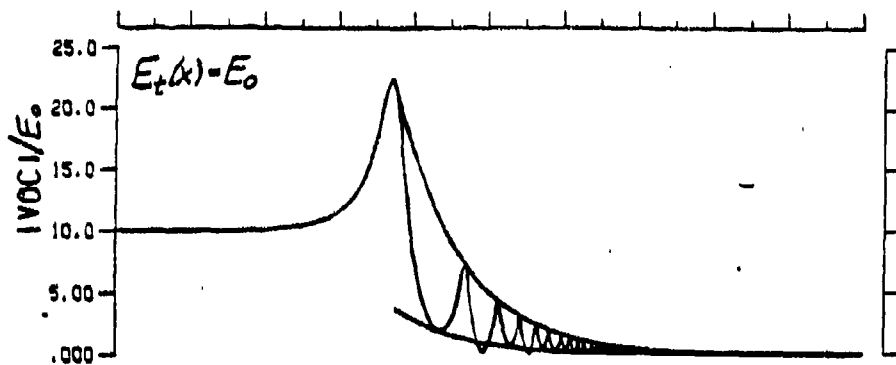
Figure 6-6. Normalized Open-Circuit Voltage as a Function of Frequency, Showing Bounds Valid in Higher-Frequency Region (Z_0 = 100, Z_L = 30, and L = 10 m)
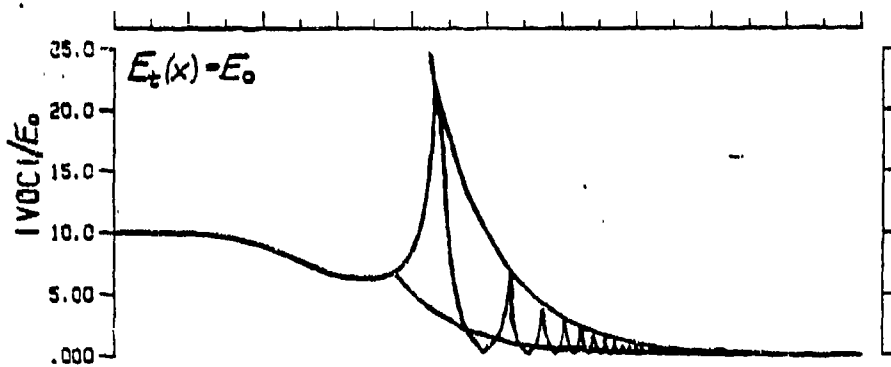
Figure 6-7. Normalized Open-Circuit Voltage as a Function of Frequency, Showing Bounds Valid in Higher-Frequency Region (Z_0 = 30, Z_L = 100, and L = 10 m)
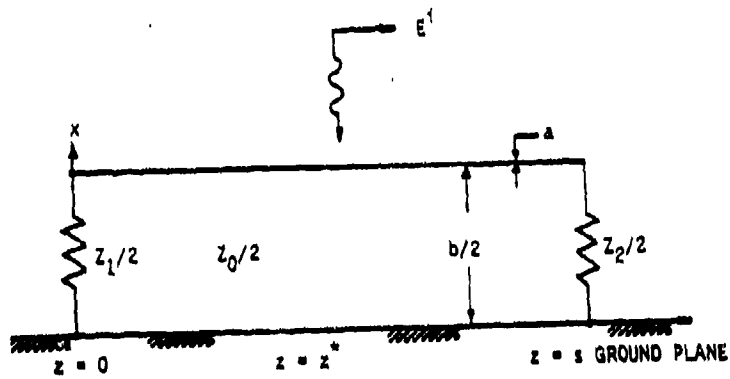
(a) PHYSICAL REPRESENTATION
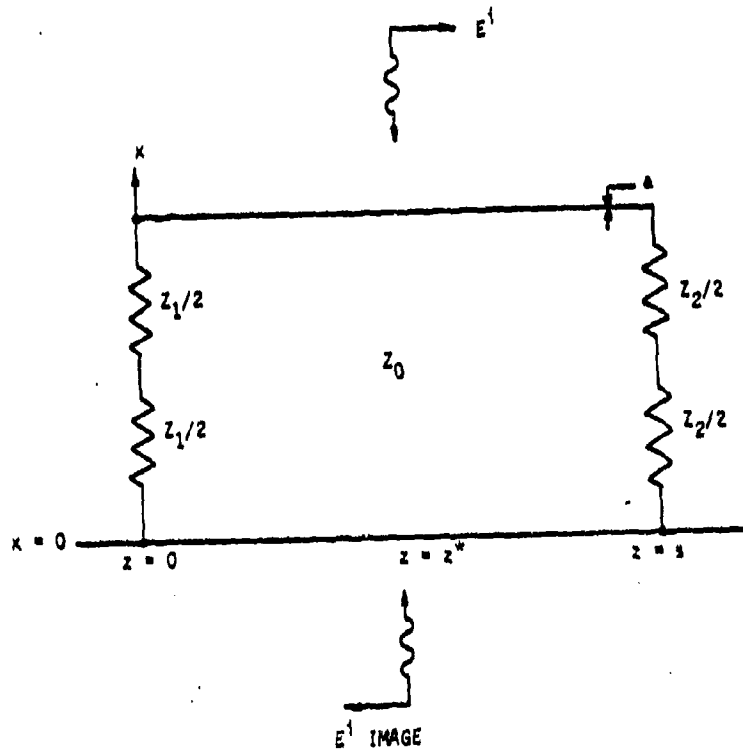
(b) IMAGE PROBLEM

Figure 6-8. Wire Over a Ground Plane

6-13

$$I_{sc}(\omega) \approx \int_{0}^{L} E_{o}(\omega) \left(\frac{Z_{o} + j Z_{2} \beta(L-z)}{Z_{o}(Z_{2} + j Z_{o}\beta L)} \right) dz \approx \frac{L E_{o}(\omega)}{Z_{2}} \qquad (28)$$

This indicates that as functions of time, the open-circuit voltage and short-circuit current are given by:

$$V_{oc}(t) \approx L E_{o}(t) \qquad (29)$$

$$I_{sc}(t) \approx (L E_{o}(t))/Z_{2} \qquad (30)$$

It should be noted that these results could also have been obtained from Equations 18 and 19 by applying the short line approximation in a straightforward manner.

6.5 SHIELDED CABLES

The illumination of a shielded cable by an external EM field excites a current distribution on the outer shield. Since the shield is not a perfect conductor, this current penetrates the shield and produces a voltage distribution along the inside length of the cable. This voltage distribution in turn produces a current in the interior load impedances. The pertinent geometry is shown in Figure 6-9, where the parameters involved are:[2]

$I(z)$	= shield current distribution
L	= cable length
b/2	= height of cable above ground plane
a	= outside diameter of cable
$z_{1}/2$, $z_{2}/2$	= terminating impedances of cable shield treated as a single-wire transmission line over a ground plane
$z_{0}/2$	= characteristic impedance of cable shield treated as a single-wire transmission line over a ground plane
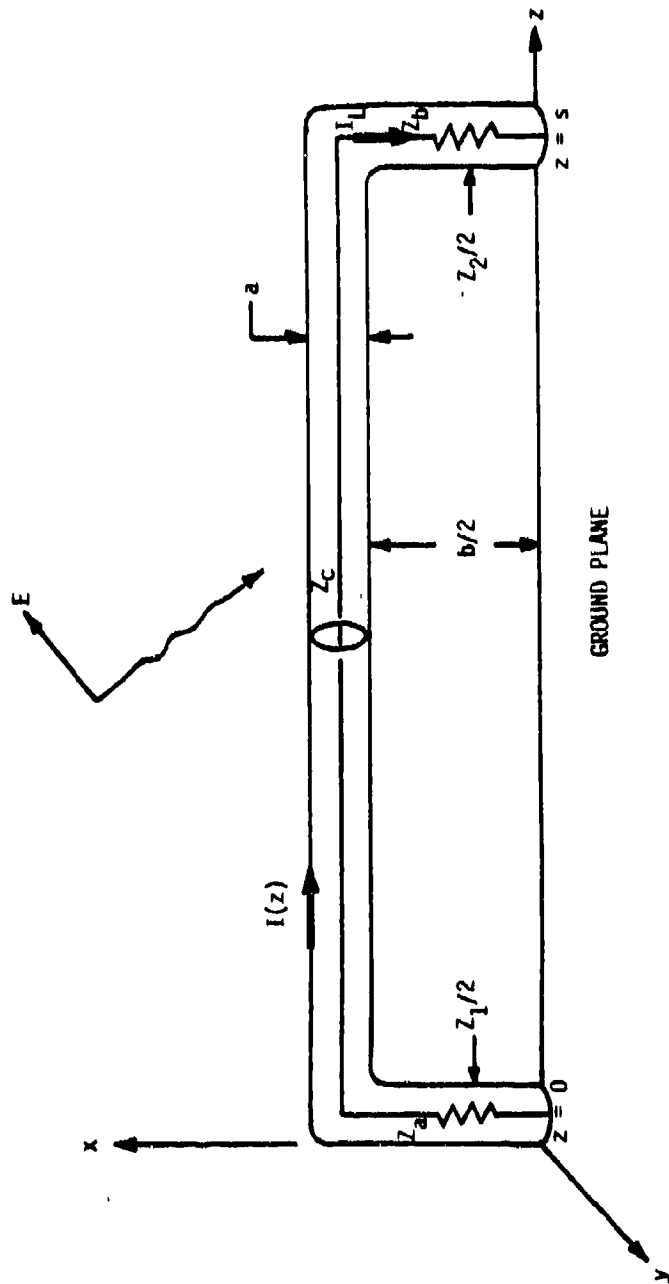
Figure 6-9. Shielded Cable Geometry

$$Z_a, Z_b = \text{interior load impedances}$$

$$Z_c = \text{characteristic impedance of interior line}$$

$$I_L = \text{current in the interior load impedance } Z_a$$

The length of the cable is taken to be much greater than its height above the ground plane, so that I(z) is the only current of consequence. Otherwise, the contribution from I(x) must be included.

The outer sheath current and the voltage induced along the inside of the cable are related by the surface transfer impedance. In particular,

$$dV(z) = Z_t \, I(z) \, dz \tag{31}$$

where

$$Z_t = \text{the surface transfer impedance}$$
$$V = \text{voltage induced along the inside of the cable}$$

The current in interior load impedance Z_a can be given by an equation analogous to Equation 1,

$$I_L(\omega) = \int_0^L Z_t \, I(z,\omega) \, \frac{(Z_c \cos\beta_i z + j Z_a \sin\beta_i z) \, dz}{[Z_c(Z_a + Z_b)\cos\beta_i L + j(Z_o^2 + Z_a Z_b)\sin\beta_i L]} \tag{32}$$

where β_1 is the wave number inside the cable.

For a uniform plane wave traveling in the -x direction with a constant electric field in the z-direction, the sheath current distribution can be given by:

$$I(z,\omega) = \frac{-2j E_z(\omega)}{Z_o \beta} \left\{ 1 - \frac{[Z_o Z_2 \cos\beta z + Z_o Z_1 \cos\beta(L-z)] +}{(Z_o Z_1 + Z_o Z_2)\cos\beta L +} \right.$$
$$\left. \frac{j[Z_1 Z_2 \sin\beta z + Z_1 Z_2 \sin\beta(L-z)}{j(Z_o^2 + Z_1 Z_2)\sin\beta L} \right\} \tag{33}$$

Using a short wire (low frequency) approximation, Equation 33 can be rewritten:

$$I(z,\omega) \approx \frac{2E_z(\omega)L}{(Z_1 + Z_2)} \qquad (34)$$

This result can be interpreted as showing that for low frequencies the effective incident electric field on the interior wire is given by

$$E_{eff} \approx \frac{2Z_t E_z(\omega)L}{(Z_1 + Z_2)} \qquad (35)$$

Combined with the low frequency approximation given in Equations 29 and 30. This gives us approximations to the open-circuit voltage and short-circuit current for a shielded cable.

$$V_{oc}(t) \approx \frac{2L^2 Z_t E_o(t)}{(Z_1 + Z_2)} \qquad (36)$$

$$Z_b I_{sc}(t) \approx \frac{2L^2 Z_t E_o(t)}{(Z_1 + Z_2)} \qquad (37)$$

6.6 UPPER BOUNDS FOR VOLTAGE, CURRENT, POWER AND ENERGY FOR A GENERAL INCIDENT FIELD

Using the expressions for $V_{oc}(t)$ and $I_{sc}(t)$ as given in Equations 18 and 19 (or 20 and 21) various upper bounds can be found for the open-circuit voltage and short-circuit current. The accuracy of these estimates depends on the form of the incident field. If a particular incident field is assumed then better estimates can be made.

If we assume that $I_n(t)$ is positive for each n, and we define

$$I_{max} = \max_t I_o(t) \tag{38}$$

then from Equation 18, we have

$$|V_{oc}(t)| \leq I_o(t) + \sum_{n+1}^{\infty} |\Gamma|^n |I_{2n} - I_{2n-1}| \tag{39}$$

$$\leq I_{max} + \sum_{n=1}^{\infty} |\Gamma|^n I_{max} = I_{max} / (1 - |\Gamma|) \tag{40}$$

Similarly from Equation 19 we have

$$|Z_o I_{sc}(t)| \leq I_{max} + 2 \sum_{n=1}^{\infty} |\Gamma|^n I_{max} = I_{max} \frac{1 + |\Gamma|}{1 - |\Gamma|} \tag{41}$$

I_{max} can be computed for a given incident field, or it can be estimated by

$$I_{max} \leq L E_{max}^i \tag{42}$$

where

$$E_{max}^i = \max_t E_o(t) \tag{43}$$

For an incident field with a very rapid rise and decay, such as a nuclear EMP, the peak voltage and current will occur shortly after the commencement of the incident field. If the rise time to peak for the field is comparable to the length of the line, T_o, then only the first several terms of Equations 18 and 19 will be nonzero at the time the peak occurs. Therefore,

$$|V_{oc}(t)| \leq \max_t |I_o(t) - \Gamma I_1(t) + \Gamma I_2(t)| \leq I_{max}(1 + |\Gamma|) \tag{44}$$

6-18

and

$$|Z_o I_{sc}(t)| \le \max_t |I_o(t) - \Gamma I_1(t) - \Gamma I_2(t)| \le I_{max}(1 + 2|\Gamma|) \tag{45}$$

If a resistance R is placed across the left-hand terminals of our transmission line model, then the delivered instantaneous power, P(t), can be bounded in three ways:

$$P(t) \le V_{oc}^2(t) / R \tag{46}$$

$$P(t) \le I_{sc}^2(t) \ R \tag{47}$$

$$P(t) \le V_{oc}(t) I_{sc}(t) \tag{48}$$

It can easily be seen that Equation 46 will give the best estimate if $R > V_{oc}(t)/I_{sc}(t)$ and Equation 47 will be best if $R < V_{oc}(t)/I_{sc}(t)$. If $R = V_{oc}(t)/I_{sc}(t)$, then all three bounds are equal. If no specific value of R is known then Equation 48 should be used.

Using Equation 48, together with our previous estimates for V^{peak} and I_{sc}^{peak}, given in Equations 40 and 41, we have

$$P^{peak} \le V_{oc}^{peak} I_{sc}^{peak} \le \frac{I_{max}^2(1 + |\Gamma|)}{|Z_o|(1 - |\Gamma|)^2} \tag{49}$$

If $\Gamma < 0$, then the following is valid:

$$P^{peak} \le \frac{L^2 E_{max}^2 (Z_o + Z_2)}{2(Z_2)^2} \tag{50}$$

Upper bounds for the maximum energy which the incident field can deliver to the line can be obtained as follows. We have from Equations 18 and 19,

$$V_{oc}(t) = I_o(t) + \sum_{n=1}^{\infty} \Gamma^n [I_{2n}(t) - I_{2n-1}(t)] \tag{51}$$

6-19

and

$$Z_o I_{sc}(t) = I_o(t) + \sum_{n=1}^{\infty} (-\Gamma)^n \left[I_{2n}(t) + I_{2n-1}(t) \right]$$ (52)

The energy delivered across the left-hand terminals is given by

$$E = \int_0^{\infty} P(t)\, dt$$ (53)

Using Equations 46 and 47, this becomes

$$E \leq \frac{1}{R} \int_0^{\infty} V_{oc}^2(t)\, dt$$ (54)

$$E \leq R \int_0^{\infty} I_{sc}^2(t)\, dt$$ (55)

We introduce here the L^2 normal of a function, which is defined by

$$\| f \| = \left\{ \int_{-\infty}^{\infty} |f(t)|^2 dt \right\}^{1/2}$$ (56)

Since $V_{op}(t)$ and $I_{sc}(t)$ are both zero for $t < 0$, Equations 54 and 55 can be re-written as

$$E \leq \frac{1}{R} \| V_{oc} \|^2$$ (57)

and

$$E \leq R \| I_{sc} \|^2$$ (58)

Using the fact that the triangle inequality holds for the L^2 norm, the fact that $\|I_o\| = \|I_n\|$ for each n, and the assumption that $I_n(t) \geq 0$, we have

$$\|V_{oc}\| \leq \|I_o\| \left(1 + \sum_{n=1}^{\infty} |\Gamma|^n\right) = \|I_o\| \frac{1}{1-|\Gamma|} \qquad (59)$$

$$|Z_o| \|I_{sc}\| \leq \|I_o\| \left(1 + 2\sum_{n=1}^{\infty} |\Gamma|^n\right) = \|I_o\| \frac{1+|\Gamma|}{1-|\Gamma|} \qquad (60)$$

therefore, Equations 57 and 58 become

$$E \leq \|I_o\|^2 \frac{1}{R(1-|\Gamma|)^2} \qquad (61)$$

and

$$E \leq \|I_o\|^2 \frac{R(1+|\Gamma|)^2}{|Z_o|^2(1-|\Gamma|)^2} \qquad (62)$$

Since Equation 61 is a better bound for large R ($R > \dfrac{|z_0|}{(1+|\Gamma|)}$) and Equation 62 is better for small R ($R < \dfrac{|z_0|}{(1+|\Gamma|)}$) we can obtain a bound independent of R by assuming the worst-case R; i.e., $R = \dfrac{|z_0|}{(1+|\Gamma|)}$, to obtain

$$E \leq \|I_o\|^2 \frac{(1+|\Gamma|)}{|Z_o|(1-|\Gamma|)^2} \qquad (63)$$

It should be noted that if a particular value of R is of interest, either Equation 61 or Equation 62 will give a better estimate for the energy than Equation 63, depending on the value of R.

The expression $\|I_o\|^2$, can be approximated in terms of the incident field. By defintion,

$$\|I_o\|^2 = \int_0^{\infty} \left| v \int_0^{T_o} E^i(t-\gamma) d\gamma \right|^2 dt \qquad (64)$$

But by the Schwarz Inequality,

$$\left| v \int_0^{T_o} E^{\dot{v}}(t-\tau) d\tau \right|^2 \leq T_o v \int_0^{T_o} |E^v(t-\tau)|^2 d\tau = L \int_{t-T_o}^{t} |E^{\dot{v}}(\tau)| d\tau \qquad (65)$$

Using this in Equation 64 and switching the order of integration, we have

$$\| I_o \|^2 \leq v L \int_o^{\infty} \int_\tau^{\tau+T_o} |E^{\dot{v}}(\tau)|^2 dt d\tau = L^2 \| E^{\dot{v}} \|^2 \qquad ((66)$$

The quality $\|E^1\|^2$ can be thought of as the "energy density" of the incident field. Combining this with Equation 63 we have

$$E \leq \frac{L^2 \| E^{\dot{v}} \|^2 (1 + |\Gamma|)}{|Z_o| (1 - |\Gamma|)^2} \qquad (67)$$

6.7 DOUBLE EXPONENTIAL INCIDENT FIELD

We will consider now the special case where the incident electric field is described by a double exponential function, namely

$$E_o(t) = E_o \left(e^{-\alpha t} - e^{-\beta t} \right) \qquad (t \geq 0) \qquad (68)$$

This waveform is commonly used to describe both nuclear EMP and lightning EMP threats. Typical values for α and β in these case are

$$\text{Nuclear EMP} \qquad \alpha = 6.3 \text{ MHz} \qquad \beta = 189 \text{ MHz} \qquad (69)$$
$$\text{Lightning EMP} \qquad \alpha = 0.017 \text{ MHz} \qquad \beta = 3.5 \text{ MHz} \qquad (70)$$

For an incident field of the form given in Equation 68, the calculations involved in evaluating Equations 18 and 19 for the open-circuit voltage and short-circuit current can be carried out exactly for any given value of t. Unfortunately, because only a finite number of terms in these series are nonzero and this number changes with time, simple closed form expressions for

6-22

$V_{oc}(t)$ and $I_{sc}(t)$ do not result. However, the resultant expressions can be incorporated into a computer program to efficiently calculate these qualitites.

In order to check the validity of the expressions given in Equations 18 and 19 and also check the accuracy of the estimates given in Subsections 6.4 and 6.6, comparisons are made with results obtained by a much more detailed analysis. In particular, in Reference 1, hereafter referred to as the Boeing report, an elaborate computer simulation is described. This simulation uses a wire grid model of an F-18 to predict through a moment method code the fields incident on internal wires. The open-circuit voltage and short-circuit current are then calculated. Figure 6-10 shows the configuration under discussion.

Following the Boeing report, we assume the following values for the pertinent parameters:

$$
\begin{aligned}
L &= \text{length of wire, } 12.0 \text{ m} \\
C &= \text{average circumference at aircraft along} \\
  &\quad \text{attachment path, } 3.1 \text{ m} \\
\sigma &= \text{composite conductivity, } 10^4 \text{ mhos/m} \\
d &= \text{composite thickness, } 2.5 \times 10^{-3} \text{ m} \\
Z_0 &= 100 \ \Omega \\
Z_1 &= 30 \ \Omega
\end{aligned}
\tag{71}
$$

For the case of a nuclear EMP threat, the electric field incident on the aircraft is assumed to be in the form of a double exponential function as in Equation 68, with $E_o = 50$ kV/m, $\alpha = 6.3$ MHz, and $\beta = 189$ MHz. This incident field can be related to the field interior to the fuselage using the (admittedly crude) estimates:

$$
E_{int}(t) \approx \frac{2E_e(t)}{\eta_o}\left(\frac{1}{\sigma d}\right) = \left(10.6 \text{ V/m}\right)\left(e^{-\alpha t} - e^{-\beta t}\right)
\tag{72}
$$

Using this expression for the electric field incident on a transmission line, the resulting open-circuit voltage and closed-circuit current obtained by evaluating Equations 18 and 19 are shown in Figure 6-11. The corresponding plots presented in the Boeing report obtained through their simulation program are shown in Figure 6-12.
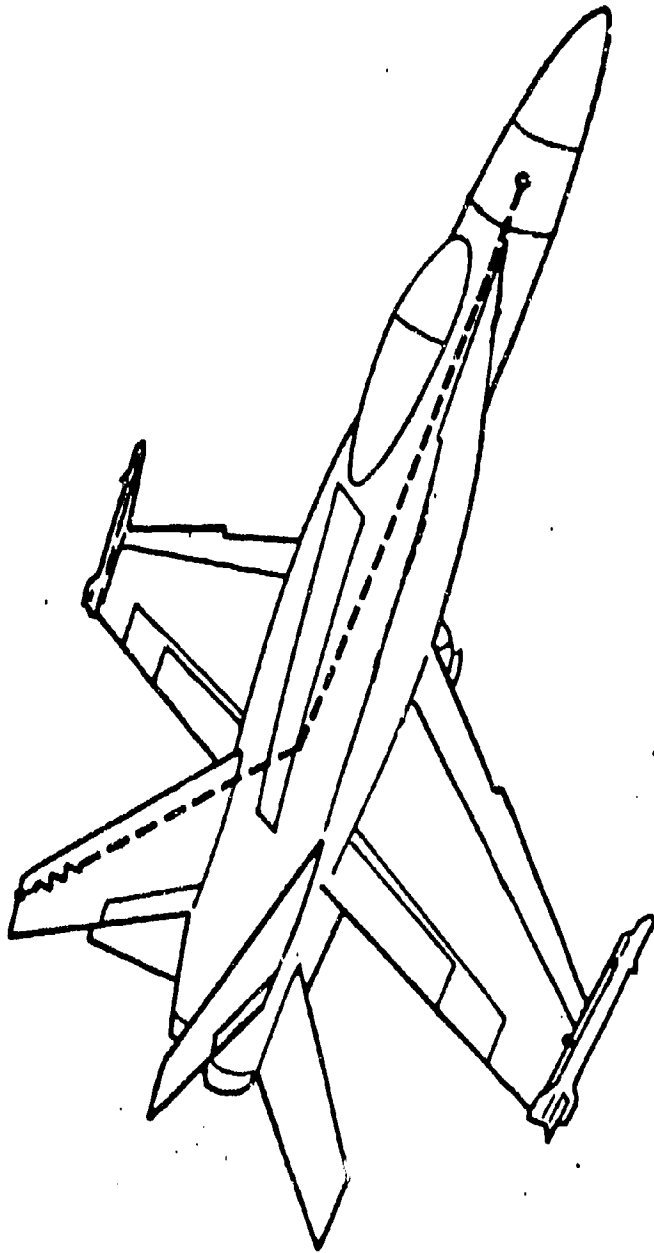
Figure 6-10. Baseline (All Composite) Geometry[1]
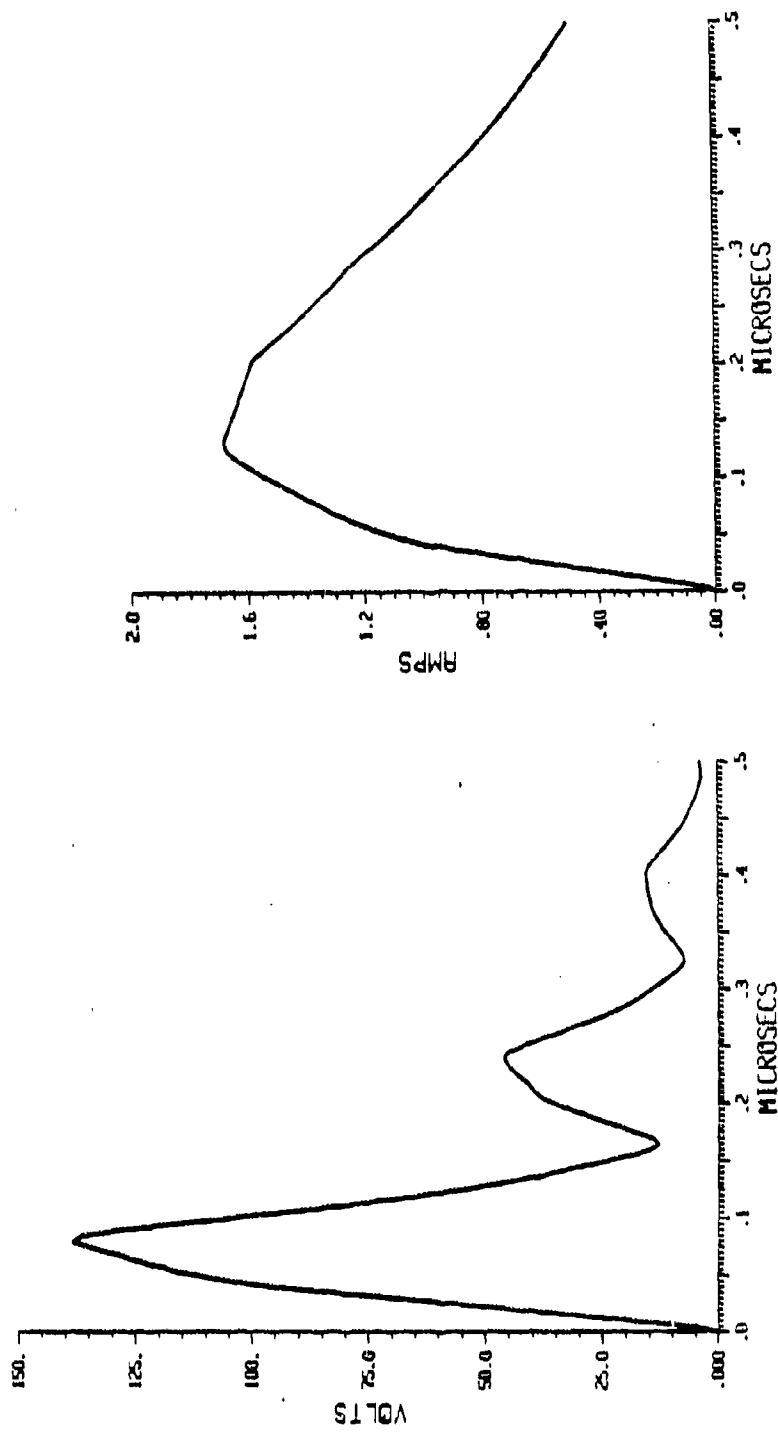
(a) Open-Circuit Voltage

(b) Short-Circuit Current

Figure 6-11. Voltage and Current on Nose/Tail Wire for Nuclear EMP Threat
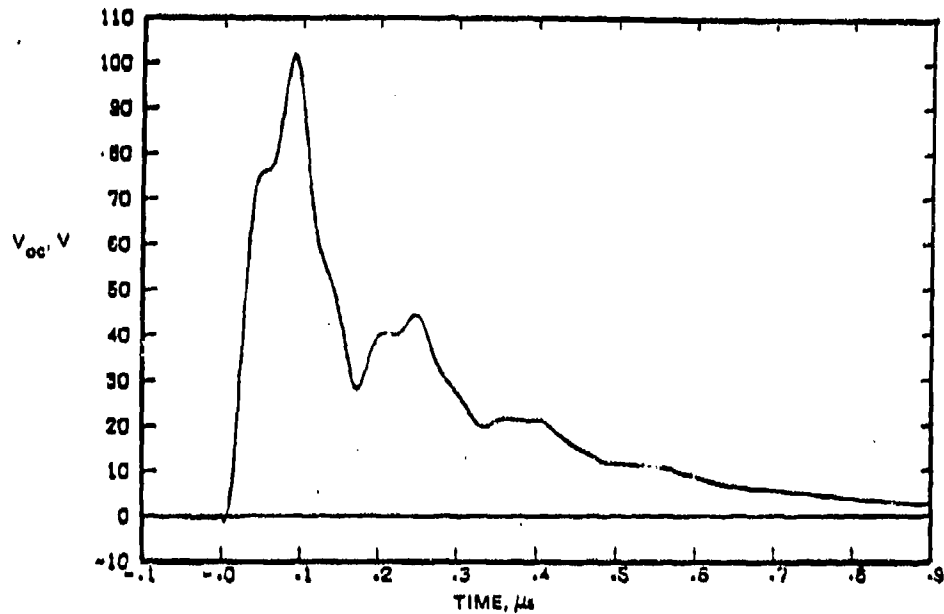
(a) Nose/Tail Short-Circuit Current
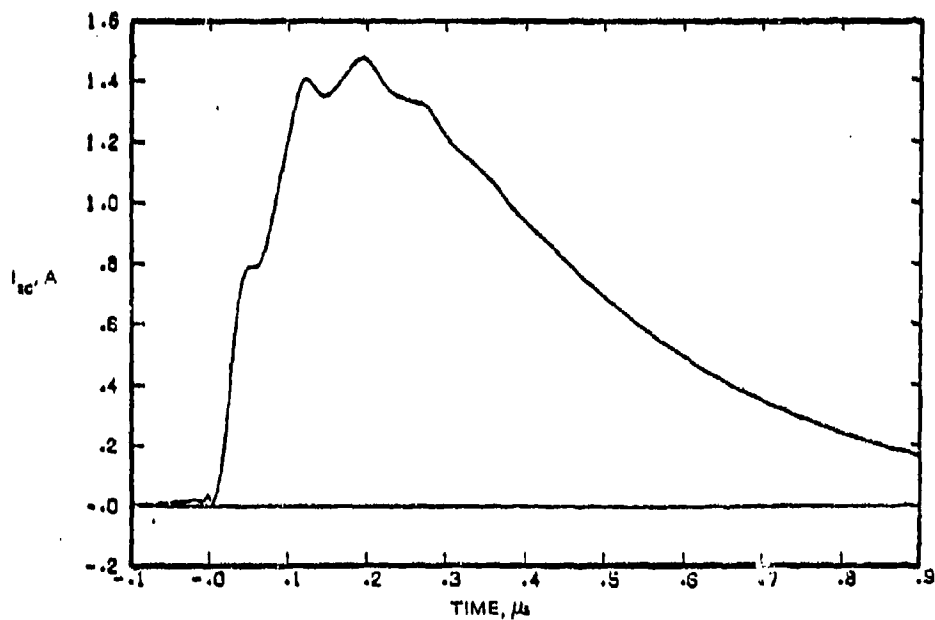
(b) Nose/Tail Short-Circuit Current

Figure 6-12. V_{oc}, I_{sc} on Nose/Tail Wire for Nuclear EMP, E Parallel to Fuselage All Composite (from Boeing Report)[1]

The general shapes of the corresponding curves are remarkably similar, with the locations of the relative maxima and minima being virtually identical. The additional fluctations in the curves from the Boeing report are probably due to the nonuniformity of the fuselage surface and the fact that they consider a transmission line which is not uniformly straight.

Applying the results of Subsection 6.6 and using the parameters given in Equations 71 and 72, we have

$$I_{max} = \max_{t} \left\{ \int_0^{T_o} v E_o \left(e^{-\alpha(t-\gamma)} - e^{-\beta(t-\gamma)} \right) d\gamma \right\} = 103 \, V \tag{73}$$

(whereas from Equation 42, we have $I_{max} \leq 127$ V). Therefore, Equations 40 and 41, give us

$$V_{op} \leq (103V) \frac{1}{(1-0.54)} = 223.9 \, V \tag{74}$$

$$I_{sc} \leq \left(\frac{103V}{100\Omega} \right) \left(\frac{1+0.54}{1-0.54} \right) = 3.45 \, A \tag{75}$$

The actual peak values, taken from the curves in Figure 6-11, are

$$V_{op}^{Peak} = 138 \, V \tag{76}$$

$$I_{sc}^{Peak} = 1.7 A \tag{77}$$

Because the incident field under consideration has a very rapid rise time (approximately 0.018 µs to peak) it is appropriate to use the estimates given by Equations 44 and 45. These yield considerably better results, namely

$$V_{oc} \leq (103V)(1+0.54) = 158.6 \, V \tag{78}$$

$$I_{sc} \leq \left(\frac{103V}{100\Omega} \right) (1+2(0.54)) = 2.14 \, A \tag{79}$$

Consider now the case of a direct lightning strike. The current wave form is assumed to be a double exponential of the form

$$I(t) = (206.3 \ v)(e^{-\alpha t} - e^{-\beta t}) \qquad (80)$$

The electric field interior to the fuselage is then approximated by

$$E^i(t) \approx \frac{I(t)}{C\sigma d} = (2.66 \ kV/m)(e^{-\alpha t} - e^{-\beta t}) \qquad (81)$$

with $\alpha = 0.017$ MHz and $\beta = 3.5$ MHz.

Figure 6-13 shows the results of applying Equations 18 and 19 to this situation. Figure 6-14 shows the corresponding curves given in the Boeing report. Other than the sign convention, the two sets of curves agree extraordinarily well. Again applying the results of Subsection 6.6, we have

$$I_{max} = 31.0 \ kV \qquad (82)$$

(whereas $I_{max} \leq L \ E^i_{max} = 31.0$ kV)

Equations 40 and 41 give us

$$V_{oc} \leq (31 \ kV)\left(\frac{1}{1-5.4}\right) = 67.3 \ kV \qquad (83)$$

$$I_{sc} \leq \frac{31 \ kV}{100 \ \Omega}\left[\frac{(1+0.54)}{(1-0.54)}\right] = 1.04 \ kA \qquad (84)$$

From Figure 6-13, we see that

$$V_{oc}^{Peak} = 31 \ kV \qquad (85)$$

$$I_{sc}^{Peak} = 1.03 \ kA \qquad (86)$$

6-28
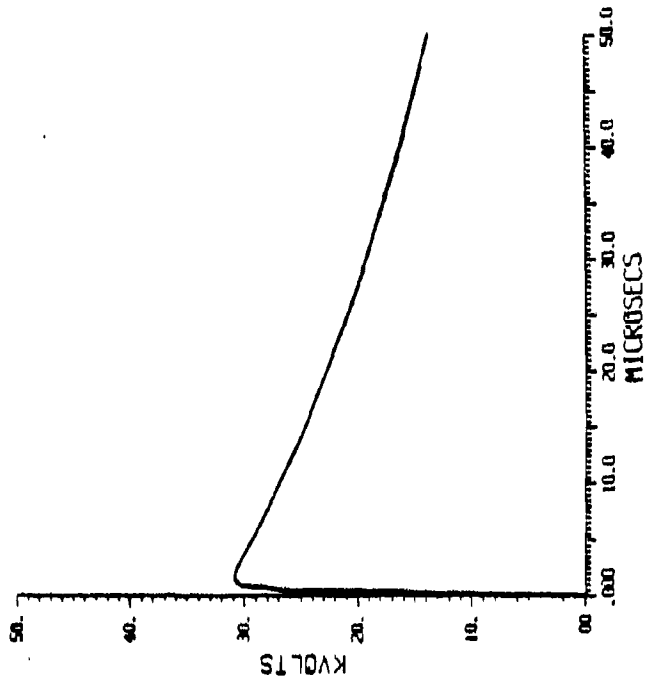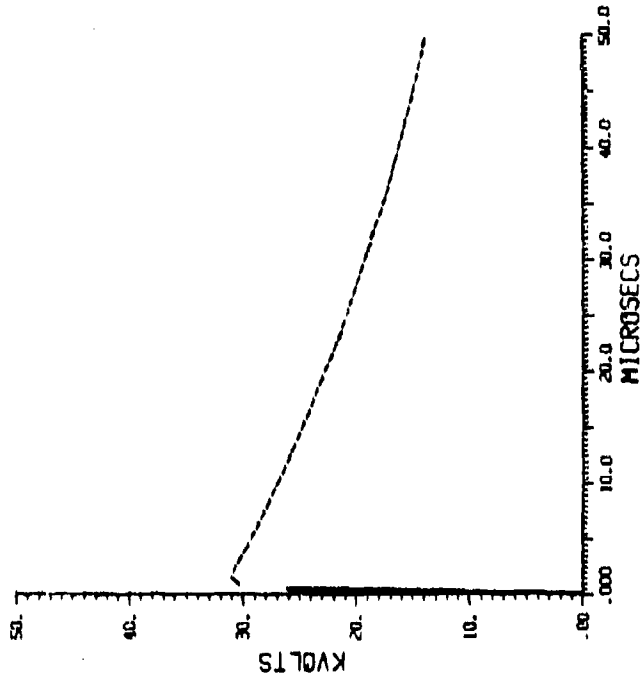
(a) Open-Circuit Voltage   (b) Short-Circuit Current

Figure 6-13. Voltage and Current on Nose/Tail Wire for Direct Lightning Strike

6-29
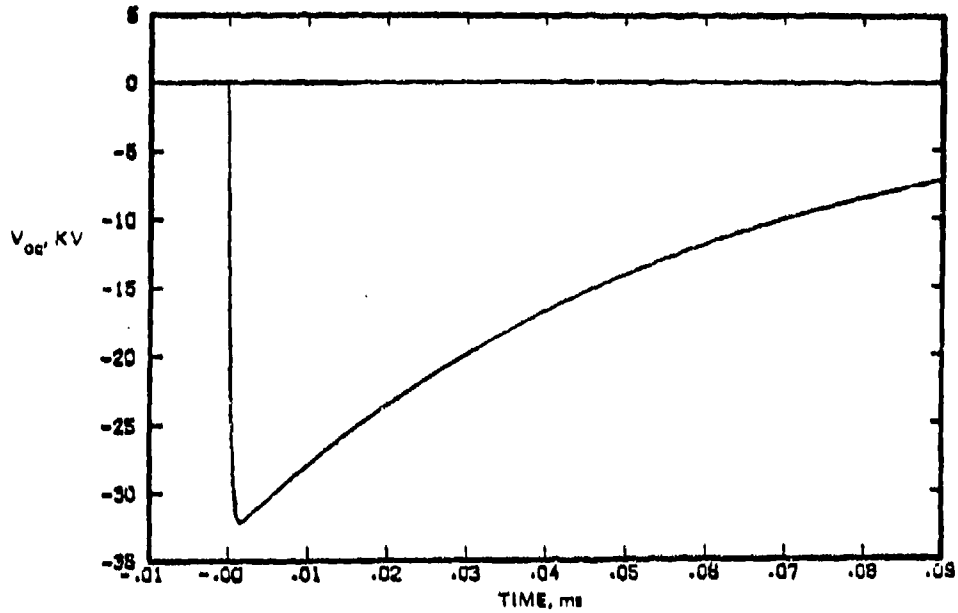
(a) Nose/Tail Open-Circuit Voltage
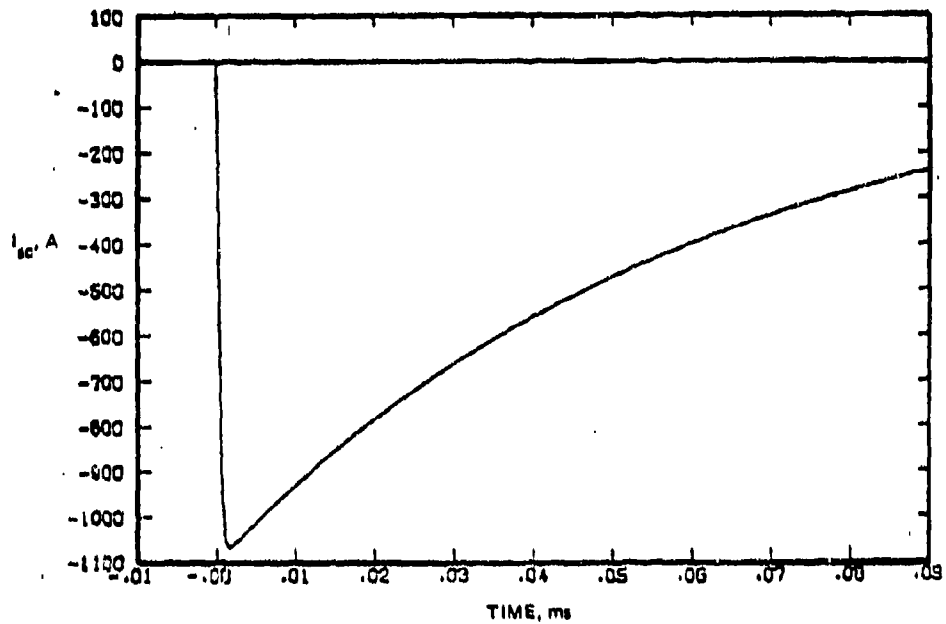
(b) Nose/Tail Short-Circuit Current

Figure 6-14. V_{OC}, I_{SC} on Nose/Tail Wire for Nose/Tail Lightning, All
Composite (from Boeing Report)[1]

6-30

Because this particular incident field has mostly a low frequency content, it is permissible to use the low frequency approximations derived in Subsection 6.4. That is to say, in this case

$$V_{oc}(t) \simeq (31.92 \ kV)(e^{-\alpha t} - e^{-\beta t}) \qquad (87)$$

$$I_{sc}(t) \simeq (1.064 \ kA)(e^{-\alpha t} - e^{-\beta t}) \qquad (88)$$

These functions are shown in Figures 6-15 and 6-16. They are virtually identical to the curves shown in Figure 6-13. In particular, the corresponding peak values are identical. Hence for this set of parameters, the low frequency approximations can be used with confidence.

We may use the analytic expressions given in Equations 87 and 88 to calculate bounds for the instantaneous power and total energy seen from the left-hand terminals of the transmission line. These can then be compared to the estimates derived in Subsection 6.6.

The instantaneous power is given by

$$P(t) \le V_{oc}(t) \ I_{sc}(t) = (33.96 \ MW)(e^{-\alpha t} - e^{-\beta t})^2 \qquad (89)$$

Because the time dependence of V_{oc} and I_{sc} are assumed to be the same, obviously the peak power estimate obtained from Equation 88 is just the product of the peak voltage and the peak current. That is

$$P^{Peak} \le (31 \ kV)(1.03 \ kA) = 31.93 \ MW \qquad (90)$$

Using Equation 49 to estimate the peak power results in

$$P^{Peak} \le \frac{(31 \ kV)^2}{100 \ \Omega} \left[\frac{(1 + 0.54)}{(1 - 0.54)^2} \right] = 70.0 \ MW \qquad (91)$$

This is seen to be a little over twice the value calculate in Equation 89.
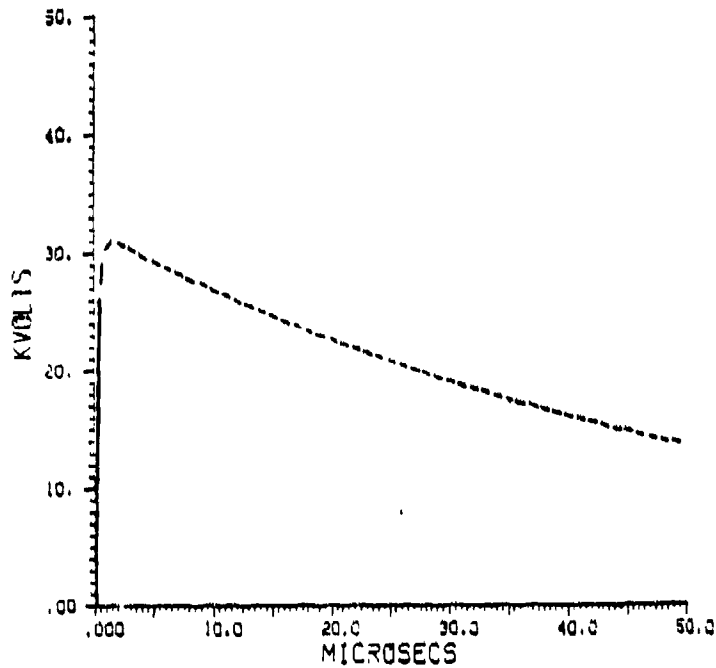
Figure 6-15. Low Frequency Approximation to Open-Circuit Voltage on Nose/ Tail Wire for Direct Lightning Strike
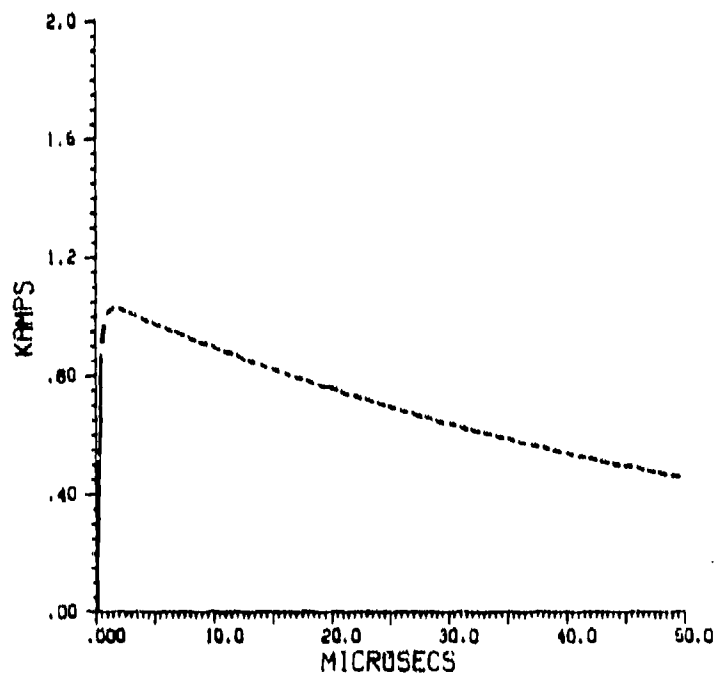
Figure 6-16. Low Frequency Approximation to Short-Circuit Current on Nose/ Tail Wire for Direct Lightning Strike

6-32

The energy which could be dissipated by a resistance across the terminals is bounded by

$$E \leq \int_0^\infty P(t)\,dt \tag{92}$$

By using Equation 89, this yields

$$E \leq (33.96 \text{ MW}) \frac{(\beta-\alpha)^2}{2\alpha\beta(\beta+\alpha)} = 984.4 \text{ J} \tag{93}$$

The estimate given by Equation 67 is

$$E \leq \frac{L^2 \|E^i\|^2 (1+|\Gamma|)}{|Z_o| (1-|\Gamma|)^2} \tag{94}$$

but

$$\|E^i\|^2 = (2.66 \text{ kV/m})^2 \int_0^\infty (e^{-\alpha t} - e^{-\beta t})^2\,dt = (2.66 \text{ kV/m})^2 (29.0 \,\mu s) \tag{95}$$

Therefore,

$$E \leq \frac{(12m)^2(2.66 \text{ kV/m})^2(29.0\,\mu s)(1.54)}{(100\,\Omega)(0.46)^2} = 2.15 \text{ kJ} \tag{96}$$

This estimate is about 2.2 times the value calculated in Equation 93.

6.8 EQUIVALENT SQUARE-WAVE POWER PULSES

The damage constant derived by Wunsch for semiconductor junction devices is used in estimating the vulnerability of electronic devices to burnout. This constant is obtained under the assumption of a square-wave power pulse. In order to use the Wunsch damage constant for other power pulses, it is useful to relate a given waveform to a rectangular pulse with the same peak amplitude which produces the same (or greater) device damage. Two different "equivalent" square-wave power pulses are considered. The first is equivalent in the sense that it has the same damage threshold as the original pulse. The second is equivalent in that it has the same energy content as the original.

6-33

The damage constant, K, is related to the energy required for failure, E_F, and the time to failure, t_F, by[4]

$$E_F = K \, t_F^{1/2} \quad \text{(or)} \quad K = E_F \, t_F^{-1/2} \tag{97}$$

In order words, if within a time τ more energy than $K \, \tau^{1/2}$ is delivered to the device then burnout will occur. This relation, although obtained for a rectangular pulse, is assumed to be valid for other waveforms also.

For a power waveform, $P(t)$, the quantity that must be compared to the damage constant is given by

$$\tau^{-1/2} \cdot \max_{0 \le t < \infty} \left\{ \int_t^{t+\tau} P(s)\,ds \right\} = \tau^{-1/2} E_{max}(\tau) \tag{98}$$

Here $E_{max}(\tau)$ is defined as the maximum energy which can be delivered in time τ. If this expression is less than K for all values of τ, then no burnout will occur. Otherwise, there is a time interval in which enough energy is delivered to cause burnout.

For a square-wave pulse of amplitude P_o and duration τ_s, Equation 98 attains its maximum for $\tau = \tau_s$. Hence, for a square pulse the critical values for τ_s and P_o are related by:

$$K = P_o \, \tau_s^{1/2} \tag{99}$$

For a more general waveform, $P(t)$, whose peak amplitude is P_o, we can define an equivalent square-wave power pulse with amplitude P_o, which produces the same device damage. We will denote the duration of this damage equivalent square-wave pulse by τ_d. By definition, we have from Equations 98 and 99

$$P_o \tau_d^{1/2} = \tau_{max}^{-1/2} \, E_{max}(\tau_{max}) \tag{100}$$

or

$$\tau_d = (E_{max}(\tau_{max}))^2 / P_o^2 \tau_{max} \tag{101}$$

Here τ_{max} is that value of τ which maximizes $\tau^{-1/2} E_{max}(\tau)$.

The other equivalent square-wave pulse, which is easier to calculate but which yields more conservative results, is defined to have amplitude P_o and a duration such that it has the same energy content as $P(t)$. We will denote the duration of this energy equivalent pulse by τ_e. Specifically, we have

$$P_o \cdot \tau_e = \int_0^\infty P(t)dt = E_{tot} \tag{102}$$

We will see from the following inequalities that using the energy equivalent time in Equation 99 to calculate the smallest allowable damage constant will always result in larger constant than would result from using the more precise (and complicated) Equation 98. This means that it is on the safe side to use the energy equivalent time to determine whether particular device is susceptible to burnout for a given power pulse.

We have the following relationships:

$$\tau^{-1/2} \int_t^{t+\tau} P(s)ds \leq \tau^{-1/2} \cdot \tau^* P_o \leq \tau_e^{1/2} P_o \tag{103}$$

where τ^* is $min(\tau, \tau_e)$.

Two power pulses will be analyzed to show the relative values for the two equivalent times τ_d and τ_e.

The first power pulse which we will examine is the damped sinewave through a semiconductor junction. This is of interest because some specifications are given in terms of the damping constant and frequency of a damped sinewave. We will consider only the effects due to a single period and so can ignore the damping effects. The results obtained are somewhat different than those

presented elsewhere.[4] Analysis has also been performed for the damped sine-wave extending over many periods.[5] The techniques outlined above could be applied to that case also.

We will consider, as in the previously cited references, the power pulse given by

$$P(t) = P_o \sin \left(\frac{2\pi}{T} t \right) \text{ for } 0 \leq t \leq \frac{T}{2} \qquad (104)$$

Our goal is to relate the equivalent square-wave times to the period, T, of the sinewave. We first analyze the situation relative to the damage equivalent time, τ_d,

$$E_{max}(\tau) = P_o \int_{\frac{T-\tau}{2}}^{\frac{T+\tau}{2}} \sin \left(\frac{2\pi}{T} t \right) dt = 2P_o \int_0^{\frac{\tau}{2}} \cos \left(\frac{2\pi}{T} t \right) dt$$

$$= \frac{P_o T}{\pi} \sin \left(\frac{\pi \tau}{T} \right) \qquad (105)$$

The equation $\tau^{-1/2} \frac{P_o T}{\pi} \sin \left(\frac{\pi \tau}{T} \right)$ attains its maximum for $\tau_{max} = 0.371$ T. Therefore from Equation 101 we have

$$\tau_d = T(0.293)^2/(0.371) = 0.231 \text{ T} \qquad (106)$$

This is in comparison to the result $\tau_d \approx 0.203$ T given in Reference 4.

The discrepancy between these results is due to the fact that the factor of 0.203 was obtained by using the full half period sinewave to calculate the burnout constant, instead of finding the subinternal (of length τ_{max}) which maximizes the allowed burnout constant. This causes the estimated critical value of the burnout constant to be too small.

It is considerably easier to calculate the energy equivalent time, τ_e. We have:

$$E_{tot} = P_0 \int_0^{T/2} \sin\left(\frac{2\pi}{T} t\right) dt = \frac{P_0 T}{\pi} \qquad (107)$$

Therefore, from Equation 102, we have

$$\tau_e = (1/\pi)T \approx 0.318 \, T \qquad (108)$$

These results can be contrasted to the equivalent time obtained in Reference 5 for the damped sinewave over many periods. Here the power waveform is taken to be $P(t) = P_0 e^{-\left(\frac{\pi}{24T}\right)t} \sin\left(\frac{2\pi}{T} t\right)$. The value obtained is

$$\tau_e = 0.380 \, T \qquad (109)$$

This result is larger than the previous ones because it takes into account the additive effect of successive pulses.

For a low frequency field incident on a transmission line both the open-circuit voltage and short-circuit current are proportional to the electric field. Hence, the power waveform will be proportional to the square of the electric field.

Using this fact we will analyze the equivalent times due to a power surge caused by a lightning strike. To simplify the calculations we will use the single exponential which describes the model lightning waveform for large t, and in fact is an upper bound for the double exponential waveform for all t. We have

$$P(t) = P_0 e^{-2\alpha t} \qquad (110)$$

therefore

$$E_{max}(\tau) = P_0 \int_0^\tau e^{-2\alpha t} = P_0 \frac{1-e^{-2\alpha\tau}}{2\alpha}$$

the expression $\dfrac{\tau^{1/2} P_o \ (1 - e^{-2\alpha\tau})}{2\alpha}$ attains its maximum for $\tau_{max} \approx 0.628$.

From Equation 101 we have

$$\tau_d \approx \frac{(0.358)^2}{(0.628)\alpha} = \frac{0.204}{\alpha} \quad \frac{1}{4.9 \ \alpha} \tag{111}$$

Using Equation 102 to calculate the energy equivalent time yields:

$$\tau_e = \int_0^\infty e^{-2\alpha t} \ dt = \frac{1}{2\alpha} \tag{112}$$

As can be seen from these calculations, it is in general much easier to compute τ_e than it is to compute τ_d. In fact, for both of the examples given, it was necessary to find the root of a nonlinear equation in order to calculate τ_{max}. Moreover, it seems that as a practical matter, τ_d can not be computed reasonably unless the power waveform is given as a simple analytic expression. On the other hand, τ_e could be calculated efficiently even for power waveforms given in the form of real or simulated data.

Applying the results derived above for a lightning waveform, it is possible to bound the energy delivered to a device due to coupling to a transmission line given the peak open-circuit voltage and short-circuit current. In particular,

$$E \leq V_{oc}^{peak} \cdot I_{sc}^{peak} \cdot \tau_e \tag{113}$$

The Boeing report gives values for V_{oc}^{peak} and I_{sc}^{peak} in Table 5.1, page 87, for the cases of a direct lightning strike and a nearby lightning strike. The wires under consideration are as shown in Figure 6-10. These values are presented in Table 6-1 along with the peak power and maximum energy associated with them. We assume that $\alpha \approx 0.017$ MHz, so that $\tau_e = 29.41 \ \mu s$.

Table 6-1. Peak Power and Maximum Energy

Direct Strike		V_{oc}	I_{sc}	P^{peak}	E
Nose/Tail Wire	(Nose/Tail Attachment)	-32 kV	-1.1 kA	35.2 MW	1035.2 J
	(Nearby Strike)	250 V	8.2 A	2 kW	0.059 J
Nose/Wing Tip Wire	(Nose/Tail Attachment)	-6.5 kV	-0.22 kA	1.43 MW	42.06 J
	(Nose/Wing Tip Attachment)	-17 kV	-0.55 kA	9.35 MW	275.0 J

6.9 REFERENCES

1. D. Strawe and L. Piszker, Interaction of Advanced Composites with Electromagnetic Pulse (EMP) Environment, Final Report prepared by Boeing Aerospace Company for Wright-Patterson Air Force Base under Contract F33615-74-C-5158, AFML-TR-75-141, September 1975.

2. A.A. Smith, Jr., Coupling of External Electromagnetic Fields to Transmission Lines, J. Wiley and Sons, 1977.

3. A.A. Smith, Jr., "The Respace of a Two-Wire Transmission Line Excited by the Nonuniform Electromagnetic Fields of a Nearly Loop", IEEE Transactions on ECM, Vol. EMC-16, No. 4, November 1974, pp. 196-200.

4. EMP Susceptibility Threshold Handbook (Appendix B).

5. J.L. Bodganor, R.A. Pearlman, and M.D. Siegel, Intersystem Electromagnetic Compatibility Analysis Program, Vol. I: "User's Manual Engineering Section," Final Report prepared by McDonnell Aircraft Company for Rome Air Development Center under Contract F30602-72-C-0277, RADC TR-74-342, December 1974

6. A.A. Smith, Jr., "A More Convenient Form of the Equation for the Response of a Transmission Line Excited by Nonuniform Fields," IEEE Transactions on ECM, pp. 151-152, August 1973.

7. [*] W.S. McCormick, "The Estimation of Induced-Voltage Peak Magnitude and Energy Level under LTA/EMP Excitation of Low-Loss Aircraft Cabling", IEEE Transactions on ECM, May 1979, pp. 136-146.

---

[*]Not referred to in text; included for additional information.

SECTION 7

VULNERABILITY OF SEMICONDUCTOR DEVICES TO EMP THREAT

Modern aircraft are equipped with complex electrical systems such as computers, radar, and communications equipment. These systems are vulnerable to electromagnetic radiation from outside sources. If this electromagnetic radiation is of a high enough power level, then the electronic components aboard the aircraft are in danger of being damaged and causing equipment failure. The devices which are most vulnerable to the EMP threat are semiconductors and integrated circuits, so the following discussion is a summary of some of the techniques used to determine power threshold levels for integrated circuits (ICs) and semiconductor devices.

7.1 SEMICONDUCTOR JUNCTION DEVICES

To determine semiconductor damage thresholds, a model is needed which will predict device burnout characteristics as a function of electromagnetic pulsewidth. The most widely used model is the Wunsch model, given by:

$$\boxed{P = Kt^{-1/2}}$$ Wunsch Model

where:

t is in seconds

P is in watts

K is in units of watts-seconds$^{1/2}$

P is the power required to fail the junction, K is the damage constant determined by junction properties and geometry, and t is the pulse time to failure.

In order to carry out an analysis of junction burnout characteristics using the Wunsch model, the damage constant K must be determined. There are four ways to determine this K factor.

7.1.1 Experimental Determination of K Factor

To determine the K factor experimentally, a series of power pulses is injected into the semiconductor junction, starting at low power levels, and then

7-1

increasing the levels until either failure or serious degradation of the junction occurs. Figures 7-1 and 7-2 show the range of K for typical diodes and transistors.

7.1.2 K Factor Determined from Junction Area

The most accurate method of determining the K factor requires a knowledge of the junction area. Then the K factor can be determined from the following:

$$
\begin{array}{ll}
\text{for Diodes,} & K = 550A \\
\text{for Transistors,} & K = 470A
\end{array}
$$

where A is given in cm^2. However, the junction areas for a device are not given on a manufacturer's data sheet and are not otherwise readily available. Therefore, one of the two remaining methods of choosing K must be incorporated.

7.1.3 K Factor Determined from Thermal Resistance

Three categories of semiconductor devices will be considered in the analysis:

> Category 1 - Germanium diodes and transistors
>
> Category 2 - Silicon diodes, all silicon transistor structures except planar and mesa
>
> Category 3 - Silicon planar and mesa transistors

The relationships are as follows:

$$
\begin{array}{ll}
\text{Category 1:} & \text{insufficient data available} \\[4pt]
\text{Category 2:} & K = 31.5\, \theta_{jc}^{(-1.11)} \\[4pt]
& K = 972.2\, \theta_{ja}^{(-1.24)} \\[4pt]
\text{Category 3:} & K = 338.3\, \theta_{jc}^{(-1.73)} \\[4pt]
& K = 4.625 \times 10^6\, \theta_{ja}^{(-3.08)}
\end{array}
$$
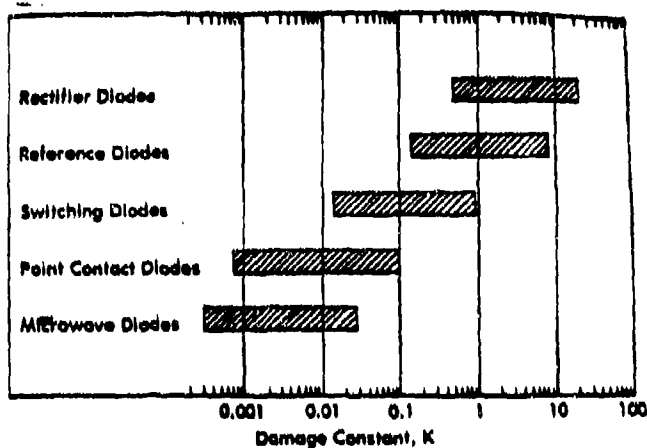
Figure 7-1. Range of Pulse Power Damage Constants for
Representative Diodes
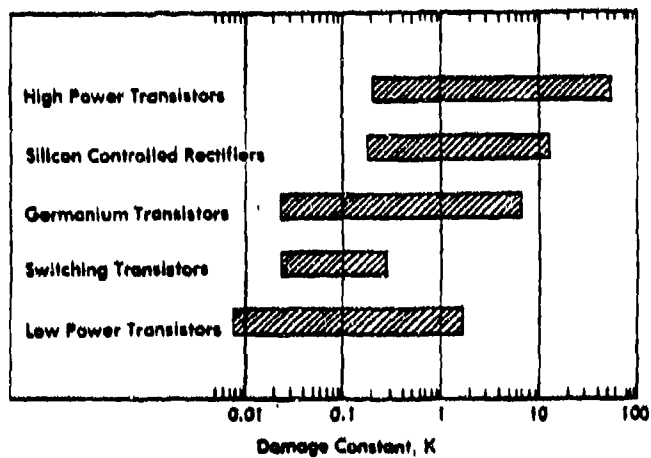
Figure 7-2. Range of Pulse Power Damage Constants for
Representative Transistors

7-3

where θ_{jc} and θ_{ja} are found from the following expressions:

$$\theta_{jc} = \frac{T_j(max) - T_c}{P_d}$$

$$\theta_{ja} = \frac{T_j(max) - T_{amb}}{P_d}$$

with

$T_j(max)$ = maximum operating junction temperature
T_c = case temperature
T_{amb} = ambient temperature
P_d = total power dissipated

Generally, at least one of the these thermal resistances may be calculated using manufacturer's data sheets.

7.1.4 K Factor Determined from Junction Capacitance

The last, and most reliable, means of calculating K is from a knowledge of the junction capacitance (C_j), and breakdown voltage (V_{BD}). For the same three categories of devices, the equations are:

Category 1: $K = 2.2 \times 10^{-3} \, C_j \, V_{BD}^{(0.20)}$

Category 2: $K = 1.1 \times 10^{-3} \, C_j \, V_{BD}^{(0.81)}$

Category 3: $K = 0.008 \times 10^{-3} \, C_j \, V_{BD}^{(1.63)}$

The value of the junction capacitance can be found on a manufacturer's data sheet. This junction capacitance model suggests a more accurate determination of K, and works for both silicon and germanium devices.

7.2 EXAMPLE CALCULATION OF K AND PLOT OF POWER VERSUS TIME

As an illustrative example, an analysis of a 2N4026 silicon planar transistor is done. Since the device is silicon planar, it fits the models of Category 3.

The following specifications are available from the manufacturer:

$$T_j(max) = 200°C$$
$$P_d = 2.0 \text{ W}$$
$$T_c = 25°C$$

so,

$$\theta_{jc} = \frac{T_j(max) - T_c}{P_d} = \frac{200 - 25}{2} = 87.5°C/W$$

Also, from data sheet we find:

$$P_d = 0.5 \text{ W}$$
$$T_{amb} = 25°C$$

so,

$$\theta_{ja} = \frac{T_j(max) - T_{amb}}{P_d} = \frac{200 - 25}{0.5} = 350°C/W$$

From the data sheet we obtain $C_j = 15$ pfd, $V_{BD} = 60$ V. So now we are able to calculate three values of K:

$$*solutions \begin{cases} K = 0.15 \text{ from } \theta_{jc} \\ K = 0.068 \text{ from } \theta_{ja} \\ K = 0.095 \text{ from } C_j, V_{BD} \end{cases}$$

---

*When more than one value of K is obtained, then the average value is suggested for use. However, for large variations in K, the value obtained from the junction capacitance and breakdown voltage should be favored. Figure 7-3 plots $P = Kt^{-1/2}$ using an average value $K = 0.10$ for the 2N4026.
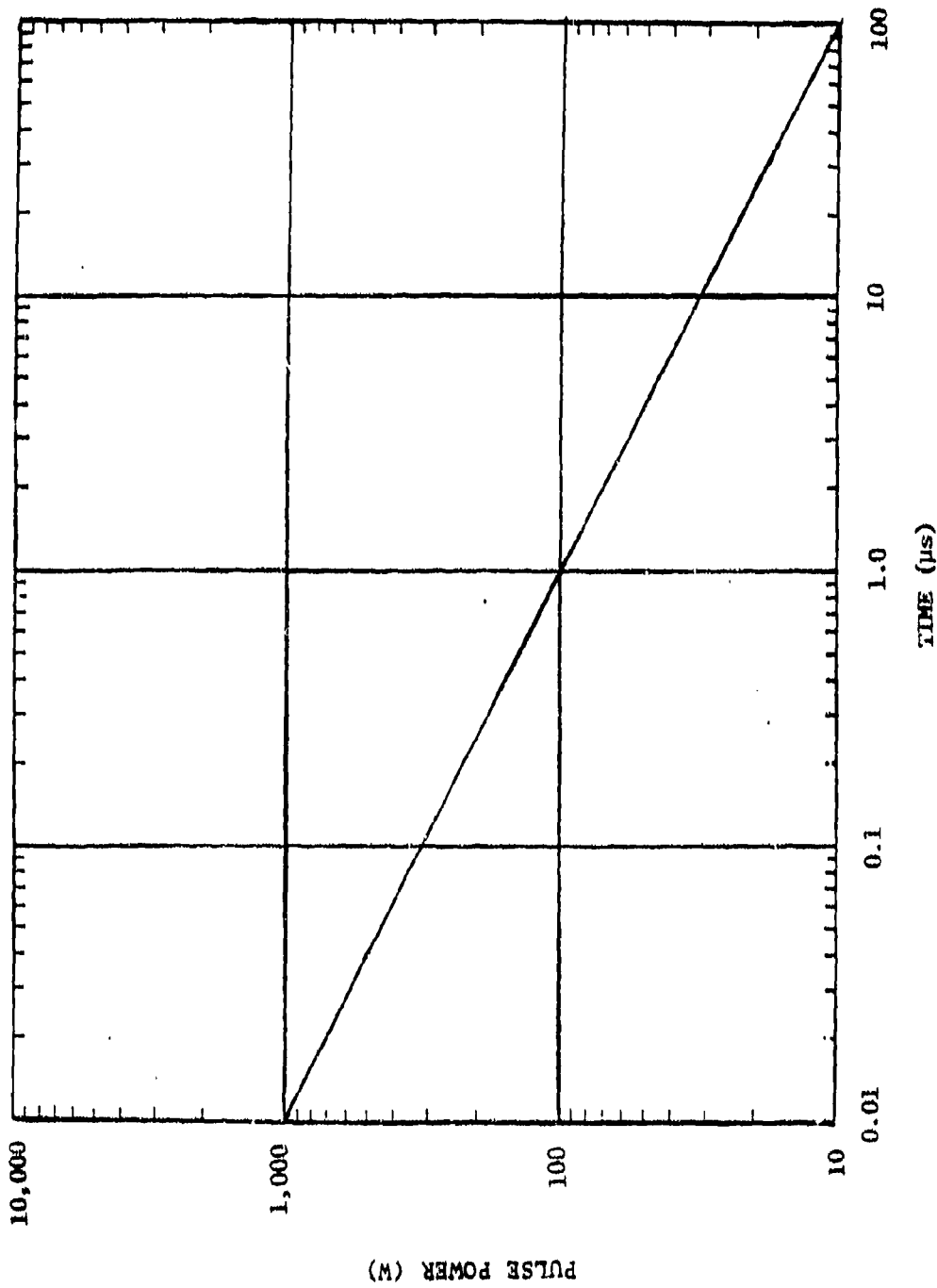
Figure 7-3. Power versus Time Failure Curve for 2N4026 Transistor

7.3 INTEGRATED CIRCUITS

7.3.1 Damage

Up to now, there are no models analogous to the Wunsch model for predicting the damage thresholds of integrated circuits. A general conclusion which may be drawn about ICs is that linear ICs are less susceptible to EMP damage than digital ICs. Figure 7-4 illustrates the general conclusion.
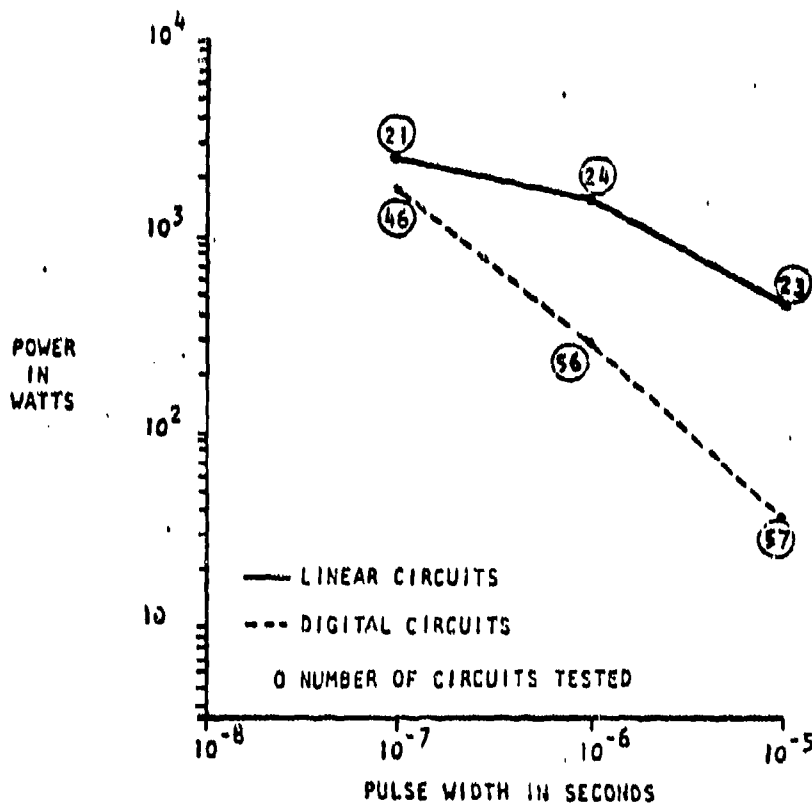
Figure 7-4. Damage Threshold for Integrated Circuits

While there are no models or hard supportive data for integrated circuit damage thresholds, survey tests have revealed the following trends:

1. Damage threshold for a given functional logic varies with manufacturer.

2. High noise immunity logic may be more susceptible to burnout than standard logic.

3. Passive components in ICs are extremely transient sensitive and can determine device damage threshold.

4. Application of the Wunsch model to junction devices on an IC chip does not give meaningful results.

7.3.2 Upsets

Figure 7-5 shows a typical logic transfer function. Logic upset occurs if the EMP transient is large enough, and if the duration transient exceeds the circuit's propogation delay time. Figure 7-6 shows the form of a typical upset characteristic. EMP transient pulse energy is usually concentrated in the 10 kHz to 100 MHz frequency region. A design technique for attenuating the high frequency content of the EMP-induced transients is to increase the propogation delay time. This, however, lowers the permissible bit rate of the system, so an evaluation of these trade-offs must be made.
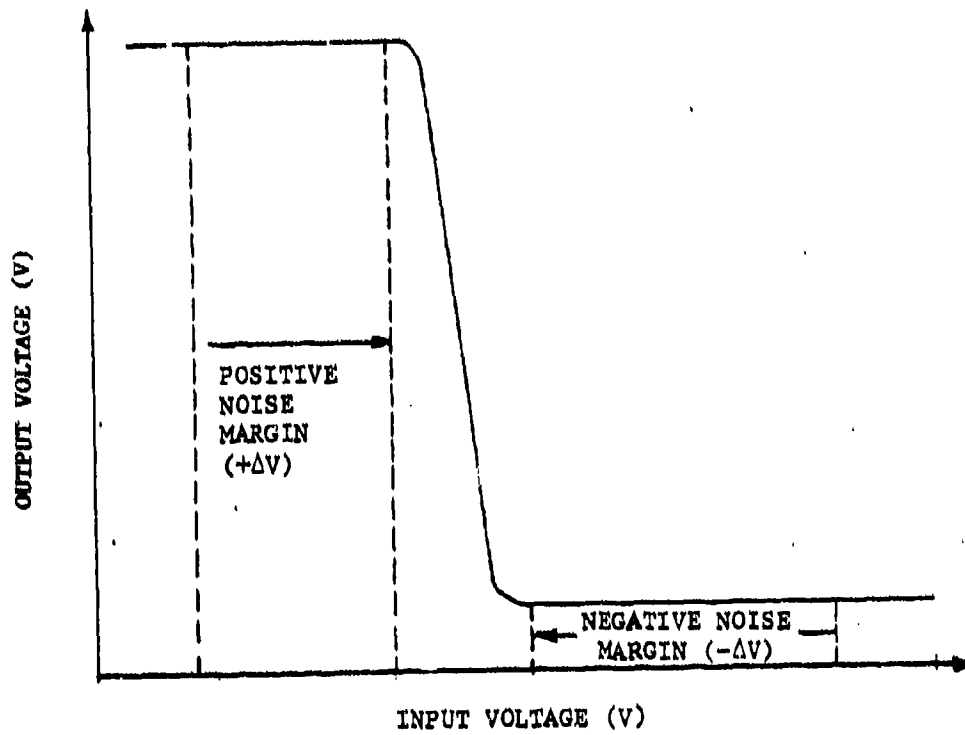
Figure 7-5.   IC Transistor Function
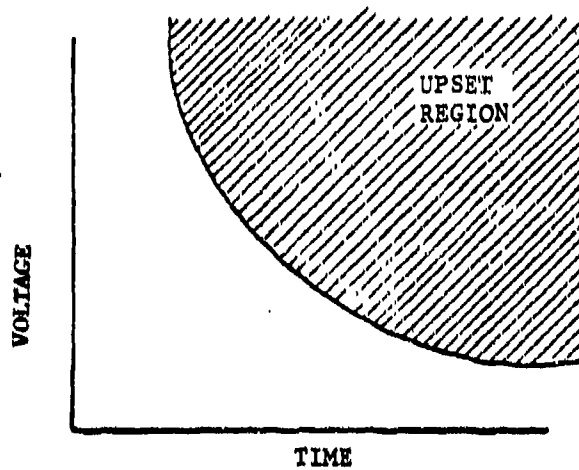
Figure 7-6. Minimum V-T Characteristic for Upset

SECTION 8

INTEGRATED CIRCUIT EM SUSCEPTIBILITY

Integrated circuits (ICs), just like discrete components, are susceptible to high power microwave radiation effects. These EM effects can interfere with or permanently damage an IC chip, and a single chip could cause failure in an entire electronic system. Analytical models such as the Wunsch model exist for determining the susceptibility of individual junctions on an IC chip, but as yet a model does not exist for determining the susceptibility levels of entire chips. Translating individual pn junction effects into an integrated circuit model appears to be a matter of applying conventional circuit analysis techniques to a chip. This, however, is not so easily accomplished due to the immense number of components and circuit interconnections which generally exist on a single tiny chip. As a result, most of the susceptibility data that we have for ICs comes from actual laboratory testing and not analytical analysis.

8.1 IC SUSCEPTIBILITY DATA

Following is a brief discussion of the IC susceptibility data available at the present time, with some examples shown. The data is contained in the McDonnel Douglas <u>IC Susceptibility Handbook</u>[1]. The following three degrees of susceptibility can be considered.

- ° Interference
- ° Degradation
- ° Catastrophic Failure

Interference means some effect is induced on the IC by the external signal (microwave in this case) but no permanent damage is done to the device. Degradation is defined as limited permanent damage to the device. In other words, the device is still operational, but only in a limited manner. Catastrophic failure means extensive permanent damage is done to the device, and the device becomes inoperational in any manner.

When determing IC susceptibility, two factors must be considered:

        °   The type of device used (digital or linear)

        °   The parameters of the microwave signal (i.e., power
                level, frequency, pulse rate, etc.)

Digital and linear devices are defined in the following manner: digital
devices operate in only one of two states (high or low); linear devices oper-
ate over a continuous range of values or have a smooth output. The operating
conditions of the device influence its IC susceptibility to microwave signals.
As an example, a 7400 TTL* NAND gate is susceptible to microwave signals in-
jected into the output when the output state is low, but not when the output
state is high. The opposite is true when the microwave signal is injected
into the input of the 7400.

In the frequency region between 100 MHz and 10 GHz, the worst-case
signal absorption by unshielded wires can be characterized as that collected
by half-wave dipole (aperture = $0.13\lambda^2$). Hence, the absorbed power is

$$P = 0.13\lambda^2 P_d \tag{1}$$

where:

$$P_d = \text{power density, W/m}^2$$

$$\lambda = \text{wavelength, m}$$

This indicates an inverse frequency squared relationship, which was confirmed
in the frequency region of 220 MHz to 9.1 GHz where measurements were made by
McDonnell Douglas using many combinations of wires in bundles of cables. This
is shown in Figure 8-1. The results in dB were distributed normally with a
3 dB to 6 dB standard deviation.

This expression is only valid in the above frequency region. Mis-
match losses counter the inverse frequency squared relationship at lower fre-
quencies. Also, it should be noted that the wires could pick up more signal
if focusing effects take place.

---

*Transistor-transistor logic.
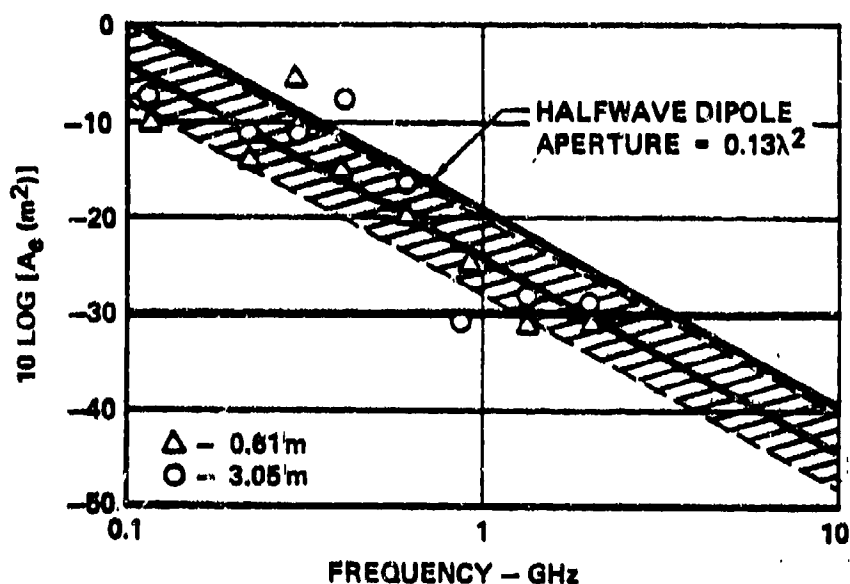
Figure 8-1. Measured Maximum Effective Apertures (A_e) of Various
Wire Lengths[1]

Based on analyses and measurements, the primary interference effect
is caused by rectification of the microwave signal in the nonlinear pn or np
function in the transistors or diodes of the IC. This causes a change in the
circuit voltage and/or current, thus shifting the operating point. In the case
of threshold sensitive devices such as digital circuits, the circuit could be
driven from a "low" state to a "high" state or vice versa.

A typical plot of interference effects versus frequency is shown in
Figure 8-2 for a 741 operational amplifier IC. The curve shows the increases
in the input offset voltage due to rectification of the microwave signal. Also
in the cut-off region, the effect is a function of the square of the frequency.

The modulation parameters of the interfering microwave signal also
have an affect on IC susceptibility. Since the transistor junctions on an IC
chip tend to rectify the interfering signal, envelope detection takes place.
So, the interfering signal has the same amplitude modulation as the RF signal.
Thus, continuous wave signals produce a dc interference such as shown in Fig-
ure 8-2, and pulse modulated signals produce video pulse interference. The
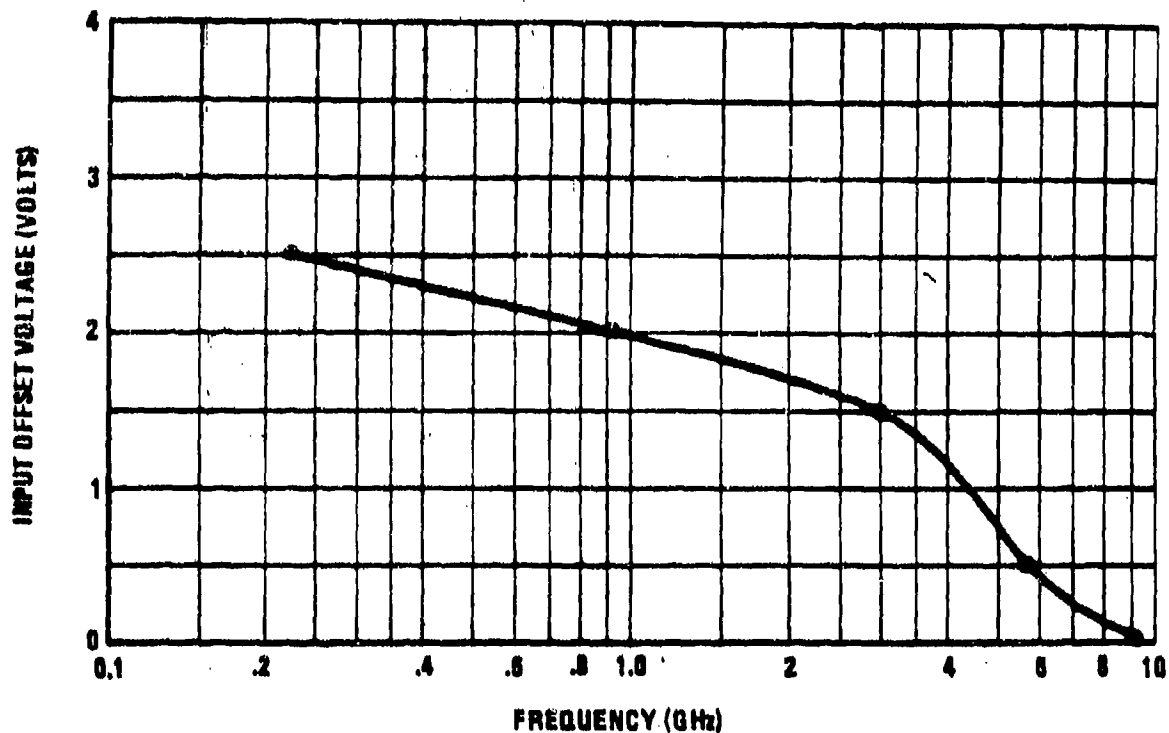
Figure 8-2. Data Points for 100 mW Absorbed Power

total effect is thus dependent upon the individual circuit's ability to process the demodulated RF signal.

8.2 IC INTERFERENCE SUSCEPTIBILITY AND FAILIURE

A brief summary of some representative susceptibility data follows. The failure mechanism is discussed first, followed by interference susceptibility data for digital circuits, linear amplifiers, and voltage regulators.

8.2.1 Failure Mechanism

Two general types of failure mechanisms might be anticipated in semi-conductor devices. One is voltage breakdown, commonly referred to as punch

8-4

through, and the other is thermal failure due to burn out. Whether the failure is catastrophic or just produces a degradation depends upon where in the circuitry the failure occurs, and hence the effect on performance. Predominant failure mechanisms observed in the McDonnell Douglas tests were all thermal in nature: Bond wire failure, junction failure, and metalization failure.

Since the damage mechanisms are thermal in nature, the damage models used by McDonnell Douglas were derived from basic heat flow analysis. For worst-case analysis, the heat is assumed to be produced by the absorbed RF signal, and there is no frequency dependence. At pulse durations in excess of about 10 μs, Figure 8-3, the amount of power required for damage is 0.5 W. This value is set by the rate at which heat can be conducted away from the hot spot. For pulse durations in excess of 30 μs, the average power is

$$P_{avg} = P_{peak} \times PW \times PRF \tag{2}$$

where:

P_{avg} = average power

P_{peak} = pulse peak power

PW = pulse width

PRF = pulse repetition frequency

8.2.2 Digital Interference Data

Other sources[2] report that the failure mechanism in ICs due to the EMP from nuclear explosions is due largely to semiconductor junction breakdown. A model paralleling that used for semiconductor failure (Wunsch model) has been reported using the empirical model

$$P = At^{-B} \tag{3}$$

where:

P = average failure power, W

t = pulse duration, s

A,B = experimental determined

8-5
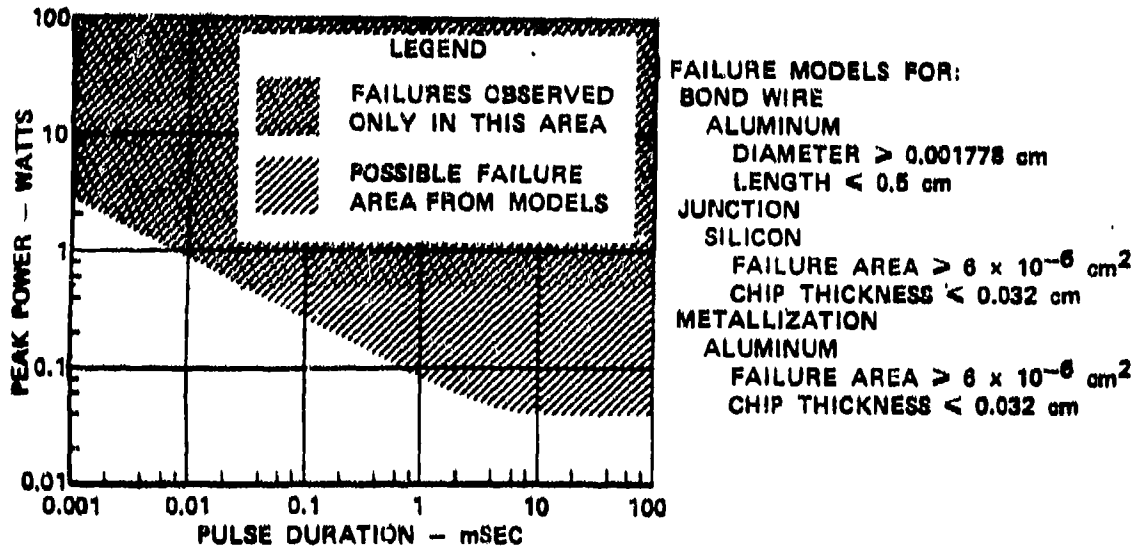
Figure 8-3. Measured and Predicted Worst-Case Burnout Levels

Figure 8-4 shows ranges of values obtained for A (and K for the Wunsch constant). Using data from Figure 8-3, a value for A of 3.5×10^{-3} and a value for B of 0.5 is obtained. This indicates that the IC burnout data found experimentally by McDonnel Douglas and the Bechtold parallel to the Wunsch model are in close agreement eventhough the failure mechanism may be different.

Table 8-1 shows the electrical characteristics of some transistor-transistor logic (TTL) devices. Listed in the table are several voltage levels for the "high" and low" states (V_{IH} and V_{IL}, respectively) and the worst-case output levels for the "high" and "low" states (V_{OH} and V_{OL}, respectively). Figure 8-5 is a diagram which illustrates the relationship between these voltages. It shows a forbidden region in which the device makes uncertain decisions, as well as two regions of noise margin. In the "low" state, the noise may increase the drive level (input source being a TTL device) from V_{OL} to V_{IL} without causing a failure.

In the curves of Figure 8-6, the criterion for worst-case susceptibility for the "low" state, the voltage values chosen are V_{OL}, V_{IL}, and a value

Figure 8-4. Ranges of A (or Wunsch K) for Various Device Families

Table 8-1. Specifications for Typical TTL Device

Electrical Characteristics over recommended operating free-air temperature range (unless otherwise noted).

PARAMETER		CONDITIONS	H103			DM54H/74H H106			H108			UNITS
			MIN	TYP(1)	MAX	MIN	TYP(1)	MAX	MIN	TYP(1)	MAX	
V_{IH}	High Level Input Voltage		2			2			2			V
V_{IL}	Low Level Input Voltage				0.8			0.8			0.8	V
V_I	Input Clamp Voltage	V_{CC} = Min, I_I = -8 mA			-1.5			-1.5			-1.5	V
I_{OH}	High Level Output Current				-500			-500			-500	μA
V_{OH}	High Level Output Voltage	V_{CC} = Min, V_{IH} = 2V V_{IL} = 0.8V, I_{OH} = -500μA	2.4	3.4		2.4	3.4		2.4	3.4		V
I_{OL}	Low Level Output Current				20			20			20	mA
V_{OL}	Low Level Output Voltage	V_{CC} = Min, V_{IH} = 2V V_{IL} = 0.8V, I_{OL} = 20 mA		0.2	0.4		0.2	0.4		0.2	0.4	V
I_I	Input Current at Maximum Input Voltage	V_{CC} = Max, V_I = 5.5V			1			1			1	mA
I_{IH}	High Level Input Current Any J or K	V_{CC} = Max, V_I = 2.4V			50			50			50	μA
	Clear				100			100			200	
	Preset				N/A			100			100	
	Clock		0	-1	-1	0	-1	-1	0	-1	-1	mA
I_{IL}	Low Level Input Current Any J or K	V_{CC} = Max, V_I = 0.4V		-1	-2		-1	-2		-1	-2	mA
	Clear			-1	2		-1	-2		-2	-4	
	Preset				N/A		-1	-2		-1	-2	
	Clock			-3	-4.8		-3	-4.8		-6	-9.6	
I_{OS}	Short Circuit Output Current	V_{CC} = Max(2)	-40		-100	-40		-100	-40		-100	mA
I_{CC}	Supply Current	V_{CC} = Max, (3)	40		76	40		76	40		76	mA

Notes:
(1) All typical values are at V_{CC} = 5V, T_A = 25°C.
(2) Not more than one output should be shorted at a time, and duration of short circuit should not exceed one second.
(3) With all outputs open, I_{CC} is measured with the Q and $\bar{Q}$ outputs high in turn. At the time of measurement, the clock input is grounded.

1-74

2-8

3.4 — Typical output level a device will provide in "high" state

2.4 — V_{OH}, Minimum output level a device will provide in "high" state

2.2 —

Noise Margin

2.0 — V_{IH}, Minimum input level a device will recognize as "high" state

Forbidden Region

1.0 —

0.8 — V_{IL}, Maximum input level a device will recognize as "low" state

Noise Margin

0.6 —

0.4 — V_{OL}, Maximum output level a device will provide in "low" state

0.2 — Typical output level a device will provide in "low" state

0 —

Figure 8-5.   Diagram Explaining Voltages Used for Worst-Case
Susceptibility Levels for TTL Devices

8-9

Figure 8-6. Worst-Case Susceptibility Levels for TTL Devices

8-10

half-way between. A similar selection was made for the "high" state worst-case susceptibility. Figure 8-7 summarizes the worst-case susceptibility for both the "high" and the "low" states.

Figure 8-8 shows the worst-case susceptibility for complementary metal oxide semiconductor (CMOS) devices. Here the specification value for the low state is about a maximum of 0.05 V and the minimum specification value for the high state is 4.95 V. A comparison of this data with that shown in Figure 8-6 for the TTL devices shows that the CMOS devices are much less susceptible to interference than the TTL devices. In both cases, it can be seen that as the frequency of the microwave signal increases, the device is able to absorb more power before interference occurs. Figure 8-9 summarizes the worst-case susceptibility condition for both the high and low states.

In measuring TTL and CMOS susceptibility, the package supply current was also measured to determine how much RF power was required to cause significant increases in power supply current. It was found that the significant increase did not occur until the RF power level was far above the levels sufficient to induce state changes in the output voltage. The modeling activity conducted by McDonnell Douglas also confirmed that conclusion. Therefore, in TTL circuits, output voltage state changes are expected to occur before significant supply current changes are noted.

8.2.3 Linear Interference Data

The most common example to show giving linear interference data is the operationl amplifier. The operational amplifier was found to be most susceptible to RF energy conducted into either of the input circuits. The rectified RF produces an offset in operating voltage. Figure 8-10 shows the worst-case susceptibility levels for operational amplifiers for four values of offset voltage. Typically, voltage offsets of 0.05 V produce significant interference.

8.2.4 Voltage Regulators

Measurements were made of the interference susceptibility of both three-pin and multi-pin voltage regulators under various load current conditions.

(Maximum Specification Value for Low V_{OUT} = 0.4 Volt and
Minimum Specification Value for High V_{OUT} = 2.4 Volts)
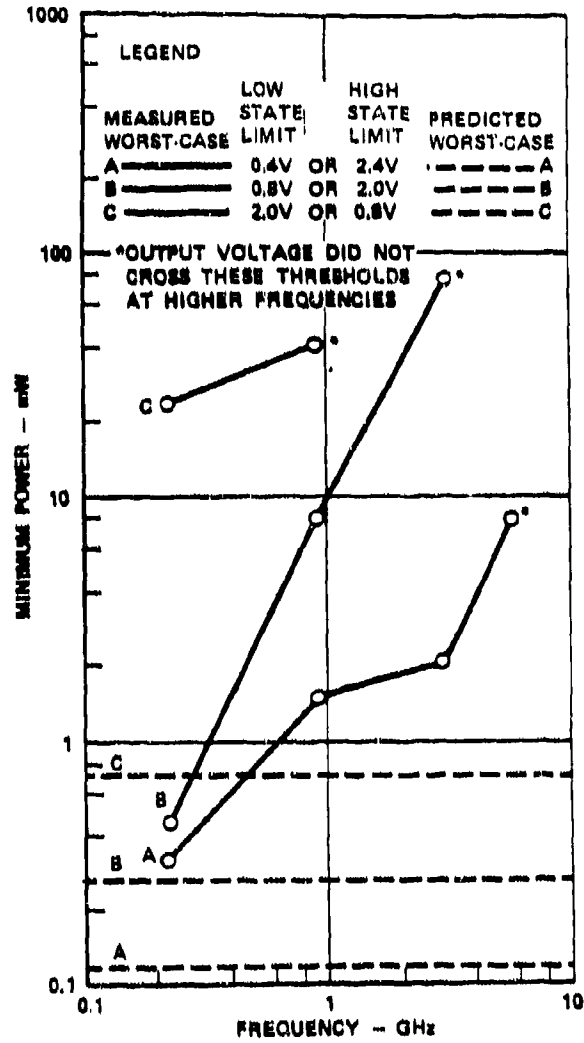
Figure 8-7. Worst-Case Susceptibility Values for TTL Devices
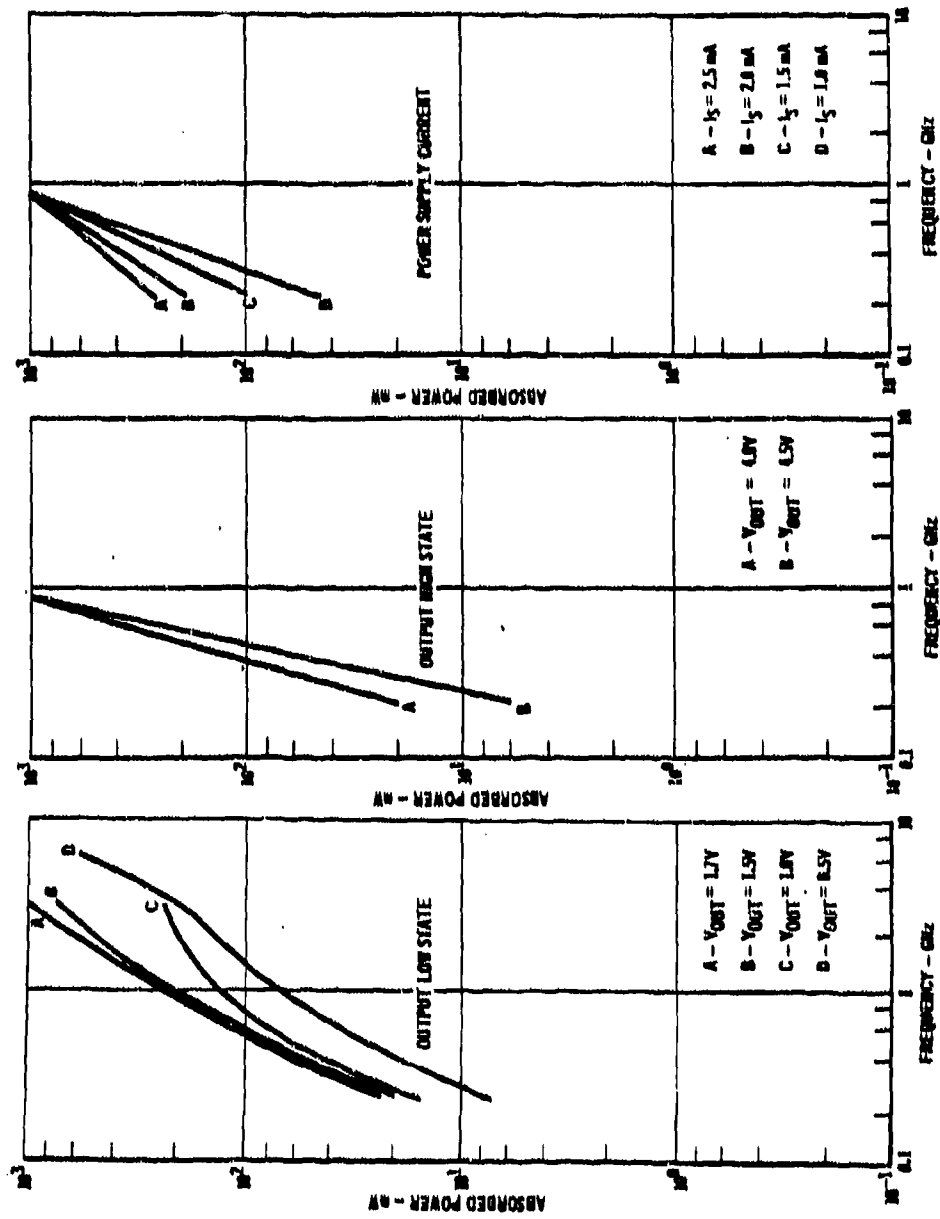
Figure 8-8. Worst-Case Susceptibility Levels for CMOS Devices

(Maximum Specification Value for Low V$_{OUT}$ = 0.05 Volt and Minimum
Specification Value for High V$_{OUT}$ = 4.95 Volts)
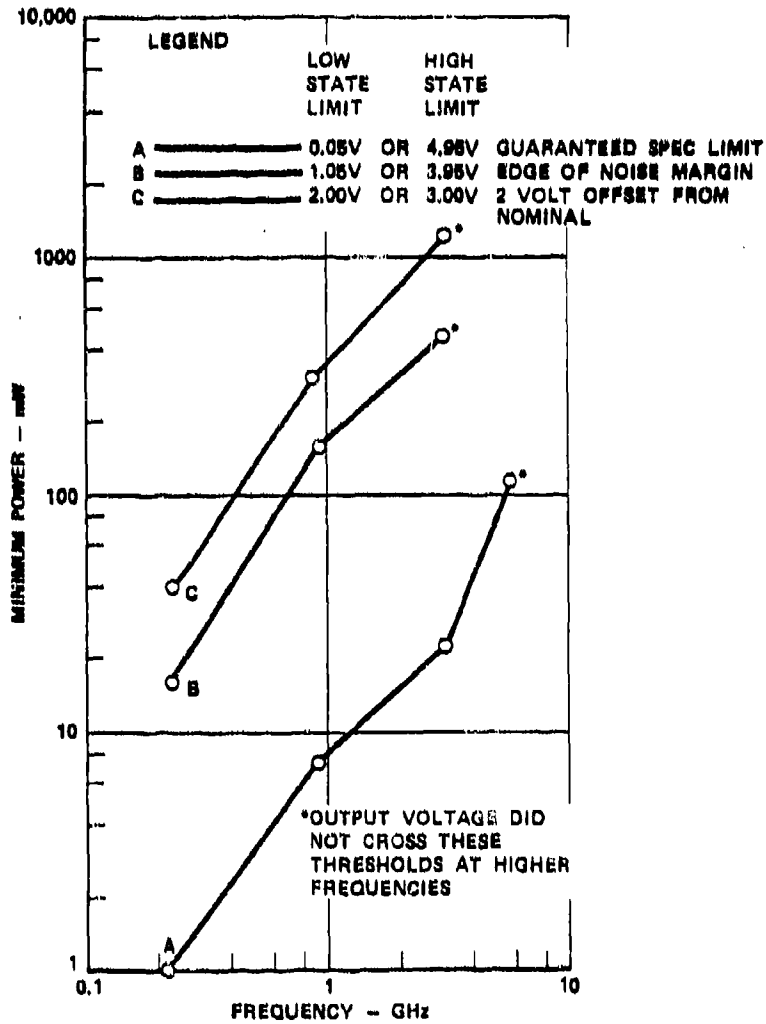
Figure 8-9. Worst-Case Susceptibility Values for CMOS Devices
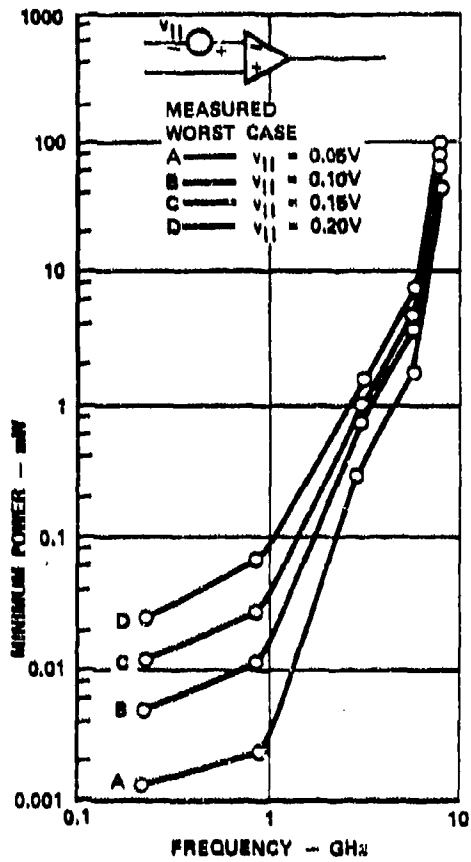
Figure 8-10. Worst-Case Susceptibility Values for Operational Amplifiers

Figure 8-11 shows the absorbed power as a function of frequency to produce a change of 0.25 V in the output of the regulators. The data for the multi-pin regulator shows a susceptibility of the same order of magnitude as the operational amplifier for 0.2 V offset voltage. This is probably caused by the input to the operational amplifier in the multi-pin regulator being available as an input as shown in Figure 8-12 resulting in pick up by the operational amplifier.

8.3 SUMMARY

The information contained in this report covers the susceptibility of individual ICs over the frequency region from 200 MHz to 10 GHz. The sample curves shown represent only a small portion of the data available from the source documents generated by McDonnell Douglas. The data in Figure 8-13 shows that the most sensitive devices are operational amplifiers, followed by multi-pin regulators and TTL devices. The worst-case susceptibility, in terms of absorbed power to cause a minimal interference, covers a range of almost three orders of magnitude. The three-pin regulator and the CMOS circuitry are less susceptible than the TTL and multi-pin regulator.

The susceptibility of an IC is naturally dependent on the contents of the IC. If only TTL circuitry is contained in the IC, the susceptibility of the TTL devices would prevail. If operational amplifiers are also contained in the IC, the IC would be susceptible to lower power levels, especially if the operational amplifier is accessible at the IC terminals.

The operational amplifier is most susceptible to interference at one of its input circuits, where the absorbed power is rectified (detected) by the semiconductor junction and inserts a dc offset in voltage. The digital circuits appear to be most susceptible to power absorbed in their output circuits, where the rectified signal changes the high/low state thresholds to cause incorrect logic decisions to be made.

When the absorbed power is a modulated signal such as AM or a pulsed source, the device semiconductor junctions produce pulses which propagate

8-16
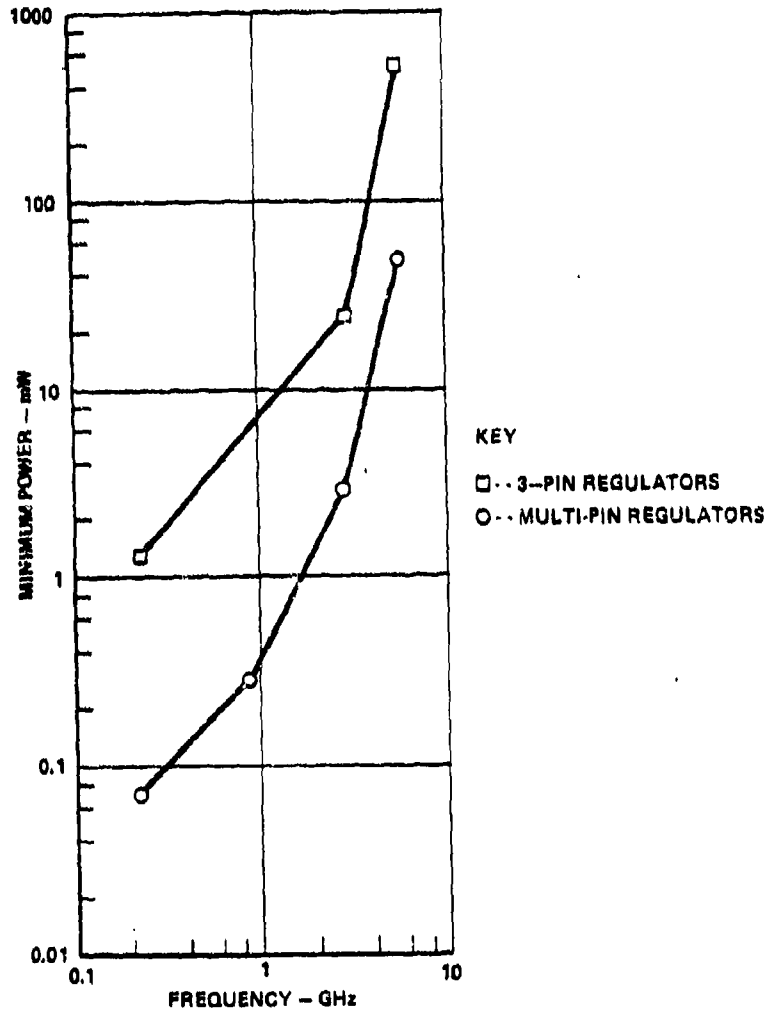
Figure 8-11. Worst-Case Susceptibility Values for Voltage Regulators;
Output Voltage Change of 0.25 V is Susceptibility
Criterion

UNREGULATED INPUT — SERIES PASS ELEMENT — REGULATED OUTPUT

R1

OP AMP

R2

VREF

GROUND

"ON CHIP" ELEMENTS

"ON CHIP" FOR 3-PIN
"EXTERNAL" FOR MULTI-PIN
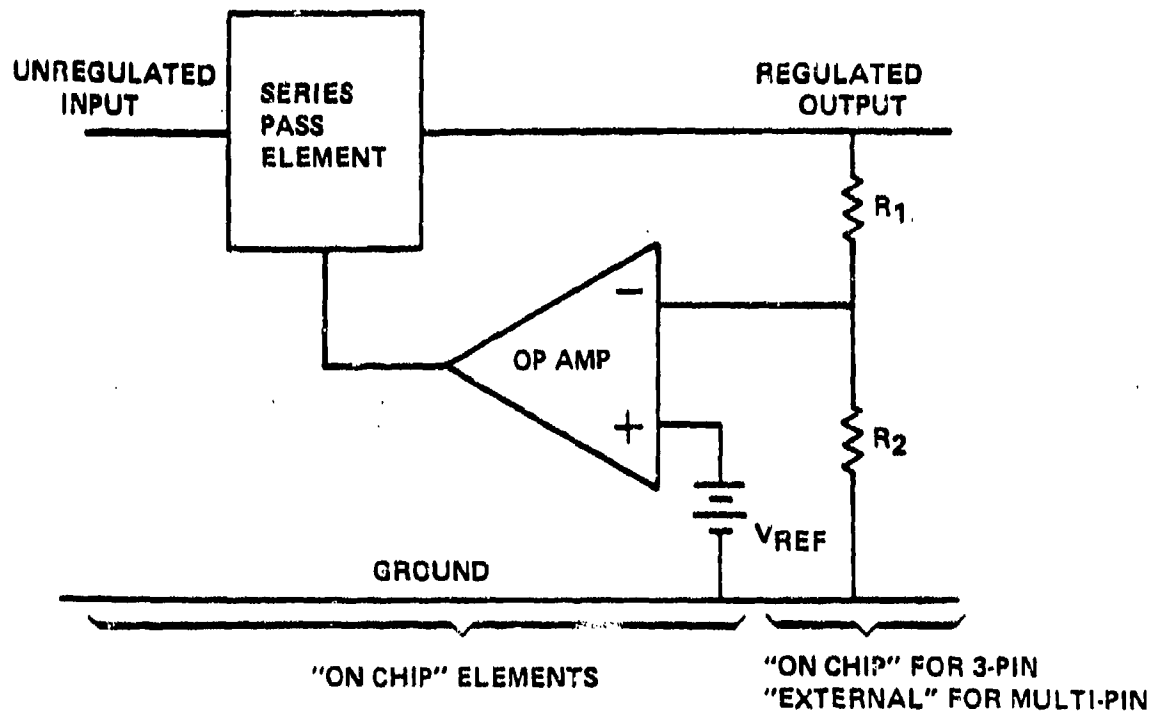
Figure 8-12. Basic Series Regulator Circuit
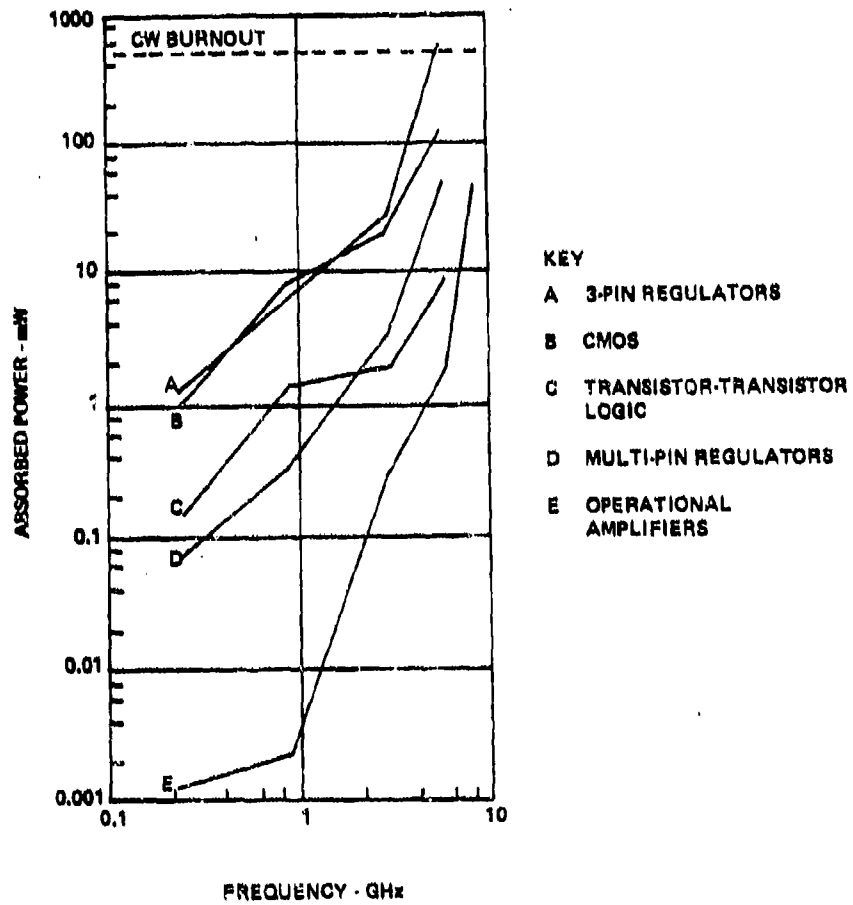
Figure 8-13. Worst-Case Absorbed Power Susceptibility

through the following circuitry. The passband characteristics of those circuits compared to the modulating frequency determines how well the detected signal will propagate. In general, it would be anticipated that the lower frequencies would propagate most readily in such circuits as operational amplifiers and Schmitt trigger circuits.

In the experiments and analysis performed, the shielded cabling presented a worst-case aperture of a half-wave dipole $(0.13\lambda^2)$, so that the power absorbed by the cabling, P, without considering losses can be related to the power density, P_d, incident on the cabling by

$$P = 0.13\lambda^2 P_d \qquad (3)$$

where λ is the wavelength of operation. Using this relationship with the curves shown in Figure 8-13, the worst-case power density susceptibility shown in Figure 8-14 was obtained. These curves exhibit a very wide range of power density susceptibility over the frequency range. Using these curves, with the environmental RF threat provides a means for assessing the increased shielding required. As an example, the power density at a range of 1 nmi from a 10 kW transmitter with a 40 dB gain antenna is shown in dotted lines across the top of Figure 8-14. At the 220 MHz end of the spectrum over 60 dB increases in shielding might be required. Even an increase in distance from the antenna to 10 nmi would only reduce the requirements to 40 dB more shielding. The requirement is considerably less at the higher frequencies due to the inverse frequency square properties of the dipole absorption apertures.

The preceding information pertains to interference susceptibility, which goes away when the interfering source is removed. However, permanent damage results at some level higher than the interference level. Depending upon the effect on performance. it would be classified as degradation or catastrophic. The failure mechanism is due to the increase in temperature caused by the absorption of power (energy) reaching a damaging level in the silicon junctions, the metalization stripes or the bond wires. Figure 8-3 shows the peak power absorbed as a function of pulse duration required to cause a failure of this

KEY

A 3-PIN REGULATORS

B CMOS

C TRANSISTOR-TRANSISTOR
   LOGIC

D MULTI-PIN REGULATOR

E OPERATIONAL AMPLIFIERS

$$P_d = \frac{P}{0.13\lambda^2}$$

10 kW
40 dB antenna gain
1 nmi

CW BURNOUT

POWER DENSITY - mW/m²

POWER DENSITY - W/cm²

FREQUENCY - GHz
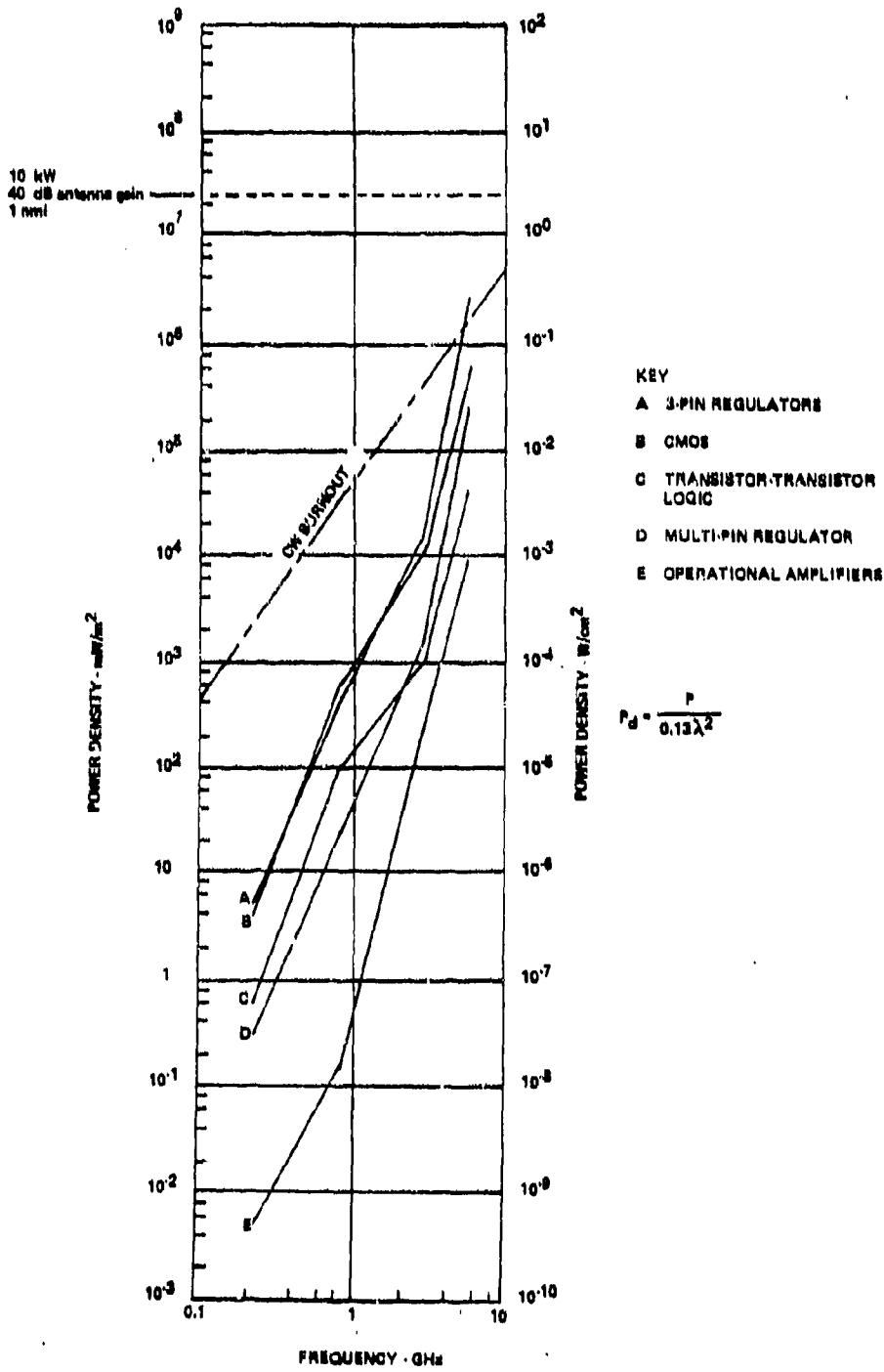
Figure 8-14.   Worst-Case Power Density Susceptibility Values
Assuming λ/2 Aperture

type. The thermal dissipation time constant of the devices was such that pulse durations in excess of 30 μs had the same effect as CW signals. At pulse durations in excess of 30 μs, the peak power times pulse duration times pulse repetition frequency product (i.e., the energy absorbed) is the critical issue since the effect is thermal destruction. The data shows that a minimum of 0.5 W of absorbed power is required to cause burnout. Using the half-wave dipole aperture absorption model, the CW power density for burnout ranges from 0.43 W/m^2 (0.043 mW/cm^2) at 100 MHz to 4273 W/m^2 (0.43 W/cm^2) at 5.6 GHz.

The failure mechanism due to the EMP generated by nuclear blasts is reported to be dominantly due to semiconductor junction failure. For ICs, a model paralleling that for the semiconductors was empirically generated. This model is

$$P = At^{-B} \tag{4}$$

where:

    P = average failure power, W
    t = pulse duration, s
    A,B = experimentally determined constants (values for B not available at time of writing)

A chart showing the range of values for A (and the equivalent Wunsch constant K) is shown in Figure 8-4. The data from Figure 8-3 found experimentally by McDonnell-Douglas for microwave power absorption shows a value for B of 0.5 and a value for A of 3.5 x 10^{-3}. This implies that the IC burnout and failures due to EMP cause failures at about the same level of absorbed power.

Figure 8-15 shows the energy levels for EMP due to nuclear blasts. This data was compiled by the authors from their in-house experiments[3] and also from the Defense Nuclear Agency Handbook. The energy level for IC burnout from Figure 8-3 ranges from 3.5 x 10^{-6} J to about 1.5 x 10^{-5} J compared to about 10^{-5} J for ICs due to the EMPs from nuclear blasts.
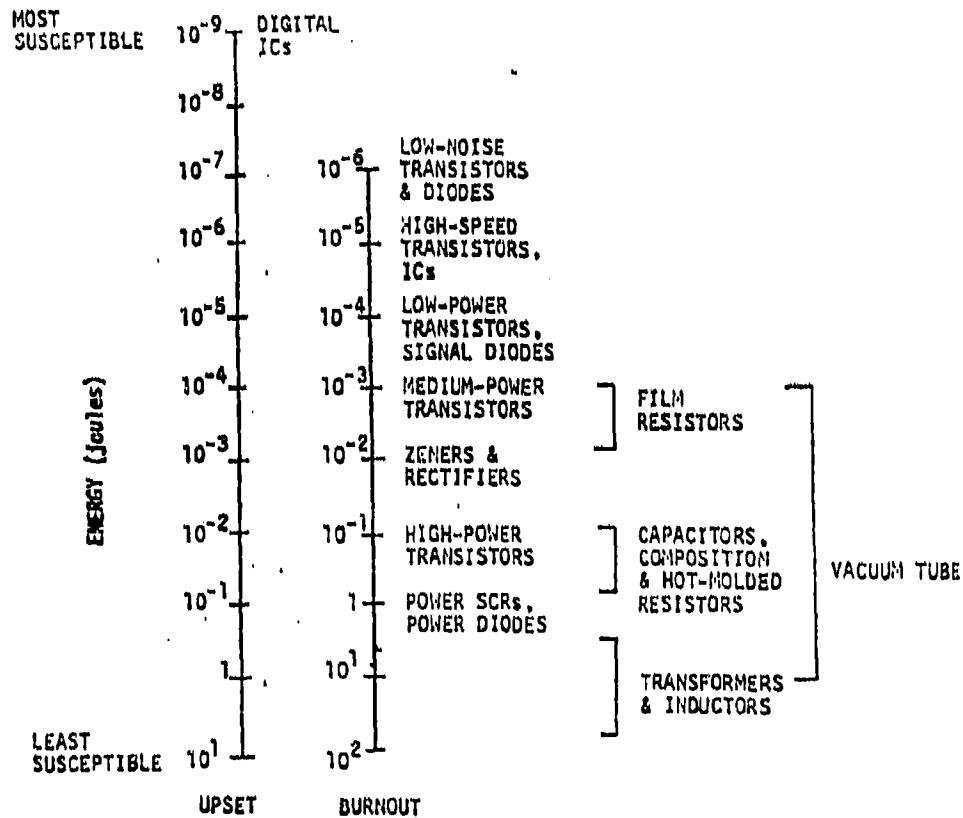
Figure 8-15. Upset and Burnout Energies (µs region transients)
for Various Circuit Elements(3)

8-23

8.4 REFERENCES

1. IC Susceptibility Handbook, McDonnell-Douglas Company, Report No. MDC E1929, August 1978.

2. Dr. G.W. Bechtold, VSTOL Survival Levels Component Damage.

3. E. Blum and M. Rose, "Electromagnetic Pulse (EMP)", Interference Technology Engineers Masters, Plymouth Meeting, PA, 1975.

SECTION 9

EM SHIELDING/WEIGHT TRADE-OFFS

This section details some preliminary work on the trade-offs involved in the use of different materials and coating of graphite/epoxy laminates with conducting foils, meshes, and flame sprays.

The data used in developing the charts of this section are tabulated in Table 9-1. The measure of EM shielding used in the charts is the transfer impedance given by

$$Z_{st} = \frac{\eta}{\sinh \gamma d} \tag{1}$$

where

$$\eta = \sqrt{\frac{j\omega\mu}{\sigma}}$$

$$\gamma = \sqrt{j\omega\mu\sigma} \tag{2}$$

For the materials considered, below 10^5 Hz, Z_{st} is indepedent of frequency and given by

$$Z_{st} \propto \frac{1}{\sigma d} \tag{3}$$

Figure 9-1 plots the transfer impedance in bar chart form. The figure illustrates the shielding effectiveness of the various foils on an absolute scale including an 8-ply laminate of graphite/epoxy. Its thickness is 42 mils (0.0011 m).

Figure 9-2 shows the improvement of various protective coatings on 8-ply graphite/epoxy. The plot is on an absolute scale with all coating thickness fixed at 4 mils. For the coatings considered, the effect of the coatings dominates the shielding the graphite/epoxy. It is shown in Appendix A of a Boeing report[1] that the equivalent transfer impedance of a coated material is given by

Table 9-1. Material Parameters Used in EM/Weight Trade-Offs
(Valid for Frequencies below 10^5 Hz)

MATERIAL	CONDUCTIVITY (U/m)	DENSITY (lb/ft²) ρ_s	20 LOG Z_{ST} AT 10^5 Hz (dB)	Δ Z_{ST} WRT G/E (dB)	$\left\|\dfrac{Z_{ST}\ G/E}{Z_{ST}\ mat}\right\|$	WEIGHT PENALTY (lb) AREA = 98.6 sq ft	SHIELDING MERIT
8 ply Aluminum	3.12×10^7	-	-102.32	-	-	-	-
Aluminum Foil (4 mil)	3.12×10^7	0.056	-70.04	43	141.3	5.52	2523.2
Cufoil (4 mil)	7.29×10^7	0.1866	-77.0	50	327.3	18.4	1754.0
120 Mesh Aluminum (4 mil)	-	0.045	-50.0	23	14.1	4.44	313.3
Titanium Foil (4 mil)	2.1×10^6	0.0965	-46.6	19.6	9.55	9.5	98.9
Aluminum Flame Spray (4 mil)	-	0.00971	-47.98	20.98	11.2	0.96	1153.0
Nickel Foil (4 mil)	1.28×10^7	0.162	-62.3	35.3	58.2	15.97	359.3
Tin Foil (4 mil)	8.78×10^6	0.146	-59.0	32.0	39.8	14.4	272.6
8-Ply T-300 Graphite Epoxy	2×10^4	-	-27.0	-	-	-	-
Boron Epoxy	-	-	30.0	-	-	-	-
Kelvar	-	-	224.0	-	-	-	-

Figure 9-1. Transfer Impedance Shielding of Structural Materials and Protective EM Coatings (Valid for Frequencies below 10^5 Hz)
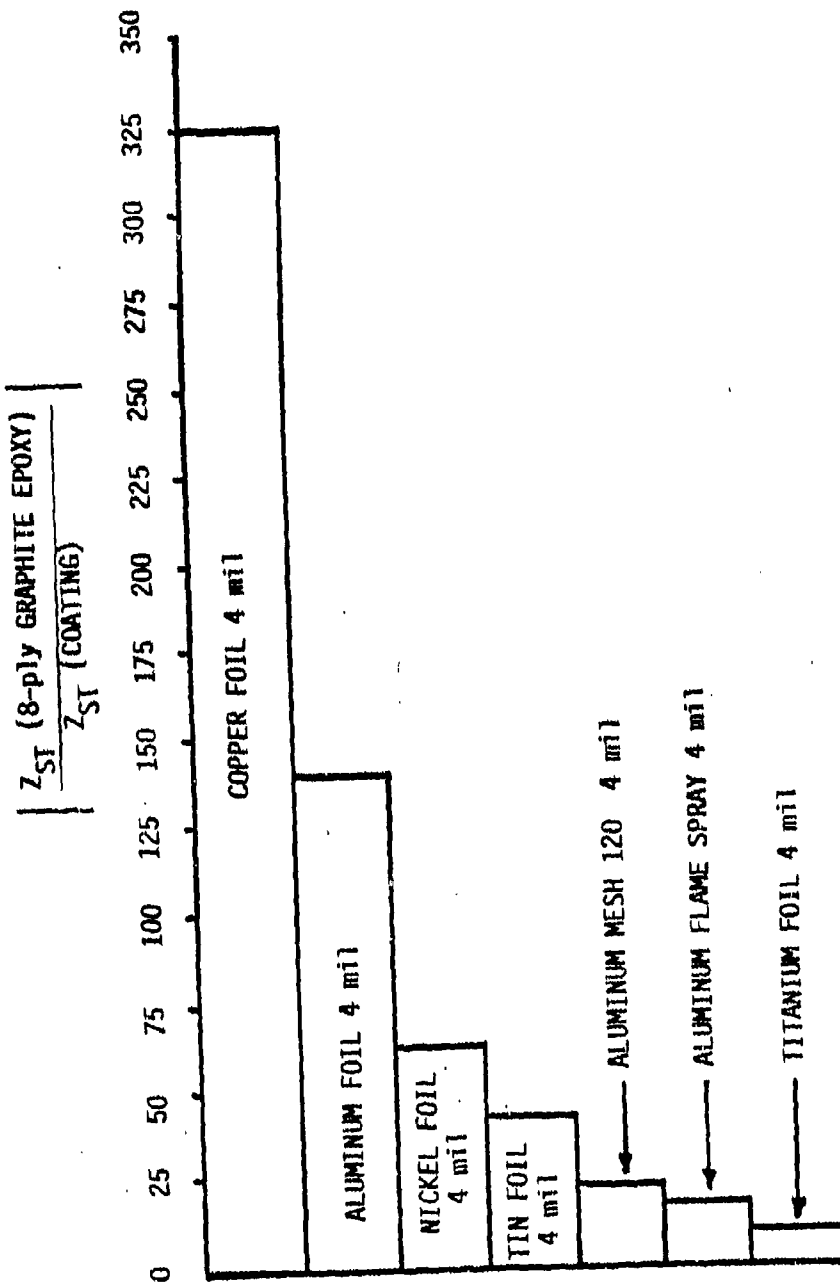
Figure 9-2. Improvement Protective Coatings Provide Relative to 8-Ply Graphite/Epoxy (Valid for Frequencies below 10^5 Hz)

$$Z_{st} = \frac{Z_{st}(a) \, Z_{st}(b)}{Z_L(a) + Z_L(b)} \tag{4}$$

at low frequency. Here $Z_{st}(a)$ and $Z_{st}(b)$ are the transfer impedances of the two materials and $Z_L(a)$ and $Z_L(b)$ are the surface impedances of the materials defined in Section 3. At low enough frequency, both Z_L and Z_{st} approach $1/\sigma d$ in which case

$$Z_{st} \approx \frac{(1/\sigma_a d_a)(1/\sigma_b d_b)}{(1/\sigma_a d_a) + (1/\sigma_b d_b)} \tag{5}$$

For $\sigma_a d_a \ll \sigma_b d_b$

$$Z_{st} \approx \frac{1}{\sigma_b d_b} \tag{6}$$

so on applying a conducting film to graphite/epoxy the resultant shielding is almost totally due to the conducting film. Hence, the improvement is given that protective coatings provide relative to 8-ply graphite/epoxy (G/E) is just the ratio of their transfer impedance or

$$\text{Improvement} = \frac{Z_{st}(G/E)}{Z_{st}(\text{coat})} \approx \frac{1/\sigma_{G/E} d_{G/E}}{1/\sigma_c d_c} = \frac{\sigma_c d_c}{\sigma_{G/E} d_{G/E}} \tag{7}$$

The weight penalty paid by coating with 4 mils of various foils meshes and flame spray is shown in Figure 9-3. This is based on 98.6 ft^2 of coating which is the estimate surface areas of the AV-8B forward fuselage to be covered with graphite/epoxy.

The combined measure of shielding and weight penalty for the various coatings is given in Figure 9-4. It is defined as

$$\text{Figure of Merit} = \frac{\text{Improvement}}{\text{Surface Density}} = \frac{Z_{st}(G/E)/Z_{st}(\text{coat})}{\rho_s} \tag{8}$$

Rather than simply use transfer impedance as a measure of shielding, it can sometimes be desirable to use electric or magnetic shielding effectiveness.

9-5
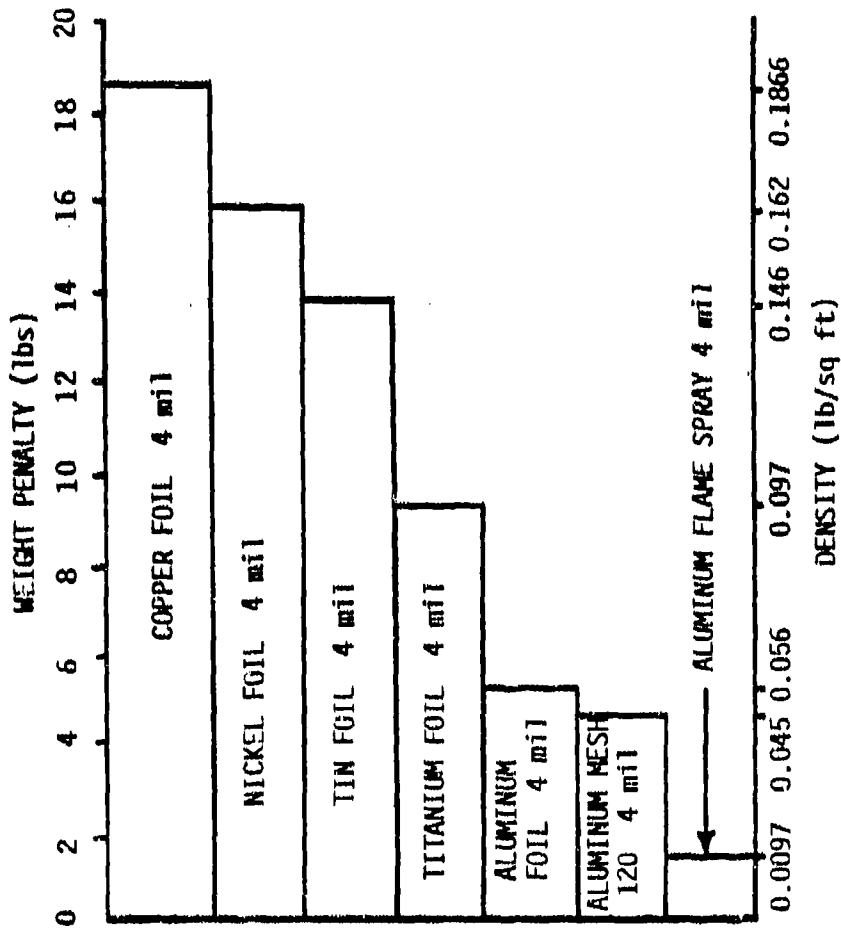
Figure 9-3. Forward Fuselage (Area = 100 ft^2) Weight Penalty (lbs) Imposed by EM Protective Coatings
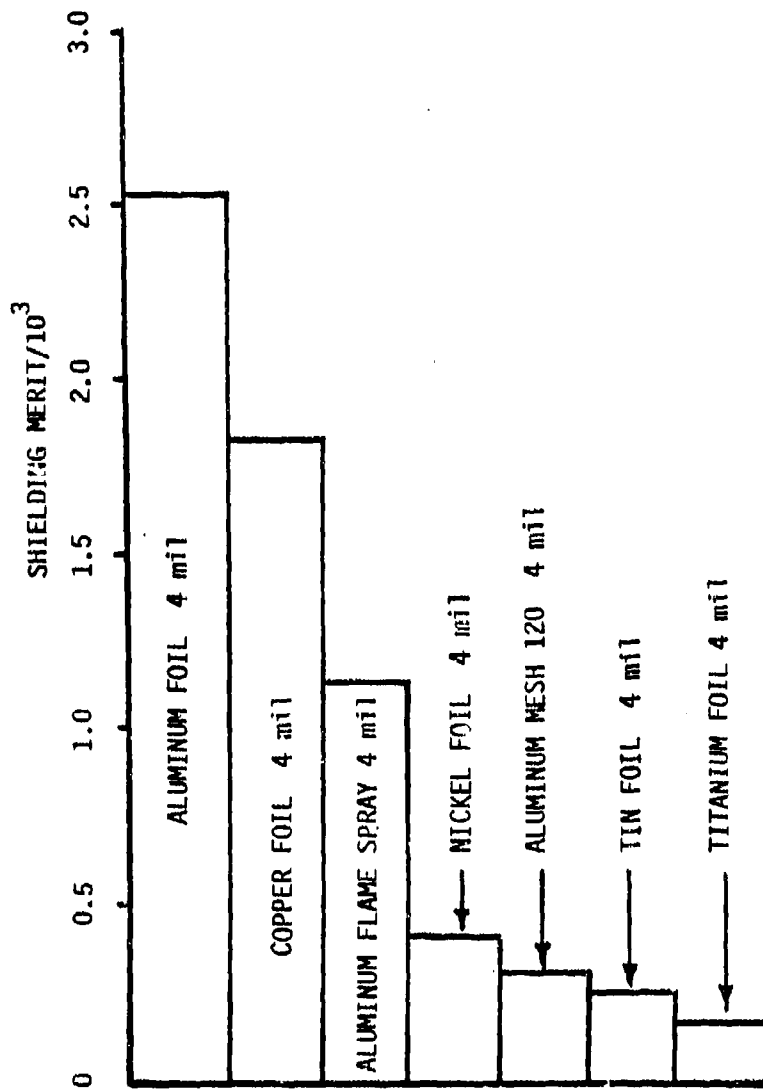
Figure 9-4. Weight Shielding Figure of Merit (Shielding Beyond 8-Ply Graphite/Epoxy) of EM Protective Coatings

(Electric shielding effectiveness (ESE) and magnetic shielding effectiveness (MSE), respectively.) The definitions and relations for these quantities are given in Section 4. Figures 9-5 and 9-6 plot the gain in MSE when different coatings are applied to mixed-orientation graphite/epoxy. Figure 9-5 is taken from Section 4 and is for a flat plate geometry. It plots the improvement in MSE provided by various coatings on 24-ply graphite/epoxy. The curves of Figure 9-5 were obtained using

$$\text{Improvement} = \frac{Z_{st}(G/E)}{Z_{st}(G/E + \text{coating})} \tag{9}$$

The transfer impedance for the combination graphite/epoxy with coating was taken from Reference 1.

Figure 9-6 shows the gain in MSE provided by coatings over an 8-ply graphite/epoxy cylinder of 0.5 m radius (a rough estimate of the F-18 forward fuselage radius). The shielding of the coating again dominates the composite so that

$$\text{Improvement for Cylinder} = \text{MSE} = 20 \log_{10}(\text{MSR}^{-1}) \tag{10}$$

where, from Section 4,

$$\text{MSR}^{-1} = \cosh(\gamma d) + Z/\eta \, \sinh(\gamma d) \tag{11}$$

where $Z = j\omega\mu r$ as in Table 4-1. For electric shielding, the shape of the curves would change, but the separation versus frequency would remain the same.

A more revealing parameterization of data is the plot the thickness of different coatings required to provide a given amount of shielding. Again the equivalent transfer impedance of graphite/epoxy coated with a highly conducting material is dominated by the coating. Table 9-2 lists the thickness of coating required for 40, 60, or 72 dB of shielding along with the weight penalty per square foot of coating.
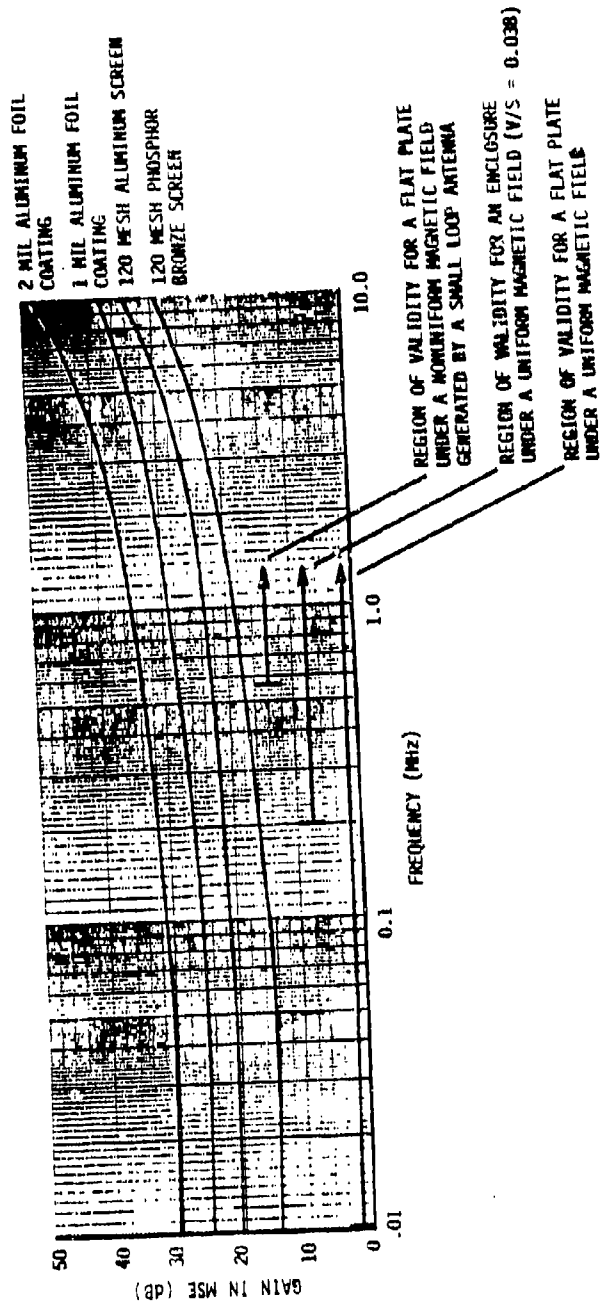
Figure 9-5. Gain in the Magnetic Shielding Effectiveness of 24-Ply T-300 Graphite Composite Through Applications of Aluminum Foil, Aluminum Screen, and Phosphor Bronze Screen to 24-Ply T-300 Graphite
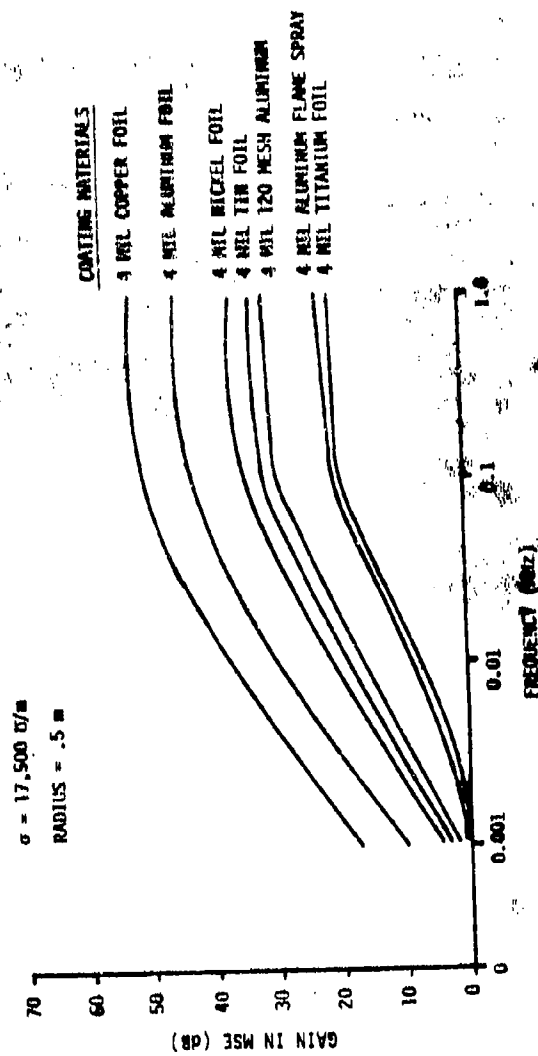
Figure 9-6. Gain in Magnetic Shielding Effectiveness Over an 8-Ply Mixed-Orientation Graphite/Epoxy Cylinder under a Uniform Magnetic Field

Table 9-2. Coating Thickness and Weight Penalty
for Fixed Shielding

Shielding	σ	Coating Thickness in mils $20 \log_{10} Z_{st}$		
		40 dB	60 dB	72 dB
Aluminum Foil	3.12×10^7	0.1259	1.259	5.0121
Copper Foil	7.29×10^7	0.054	0.54	2.1451
Titanium Foil	2.1×10^6	1.87	18.7	74.46
Nickel Foil	1.28×10^7	0.31	3.1	12.217
Tin Foil	8.78×10^6	0.45	4.47	17.81
Aluminum Flame Spray	2.46×10^6	1.6	16.0	63.6
Graphite/Epoxy	10^4	392.8	3928.0	15638.0

Shielding	Density (lb/ft^2) for 1 mil coating (lb)	Weight Penalty/ft^2 Applied Coating (lb) $20 \log_{10} Z_{st}$		
		40 dB	60 dB	72 dB
Aluminum Foil	0.014	0.00177	0.0177	0.0702
Coppler Foil	0.04665	0.00252	0.0252	0.100
Titanium Foil	0.024125	0.45	0.45	0.797
Nickel Foil	0.0405	0.0126	0.126	0.495
Tin Foil	0.0365	0.016	0.16	0.65
Aluminum Flame Spray	0.00243	0.004	0.04	0.155

The thickness of coating is calculated from

$$\text{Shielding (dB)} = 20 \log_{10}(1/\sigma d) \tag{12}$$

The results of plotting the tabulation are shown in Figures 9-7, 9-9, and 9-9.

9.1 REFERENCE

1. D. Strawe and L. Piszker, <u>Interaction of Advanced Composites with Electromagnetic Pulse (EMP) Environment</u>, Final Report, prepared by Boeing Aerospace Company for Wright-Patterson Air Force Base under Contract F33615-74-C-5158, AFML-TR-75-141, September 1975.
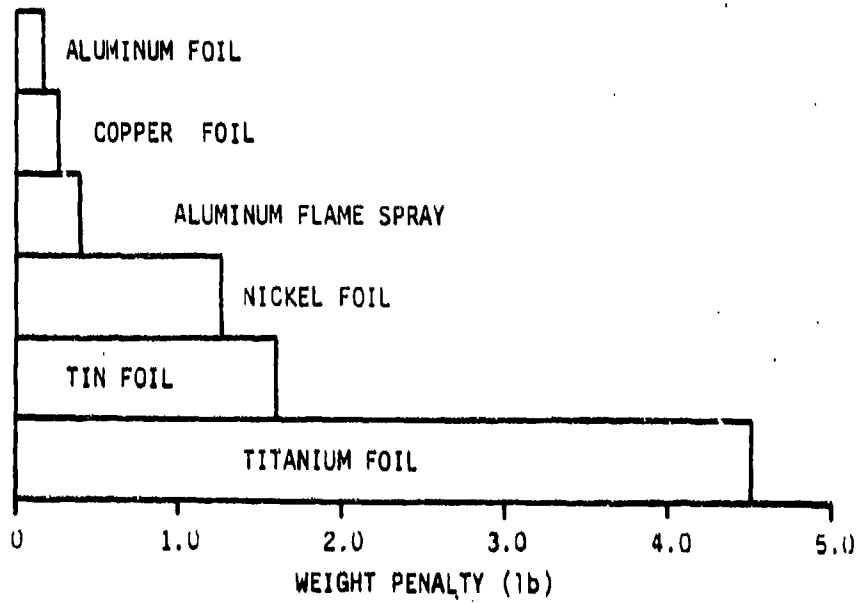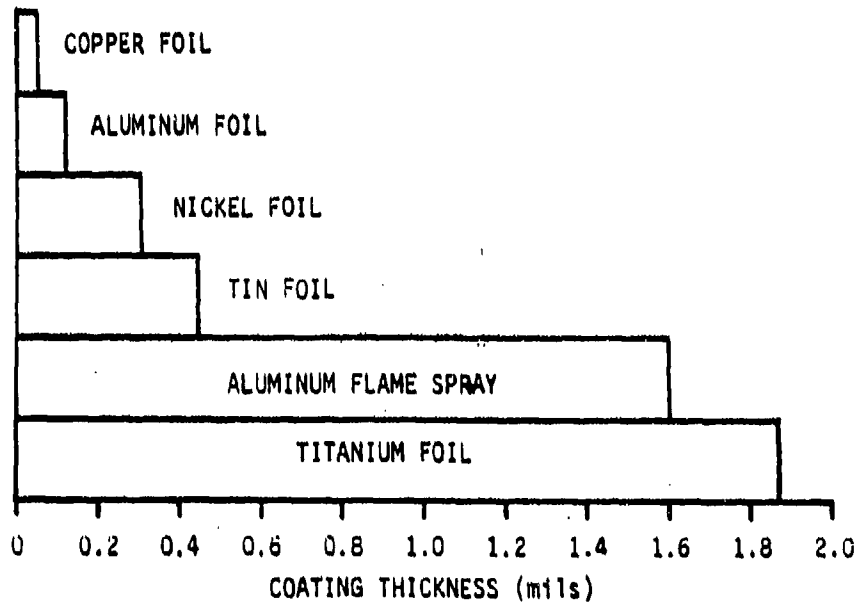
Figure 9-7. Coating Thickness and Weight Penalty for $Z_{st} = -40$ dB at Low Frequency
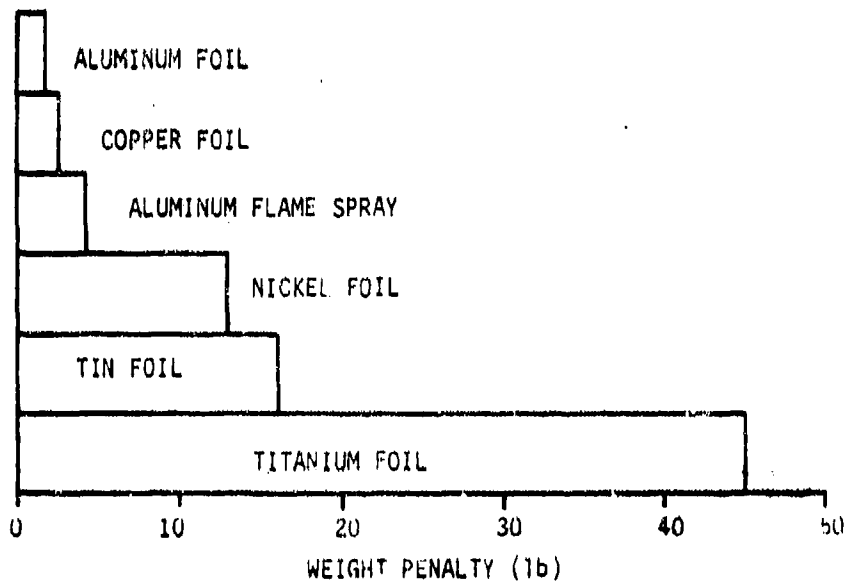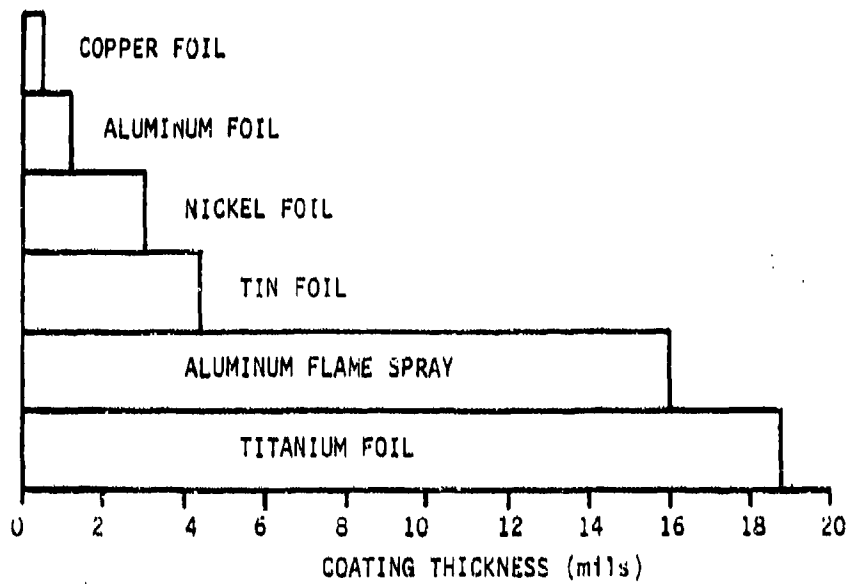
Figure 9-8. Coating Thickness and Weight Penalty for $Z_{st} = -60$ dB at Low Frequency
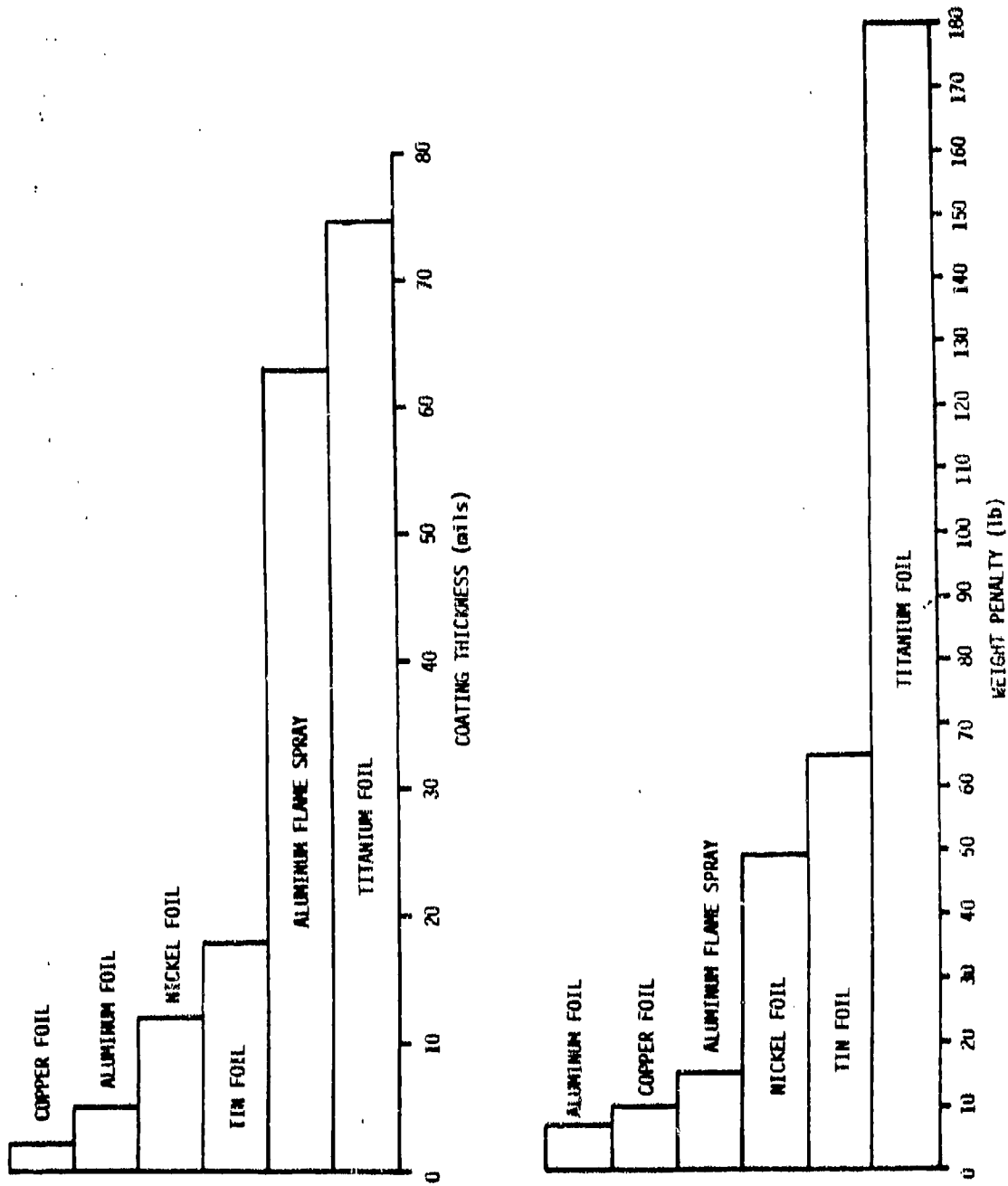
Figure 9-9. Coating Thickness and Weight Penalty for $Z_{st} = -72$ dB at Low Frequency

SECTION 10

BIBLIOGRAPHY

THREAT

1. R.A. Perala and T.F. Ezell, _Engineering Design Guidelines for EMP Hardening of Naval Missiles and Airplanes_, prepared by Mission Research Corporation for Naval Ordance Laboratory under Contract N60921-73-C-0033, AMRC-R-17 (AD 917 958), December 1973.

2. _Protection Optimization for Advanced Composite Structures_, Third Quarterly Progress Report prepared by Grumman Aerospace Corporation for Air Force Systems Command, Wright-Patterson Air Force Base under Contract F33615-77-C-5169, March 1978.

3. _Lightning Analysis for Aircraft Design Workshop_, prepared by Naval Air Systems Command, July 1978.

4. _Engineering Design Handbook Electromagnetic Compatibility_, prepared by Headquarters US Army Materiel Development and Readiness Command, DARCOM-P 706-410, March 1977.

5. _Protection Optimization for Advanced Composite Structures_, Sixth Quarterly Progress Report prepared by Grumman Aerospace Corporation for Wright-Patterson Air Force Base under Contract F33615-77-C-5169, December 1978.

6. _Protection Optimization for Advanced Composite Structures_, Fourth Quarterly Progress Report prepared by Grumman Aerospace Corporation for Wright-Patterson Air Force Base under Contract F33615-77-C-5169, June 1978.

7. R.F. Hess, "Properties of Induced Transients Associated With EM Fields Produced by Lightning or Other Relatively Slow Rise-Time EMP," _IEEE 1978 International Symposium on Electromagnetic Compatibility_, June 1978.

8. R.F. Hess, "EMP Coupling Analysis Using the Frequency (Transfer Function) Method with the SCEPTRE Computer Program," _IEEE Transactions on Electromagnetic Compatibility_, August 1975.

9. _Lightning Test Waveforms and Techniques for Aerospace Vehicles and Hardware_, Report of SAE Committee AE4L, January 1978.

10. _Space Shuttle Program Lightning Protection Criteria Document_, prepared by National Aeronautics and Space Administration, Lyndon B. Johnson Space Center, JSC-07636, Revision A, November 1975.

11. J.E. Nanevicz and D.G. Douglas, <u>Static-Electricity Analysis Program</u>, Volume 1, prepared by Stanford Research Institute for HQ Space & Missile Systems Organization under Contract F04701-73-C-0401, SAMSO TR75-44, October 1974.

12. D.G. Douglas and J.E. Nanevicz, <u>Static-Electricity Analysis Program</u> (Users Manual), Volume II, prepared by Stanford Research Institute for HQ Space & Missile Systems Organization under Contract F04701-73-C-0401 SAMSO TR 75-44, October 1974.

13. R.L. Tanner and J.E. Nanevicz, "An Analysis of Corona-Generated Interference in Aircraft," <u>Proceedings of the IEEE</u>, January 1964.

14. R.A. Perala and J.D. Robb, "The Experimental Verification of Circuit Modeling Techniques used to Determine Lightning Current Distribution as Applied to the NASA Space Shuttle Vehicle," <u>IEEE EMC Symposium</u>, Seattle, WA, August 1977.

15. F.A. Fisher and J.A. Plumer, <u>Lightning Protection of Aircraft</u>, prepared by the General Electric Company for NASA Lewis Research Center, NASA Reference Publication 1008, October 1977.

16. R.B. Cook and R.A. Perala, <u>Coupling of Lightning Stroke Currents to F-18 Balanced Twisted Shielded Pair Cables</u>, prepared by Electro Magnetic Applications, Inc. for the Naval Air Systems Command, March 1979.

17. D.M. LeVine and R. Meneghini, <u>Radiation From A Current Filament Driven by A Traveling Wave</u>, prepared by NASA, NASA TN D-8302, October 1976.

18. D.M. LeVine and R. Meneghini, "Simulation of Radiation from Lightning Return Strokes," <u>Radio Science</u>, Vol. 13, No. 5, PP. 801-809, October 1978.

19. Price and Pierce, "The Modeling of Channel Current in the Lightning Return Stroke," <u>Radio Science</u>, Vol. 12, No. 13, PP. 381-388, May-June 1977.

SHIELDING

1. R.A. Perala and T.F. Ezell, <u>Engineering Design Guidelines for EMP Hardening of Naval Missiles and Airplanes</u>, prepared by Mission Research Corporation for Naval Ordance Laboratory under Contract N60921-73-C-0033, AMRC-R-17 (AD 917 958), December 1973.

2. C.D. Skouby, <u>Electromagnetic Effects of Advanced Composites</u>, Final Report prepared by McDonnell Aircraft Company for Office of Naval Research under Contract N00014-74-C-0200, AD-A010 882, January 1975.

3. <u>Electromagnetic Pulse Handbook for Missiles and Aircraft In Flight</u>, prepared by Sandia Laboratories for Air Force Weapons Laboratory under Contract F29601-72-C-0087, AFWL-TR-73-68 (AD-919 395), September 1972.

4. *Protection Optimization for Advanced Composite Structures*, Fourth Quarterly Progress Report prepared by Grumman Aerospace Corporation for Air Force Systems Command, Wright-Patterson Air Force Base under Contract F33615-77-C-5169, June 1978.

5. S. Shenfeld, "Coupling Impedance of Cylindrical Tubes," *IEEE Transactions on Electromagnetic Compatibility*, Vol. EMC-14, No. 1, February 1972.

6. D.F. Strawe and L.D. Piszker, *Investigation of Penetration of Electromagnetic Energy Through Joints in Advanced Composite Structures*, Interim Report prepared by The Boeing Company for Naval Air Systems Command (D180-25240-1), April 1979.

7. T.K. Wu and L.L. Tsai, "Shielding Properties of Thick Conducting Cylindrical Shells with an Obliquely Incident Plane Wave," *IEEE Transactions on Electromagnetic Compatibility*, August 1975.

8. T.K. Wu and L.L. Tsai, "Time Domain Shielding Properties of Conducting Cylindrical Shells," *IEEE Transactions on Electromagnetic Compatibility*, August 1975.

9. T.K. Wu and L.L. Tsai, "Low-Frequency Sheilding Properties of Conducting Cylindrical Shells of Arbitrary Cross Section," *IEEE Transactions on Electromagnetic Compatibility*, Vol. EMC-20, No. 2, May 1978.

10. K.S. K. Lee and G. Bedrosian, "Diffusive Electromagnetic Penetration into Metallic Enclosures," *IEEE Transactions on Antennas and Propagation*, Vol. AP-27, No. 2, March 1979.

11. J.J. Bowman and V.H. Weston, "The Effect of Curvature on the Reflection Coefficient of Layered Absorbers," *IEEE Transactions on Antennas and Propagation*, Vol. AP-14, No. 6, November 1966.

12. K.F. Casey, "On the Effective Transfer Impedance of Thin Coaxial Cable Shields," *IEEE Transactions of Electromagnetic Compatibility*, Vol. EMC-18, No. 3, August 1976.

13. *Protection Optimization for Advanced Composite Structures*, Seventh Quarterly Progress Report prepared by Grumman Aerospace Corporation for Air Force Systems Command, Wright-Patterson Air Force Base under Contract F33615-77-C-5169, March 1979.

14. *Protection Optimization for Advanced Composite Structures*, Eighth Quarterly Progress Report prepared by Grumman Aerospace Corporation for Air Force Systems Command, Wright-Patterson Air Force Base under Contract F33615-77-C-5169, June 1979.

15. J.L. Bean and R.A. Hall, "Electromagnetic Susceptibility Measurements Using a Mode-Stirred Chamber," *IEEE EMC Symposium*, Atlanta, GA, June 1978.

16. J.H. Richmond, "Transmission Through Inhomogeneous Plane Layers," *IRE Transactions on Antennas and Propagation*, May 1962.

17. S. Shenfeld, "Shielding of Cylindrical Tubes," *IEEE Transactions on Electromagnetic Compatibility*, Vol. EMC-10, No. 1, March 1968.

18. S.Y. Liao, "Light Transmission and RF Shielding Effectiveness of a Metallic-Film Coating on a Plastic Substrate," *IEEE EMC Symposium*, Seattle WA, August 1977.

19. D.A. Miller and J.E. Bridges, "Review of Circuit Approach to Calculate Shielding Effectiveness," *IEEE Transactions on Electromagnetic Compatibility*, March 1968.

20. R.B. Schulz, G.C. Huang and W.L. Williams, "RF Shielding Design," *IEEE Transactions on Electromagnetic Compatibility*, Vol. EMC-10, No. 1, March 1968.

21. *Protection Optimization for Advanced Composite Structures*, First Quarterly Progress Report prepared by Grumman Aerospace Corporation for Air Force Systems Command, Wright-Patterson Air Force Base under Contract F33615-77-C-5169, September 1977.

22. *Protection Optimization for Advanced Composite Structures*, Second Quarterly Progress Report prepared by Grumman Aerospace Corporation for Air Force Systems Command, Wright-Patterson Air Force Base under Contract F33615-77-C-5169, December 1977.

23. *Protection Optimization for Advanced Composite Structures*, Third Quarterly Progress Report prepared by Grumman Aerospace Corporation for Air Force Systems Command, Wright-Patterson Air Force Base under Contract F33615-77-C-5169, March 1978.

24. K.F. Casey, *Electromagnetic Shielding by Advanced Composite Materials*, Final Report prepared by Kansas State University for Bolling Air Force Base under Contract AFWL-PD-76-174 to AFOSR, AFWL-TR-77-201, January 1978.

25. *Lightning Analysis for Aircraft Design Workshop*, prepared by Naval Air Systems Command, July 1978.

26. *Effectiveness of Shielding Materials and Techniques*, prepared by Sperry Gyroscope Company, June 1964.

27. *Electromagnetic Properties and Effects of Advanced Composite Materials: Measurement and Modeling*, prepared by Notre Dame University and Rochester Institute of Technology subcontracting through Syracuse University, by the University of South Florida subcontracting through Georgia Institute of Technology by the Air Force Academy and by a Syracuse University professor

subcontracting through the State University of New York under the sponsor-
ship of the Rome Air Development Center Post-Doctral Program for Rome Air
Development Center for Rome Air Development Center under Contracts F30602-
75-C-0118, F30602-75-C-0122, F30602-75-C-0121, and JON #05670212, RADC-TR-
78-156, June 1978.

28. Engineering Design Handbook Electromagnetic Compatibility, prepared by
Headquarters US Army Materiel Development and Readiness Command, DARCOM-P
706-410, March 1977.

29. K.F. Casey, "EMP Penetration Through Advanced Composite Skin Panels,"
Interaction Note 315, Air Force Weapons Laboratory, December 1976.

30. K.F. Casey, "Electromagnetic Shielding by Advanced Composite Materials,"
Interaction Note 341, Air Force Weapons Laboratory, June 1977.

31. Protection Optimization for Advanced Composite Structures, Sixth Quarterly
Progress Report prepared by Grumman Aerospace Corporation for Wright-Pat-
terson Air Force Base under Contract 33615-77-C-5169, December 1978.

32. L.V. King, "Electromagnetic Shielding at Radio Frequencies," Philosophical
Magazine and Journal of Science, Series 7, Vol. 15, No. 97, February 1933.

33. P.R. Bannister, "Further Notes for Predicting Shielding," IEEE Transactions
On Electromagnetic Compatibility, Vol. EMC-11, No. 2, May 1969.

34. P.R. Bannister, "New Theoretical Expressions for Predicting Shielding
Effectiveness for the Plane Shield Case," IEEE Transactions On Electromag-
netic Compatibility, Vol. EMC-10, No. 1, March 1968.

35. G. Bedrosian and K.S.H. Lee, "EMP Penetration Through Metal Skin Panels and
Into Aircraft Cavities," Air Force Weapons Laboratory Interaction Note 314,
Kirtland Air Force Base, New Mexico, August 1976.

36. D. Strawe and L. Piszker, Interaction of Advanced Composites with Electro-
magnetic Pulse (EMP) Environment, Final Report prepared by Boeing Aerospace
Company for Wright-Patterson Air Force Base under Contract F33615-74-C-5158,
AFML-TR-75-141, September 1975.

COUPLING

1. R.A. Perala and T.F. Ezell, Engineering Design Guidelines for EMP Hardening
of Naval Missiles and Airplanes, prepared by Mission Research Corporation
for Naval Ordance Laboratory under Contract N60921-73-C-0033, AMRC-R-17
(AD 917 958), December 1973.

2. _Electromagnetic Pulse Handbook for Missiles and Aircraft In Flight_, prepared by Sandia Laboratories for Air Force Weapons Laboratory under Contract F39601-62-C-0087, AFWL-TR-73-68 (AD-919 395), September 1972.

3. _Protection Optimization for Advanced Composite Structures_, Fourth Quarterly Progress Report prepared by Grumman Aerospace Corporation for Air Force Systems Command, Wright-Patterson Air Force Base under Contract F33615-77-C-5169, June 1978.

4. _Report of EMX Technical Review_, Volumes I and II, prepared by Naval Ocean Systems Center, July 1978.

5. _Protection Optimization for Advanced Composite Structures_, First Quarterly Progress Report prepared by Grumman Aerospace Corporation for Air Force Systems Command, Wright-Patterson Air Force Base under Contract F33615-77-C-5169, September 1977.

6. _Protection Optimization for Advanced Composite Structures_, Second Quarterly Progress Report prepared by Grumman Aerospace Corporation for Air Force Systems Command, Wright-Patterson Air Force Base under Contract F33615-77-C-5169, December 1977.

7. _Protection Optimization for Advanced Composite Structures_, Third Quarterly Progress Report prepared by Grumman Aerospace Corporation for Air Force Systems Command, Wright-Patterson Air Force Base under Contract F33615-77-C-5169, March 1978.

8. _Lightning Analysis for Aircraft Design Workshop_, prepared by Naval Air Systems Command, July 1978.

9. J.L. Bogdanor, R.A. Pearlman, and M.D. Siegel, _Intrasystem Electromagnetic Compatibility Analysis Program_, Volume I: "User's Manual Engineering Section," Final Report prepared by McDonnel Aircraft Company for Rome Air Development Center under Contract F30602-72-C-0277, RADC-TR-74-342, December 1974.

10. J.L. Bogdanor, R.A. Pearlman, and M.D. Siegel, _Intrasystem Electromagnetic Compatibility Analysis Program_, Volume II: "User's Manual Usage Section," Final Report prepared by McDonnel Aircraft Company for Rome Air Development Center under Contract F30602-72-C-0277, RADC-TR-74-342, December 1974.

11. J.L. Bogdanor, R.A. Pearlman, and M.D. Siegel, _Intrasystem Electromagnetic Compatibility Analysis Program_, Volume III: "Computer Program Documentation," Final Report prepared by McDonnel Aircraft Company for Rome Air Development Center under Contract F30602-72-C-0277, RADC-TR-74-342, December 1974.

12. _Engineering Design Handbook Electromagnetic Compatibility_, prepared by Headquarters US Army Material Development and Readiness Command, DARCOM-P 706-410, March 1977.

13. C. M. Butler, "Integral Equations for Currents Induced on a Wire Model of a Parked Aircraft," Interaction Note 139, Air Force Weapons Laboratory, Kirtland Air Force Base, New Mexico, January 1972.

14. M. G. Harrison and C. M. Butler, "Numerical Solutions of Integral Equations for Currents Induced on a Wire Model of a Parked Aircraft," Interaction Note 140, Air Force Weapons Laboratory, Kirtland Air Force Base, New Mexico, May 1972.

15. F. M. Tesche, M. A. Morgan and B. H. Fishbine, "Evaluation of Present Internal EMP Interaction Technology: Description of Needed Improvements," Interaction Note 264, Air Force Weapons Laboratory, Kirtland Air Force Base, New Mexico, October 1975.

16. A. D. Varvatsis and M. I. Sancer, "Electromagnetic Pulse Penetration Through Dielectric Skin Panels on the Leading Edge of Aircraft Wings," Interaction Note 325, Air Force Weapons Laboratory, Kirtland Air Force Base, New Mexico, May 1977.

17. G. Bedrosian, "Stick-Model Characterisation of the Natural Frequencies and Natural Modes of the Aircraft," Interaction Note 326, Air Force Weapons Laboratory, Kirtland Air Force Base, New Mexico, September 1977.

18. G. Bedrosian, "Stick-Model Characterization of the Total Axial Current and Linear Charge Density on the Surface of an Aircraft Subjected to and EMP: Frequency-Domain External-Interaction Current and Charge Transfer Function," Interaction Note 327, September 1977.

19. K. R. Umashankar and J. R. Wait, "Electromagnetic Coupling to an Infinite Cable Placed Behind a Slot Perforated Screen," Interaction Note 330, Air Force Weapons Laboratory, Kirtland Air Force Base, New Mexico, June 1977.

22. H. J. Fletcher and A. K. Harrison, "Fields in a Rectangular Cavity Excited by a Plane Wave on an Elliptical Aperture," Interaction Note 342, Air Force Weapons Laboratory, Kirtland Air Force Base, New Mexico, June 1978.

21. K. R. Umashankar and C. E. Baum, "Transient Electromagnetic Characterization of Arbitrary Conducting Bodies Through an Aperture-Perforated Conducting Screen," Interaction Note 343, Air Force Weapons Laboratory, Kirtland Air Force Base, New Mexico, March 1978.

22. D. B. Seidel, D. G. Dudley and C. M. Butler, "Aperture Excitation of a Wire in a Rectangular Cavity," Interaction Note 345, Air Force Weapons Laboratory, Kirtland Air Force Base, New Mexico, June 1977.

23. H. J. Fletcher and A. Harrison, "Diffraction Through a Circular Aperture in a Screen Separating Two Different Media," Interaction Note 352, prepared by Eyring Research Institute, December 1978.

24. S. Shenfeld, "Coupling Impedance of Cylindrical Tubes," IEEE Transactions on Electromagnetic Compatibility, Vol. EMC-14, No. 1, February 1972.

25. R. Holland, "Threde: A Free-Field EMP Coupling and Scattering Code," *IEEE Transactions on Nuclear Science*, Vol. NS-24, No. 6, December 1977.

26. K. S. Yee, "Numerical Solution of Initial Boundary Value Problems Involving Maxwell's Equations in Isotropic Media," *IEEE Transactions on Antennas and Propagation*, Vol. AP-14, No. 3, May 1966.

27. K. F. Casey, "Advanced Composite Materials and Electromagnetic Shielding," *IEEE 1978 International Symposium on Electromagnetic Compatibility*, June 1978.

28. R. A. Perala, K. M. Lee, and R. B. Cook, "EMP Coupling to a Composite Aircraft," *IEEE 1978 International Symposium on Electromagnetic Compatibility*, June 1978.

29. K. S. Kunz and K. M. Lee, "A Three-Dimensional Finite-Difference Solution of the External Response of an Aircraft to a Complex Transient EM Environment: Part I - The Method and its Implementation," *IEEE Transactions on Electromagnetic Compatibility*, Vol. EMC-20, No. 2, May 1978.

30. B. J. Wallace, R. T. Zeitler, R. H. Roberts, B. R. Smith and K. G. Wiles, *Composite Forward Fuselage Systems Integration*, Vol. I, Final Report prepared by General Dynamics Corporation for Air Force Flight Dynamics Laboratory (FBC) Wright-Patterson Air Force Base under Contract F33615-76-C-5439, AFFDL-TR-78-110, September 1978.

31. J. C. Burrows and A. J. Ludwig, *Composite Forward Fuselage Systems Integration*, Vol. II, Final Report prepared by General Dynamics Corporation for Air Force Flight Dynamics Laboratory (FBC) Wright-Patterson Air Force Base under Contract F33615-76-C-5439, AFFDL-TR-78-110, September 1978.

32. F. J. Darms, Jr., J. W. Haffner and E. S. Hughes, *Advanced Composites Equipment Support Module*, prepared by Rockwell International Corp. for Air Force Systems Command, Wright-Patterson Air Force Base under Contract F33615-77-C-5264, AFFDL-TR-78-125, September 1978.

33. C. H. Bixler, *Advanced Composite Equipment Support Module*, prepared by General Electric Space Division for Air Force Systems Command, Wright-Patterson Air Force Base under Contract F33615-77-C-5213, AFFDL-TR-78-132, September 1978.

34. K. M. Lee, R. A. Perala and R. B. Cook, *Induced Effects of Lightning on the Advanced Design Composite Aircraft*, prepared by Mission Research Corporation for Grumman Aerospace Corporation under Contract F33615-77-C-5169, AMRC-R-137, July 1978.

35. D. F. Strawe and L. D. Piszker, *Investigation of Penetration of Electromagnetic Energy Through Joints in Advanced Composite Structures*, Interim Report prepared by The Boeing Company for Naval Air Systems Command, D180-25240-1, April 1979.

36. Lightning Protection Criteria Document, prepared by National Aeronautics and Space Administration, Lyndon B. Johnson Space Center, JSC-07636, Revision A, November 1975.

37. T. J. Kalafarski, Electromagnetic Compatibility Plan for E-4B Phase 1B-2, prepared by The Boeing Company under Contract F19628-74-C-0127, D226-20158-1, August 1974.

38. T. K. Wu and L. L. Tsai, "Shielding Properties of Thick Conducting Cylindrical Shells with an Obliquely Incident Plane Wave," IEEE Transactions on Electromagnetic Compatibility, August 1975.

39. T. K. Wu and L. L. Tsai, "Time Domain Shielding Properties of Conducting Cylindrical Shells," IEEE Transactions on Electromagnetic Compatibility, August 1975.

40. T. K. Wu and L. L. Tsai, "Low-Frequency Shielding Properties of Conducting Cylindrical Shells of Arbitrary Cross Section," IEEE Transactions on Electromagnetic Compatibility, Vol. EMC-20, No. 2, May 1978.

41. K. S. H. Lee and G. Bedrosian, "Diffusive Electromagnetic Penetration into Metallic Enclosures," IEEE Transactions on Antennas and Propagation, Vol. AP-27, No. 2, March 1979.

42. F. A. Fisher and J. A. Plumer, Lightning Protection of Aircraft, prepared by the General Electric Company for NASA Lewis Research Center, NASA Reference Publication 1008, October 1977.

43. F. Force, P. Geren, D. Strawe, and A. Schmidt, Investigation of Effects of Electromagnetic Energy on Advanced Composite Aircraft Structures and Their Associated Avionic/Electrical Equipment, Phase II, Vol. 1, prepared by the Boeing Company for Naval Air Systems Command under Contract N00019-76-C-0497, Final Report D180-20186-4, September 1977.

44. R. B. Cook and R. A. Perala, Coupling of Lightning Stroke Currents to F-18 Balanced Twisted Shielded Pair Cables, prepared by Electro Magnetic Applications, Inc. for the Naval Air Systems Command, March 1979.

45. G. Bedrosian and K. S. H. Lee, "EMP Penetration Through Metal Skin Panels and Into Aircraft Cavities," Air Force Weapons Laboratory Interaction Note 314, Kirtland Air Force Base, New Mexico, August 1976.

TRANSMISSION LINES

1. C. R. Paul, Applications of Multiconductor Transmission Line Theory To The Prediction of Cable Coupling, Volume I: "Multiconductor Transmission Line Theory," Final Report prepared by University of Kentucky for Rome Air Development Center under Contract F30602-72-C-0418, RADC-TR-76-101 (AD-A025 028), April 1976.

2. A. E. Feather and C. R. Paul, <u>Applications of Multiconductor Transmission Line Theory To The Prediction of Cable Coupling</u>, Volume II: "Computation of the Capacitance Matrices for Ribbon Cables," Final Report prepared by University of Kentucky for Rome Air Development Center under Contract F30602-72-C-0418, RADC-TR-76-101 (AD-A025 029), April 1976.

3. C. R. Paul, <u>Applications of Multiconductor Transmission Line Theory To The Prediction of Cable Coupling</u>, Volume III: "Prediction of Crosstalk in Random Cable Bundles," Final Report prepared by University of Kentucky for Rome Air Development Center under Contract F30602-75-C-0118, RADC-TR-76-101 (AD-A038 316), February 1977.

4. C. R. Paul, <u>Applications of Multiconductor Transmission Line Theory To The Prediction of Cable Coupling</u>, Volume IV: "Prediction of Crosstalk in Ribbon Cables," Final Report prepared by University of Kentucky for Rome Air Development Center under Contract F30602-75-C-0118, RADC-TR-76-101 (AD-A053 548), February 1978.

5. J. W. McKnight and C. R. Paul, <u>Applications of Multiconductor Transmission Line Theory To The Prediction of Cable Coupling</u>, Volume V: "Prediction of Crosstalk Involving Twisted Wire Pairs," Final Report prepared by University of Kentucky for Rome Air Development Center under Contract F30602-75-C-0118, RADC-TR-76-101 (AD-A053 559), February 1978.

6. C. R. Paul, <u>Applications of Multiconductor Transmission Line Theory To The Prediction of Cable Coupling</u>, Volume VI: "A Digital Computer Program for Determining Terminal Currents Induced in a Multiconductor Transmission Line by an Incident Electromagnetic Field," Final Report Prepared by University of Kentucky for Rome Air Development Center under Contract F30602-75-C-0118, RADC-TR-76-101 (AD-A053 560), February 1978.

7. R. A. Perala and T. F. Ezell, <u>Engineering Design Guidlines for EMP Hardening of Naval Missiles and Airplanes</u>, prepared by Mission Research Corporation for Naval Ordance Laboratory under Contract N60921-73-C-0033, AMRC-R-17 (AD 917 958), December 1973.

8. J. R. Baird and J. E. Shaunfield, <u>Wideband Fiber Optic Data links</u>, Final Report prepared by Spectronics, Inc. for Air Force Avionics Laboratory, Wright-Patterson Air Force Base under Contract F33615-74-C-1160, AFAL-TR-77-55, October 1977.

9. <u>Electromagnetic Pulse Handbook for Missiles and Aircraft In Flight</u>, prepared by Sandia Laboratories for Air Force Weapons Laboratory under Contract F29601-72-C-0087, AFWL-TR-73-68 (AD-919 395), September 1972.

10. <u>Lightning Analysis for Aircraft Design Workshop</u>, prepared by Naval Air Systems Command, July 1978.

11. E.F. Vance, <u>Coupling to Cables</u>, DNA Handbook Revision, Chapter II, prepared by Stanford Research Institute for Harry Diamond Laboratories under Contract DAAG39-74-C-0086, December 1974.

12. <u>Engineering Design Handbook Electromagnetic Compatibility</u>, prepared by Headquarters US Army Materiel Development and Readiness Command, DARCOM-P 706-410, March 1977.

13. D. Kajfez, "Excitation of a Terminated TEM Transmission," Interaction Note 215, Air Force Weapons Laboratory, Kirtland Air Force Base, New Mexico, June 1974.

14. F.M. Tesche, M.A. Morgan, and B.H. Fishbine, "Evaluation of Present Internal EMP Interaction Technology: Description of Needed Improvements," Interaction Note 264, October 1975.

15. K.R. Umashankar and J.R. Wait, "Electromagnetic Coupling to an Infinite Cable Placed Behind a Slot Perforated Screen," Interaction Note 330, Air Force Weapons Laboratory, Kirtland Air Force Base, New Mexico, June 1977.

16. D. Kajfez and D.R. Wilton, "Small Aperture on a Multiconductor Transmission Line Filled with Inhomogeneous Dielectrics," Interaction Note 347, prepared by University of Mississippi, November 1977.

17. C.D. Taylor and J.P. Castillo, "On the Electromagnetic Field Excitation of Unshielded Multiconductor Cables," Interaction Note 348, Air Force Weapons Laboratory, Kirtland Air Force Base, New Mexico, January 1978.

18. D.V. Giri, S.K. Chang, and F.M. Tesche, "A Coupling Model for a Pair of Skewed Transmission Lines," Interaction Note 349, prepared by Science Applications, Inc., September 1978.

19. F.M. Tesche, T.K. Lie, S.K. Chang, and D.V. Giri, "Field Excitation of Milticonductor Transmission Lines," Interaction Note 351, prepared by LuTech, Inc., September 1978.

20. R.F. Hess, "Properties of Induced Transients Associated with EM Fields Produced by Lightning or Other Relatively Slow Rise-Time EMP", <u>IEEE 1978 International Symposium on Electromagnetic Compatibility</u>, June 1978.

21. R.F. Hess, "EMP Coupling Analysis Using the Freuqency (Transfer Function) Method with the SCEPTRE Computer Program," <u>IEEE Transactions on Electromagnetic Compatibility</u>, August 1975.

22. <u>Lightning Protection Criteria Document</u>, prepared by National Aeronautics and Space Administration, Lyndon B. Johnson Space Center, JSC-07636, Revision A, November 1975.

10. *Lightning Analysis for Aircraft Design Workshop*, prepared by Naval Ocean Systems Center, July 1978.

11. E. F. Vance, *Coupling to Cables*, DNA Handbook Revision, Chapter II, prepared by Stanford Research Institute for Harry Diamond Laboratories under Contract DAAG39-74-C-0086, December 1974.

12. *Engineering Design Handbook Electromagnetic Compatibility*, prepared by Headquarters US Army Material Development and Readiness Command, DARCOM-P 706-410, March 1977.

13. D. Kajfez, "Excitation of a Terminated TEM Transmission," Interaction Note 215, Air Force Weapons Laboratory, Kirtland Air Force Base, New Mexico, June 1974.

14. F. M. Tesche, M. A. Morgan and B. H. Fishbine, "Evaluation of Present Internal EMP Interaction Technology: Description of Needed Improvements," Interaction Note 264, October 1975.

15. K. R. Umashankar and J. R. Wait, "Electromagnetic Coupling to an Infinite Cable Placed Behind a Slot Perforated Screen," Interaction Note 330, Air Force Weapons Laboratory, Kirtland Air Force Base, New Mexico, June 1977.

16. D. Kajfez and D. R. Wilton, "Small Aperture on a Multiconductor Transmission Line Filled with Inhomogeneous Dielectrics," Interaction Note 347, prepared by University of Mississippi, November 1977.

17. C. D. Taylor and J. P. Castillo, "On the Electromagnetic Field Excitation of Unshielded Multiconductor Cables," Interaction Note 348, Air Force Weapons Laboratory, Kirtland Air Force Base, New Mexico, January 1978.

18. D. V. Giri, S. K. Chang and F. M. Tesche, "A Coupling Model for a Pair of Skewed Transmission Lines," Interaction Note 349, prepared by Science Applications, Inc., September 1978.

19. F. M. Tesche, T. K. Lie, S. K. Chang and D. V. Giri, "Field Excitation of Milticonductor Transmission Lines," Interaction Note 351, prepared by LuTech, Inc., September 1978.

20. R. F. Hess, "Properties of Induced Transients Associated with EM Fields Produced by Lightning or Other Relatively Slow Rise-Time EMP", *IEEE 1978 International Symposium on Electromagnetic Compatibility*, June 1978.

21. R. F. Hess, "EMP Coupling Analysis Using the Freuqency (Transfer Function) Method with the SCEPTRE Computer Program," *IEEE Transactions on Electromagnetic Compatibility*, August 1975.

22. *Lightning Protection Criteria Document*, prepared by National Aeronautics and Space Administration, Lyndon B. Johnson Space Center, JSC-07636, Revision A, November 1975.

23. T. J. Kalafarski, _Electromagnetic Compatibility Plan for E-4B Phase 1B-2_, prepared by The Boeing Company under Contract F19628-74-C-0127, D226-20158-1, August 1974.

24. W. H. Haynes and C. L. Wilkerson, "Investigation of a Dipole Model for Transient Analysis of Electromagnetic Field Coupling into Long Cables," _IEEE Transactions on Electromagnetic Compatibility_, Vol. EMC-12, No. 3, August 1970.

25. C. D. Taylor and J. P. Castillo, "On the Electromagnetic Field Excitation of Unshielded Multiconductor Cables," Interaction Note 348, Air Force Weapons Laboratory, Kirtland Air Force Base, January 1978.

26. K. S. H. Lee, "Two Parallel Terminated Conductors in External Fields," _IEEE Transactions on Electromagnetic Compatibility_, Vol. EMC-20, No. 2, May 1978.

27. W. S. McCormick, "The Analysis and Identification of Flux-Induced Voltage Transients on Low-Loss Transmission Lines with Application to the Lightning-Transient-Analysis (LTA) Problem," _IEEE Transactions on Electromagnetic Compatibility_, Vol. EMC-21, No. 1, February 1979.

28. C. D. Taylor and J. P. Castillo, "On Electromagnetic-Field Excitation of Unshielded Multiconductor Cables," _IEEE Transactions on Electromagnetic Compatibility_, Vol. EMC-20, No. 4, November 1978.

29. E. F. Vance, "Shielding Effectiveness of Braided-Wire Shields," _IEEE Transactions on Electromagnetic Compatibility_, Vol. EMC-17, No. 2, May 1975.

30. W. S. McCormick and K. J. Maxwell, "Identification of Voltage Transients on Aircraft Cabling Under LTA Excitation," _IEEE Transactions on Aerospace and Electronic Systems_, Vol. AES-15, No. 3, May 1979.

31. W. D. McKerchar, "Electromagnetic Compatibility of High Density Wiring Installations by Design ro Retrofit," _IEEE Transactions on Electromagnetic Compatibility_, March 1965.

32. R. W. P. Kinh and C. W. Harrison, Jr., "Excitation of an External Terminated Longitudinal Conductor on a Rocket by a Transverse Electromagnetic Field," _IEEE Transactions on Electromagnetic Compatibility_, Vol. EMC-14, No. 1, February 1972.

33. C. W. Harrison, Jr., "Bounds on the Load Currents of Exposed One- and Two-Conductor Transmission Lines Electromagnetically Coupled to a Rocket," _IEEE Transactions on Electromagnetic Compatibility_, Vol. EMC-14, No. 1, February 1972.

34. C. R. Paul, "Efficient Numerical Computation of the Frequency Response of Cables Illuminated by an Electromagnetic Field," _IEEE Transactions on Microwave Theory and Techniques_, April 1974.

35. A. K. Agrawal, K. M. Lee, L. D. Scott and H. M. Fowles, "Experimental Characterization of Multiconductor Transmission Lines in the Frequency Domain," _IEEE Transactions on Electromagnetic Compatibility_, Vol. EMC-21, No. 1, February 1979.

36. S. Frankel, "Terminal Response of Braided-Shield Cables to External Monochromatic Electromagnetic Fields," _IEEE Transactions on Electromagnetic Compatibility_, Vol. EMC-16, No. 1, February 1974.

37. A. A. Smith, Jr., _Coupling of External Electromagnetic Fields to Transmission Lines_, John Wiley and Sons, New York, 1971.

38. H. J. Price and A. K. Agrawal, "The Response of a Transmission Line Illuminated by Lightning-Induced Electromagnetic Fields," Lightning Phenomenology Note 1, June 1979.

39. R. J. Mohr, "Coupling Between Open and Shielded Wire Lines Over a Ground Plane," _IEEE Transactions on Electromagnetic Compatibility_, Vol. EMC-9, No. 2, September 1967.

41. J. R. Moser, "Low-Frequency Shielding of a Circular Loop Electromagnetic Field Source," _IEEE Transactions on Electromagnetic Compatibility_, Vol. EMC-9, No. 1, March 1967.

42. K. S. H. Lee and C. E. Baum, "Application of Model Analysis to Braided-Shield Cables," _IEEE Transactions on Electromagnetic Compatibility_, Vol. EMC-17, No. 3, August 1975.

43. R. Force, P. Geren, D. Strawe, and A. Schmidt, _Investigation of Effects of Electromagnetic Energy on Advanced Composite Aircraft Structures and Their Associated Avionic/Electrical Equipment_, Phase II, Vol. 1, prepared by the Boeing Company for Naval Air Systems Command, Final Report, September 1977.

44. R. B. Cook and R. A. Perala, _Coupling of Lightning Stroke Currents to F-18 Balanced Twisted Shielded Pair Cables_, prepared by Electro Magnetic Applications, Inc. for the Naval Air Systems Command, March 1979.

DEVICE SUSCEPTIBILITY

1. R. A. Perala and T. F. Ezell, _Engineering Design Guidelines for EMP Hardening of Naval Missiles and Airplanes_, prepared by Mission Research Corporation for Naval Ordance Laboratory under Contract N60921-73-C-0033, AMRC-R-17 (AD 917 958), December 1973.

2. B.P. Gage, _EMP Electronic Analysis Handbook_, Final Report prepared by the Boeing Company for U.S. Air Force Weapons Laboratory under Contract F29601-72-C-0028, AFWL-TR-74-59 (AD-918 275), May 1973.

3. _Electromagnetic Pulse Handbook for Missiles and Aircraft In Flight_, prepared by Sandia Laboratories for Air Force Weapons Laboratory under Contract F29601-72-C-0087, AFWL-TR-73-68 (AD-919 395), September 1972.

4. D.C. Wunsch, R.L. Cline, and G.R. Case, _Semiconductor Vulnerability Phase II Report Theoretical Estimates of Failure Levels of Selected Semiconductor Diodes and Transistors_, prepared by Braddock, Dunn and McDonald, Inc. for Air Force Special Weapons Center under Contracts F29601-69-C-0132 and F29601-70-C-0019, AD 878 091, August 1970.

5. D.C. Wunsch and L. Marzitelli, _Semiconductor and Nonsemiconductor Damage Study_, Volume 1, Final Report prepared by Braddock, Dunn and McDonald, Inc. for the U.S. Army Mobility Equipment Research and Development Center under Contract DAAK02-67-C-0168, AD 745 926, April 1969.

6. B.P. Gage, _EMP Electronic Design Handbook_, prepared by the Boeing Company for U.S. Air Force Weapons Laboratory under Contract F29601-72-C-0028, AD 918 277, WL-TR-74-58, April 1973.

7. _Lightning Analysis for Aircraft Design Workshop_, prepared by Naval Air Systems Command, July 1978.

8. _Engineering Design Handbook Electromagnetic Compatibility_, prepared by Headquarters US Army Materiel Development and Readiness Command, DARCOM-P 706-410, March 1977.

9. C.E. Larson and J.M. Roe, "A Modified Ebers'Moll Transistor Model for RF Interference Analysis," _IEEE EMC Symposium_, Atlanta, GA, June 1978.

10. D.C. Wunsch and R.R. Bell, "Determination of Threshold Failure Levels of Semiconductor Diodes and Transistors due to Pulse Voltages," _IEEE Transactions on Nuclear Science_, Vol. NS-15, No. 6, December 1968.

11. _Integrated Circuit Electromagnetic Susceptibility Investigation, Phase III_, IC Susceptibility Handbook - Draft 1, prepared by McDonnell Douglas Astronautics Company-East for US Naval Surface Weapons Center under Contract N60921-76-C-A030, MDC E1515, June 1976.

12. _Integrated Circuit Electromagnetic Susceptibility Investigation, Phase III_, Technical Report No. 1, prepared by McDonnell Douglas Astronautics Company-East for US Naval Surface Weapons Center under Contract N60921-76-C-A030, MDC E1513, June 1976.

13. <u>Integrated Circuit Electromagnetic Susceptibility Handbook</u>, Integrated Circuit Electromagnetic Susceptibility Investigation-Phase III, prepared by McDonnell Douglas Astronautics Company for US Naval Surface Weapons Center under Contract N60921-76-C-A030, MDC E1929, August 1978.

14. F.A. Fisher and J.A. Plumer, <u>Lightning Protection of Aircraft</u>, prepared by the General Electric Company for NASA Lewis Research Center, NASA Reference Pulbication 1008, October 1977.

15. R. Force, P. Geren, D. Strawe, and A. Schmidt, <u>Investigation of Effects of Electromagnetic Energy on Advanced Composite Aircraft Structures and Their Associated Avionic/Electrical Equipment</u>, Phase II, Vol. 1, prepared by the Boeing Company for Naval Air Systems Command, Final Report, September 1977.

MISCELLANEOUS

1. W.J. Gajda, <u>A Fundamental Study of the Electromagnetic Properties of Advanced Composite Materials</u>, Phase Report prepared by Syracuse University for Rome Air Development Center under Contract F03062-75-C-0121, RADC-TR-78-158, July 1978.

2. K. Homberg, K. Effelsberg, and C. Kontje, <u>The Investigations on the Generation of Electrostatic Charges During Fueling of Aircraft with High Fuel Flow Rates</u>, prepared by the German Air Force, October 1975.

3. J.S. Yu, C-L. J. Chen, and C.E. Baum, "Multipole Radiations: Formulation and Evaluation for Small EMP Simulators," Sensor and Simulation Note 243, prepared by Dikewood Industries, Inc. and Air Force Weapons Laboratory, July 1978.

4. V.R. Latorre and L.R. Spogen, Jr., <u>Ingredients of an EMP Protection Engineering Methodology</u>, prepared by Lawrence Livermore Laboratory for the Defense Nuclear Agency under Subtask R99QAXEC091, PEM-57, February 1977.

5. G.A. Van Fo Fy, <u>Electro- and Magnetostatics of Reinforced Polymers</u>, translated from Mekhanika Polimerov, Vol. 4, No. 6, November-December 1968.

6. G.A. Van Fo Fy, <u>Electromangetic Field in Fiber Composites</u>, translated from Composite Fibrous Materials, Kiev, 1970, as requested by Wright-Patterson Air Force Base.

7. G.A. Van Fo Fy, <u>Theory of Reinforced Materials with Coatings</u>, Kiev Naudona Press, 1971.

8. <u>Electrostatic Stress Effects on Graphite Composite Materials</u>, Final Report prepared by The Truax Company for NASC under Contract N00019-76-C-0413, TRX 78-2, March 1978.

9. F.M. Greene, <u>Development of Electric Magnetic Near-Field Probes</u>, prepared by US Department of Commerce, National Bureau of Standards, January 1975.

10. M.F. Amateau, W.C. Harrigan, Jr., and E.G. Kendall, <u>Mechanical Properties of Aluminum Alloy-Graphite Fiber Composites</u>, prepared by the Aerospace Corporation for Space and Missile Systems Organization, Air Force Systems Command under Contract F04701-74-C-0075, SAMSO-TR-75-55, February 1975.

11. <u>Graphite Materials</u>, prepared by Hercules, Incorporated, Systems Group, April 1976.

SRC TN 79-395
September 1979

SUMMARY OF GRUMMAN PROTECTION OPTIMIZATION FOR ADVANCED COMPOSITE STRUCTURES PROGRAM

by

R. Rudolph

Prepared for

Office of Naval Research
Arlington, Virginia   22217

File No. DO165

1.0 INTRODUCTION AND OVERVIEW

This report summarizes work being done by the Grumman Aerospace Corporation (GAC) for the Advanced Composite Structures ADP, Air Force Flight Dynamics Laboratory, Wright-Patterson Air Force Base, under Contract F33615-77-C-5169. The GAC program is a 30-month technical effort entitled "Protection Optimization For Advanced Composite Structures" and is reported in eight quarterly progress reports (so far) dating from 15 September 1977. The program objective is to develop practical optimized and integrated protection and shielding methodologies for the protection of composite aircraft against multiple threats. Threats addressed included lightning (direct and indirect), nuclear electromagnetic pulse (NEMP), static electrification, electromagnetic interference (EMI), and high energy lasers (HEL). We will focus on the investigation of shielding effectiveness against electromagnetic radiation in the 10 kHz to 10 GHz frequency range.

Composite materials, such as graphite/epoxy (Gr/Ep, described in the following text) have a much lower conductivity than the material of typical aircraft (air passage) structures (conductivity is three orders of magnitude less than that of aluminum). As a result, they must be given conducting coverings to help adequately shield the aircraft interior against EMI. These coverings were also evaluated against lightning, NEMP, and HEL, and thus are called protection techniques or systems.

In evaluating and developing protection systems for shielding composite structures, a key principle to follow is maintainance of maximum electrical conductivity. Any conductor gaps may allow electromagnetic radiation to leak through, rather than conducting it away to the rest of the structure surface. Keeping this in mind, the major results of the GAC program thus far are:

- A Gr/Ep panel edge-treatment method was developed to ensure maximum ohmic electrical contact between the panel and the test fixture.

- Conductivity testing showed Gr/Ep laminate conductivity to be a linear function of the equivalent 0° orientation laminate percentage.

- A test fixture was built which measures total shielding effectiveness of test specimens.

- The plain panel test results fit the theoretical curve for magnetic shielding effectiveness versus frequency. (Close agreement was not achieved in the E-field and plane-wave cases.)

- Aluminum flame spray was found to have the greatest shielding effectiveness of all surface protection systems tested, yielding shielding effectiveness improvement over bare Gr/Ep by as much as 25 dB.

- Contrary to expectations, 24-ply Gr/Ep panels with aluminum mesh protection performed better in magnetic fields than 12-ply panels with the same protection. It was conjectured that this was due to poor electrical contact between the mesh and the 12-ply panel.

- Various fastener and doubler conditions on joined panels were tested. It was found that Hi-Loks performed about as well as stress-wave rivets, that loosening fasteners decreases the shielding effectiveness (by as much as 25 dB), but that removing fasteners is sometimes better than loosening them! This happens because at some frequencies, the loose fasteners act as independent antennas, reradiating energy through the panel.

- A secondary flame spray method was developed to ensure conductive continuity between the surface protection systems on the joined panels.

- In the access door tests, the flame-sprayed panel with the flame-sprayed door showed an improvement of 8 dB over even the plain flame sprayed panel at some frequencies, although usually the door assembly produced 20 dB less shielding.

- The latest access door design (providing flame spray to flame spray contact for electrical continuity) had not yet been tested by the period of the eighth quarterly report.

This summary, then, discusses the following:

- The Composite Material (Graphite/Epoxy)
- Conductivity of Graphite/Epoxy Laminates
- Shielding Effectiveness Measurement Fixture
- Method of Measuring Shielding Effectiveness
- Plain Panels
- Joined Panels
- Access Doors

A-3

2.0 THE COMPOSITE MATERIAL (GRAPHITE/EPOXY)

Graphite/epoxy (Gr/Ep) was selected as the advanced composite material to be investigated for the following reasons:

* Low current and forecasted cost per pound
* Ability to be molded into complex shapes
* Use on mold line surfaces that receive external threats

Hercules 3501-5A/AS-1 Gr/Ep prepreg per GAC Material Specification GM30/2A was used. This material is resin treated, parallel-in-plane, collimated, continuous fiber pre-impregnated tape, capable of being molded with low pressure (100 psi maximum) laminating methods. (For Gr/Ep, a typical fiber diameter should be about 0.3 mil, with typical ply thickness of about 5 mil.)

3.0 CONDUCTIVITY OF GRAPHITE/EPOXY LAMINATES

The room temperature conductivity of Gr/Ep laminates of the 0°/90°/±45° family (see the following text) was determined from resistance measurements of panels performed at GAC and other data (see "The Second Quarterly Progress Report", hereafter QR II). The basic assumption made is that the laminate is electrically homogeneous and thus is described by a single bulk conductivity number.

Resistance measurements were performed on 12-ply Gr/Ep laminated panels with individual plies oriented so that their graphite fibers pointed in the 0°, 90° or ± 45° direction. The specimens had a fiber volume fraction of 62% and had dimensions of 20 x 1 x 0.063 in., the last being the thickness of the laminate stack. Measurements were made using a Hewlett Packard Model 4328A milliohm meter and thin probing electrodes applied to specimens edge treated for ohmic electrical contact.

A-4

The edge treatment method evolved through three stages. The initial method, involving aluminum flame spray 1/2 in. on each end plus adjacent edges) of cured laminates, was inadequate due to insufficient adherence of the flame spray to the cured laminate plus eventual galvanic aluminum/graphite corrosion. The second method exposed the carbon fibers at the specimen ends by removing the resin with a solution of hot sulfuric acid or by carbonization. After resin removal, the exposed fibers were coated with a silver-filled epoxy resin and covered with a 1 in. x 1 in. aluminum foil electrical contact pad. This method yielded excellent results, but was slow and not desirable as an electrical connection method for aircraft structures. Finally, using the good data from the second edge treatment method, a production-oriented refinement was achieved; namely, a chamfer (i.e., bevel) on the order of three to four times the thickness from the edge, in conjunction with silver-filled epoxy and aluminum pads. Figure 1 shows the conductivities calculated from the resistance measurements (see QR II for the references). Note that conductivity in the 0° direction is a function of the equivalent 0° laminate (in percent) which is calculated by assuming that a ± 45° pair of plies is electrically equivalent to a single 0° ply and that the 90° plies do not contribute to the conductivity. Further, stacking sequence variations do not significantly affect the conductivity of the laminate.

4.0 SHIELDING EFFECTIVENESS MEASUREMENT FIXTURE

The shielding effectiveness measurement fixture is an all-welded aluminum fixture about 10 ft x 3 ft x 4 ft, divided into four vertical compartments. The transmitted signal is brought by coaxial cable from a shielded room to a transmitting antenna in one of the inner compartments. It then passes through a sample (e.g., Gr/Ep plate) mounted on an aperture in the wall between the inner and the adjacent outer compartment, where the receiving antenna is located. Finally, it is carried out of the fixture again by coaxial cable to the receiver. All apertures, both external and internal, were hardened by installing a 1/4 in. x 3/16 in. radio frequency (RF) metal gasket, Type 20-40118 (Technit Corporation), at a distance of 1/2 in. from the edge of the opening
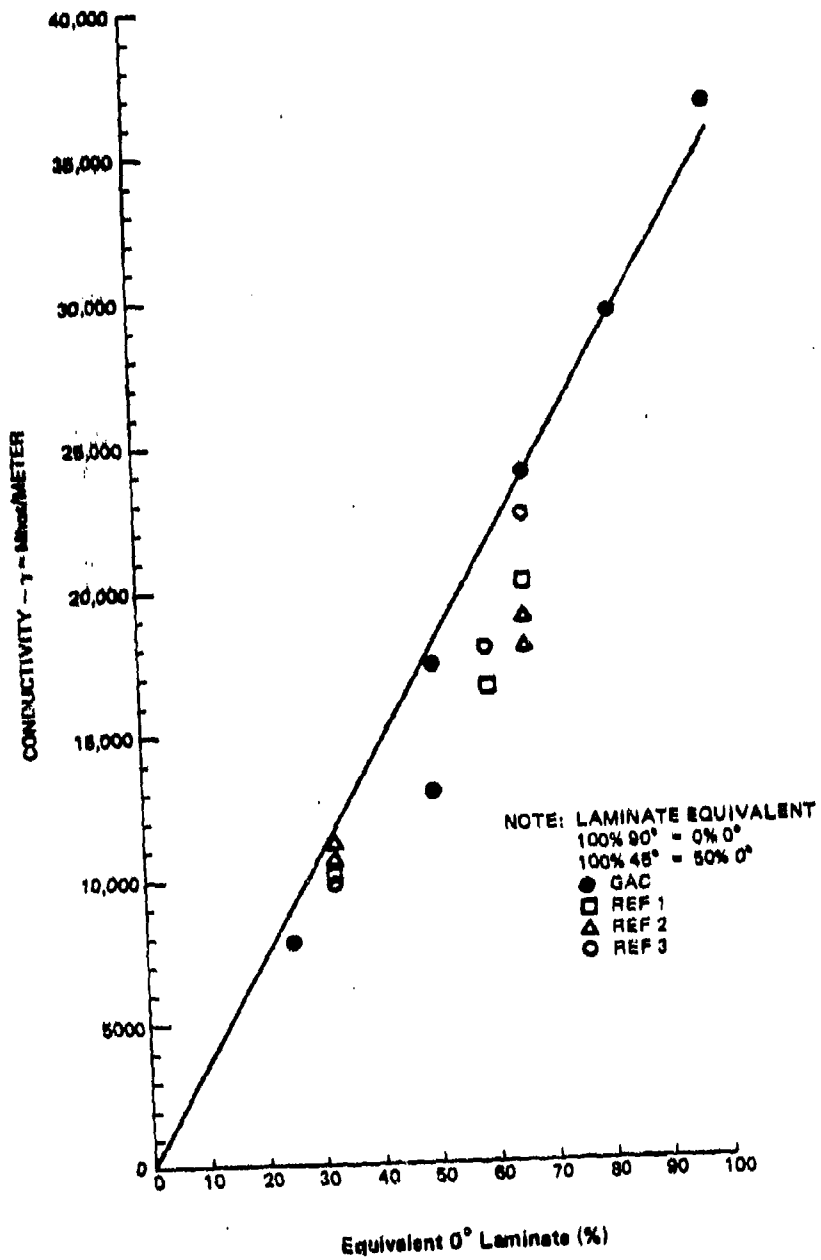
Figure 1. Relative Conductivity Values For Gr/Ep Laminates (QR II)

in a rigid recessed groove. The external doors (one on the side of each compartment) were fabricated by the Universal Shielding Corporation and are of the UQ904 type, which electrically seals the enclosure against RF leakage.

Each communicating wall in the fixture has a large aperture (24 in. x 36 in.) over which can be fit a 27 in. x 39 in. aluminum fixture plate with an additional small aperture (12 in. x 12 in). The panel and joint specimens (measuring 15 in. x 15 in.) are fitted over the small aperture, while the access door specimens (measuring, once again, 27 in. x 39 in.) are fitted over the large aperture. To ensure against RF leakage around the specimen edges the specimens were edge treated (see discussion of plain panels in the following text). They were then mounted so that the electrically continuous picture frame around the edge of the sample (resulting from the edge treatment) firmly contacted the RF gasket around the aperture. To accomplish this, a metal frame or pressure plate was installed over the sample and bolted to the mount (bolts 1 in. apart) to provide an even distribution of pressure on the sample, RF gasket, and aperture.

5.0 METHOD OF MEASURING SHIELDING EFFECTIVENESS

The method employed to measure shielding effectiveness is a two pair antenna system, using the above fixture. Shielding effectiveness is measured by first taking a reference reading in one pair of compartments with a naked aperture and then taking a measurement in the other identical pair of compartments with the sample mounted in the aperture. The difference in dBs of the two readings is the shielding effectiveness of the material under test.

Three types of fields were used: low impedance (H), high impedance (E), and plane waves above 60 MHz. To ensure true E and H near fields, the distance from the transmitting antenna to the sample was less than $\lambda/2\pi$ in. The same transmitting and receiving equipment was used for plane waves; however, in this case, the distances were greater than $\lambda/2\pi$ in. for electrically small antennas and $2D^2/\lambda$ for larger ones, where D is the largest dimension of the transmitting element. Tables 1 and 2 show the equipment list and measurement

Table 1. Shielding Effectiveness Measurement Equipment List (QR II)

FREQUENCY RANGE	TRANSMITTER	TRANS ANTENNA	RECEIVER	REC ANTENNA	TYPE OF FIELD
10 KHz TO 32 MHz	H.P. 205 AG SIG GEN	LOOP	SINGER NM-17/27	LOOP	LOW IMP (H)
10 KHz TO 32 MHz	H.P. 606 SIG GEN	ROD	NM-17/27	ROD	HIGH IMP (E)
32 MHz TO 200 MHz	PLUS I.F.I. 5000	LOOP	SINGER NM-37/57	LOOP	(H)
32 MHz TO 200 MHz	AND I.F.I. M402 PWR AMP	ROD	→	ROD	(E)
200 MHz TO 500 MHz	H.P. 608	LOOP		LOOP	(H)
200 MHz TO 500 MHz	SIG GEN AND H.P. 230 PWR AMP	ROD		ROD	(E)
500 MHz TO 1 GHz	H.P. 612	LOOP		LOOP	(H)
500 MHz TO 1 GHz	SIG GEN →	ROD	EMPIRE NF-112	ROD	(E)
1 GHz TO 2 GHz	H.P. 614 SIG GEN AND KELTEC LR605-10	LOOP		LOG PERIODIC	(H)
1 GHz TO 2 GHz		ROD			(E)
2 GHz TO 4 GHz	H.P. 616 SIG GEN AND H.P. 419C	LOOP			(H)
2 GHz TO 4 GHz		ROD			(E)
4 GHz TO 7.6 GHz	H.P. 618 SIG GEN AND H.P. 493A	LOOP			(H)
4 GHz TO 7.6 GHz		ROD			(E)
7.6 GHz TO 10 GHz	H.P. 620 SIG GEN AND H.P. 495A	LOOP			(H)
7.6 GHz TO 10 GHz		ROD			(E)

1110-022w

A-8

Table 2. H, E, and Plane-Wave Measurement Conditions (QR VII)

TYPE OF FIELD	TRANSMITTING ANTENNA (INCHES)	RECEIVING ANTENNA (INCHES)	FREQUENCY RANGE	DISTANCE FROM TRANSMITTING ANTENNA TO SAMPLE (INCHES)
H	3 (6 TURN SHIELDED LOOP)	3 (6 TURN SHIELDED LOOP)	0.014–30 MHz	3
H	3 (1 TURN SHIELDED LOOP)	3 (1 TURN SHIELDED LOOP)	30–200 MHz	3
H	1 (1 TURN LOOP)	1 (1 TURN LOOP)	1 GHz	1
H	1/8 (1 TURN LOOP)	1/8 (1 TURN LOOP)	10 GHz	1/8
E	36 (ROD)	36 (ROD EMPIRE VR-105)	0.014–0.15 MHz	3
E	36 (ROD)	36 (ROD EMPIRE VA-105)	0.15–30 MHz	3
E	1 (ROD)	1 (ROD)	1 GHz	1
E	1/8 (ROD)	1/8 (ROD)	10 GHz	1/8
PLANE-WAVE	3 (ROD)	3 (ROD)	100 MHz	32
PLANE-WAVE	1 (ROD)	1 (ROD)	1 GHz	12
PLANE-WAVE	POLARAD CA-X-HORN	1/8 (ROD)	10 GHz	12

0610-004W

conditions for the tests (except for a slight modification of measurement conditions for specimen numbers (S/Ns) 1 through 4).

Each pair of transmitting and receiving antennas was checked for equivalency to ensure that conditions are the same in each pair of compartments. This was done by setting up a field (E, H, or plane), placing a test antenna in that field, and then taking a reading with a field strength meter. If the readings compared to within 2 dB when a second antenna was substituted for the first, the two were considered equivalent.

The enclosure was checked for RF leaks and maximum measurement range of the equipment. A 1/8 in. aluminum panel was used in the sample chamber, with leaks being indicated by observing anything above the internal noise of the receiver when the system is switched to that chamber.

6.0 PLAIN PANELS

Two Gr/Ep laminates were examined, 12-ply and 24-ply thicknesses of the same type (17% 0°, 17% 90°, 66% ± 45°). Specifically, the 12-ply panels were denoted (2/2/8), indicating the number of plies in each of the orientations of the 0°/90°/± 45° family of composites. Similarly, the 24-ply panels were denoted (4/4/16).

The candidate surface protection system specimens were of the following types:

- Unprotected (bare) Gr/Ep laminates
- 120 x 120 grid aluminum mesh (0.010 in. thick) bonded and co-cured with Gr/Ep by an unsupported epoxy film adhesive (Reliabond 398U, 0.06 lb/ft^2)
- 200 x 200 grid aluminum mesh (0.005 in. thick) bonded and co-cured with Gr/Ep by an unsupported epoxy film adhesive (Reliabond 398U)

A-10

- Aluminum flame spray (4 to 6 mil) on 1 mil fiberglass/epoxy prepreg scrim co-cured with Gr/Ep laminates

- Hexcel XC484 aluminum coated conductive fiberglass/epoxy prepreg co-cured with Gr/Ep laminates

- Vapor deposited aluminum (3.0 to 5.0 x 10^{-6} in. thick) added to a bare Gr/Ep panel

- Vapor deposited aluminum (3.0 to 5.0 x 10^{-6} in. thick) added to an aluminum flame spray specimen (described above)

In addition, four panels manufactured by the Hexcel Corporation using their Thorstrand® material system, which utilizes an aluminized fiberglass (XC487/F155) with 1543/F155 fiberglass cloth, were also tested.

Table 3 details the test program for both plain and joined panels. The shielding effectiveness specimens were edge treated (in a modification of method three of the conductivity test) in order to provide intimate electrical contact with the graphite fibers. Each specimen was chamfered 3t x t/2 (where t is the panel thickness) on both sides, for all edges, creating a knife edge which effectively exposes six times the original fiber end cross sectional area. Then, for a distance of 1.5 in. on both sides around the periphery, the surface was coated with a thin continuous layer of silver-filled conductive epoxy. Finally, before the epoxy cured, a layer of 0.010 in. thick aluminum foil was applied again for a distance of 1.5 in. on both sides around the periphery, as was the epoxy. After two hours at 140°F, the epoxy had fully cured and was ready for drilling and mounting in the fixture.

Results of tests for the 2/2/8 Gr/Ep panels are shown in Figures 2 through 4. Included are curves calculated from a general shielding effectiveness equation (see QR III):

$$SE = A + R_1 + R_2 \tag{1}$$

where SE is the total shielding effectiveness in dB, A is the absorption power loss, R_1, is the reflection power loss of the boundaries of the shield, and

Table 3. Shielding Effectiveness Test Program (QR V)

	SPECIMEN NUMBER	TYPE OF PROTECTION	NO. OF PLIES	NO. OF TESTS	H-FIELD	E-FIELD	PLANE-WAVE
PLAIN PANELS	S/N 2-3 S/N 1	BARE	12 24*	2 1	x x	x	x
	S/N 8 S/N 8A	120 ALUMINUM MESH	 12	2 2	x x	x	x
	S/N 4 S/N 4A	120 ALUMINUM MESH	24	2 1	x x	x x	x x
	S/N 7 S/N 9	200 ALUMINUM MESH	12 24	1 1	x x		
	S/N 5 S/N 6	ALUMINUM FLAME SPRAY (4-6 MILS)	12 24	1 1	x x		
	S/N 10 S/N 11	ALUMINIZED FIBERGLASS	12 24	1 1	x x		
	S/N 12	VAPOR DEPOSITED ALUMINUM	12	1	x	x	x
	S/N 14	ALUMINUM FLAME SPRAY AND VAPOR DEPOSITED ALUMINUM	12	1	x	x	x
JOINED PANELS	S/N 2J1	BARE WITH HI-LOKS AND ALUM. DOUBLER VERTICAL JOINT	12	1	x	x	x
	S/N 3J1	BARE WITH STRESS RIVETS AND ALUM. DOUBLER, VERTICAL JOINT	12	1	x	x	x
	S/N 2J2	BARE WITH HI-LOKS AND 24 PLY GR/EP DOUBLER VERTICAL JOINT	12	5+	x	x	x
	————	BARE ALUM. WITH HI-LOKS AND ALUM. DOUBLER, VERTICAL JOINT	–	1	x	x	x
	S/N 2J3	BARE WITHOUT DOUBLER, FASTENERS AND LIQUID SHIM, VERT. JOINT	12	1	x	x	x
	S/N 2J4	BARE WITHOUT DOUBLER FASTENERS AND LIQUID SHIM, HORIZ. JOINT	12	1	x	x	x
	S/N 2J5	BARE WITH HI-LOKS AND 24 PLY GR/EP DOUBLER HORIZ. JOINT	12	1	x	x	x
	S/N 3J2	BARE WITH STRESS RIVETS AND ALUMINUM DOUBLER, HORIZ. JOINT	12	1	x	x	x
	S/N 5J1	ALUM. FLAME SPRAY HI-LOKS, ALUM. DOUBLER VERTICAL JOINT	12	1	x	x	x
	S/N 20J1	ALUM. FLAME SPRAY HI-LOKS, GR/EP DOUBLER VERTICAL JOINT	12	1	x	x	x
PLAIN HEXCEL PANELS	S/N 15	BARE	1	1	x	x	x
	S/N 16	BARE	2	1	x	x	x
	S/N 17	BARE	2	1	x	x	x
	S/N 18	BARE	4	1	x	x	x

* NOT EDGE TREATED, ALL OTHER SPECIMENS ARE EDGE TREATED.

+ TIGHT HI-LOKS, LOOSE HI-LOKS, NO MOUNTING BOLTS ON DOUBLER, AND NO DOUBLER

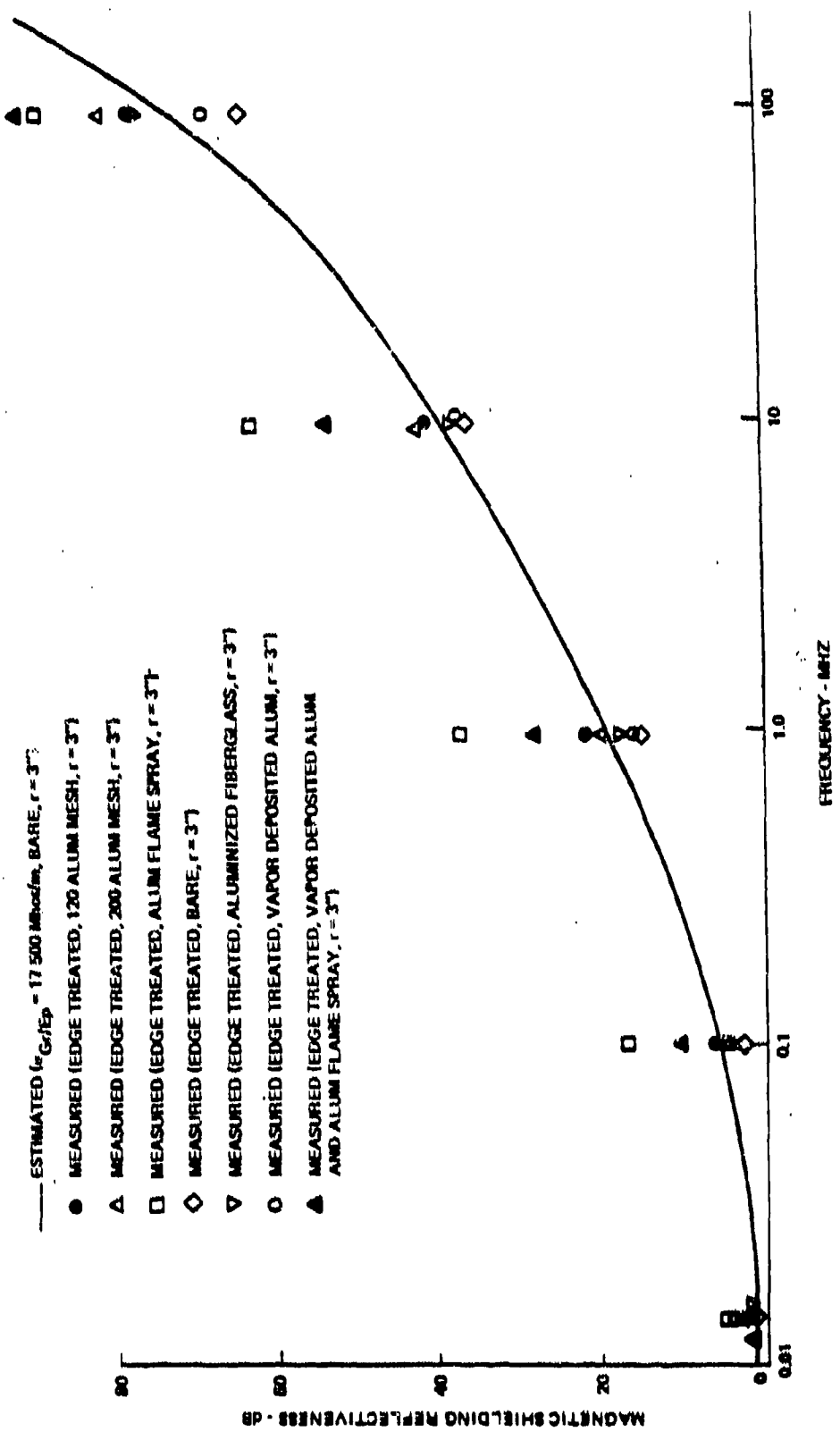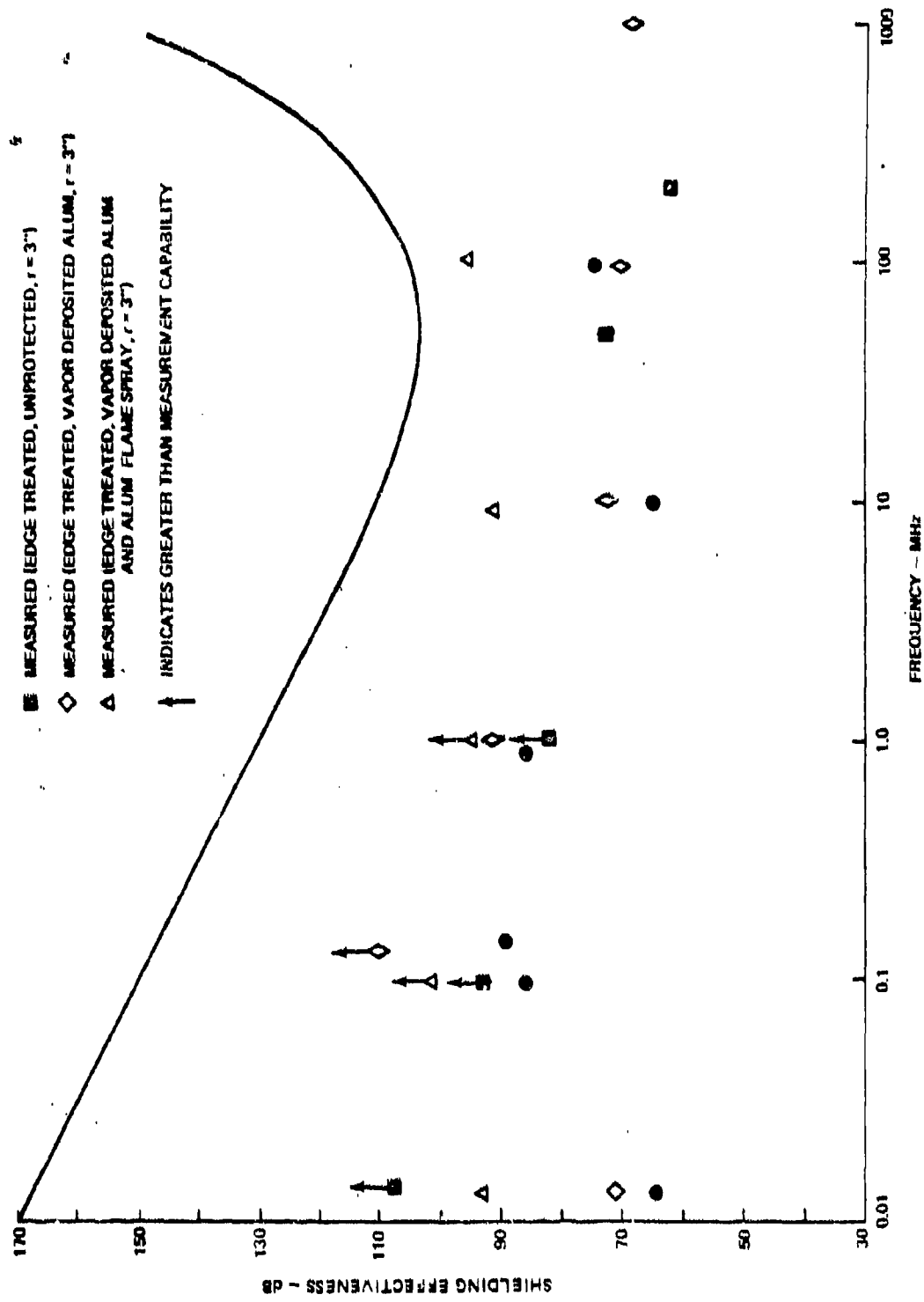Figure 2. Magnetic Shielding Effectivess for 2/2/8 Graphite/Epoxy Panel (QR V)

Figure 3. E-Field Shielding Effectiveness for 2/2/8 Graphite/Epoxy Panel (QR IV)
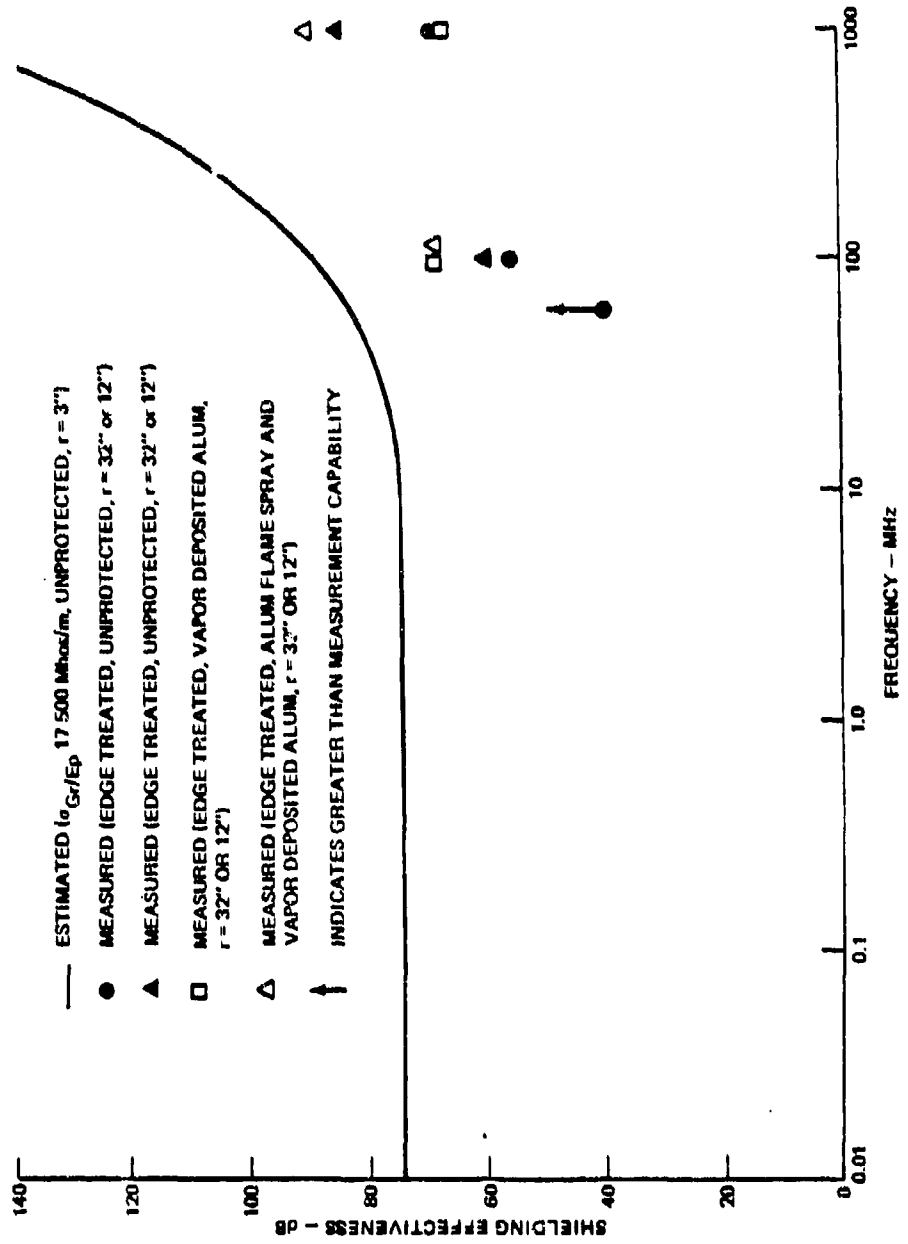
Figure 4. Plane-Wave Shielding Effectiveness for 2/2/8 Graphite/Epoxy Panel (QR V)

A-15

R_2 is the correction factor due to reflections from the far boundary of the shield.

More specifically, the absorption loss A is given by:

$$A = 3.338t \sqrt{\mu \sigma_R f} \qquad (2)$$

where f is the frequency in Hz, t is the thickness in inches, σ_R is the electrical conductivity of the material relative to copper, and μ is the permeability of the material relative to space. The total reflection power loss, R_1, has a different form for each field (H, E, or plane wave) and further depends on f, σ_R, μ, and r (the distance from the source to the shield in inches). The correction term, R_2, has the same form for all fields and depends on f, σ_R, μ, and and Z_s (the intrinsic impedance of the shield in vector form in ohms), and Z_w (the incident wave impendance in vector form in ohms).

For the 2/2/8 Gr/Ep layup (coresponding to 50% equivalent 0° laminate), Figure 1 yields a conductivity of 17,500 mhos/m (i.e., $\sigma_R = 3 \times 10^{-4}$). The same holds for the 4/4/8 Gr/Ep layup. The relative permeability, μ, is taken to be 1. From Figure 2, it will be noted that the bare Gr/Ep shielding effectiveness data fall within 3 dB below the calculated curve for from 0.01 to 10 MHz, falling to 10 dB below at 100 MHz. Therefore, the agreement is good in the magnetic field case. However, as seen from Figures 3 and 4 the data for bare 12-ply plate fall at least 30 dB below the curve for the E-field and plane wave cases. This discrepancy has not been resolved.

The same qualitative results held for the bare 24-ply plate, with lower E and plane wave data possibly due to lack of edge treatment (for that one specimen) resulting in poor electrical contact with the fixture.

Among all the plain panels tested, the ones with the aluminum flame spray provided the most shielding. This is probably due to the continuous aluminum coating. The panels with the 200 aluminum mesh did not provide any

improvement in shielding of over the bare graphite epoxy (probably due to lack of intimate contact along the edges of the panel). Also, the vapor deposited aluminum panel apparently had too little protection (i.e., 3.0 to 5.0 x 10^{-6} in. thick) to show any improvement over the bare Gr/Ep. The poor performance of the aluminized fiberglass (over Gr/Ep) panels is due to the fact that the aluminized fiber was aligned only along the transverse direction of the panel.

The four panels manufactured by HEXCEL Corporation [layups of one 0° ply (S/N 15), two 0° plies (S/N 16), one 0° ply and one 90° ply (S/N 16), and one 0° ply, one 90° ply (S/N 17) and one pair of ± 45° plies (S/N 18)] gave low results (even after edge treatment), compared with the other types of panels tested. With 12 or more plies of this material, a much higher shielding might be obtained.

Surprisingly, the 12-ply panel with 120 aluminum mesh did not perform as well as the 24-ply panel with the same type of protection. The 12-ply panels were re-edge-treated to improve electrical contact, but still gave about half the shielding effectiveness (in dB) of the 24-ply panels with 120 aluminum mesh for H-fields at frequencies from 0.014 MHz to 10 MHz. The quality of the contact area of the mesh and the Gr/Ep panel may affect this result, but at present this discrepancy is unresolved.

Finally in the investigation of plain panels, a formula for the electrical conductivity of the protected panels (e.g. flame sprayed Gr/Ep) was used as a check on the protected Gr/Ep shielding effectiveness data (see QR IV). The resulting H field shielding curves for the flame spray and aluminum mesh panels fit the data quite well, showing the validity of the parallel resistor model which resulted in the formula. (The inconsistencies for the 120 aluminum mesh on the 12-ply panel were discussed above).

7.0 JOINED PANELS

The next stage of the shielding effectiveness program was the investigation of composite air passage butt joints. Plain 12-ply Gr/Ep panels from the previous tests were cut in half and rejoined with one of the following doublers (Figure 5):

* Aluminum, 1/8 in. thick and 3 in. wide with fasteners spaced 1 in. apart
* 24-ply (4/4/16) Gr/Ep, 3 in. wide with fasteners spaced about 1 in. apart

Each joint had either Hi-Lok fasteners or stress wave rivets. To provide for air passage smoothness, the gap between the two panels (typically 0.063 in. for the 12-ply Gr/Ep joints) was filled with EA 934 liquid shim. As shown in Table 3, various conditions were tested:

* Aluminum versus Gr/Ep doublers
* Hi-Loks versus stress wave rivets
* Tight Hi-Loks, loose Hi-Loks, no fasteners, no mounting bolts on doubler, no doubler, no liquid shim
* Vertical joint versus horizontal joint
* Bare 12-ply Gr/Ep joined panels, flame sprayed joined panels, 1/16 in. aluminum joined panel

(The aluminum panel and joint were included to test the joint configuration itself.)

Lastly, the RF tight joint concept (described in the following text) was examined for several specimens not listed in Table 3.

The results of the first four joint tests listed in Table 3 showed no significant difference in shielding effectiveness between the types of fasteners used. The stress-riveted specimens showed only a slightly higher shielding
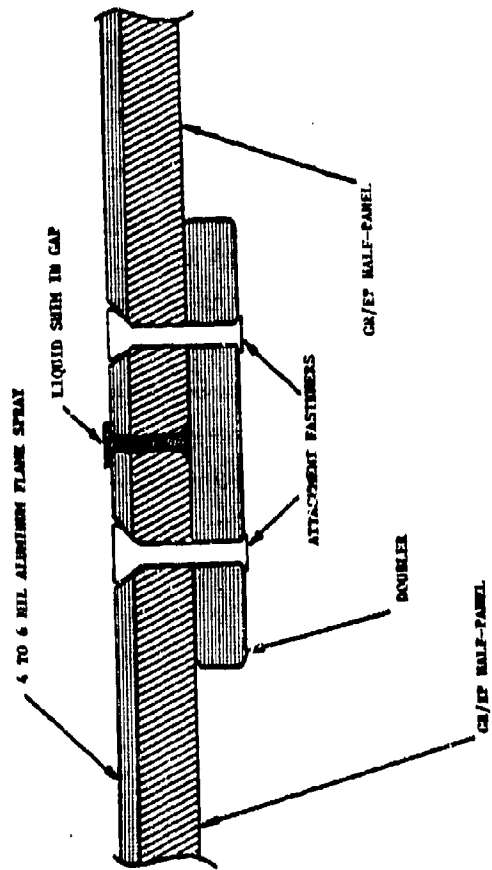
A-18

Figure 5. Cross-Section of Graphite/Epoxy Joined Panel (Not to Scale)

effectiveness at frequencies above 10 MHz. Similar results held for the doublers, except the aluminum doubler was very slightly more effective over most of the test range, rising to a 10 dB improvement over the Gr/Ep doubler in the H-field at 100 MHz.

These joined panels behaved similarly to those in the corresponding plain panel tests. However, the joined panels had three times the thickness of Gr/Ep at the joint than the plain panels, indicating RF leakage. In any case, the results showed that the joined panels provide adequate shielding.

The aluminum plate specimen performed better than any of the other configurations (about 50 dB better for the H-field, about 100 dB better at and above 10 MHz for the E-field, and about 30 dB better for the plane wave test). At 0.014 MHz the measured value for the H-field test was in agreement with the value calculated from Equation 1, using a 1/16 in. thick aluminum plate. As the frequency increased, the measured values deviated from the calculated ones, thus showing the effect of joint leakage. As a part of the test of S/N 2J2 (12-ply Gr/Ep panels joined to a 24-ply Gr/Ep doubler with Hi-Loks), various Hi-Lok tightness conditions were investigated. It was found that the magnetic shielding effectiveness decreases with a reduction in tightness. The data for the E-field, however, indicated that at low frequencies no Hi-Loks gave better shielding that any other configuration. This surprising result can be explained as follows.

The Gr/Ep of the panel and the doubler is a poor conductor compared to ordinary metals (conductivity is three orders of magnitude less than aluminum). Since the Hi-Loks are good conductors and do not make good contact with the fibers of the Gr/Ep panels, it is theorized that a small capacitance is set up between the Hi-Lok and the panel and doubler combination. As a result, the Hi-Loks act as small antennas at frequencies where this capacitance is high (around .1 MHz), increasing the coupling between the test antennas and thus decreasing the shielding effectiveness of the joint. At low frequencies, the main coupling between test antennas is through the panel, while at higher

A-20

frequencies (1 MHz to 1 GHz) the above capacitive reactance decreases and the Hi-Loks short out to the panel, leaving shielding effectiveness independent of fastener tightness.

The next four bare Gr/Ep panel joint tests (S/Ns 2J3, 2J4, 2J5, and 3J2) gave results on joint leakage and the effect of joint orientation with respect to the impinging field. The results for the (2/2/8) bare Gr/Ep joined panel without fasteners, doubler and liquid shim indicated much less shielding than the previous tight joint tests. The shielding of the bare 12-ply panel with various fastener-doubler combinations was then compared with plain panel results (Figures 6 through 8). The data indicate that the joints leak at high (>10 MHz) frequencies in a magnetic field and at low frequencies (<1.0 MHz) in an electric field. In general, the joints with a 90° orientation gave similar shielding data to the 0° orientation for H-fields at frequencies below 10 MHz, but produced at least 10 dB less shielding for E-fields at frequencies above 10 MHz.

The shielding effectiveness of the aluminum flame sprayed panels joined to an aluminum or Gr/Ep doubler with Hi-Loks (i.e. S/Ns 5J1 and 20J1) was greater than that for those without flame spray for frequencies <10 MHz in both H- and E-fields. Above this frequency the joint leaks and flame spray makes no difference. For plane waves, the panel with the Gr/Ep doubler indicated that flame spray provides additional shielding over bare Gr/Ep, but the panel with the aluminum doubler did not show the same results.

To reduce the RF leakage in a typical aircraft (air passage) Gr/Ep butt joint, an additional surface protection system was desired. The main problem was to provide electrical continuity between surface protection systems (e.g., aluminum flame spray) on either side of the joint. Of course, the ultimate goal would be to provide a butt joint specimen with the same shielding effectiveness as a continuous flat panel.
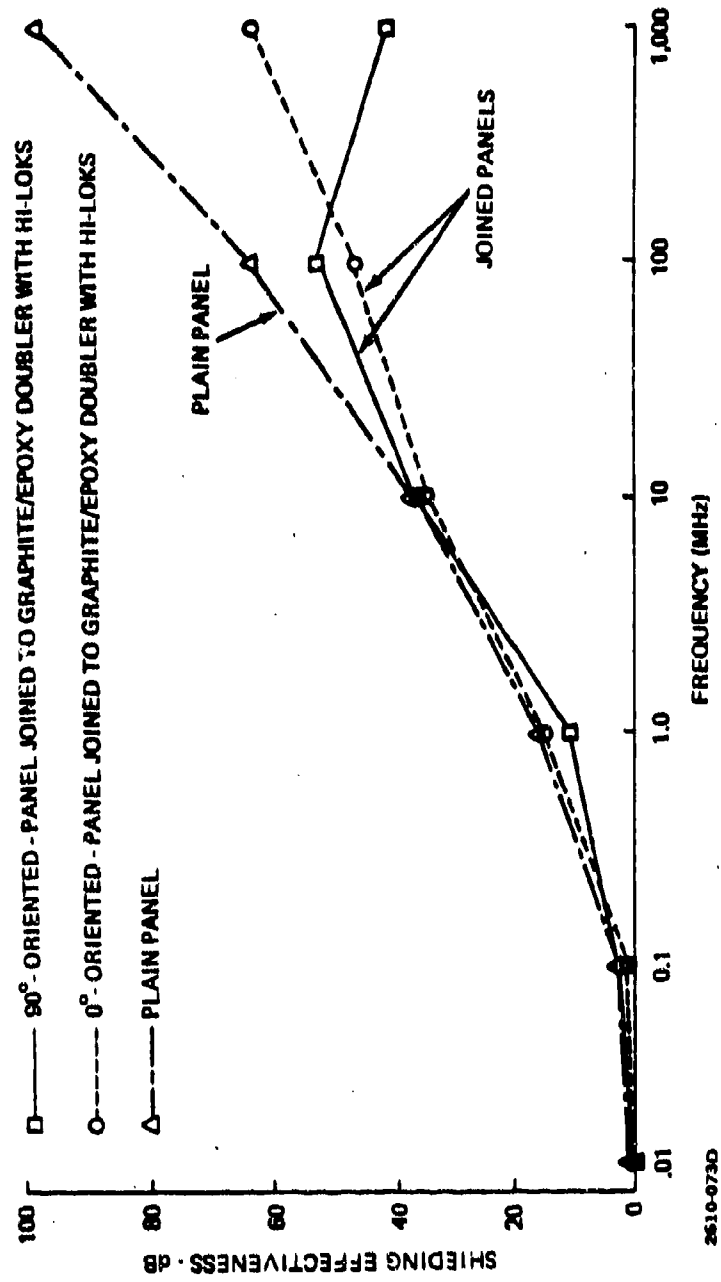
Figure 6. Magnetic Shielding Effectiveness of 2/2/8 Graphite/Epoxy Plain Panel and Panels Joined with Hi-Loks (QR V)
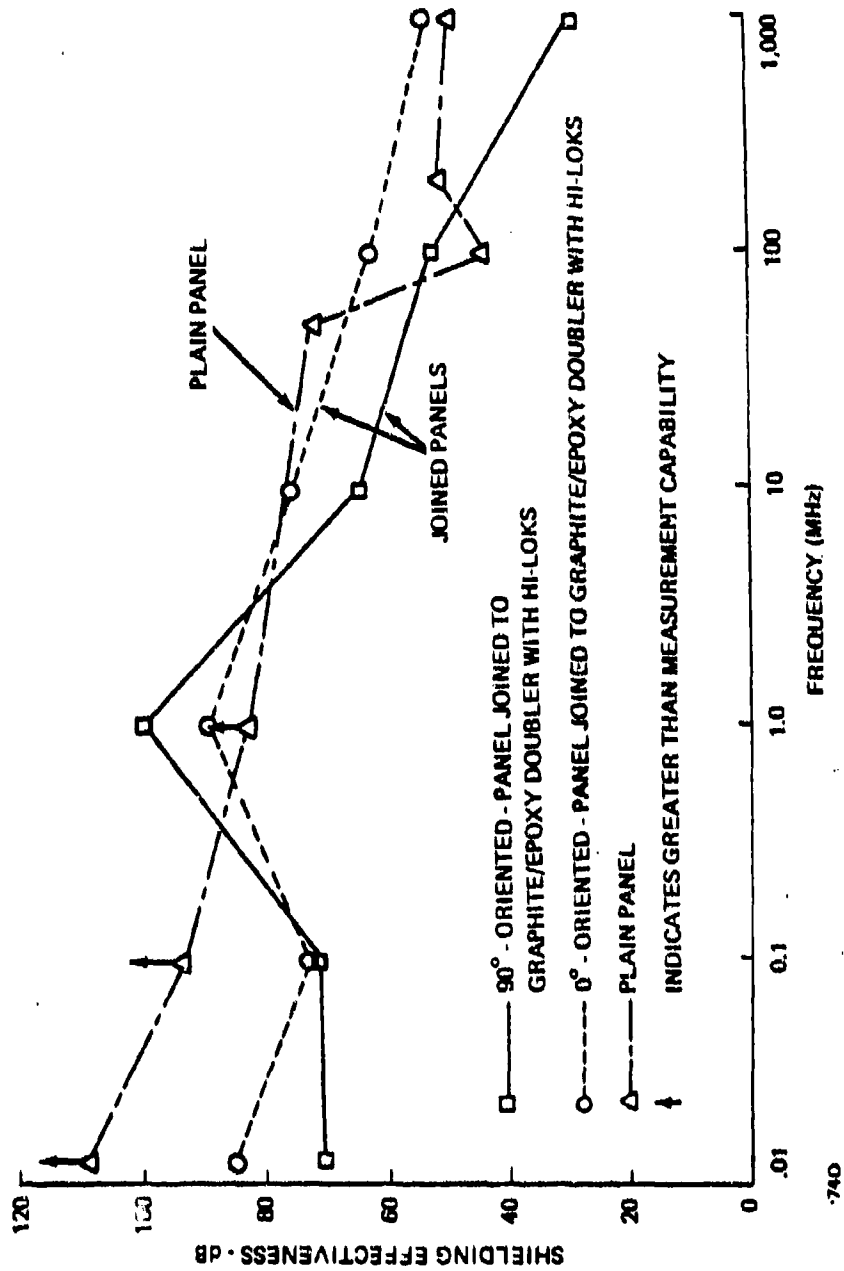
A-22

Figure 7. E-Field Shielding Effectiveness of 2/2/8 Graphite/Epoxy Plain Panel and Panels Joined with Hi-Loks (Q& V)
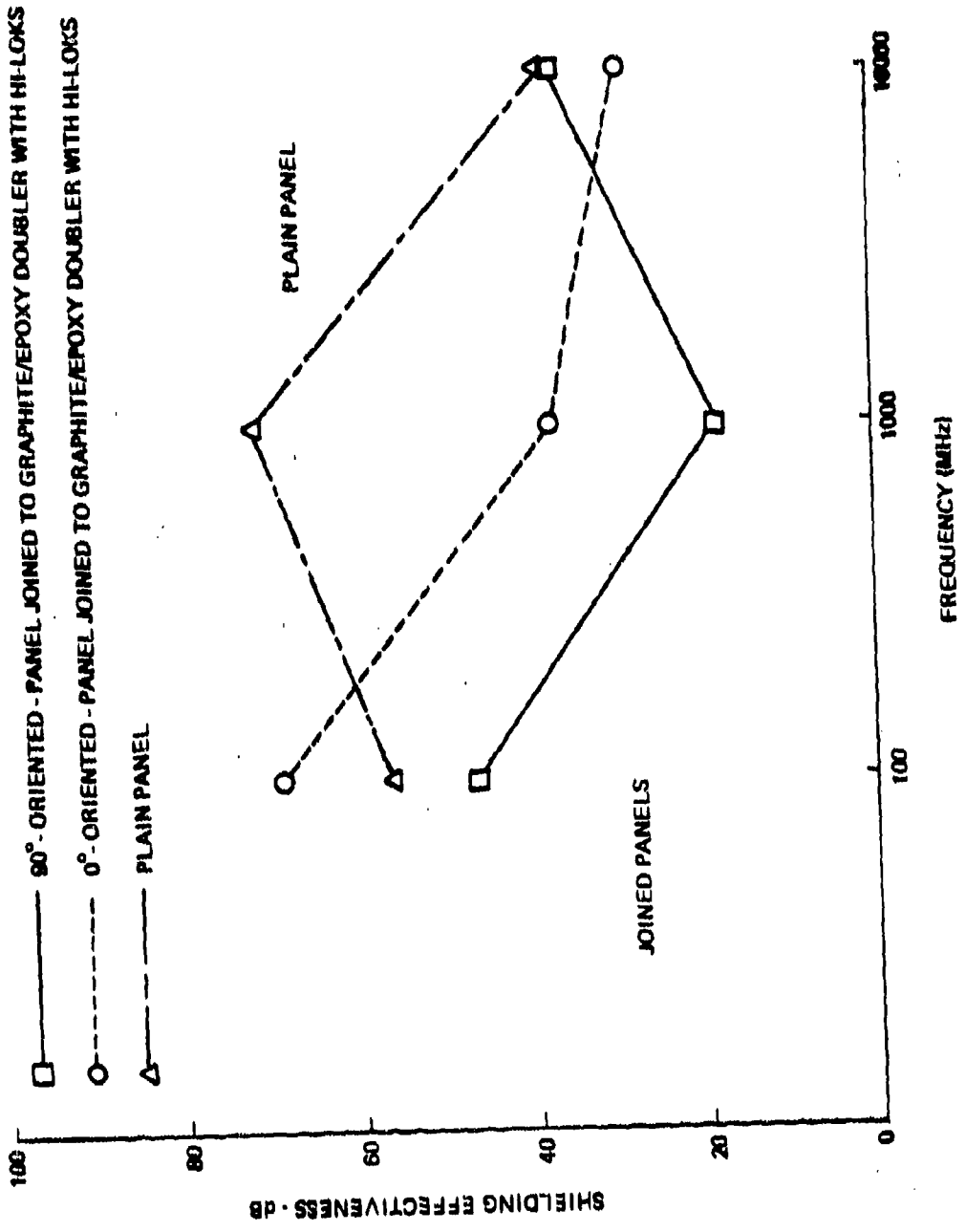
Figure 8. Plane-Wave Shielding Effectiveness of 2/2/8 Graphite/Epoxy Plain Panel and Panels Joined with Hi-Loks (QR V)

A-24

The result of this investigation was the RF tight joint concept which utilized a 1.0 in. wide strip of aluminum flame spray, applied along the length of the joint seam by means of the GAC developed secondary flame spray application technique. Four test specimens were then produced (not listed on Table 3).

The first two were 15 in. x 15 in. 24-ply (4/4/16) Gr/Ep with either 4 to 6 mil of aluminum flame spray or 120 x 120 grid aluminum mesh. They were then cut in half and rejoined (as with the other joined panels) with 24-ply Gr/Ep doublers and flush-head Hi-Loks. Finally, the secondary flame spray was applied t tue joints. After these two specimens were tested, conducting tape was added directly over the secondary flame spray to test adding more conductive material as compared to widening the joint protection area. Copper tape (1.0 in. wide and 1.5 mil thick) was applied directly over the secondary flame spray while the aluminum tape (2.0 in. wide and 3 mil thick) was applied not only over the secondary flame spray area, but also on the heads of the Hi-Loks on both sides of the joint area.

The test results showed that in tha majority of cases the RF tight joint concept displayed similar shielding effectiveness to that of the continuous flat panel of the same material makeup (i.e., 24-ply Gr/Ep with either 4 to 6 mils aluminum flame spray or 120 grid aluminum mesh). Also, although the addition of the copper tape had a slightly greater effect than the addition of aluminum tape, in most cases neither had much effect on the shielding effectiveness of the basic secondary flame sprayed RF tight joint concept.

8.0 ACCESS DOORS

The objective of the most recent stage of the shielding effectiveness investigation was to determine the extent of RF leakage through the access doors of a composite aircraft. Initially, the investigation involved conventional access door to surrounding structure interfaces, such as those

A-25

found on present day metallic aircraft, to permit a direct comparison between metal and Gr/Ep access doors. Later, interface modifications will be used to reduce the amount of RF leakage through the Gr/Ep doors.

The access door test panels were constructed as described in the test plan (Table 4). They consisted of 12-ply (2/2/8) bare or aluminum flame sprayed Gr/Ep panels (27 in. x 39 in., as described in Section 4.0) with an integral ~15 in. x ~15 in. x 0.125 in. deep recess. Further, some panels were edge treated (as described in the paragraph on plain panels), and some had a 12 in. x 12 in. cutout within the panel recess. The first two access door types were 15 in. x 15 in. bare 12-ply Gr/Ep (D-1) and 15 in. x 15 in. aluminum flame sprayed (metalized) 12-ply Gr/Ep (D-2). Other modifications, such as the addition of dimpled washers to both metalized (D-2A) and bare (D-1A) access doors, and a two piece metalized access door assembly (D-3, shown in Figure 9) have not been tested. Note that D-3 (mounted on a metalized base panel as in Figure 9) provides flame spray to flame spray contact across the door-to-panel attachment interface.

As shown on Table 4, the first three tests covered chamber equivalency, edge leakage through the large and small apertures, and the effect of removing the RF gasket around the small aperture. The results of Test Number 1 (T/N 1) showed the chambers to be, for engineering purposes, equivalent. The small differences in maximum field pickup were within the accuracy of the measuring equipment (e.g., 2 dB). T/N 2 also showed chamber equivalency, but also showed leakage around the edges of the large and small aluminum fixture plates. The total leakage was less than the internal noise of the receiver, except for H- and E-fields at 10 GHz (large aperture edge leak – about 50 dB, small aperture edge leak – about 3 dB), and the E-field at about 0.01 MHz (large aperture edge leak – ~10 dB, small aperture edge leak – ~4 dB). T/N 3 showed that the removal of the small aperture RF gasket does not have much effect on results.

Table 4. Revised Test Plan To Determine Shielding Effectiveness Of Graphite/Epoxy Access Doors (QR VIII)

TEST NO	A CHAMBER (L/H SIDE)	B CHAMBER (R/H SIDE)
1	LARGE APERTURE OPEN	LARGE APERTURE OPEN
2	ALUMINUM FIXTURE PLATE COVERING LARGE APERTURE ONLY	ALUMINUM FIXTURE PLATES COVERING LARGE AND SMALL APERTURE
3	ALUMINUM FIXTURE PLATE COVERING LARGE APERTURE ONLY	ALUMINUM FIXTURE PLATES COVERING LARGE AND SMALL APERTURE WITH SMALL APERTURE RF GASKET REMOVED
4*	PANEL 1A-1	PANEL 2A-1
5	PANEL 1A-1	PANEL 1B-1
6	PANEL 1A-2	PANEL 2A-2
7	PANEL 1A-2	PANEL 1B-2
8	LARGE OPEN APERTURE	PANEL 1B-2
9	PANEL 1A-2	PANEL 2A-3
10	PANEL 1A-2	PANEL 2A-3; D-1
11	LARGE OPEN APERTURE	PANEL 1B-3
12	LARGE OPEN APERTURE	PANEL 1B-3, D-2
13	LARGE OPEN APERTURE	PANEL 1B-3, D-1
14	LARGE OPEN APERTURE	PANEL 2A-3, D-2
15	LARGE OPEN APERTURE	PANEL 1B-3, D-1A
16	LARGE OPEN APERTURE	PANEL 1B-3, D-2A
17	LARGE OPEN APERTURE	PANEL 2A-3, D-1A
18	LARGE OPEN APERTURE	PANEL 2A-3, D-2A
19	LARGE OPEN APERTURE	PANEL 2A-3, D-3
20	LARGE OPEN APERTURE	PANEL 1B-3, D-3

*NOTE – THE SPECIFIC PANEL DESIGNATIONS AS THEY APPEAR IN TABLE 2-1 ARE DEFINED
*NOTE   AS FOLLOWS:

- 1A & 2A – 12 PLY (2/2/8) BARE GRAPHITE/EPOXY PANEL (27 INCHES x 39 INCHES) WITH INTEGRAL 0.125 INCH DEEP RECESS

- 1B – 12 PLY (2/2/8) ALUMINUM FLAME SPRAYED GRAPHITE/EPOXY PANEL (27 INCHES x 39 INCHES) WITH INTEGRAL 0.125 INCH DEEP RECESS.

THE DASH NUMBERS APPEARING IMMEDIATELY AFTER THE ABOVE SYMBOLS ARE DEFINED AS FOLLOWS:

- (-1) – NO EDGE TREATMENT, NO CUT-OUT

- (-2) – EDGE TREATED, NO CUT-OUT

- (-3) – EDGE TREATED, 12 INCHES x 12 INCHES CUT-OUT WITHIN PANEL RECESS.

(E.G., 1B-2 IS DEFINED AS EDGE TREATED ALUMINUM FLAME SPRAYED GRAPHITE/EPOXY PANEL WITH NO CUT-OUT)

SURROUNDING STRUCTURE PANEL (1B-3)

4 TO 6 MIL ALUMINUM FLAME SPRAY

TWO-PIECE ACCESS DOOR ASSEMBLY (D-3)

REMOVABLE ATTACHMENT FASTENERS

4 TO 6 MIL ALUMINUM FLAME SPRAY

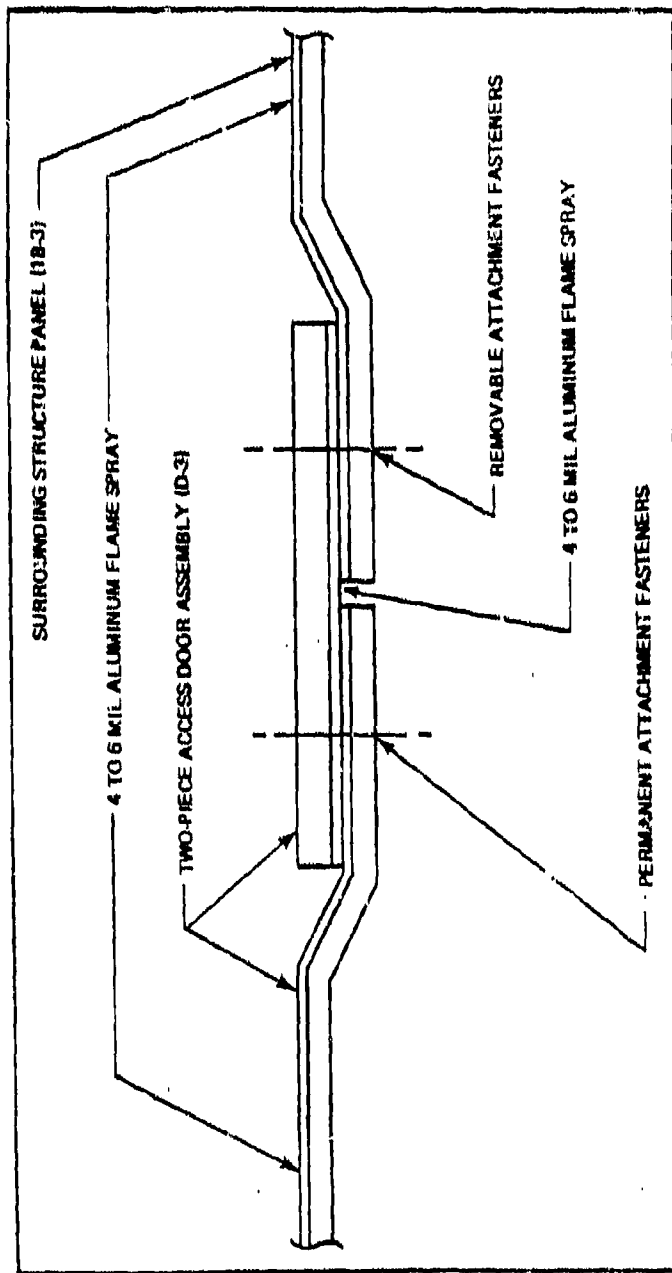PERMANENT ATTACHMENT FASTENERS

Figure 9. Attachment Interface Cross-Section of Panel 1B-3 to Access Door D-3 Assembly (QR VIII)

T/N 4 and T/N 5 showed that panel 1B-1 (flame-sprayed) had up to
15 dB increased shielding effectiveness over the unprotected specimens 1A-1
and 2A-1. However, all these large panels provided about 8 to 10 dB less
shielding than did the small plain panels tested earlier in the program. This
decrease in shielding may be attributed to the leakage through the attachment
perimeter of the large panels, which is double the length of that of the
smaller panels.

Edge treatment of the large panels (in T/Ns 6 through 8) increased
the shielding effectiveness only at frequencies above 100 MHz.

The results of T/N 9 and T/N 11 to determine the shielding effective-
ness of panels with cutouts, but without access doors, were not shown, because
they offered little to no shielding.

The rest of the completed tests (i.e., T/N 10 and T/Ns 12 through 14),
compared bare and metalized continuous panels against bare and metalized cutout
panels with bare and metalized access doors. In most cases, the continuous
panels (2A-2 and 1B-2) displayed the greatest shielding effectiveness against
H, E, and plane wave EM radiation, especially at the high frequencies. The non-
continuous panels (2A-3 and 1B-3), with the access doors mounted in place, dis-
played a maximum reduction in shielding effectiveness of 38 dB for the
1 GHz E-field measurement of panel 2A-3 with door D-2. However, in most cases,
the utilization of the aluminum flame sprayed access door (D-2), as opposed
to the bare or unprotected access door (D-1) showed an increase in shielding
effectiveness of as much as 31 dB. Further, in many cases, especially at
lower frequencies (up to 100 MHz), the utilization of access door D-2 showed
an increase in shielding effectiveness over that of the continuous panels as
well (Figures 10 through 12).
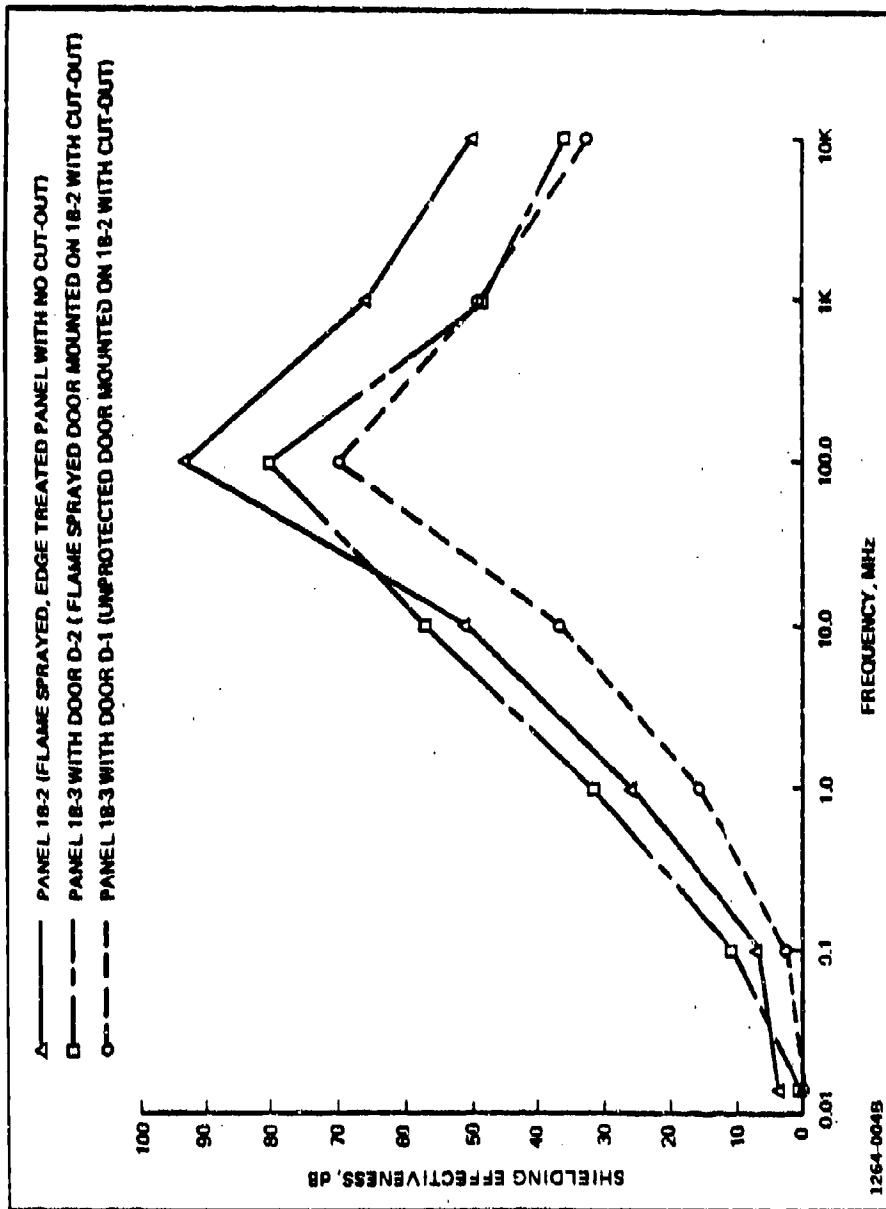
Figure 10. H-Field Shielding Effectiveness of 2/2/8 Graphite/Epoxy Access Door Specimens (QR VIII)
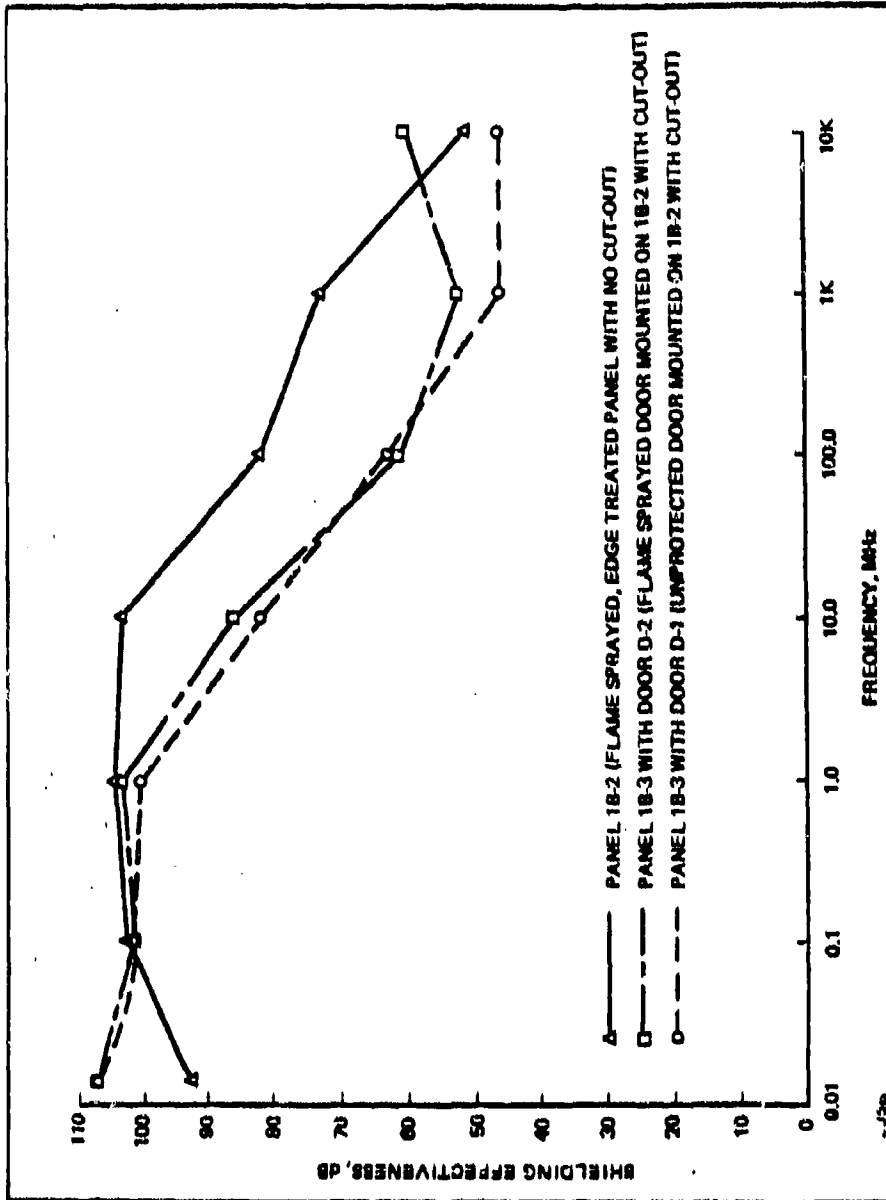
Figure 11. E-Field Shielding Effectiveness of 2/2/8 Graphite/Epoxy Access Door Specimens (QR VIII)

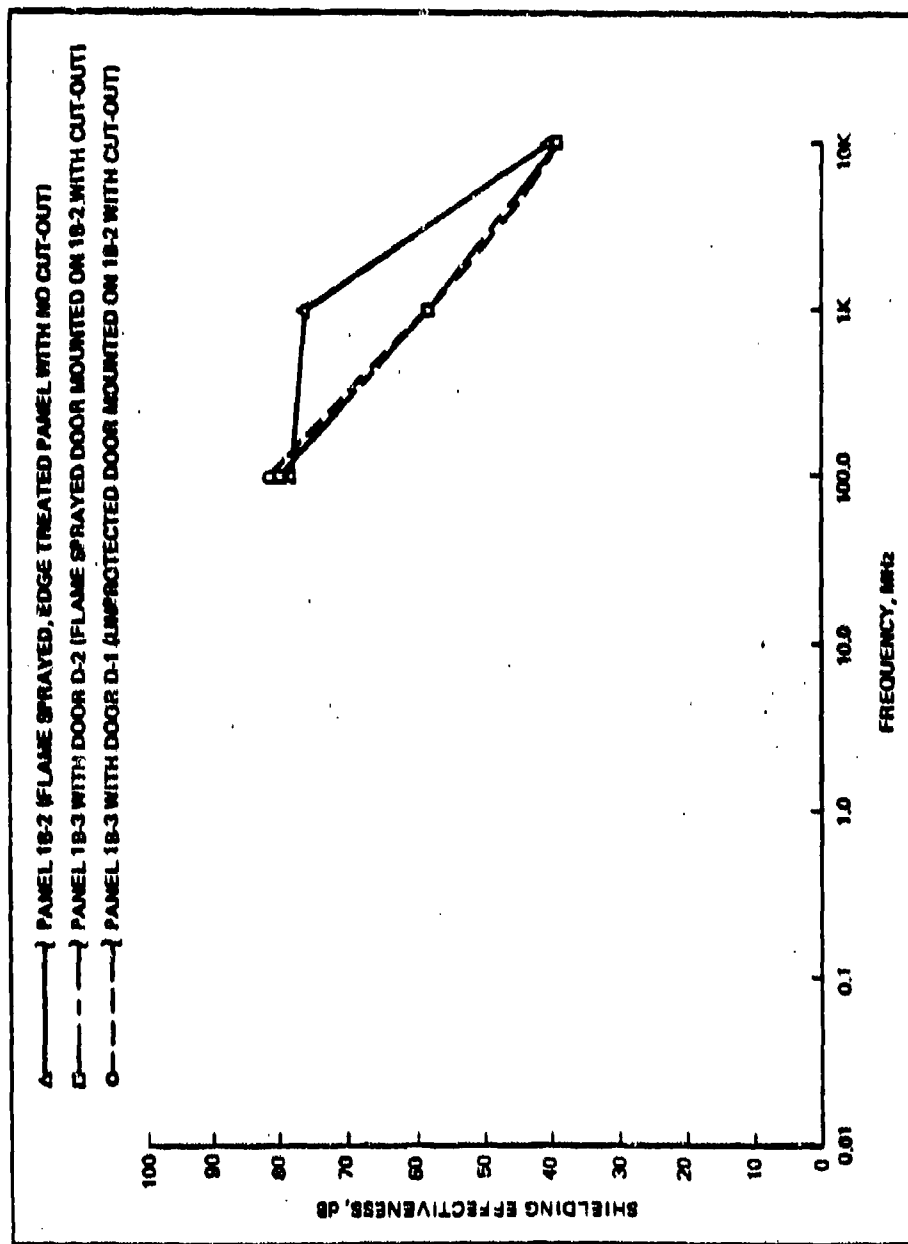Figure 12. Plane-Wave Shielding Effectiveness of 2/2/8 Graphite/Epoxy Access Door Specimens (QR VIII)

A-32

SRC TN 79-1011
November 1979

Copy __ of 5

SUMMARY OF GENERAL DYNAMICS COMPOSITE

FORWARD FUSELAGE

SYSTEMS INTEGRATION PROGRAM

By

R. Rudolph

Contract N00014-78-C-0673

Prepared for

Office of Naval Research
Arlington, Virginia 22217

TABLE OF CONTENTS

LIST OF ILLUSTRATIONS

LIST OF TABLES

SECTION 1

INTRODUCTION AND OVERVIEW

This report summarizes work done by General Dynamics Corporation, Fort Worth Division (with contributions to the effort made by Culham Laboratory, UKAEA Research Group, United Kingdom), for the Air Force Flight Dynamics Laboratory, Advanced Composite Structure ADP, Wright-Patterson Air Force Base under Contract F33615-76-C-5439. The Composite Forward Fuselage Systems Integration program, covering the period April 1977 through May 1978, was initiated to perform the development necessary to guide the integration of avionic and electrical systems into the composite aircraft structure. The final report (AFFDL-TR-78-110) was published September 1978. We will examine Volume II of that report, which covers the identification and modeling of the induced effects of lightning.

The rest of this section covers the test approach and conclusions of the program. The remaining sections of this report are:

2. Lightning Simulation and Induced Voltage Measurement Techniques

3. Comparison of Predicted and Measured Results

4. Additional Measurements

5. Driving Point Waveform and Induced Mechanisms - Theory and Prediction

In particular, Section 5 consolidates and slightly expands on the major theoretical and calculational aspects of the General Dynamics report.

1.1 TEST APPROACH

The composite material used was graphite/epoxy which, with a conductivity 10^{-3} times that of aluminum, could be expected to allow greater penetration of electromagnetic (EM) radiation into the fuselage interior, thus possibly

threatening avionic and electrical systems. In order to evaluate this situation in detail, the program focused on the following areas:

* Development of a simplified test configuration (consisting of a single-stage capacitor bank lightning simulator), a graphite/epoxy YF-16 forward fuselage test article, and a return conductor (consisting of three broad metal plates), which both completed the test circuit and ensured free-field conditions exterior to the test article (Figures 1-1 and 1-2)*. The resulting driving point waveform was a unipolar pulse with no overshoot, typically having a current maximum of 20 kA, di/dt maximum of 17.1 kA/μs. Test results (i.e., interior wiring voltage pickups) were then scaled up to simulate the effect of lightning threat parameters (200 kA; 100 kA/μs).

* Evaluation of low frequency (LF) and high frequency (HF) effects, including those related to the driving point waveform (LF), its time derivative (higher frequencies, see Figure 5-3), and to fuselage resonances (HF). (Section 2.)

* Determination and measurement of basic mechanisms coupling external EM radiation to interior wiring. (Section 3.)

* Development of simplified models and theory of induced mechanisms, including predictive calculation techniques to compare with test results. (Section 5.)

In addition to, and in conjunction with, the basic test program, special tests were conducted to evaluate the following aspects of coupling phenomena:

* Magnetic flux distribution inside fuselage

* Small aperture effects

* Effect of additional metal conductors and their impact on the circumferential variation of fuselage interior voltages

* Performance of twisted pairs, coaxial cables, and shielded twisted pairs in the presence of aperture and diffusion fields

---

*All figures and tables are taken from Report AFFDL-TR-78-110, except as noted.
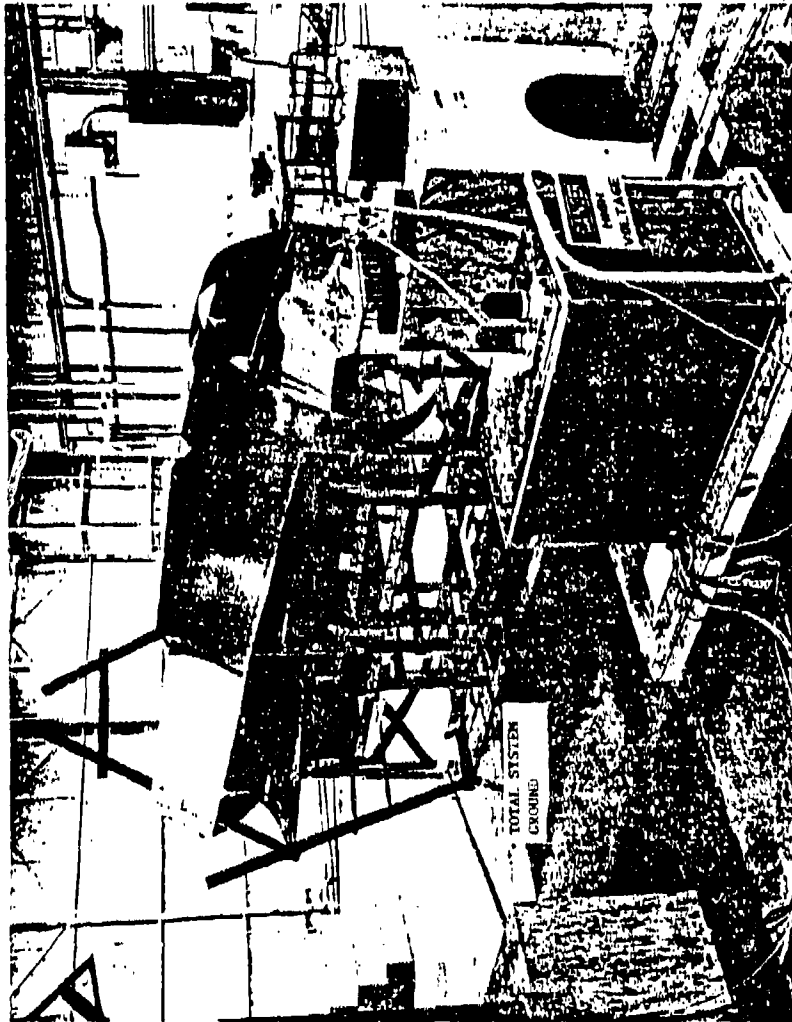
Figure 1-1. Overall Forward View of Test Setup for Simulated Lightning Strikes
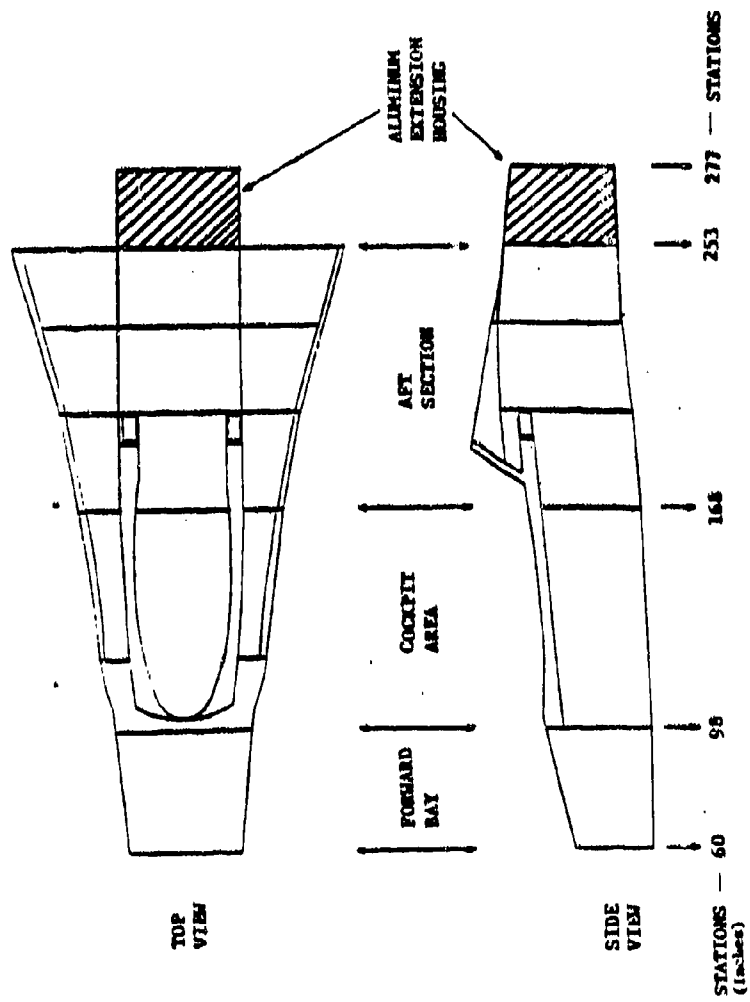
Figure 1-2. Composite Forward Fuselage and Basic Test Areas

- HF effects inside enclosed areas due to capacitive coupling

- Electronics (F-111 vintage) powered up test on the aircraft to test for interference or damage.

For this last test, with F-111 vintage avionics installed in a typical manner, the structure was tested with a 125 kA peak, 32 kA/µs maximum rate of change current pulse while the systems were operating. No failures or perturbations occurred. (Section 4.)

1.2 CONCLUSIONS

As a result of the program, a number of conclusions were drawn about lightning effects in a graphite/epoxy fuselage. Some of these conclusions are also applicable to metal airframes;

- There are three primary mechanisms of energy transfer from a lightning strike to electrical/electronic equipment. These primary transfer mechanisms assume that design precautions have been taken to prevent direct transfer of energy to the interior of the fuselage shell (e.g., by conduction of a lightning stroke down a pitot line or pitot heater wiring):

  1. IR coupling (Jρ voltage per unit length) produces a voltage drop along the interior surface of the graphite/epoxy fuselage, which may be picked up by wiring with electrical connections there.

  2. Diffusion flux coupling produces voltages in wire loops which are interior to a graphite/epoxy fuselage.

  3. Aperture flux coupling induces voltages in wire loops in the usual way (directly from the external field via Faraday's law).

  Mechanisms 1 and 2 comprise resistive/diffusion coupling mechanisms which pass the external field through imperfect conductors, such as graphite/epoxy. Case 1 is due to the large skin depth of graphite/epoxy, while Case 2 is, in addition, due to fluxes produced during current redistribution to fuselage regions of lower resistance. (Subsections 5.2 and 5.3.)

- Resistive/diffusion coupling produces voltages proportional to the driving point waveform (Corollary 1, Subsection 5.3.1), while aperture coupled voltages (which are relatively independent of fuselage resistivity) produce, as expected, voltages proportional to the injected current di/dt. (Subsection 5.7.)

- Resistive/diffusion coupled voltages are LF signals (below 1 MHz; see Figure 5-3) and will impact only those circuits which form significant loop areas and/or have multiple airframe reference points.

- High frequency effects (above 1 MHz) are primarily aperture dominated (Figure 5-3). However, due to the short diffusion time through graphite/epoxy, HF effects can appear inside a fuselage and be distributed by the E-field developed along the graphite/epoxy shell interior surfaces.

- The fuselage response (an HF longitudinal resonance) behaves in a manner predictable from transmission line theory and is independent of fuselage material (Section 2).

- The IR voltages appearing inside the fuselage will be approximately 3×10^3 higher than they would be in an aluminum fuselage. (Subsection 5.2.)

- Induced effects due to diffusion flux can never be higher than the highest $J\rho$ voltage which exists along the interior surface of the fuselage. (Corollary 3, Subsection 5.3.1.)

- Linear scaling of induced effects in a graphite/epoxy fuselage is not always permissible. If system response information is desired at high levels of I and di/dt, testing must be done at high levels to determine if nonlinear conditions exist. Once appropriate scaling factors are determined, resistive/diffusion voltages scale by I and aperture voltages scale by di/dt. (Section 2.)

SECTION 2

LIGHTNING SIMULATION AND INDUCED VOLTAGE MEASUREMENT TECHNIQUES

2.1 NATURAL LIGHTNING AND FUSELAGE RESPONSE

It has been estimated that approximately 75 percent of all natural lightning strikes to the F-16 will initially attach in the nose radome area and then be conducted through the total length of the forward fuselage, exiting toward the aft end of the aircraft in a return stroke. Other possible fuselage attachment locations would result in the lightning strike being swept back from the primary attachment point, a condition of more interest to studies of structural damage than of induced voltage. In general, the worst case for induced voltages would occur during the return stroke of a lightning strike, when the current peak amplitude and di/dt would be largest. Values of 140 kA and 100 kA/µs, respectively, have been observed in nature and correspond to strikes whose values would be exceeded only 2 percent of the time - a 2 percent severity level.

In addition to the basic waveform of the current pulse itself, lightning produces additional spatial variations in the fuselage surface current and, at high frequency, standing waves.

A circumferential redistribution of current around a graphite/epoxy fuselage (to regions of lower resistance, such as metal), occurs with LF components of the pulse (Subsection 5.3). In an all-metal fuselage, the current would be inductively (rather than resistively) shared, with the current a skin effect only.

The HF (above 1 MHz) current distribution has the same circumferential variation as the LF case, but in addition provides a longitudinal variation, since the HF currents are associated with standing waves on the fuselage excited by lightning transients. Due to the impedance mismatch between the lightning

arc channel (radius ~ 0.5 mm) and the aircraft (radius ~ 0.5 - 1.5 m) at each of the two attachment points, the standing waves should have a current node at each end of the aircraft, with frequencies given by

$$f_n = \frac{c}{\lambda} = \frac{nc}{2\ell} = n\, f_1 \quad Hz \qquad (1)$$

where:

   c = speed of EM waves = 3×10^8 m/s
   λ = wavelength of standing wave
   ℓ = total aircraft length in meters
   n = an integer corresponding to the mode

Thus for an 11 m aircraft length, f_1 = 14 MHz (a half-wave resonance). The aircraft standing wave pattern is further complicated by wing modes and fuselage/wing modes.

2.2 SIMULATION AND MEASUREMENT TECHNIQUES

The circumferential current distribution of the graphite/epoxy forward fuselage test article should accurately portray actual graphite/epoxy full fuselage response, except in the region of the inlet (absent in the test article), which starts at Station 161 and runs aft (Figure 1-2 - station numbers are in inches).

As for the HF longitudinal resonances, we note that the test article is slightly less than half the length of the full F-16 fuselage (Figure 1-2). With the current return conductor attached at Station 277 and the impedance mismatch between the capacitor bank and Station 60, the principal resonance has a node at the forward end and a current maximum at the aft end (a quarter wave resonance). The standing wave frequencies may be obtained from Equation 1, except that the even modes (corresponding to a node at Station 277) will be absent. The predominant HF contributions to the exterior surface current

waveforms (proportional to the flux density, B, measured with small loops near that surface) were observed to have frequencies of 14 MHz and 46 MHz, respectively, roughly corresponding to first- and third-order full fuselage resonances. The test loops also indicated highest maximum current toward the aft end and lowest maximum current toward the forward end, thus validating the standing wave model.

In the simulation of basic lightning waveform parameters, the test circuit itself (Subsection 1.1) may be viewed as a waveform generator in the form of a simple RLC series circuit (Subsection 5.1). The impulse generator is built around a 4 μF, 50 kV capacitor, which is capable of accepting a charging voltage sufficient to produce approximately 30 kA peak with a 20 kA/μs rate of rise. A typical test pulse had parameters of 20 kA and 17.1 kA/μs.

Since the test waveform does not achieve the severity levels specified from natural lightning (Section 2.1), all induced voltage measurements must be scaled to reflect the response to actual conditions. Scaling parameters were chosen from those involved in the two main coupling mechanisms, aperture and resistive/diffusion coupling. Aperture and other direct coupling processes produce voltages proportional to the rate of change of fields - dB/dt and dE/dt (both proportional to di/dt), while resistive/diffusion coupled voltages are proportional to the current itself (Corollary 1, Subsection 5.3.1).

Initially, each scaling factor was assumed to be a linear extrapolation from a 20 kA - 17.1 kA/μs current waveform to a 200 kA - 100 kA/μs severe lightning strike (a 0.5 percent severity level). We have, from the corresponding ratios,

$$\text{Current (I) Scaling Factor} = \frac{200 \text{ kA}}{20 \text{ kA}} = 10{:}1$$

$$\text{Current Rate of Rise (di/dt) Scaling Factor} = \frac{100 \text{ kA/μs}}{17.1 \text{ kA/μs}}$$

$$= 5.85{:}1 \tag{2}$$

IR voltage pickup tests, using current waveforms with different peak I and di/dt values, verified linearity of I scaling up to about 50 kA, but loop tests in the cockpit (aperture dominated) area showed a breakdown in linearity of di/dt scaling to a 72.9 kA - 19.4 kA/µs pulse (possibly due to arcing along the joints of the metal canopy interface). For the cockpit, the di/dt scaling factor was taken to be 10.5:1 to reflect the increased scaling of induced voltages for this high level pulse.

All measurements were made using an oscilloscope (CRO), Tektronix Model 7633 with a 7A13 differential preamplifier. The CRO inputs were provided by a coaxial (RG-58 or RG-22 cable) or fiber optic interface (Meret Inc., Part Number MDL238), with the latter being used when the coaxial setup signal-to-noise ratio was too low. Fuselage interior surface IR voltages were measured with RG-22 (twisted, shielded pair) attached to the interior surface at two longitudinally spaced sensing points. Flux measurements (both diffusion and external) were made with loops of 24 AWG copper wire, connected to RG-58 cable. The primary current pulse was measured using a Pearson Model 1080 transformer connected around Station 277 (between the forward fuselage and the return conductors).

SECTION 3

COMPARISON OF PREDICTED AND MEASURED RESULTS

To make the test results as general as possible, and to clarify the relationship between theory and experiment, the principal characteristics of the graphite/epoxy test article (a complex structure comprising graphite/epoxy, metal, and nonconductors) had to be determined (Figure 1-2). To aid this process, the forward fuselage was tested at three typical sections each with an overall, relatively uniform, electrical character:

1. Forward Equipment Bay (FEB), Stations 60-98. Fully
    enclosed, mainly graphite/epoxy with four thickened
    up longerons, but little metal, and with two remov-
    able graphite/epoxy doors, one with a small Kevlar
    access panel in it (mostly 6-ply graphite/epoxy).

2. Cockpit, Stations 98-168. Large, aperture dominated
    section with mainly graphite/epoxy walls and floor,
    two thickened up longerons, and two dissimilar front
    strake sections (thermoplastic resin 8-ply, right;
    regular resin 16-ply, left). Cockpit floor between
    the longerons is 10-ply increasing to 14-ply toward
    the back. Above the longerons to the waist joint is
    10-ply, changing to 6-ply up to the metal canopy sill,
    except at the left side rear (adjacent to the gun
    muzzle), where it is 10-ply. There is also a metal
    right-hand equipment console.

3. Upper Central and Right-Hand Aft Bays, Stations
    227-253. This section has a lot of metal in the
    strakes, the rear transverse bulkhead, and fore and
    aft panels. The graphite/epoxy bay doors are secured
    to all-metal substructure. The right-hand side panel
    has metal inserts for the screw heads. Upper (ammo
    handling) bay cover panel is 10-ply graphite/epoxy,
    right-hand strake bay is 6-ply graphite/epoxy.

These sections were then instrumented with IR sensing wires (usually separated the length of the section) and loops (Figure 3-1) to measure voltage pickup and variation with interior position. In addition, the loop voltage waveforms themselves were examined to determine the dominant flux coupling mode in that section (Figures 5-2 and 5-8, Subsection 5.3.2).

FLANGE

ACCESS DOOR

FIXED STRUCTURE

LOOPS

#1 #2 #3

IR WIRE

#1

#2

#3

#4

#5

FRONT VIEW

STA 98

STA 98 REFERENCE POINT

#1

#2

#3

#4

#5

IR WIRE ROUTING TO STA 60

LOOPS

RG-22
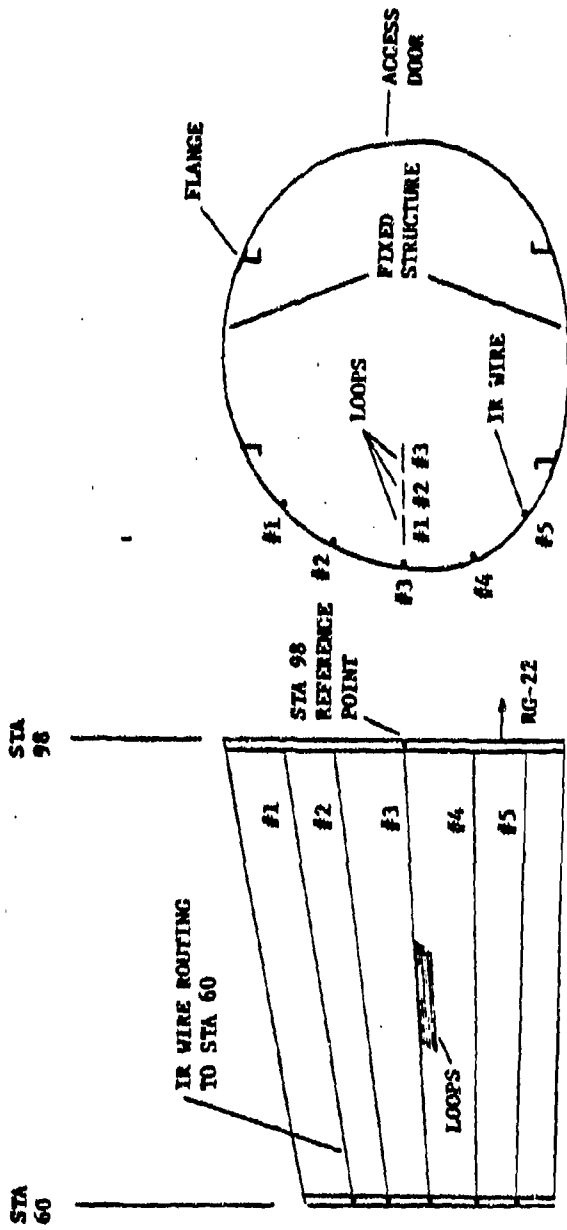
STA 60

SIDE VIEW

The grounding straps were routed along IR wire #3 between STA 60 and 98.

Figure 3-1. Test Setup in the Forward Bay

Calculations of predicted voltage pickup were made using methods discussed in Subsections 5.4 through 5.7. Input required includes driving point peak current and di/dt, fuselage cross-sectional shape (including location of highly conducting regions), ρ_{eff} (an effective conductivity for the graphite/epoxy fuselage), h (surface thickness, usually obtained from the number of graphite/epoxy plies), ℓ (IR sensing wire spacing), and flux loop dimensions, location, and orientation.

The comparison of measured and calculated IR voltages is shown in Figure 3-2. For the data displayed, sensing wire lengths were 38 in. (FEB), 38 in. (cockpit, except possibly 30 inches at the strake), 27 in. (upper aft bay), and 22 in. (aft right hand strake bay). Note that the calculated voltages at Station 75 (FEB), correspond to surface current densities (Subsection 5.5) calculated from the POTENT computer program (Subsection 5.4) and displayed in Figure 5-9(a). In addition, the resulting calculated voltages in Figure 5-9(c) contain those in Figure 3-2 as a subset. (Apparently, calculated voltages for wires 1 through 5 have been shifted up one in Figure 3-2; i.e., 470V [calculated] should correspond to 440V [measured] – compare Figure 5-9(c).)

Loop voltage comparisons (calculated versus measured) are displayed in Table 3-1 (expanded from tables in the General Dynamics report) (Subsections 5.6 and 5.7). In the upper aft bay, a variation of the diffusion flux calculation method (Subsection 5.6) used measured (instead of calculated) IR voltages as input.

For the FEB, comparison of the IR voltages in Figure 3-2 shows consistent agreement. The predictions are within 10 percent of the measured values, confirming the choice of a low value for the effective resistivity of YF-16 graphite/epoxy panels (Subsection 5.5).

In the cockpit, because of the complex geometry, including different graphite/epoxy thicknesses, the predictions were not expected to be as reliable as in the FEB. The floor had the simplest geometry and gave the best results.
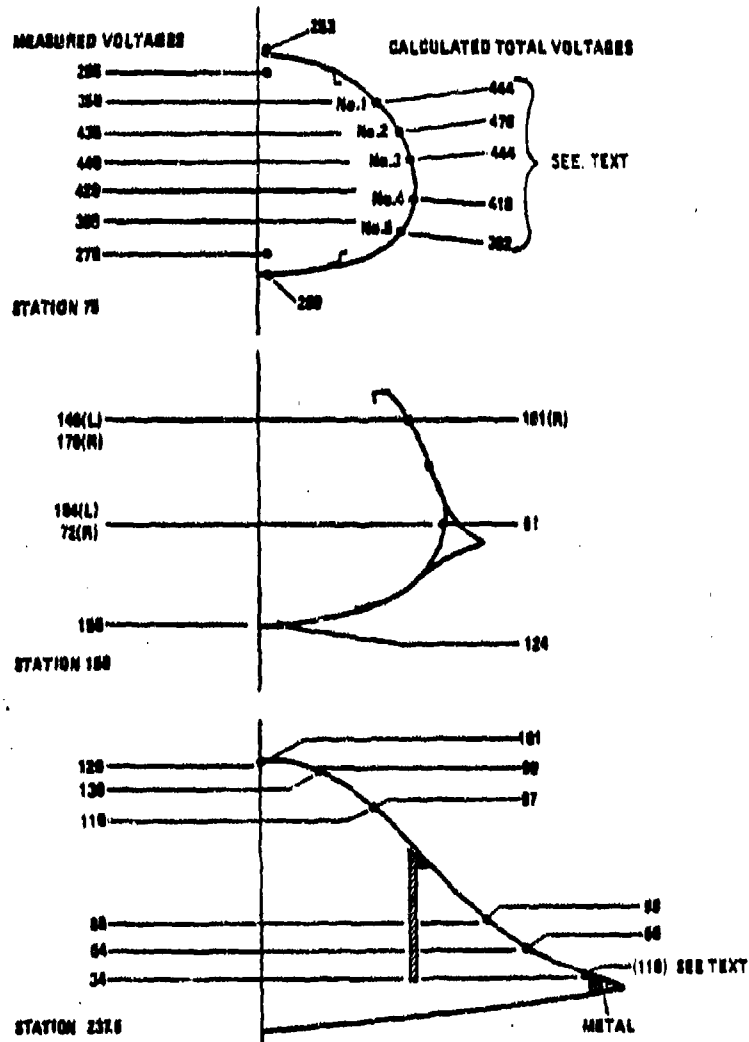
Figure 3-2. Comparison of Measured and Calculated IR Voltages on Graphite/Epoxy Interior Surface

Table 3-1. Comparison of Measured and Calculated Loop Voltages

Fuselage Section		Loops	Calculated (V)	Measured (V)
FEB (Diffusion flux)	1	8 in. x 2 in. all in the same horizontal plane and about midway up, near right side, with wire 1 nearest the wall (Figure 3-1)	7.75	7
	2		7.3	6.5
	3		6.2	5
Aft Bay (Diffusion flux)	1	26 in. long (area 0.319 m^2), centrally placed horizontal loops, 8 in. down and	90	85
	2	15.5 in. down, respectively, from the top graphite/epoxy panel	69	51
Cockpit (Aperture flux)	1	4 in. x 2 in loops, all in the same longitudinal plane normal to the left side	2.7	2.4
	2	(angled down toward the cockpit center),	3.0	2.2
	3	with wire 1 nearest the left wall	2.9	2.5
2 in. above floor		36 in. x 1.5 in., both in same vertical longitudinal plane through the cockpit center	15.8	12
14.5 in. above floor			27	24

At the "waist" level inside, the data indicate that the strakes do not con-
tribute much to fuselage conductivity (the calculated voltage is much lower
than either measured voltage), perhaps because of inadequate electrical bonding.
(Mechanical bonding strength is not being questioned.)

The aft bays have a simpler geometry, except for the metal boundary
on the upper panel around its entire periphery. In Figure 3-2, the upper bay
voltages are all higher and the right-hand bay voltage lower than the calcu-
lated values. Possibly the "end effect" of the test rig, due to the return
conductors and the aluminum extension box, tended to increase the current cen-
trally at the expense of current in the strakes. The predicted 118V at 1.5 in.
from the metal strake is in any case not reasonable since current flow in the
metal alongside influences and reduces graphite/epoxy current. Further, addi-
tional measurements have shown that the joint voltage (as a percentage of the
total panel voltage) is twice as great in the upper bay graphite/epoxy panel
as in the side panel, which has metal inserts in the graphite/epoxy for the
screw heads.

The loop voltage comparisons (Table 3-1) show excellent agreement
for the FEB and aft bays, where diffusion flux coupling was assumed for the
calculation, and good agreement for the cockpit, where aperture coupling was
assumed. This validates the assumption that aperture flux in a graphite/epoxy
cockpit can be predicted as if the cockpit were metal.

From the measured waveforms it was verified that all voltages pra-
dicted to be generated by resistive/diffusion coupling (including the measure-
ments in the FEB, aft bays, and cockpit IR tests) did in fact have voltages
generally similar to the current pulse (Subsections 5.2 and 5.3.2). All mea-
sured aperture flux voltages in the cockpit had the characteristic di/dt wave-
shape (Figure 5-2), with a fast rise to peak voltage at $t = 0+$ and a zero
crossing at approximately 3 μs. The zero crossing in one loop near the graphite/
epoxy floor occurred early because an additional diffusion flux induced volt-
age (Figure 5-8) subtracted from the aperture flux voltage.

SECTION 4

ADDITIONAL MEASUREMENTS

In addition to the data of Section 3, measurements were taken which can be grouped into four categories: magnetic flux density measurements (including effects of small apertures), effects of additional metal straps on resistive/diffusion voltages, coaxial cable and shielded twisted pair voltage pickup (including capacitive coupling effects), and "electronics powered up" tests.

The average magnetic flux density (B) at time T at a wire loop (area A) can be calculated by integrating the induced voltage waveform (V) in Ampere's law to obtain

$$B = \frac{1}{A} \int_0^T V dt \qquad W/m^2 \qquad (1)$$

Thus flux density waveforms are easily obtained from digitized induced voltage waveforms. However, there appears to be some confusion in the General Dynamics report over the flux density scaling to higher driving point waveform levels. Flux induced voltages should scale as I in the FEB and aft bay (diffusion flux), and as di/dt in the cockpit (aperture flux). But flux densities were scaled by 10 in the FEB (I scaling), 5.85 in the aft bay (di/dt scaling), and 10.5 in the cockpit (di/dt scaling).

Flux density measurements were made around a 4.5 in. x 3.25 in. access port in the left-hand side of the forward bay. From the voltage waveform shapes ($\propto$ I or di/dt) it was determined that external or aperture-type fields penetrated to about 2 inches into the bay (going from 5.9×10^{-3} W/m^2 just outside the aperture to 2.6×10^{-3} W/m^2 at the same level 4.5 in. within the aperture). Also, the peak flux density calculated just outside the aperture position, for the same fuselage but without the aperture, yielded a value of

10.5×10^{-3} W/m, about twice that measured with the aperture. These qualitative results are identical with those expected from an aperture in a metal fuselage, except that the composite fuselage will contribute a slight additional diffusion flux component.

Elsewhere in the forward fuselage, flux densities were also measured. In the cockpit a peak of 6×10^{-4} W/m^2 was observed, while in the aft bay the value was 31.2×10^{-4} W/m (in the aft left-hand strake bay). Just outside the aft left-hand strake bay the peak flux density was 49.1×10^{-4} W/m^2.

To analyze the effects of additional metal straps on resistive/diffusion voltages, the forward bay was instrumented as in Figure 3-1. Measurements were then taken with various metal straps (copper wire or aluminum strip, described in Table 4-1) routed along IR wire 3 and connected to the metal ring fuselage members at Stations 60 and 98.

Table 4-1. Metal Straps/Resistance and Symbols for Graphs

Symbol	Metal Strap Size	Resistance (mΩ)
○	No strap	N/A
△	38 in. x 24 AWG wire (Cu)	81
✕	38 in. x 1 in. x 0.6 mil strip	65
⬡	38 in. x 1 in. x 25 mil strip } Al	1.6
◇	38 in. x 2 in. x 25 mil strip	0.8

The results of the measurements are shown in Figures 4-1 and 4-2. Note that the dashed lines in Figure 4-1 are an estimate of the actual voltage variation. IR wire spacing was about 3 in., indicating the substantial localized influence of grounding straps. The flux density data (Figure 4-1) show that, although a grounding strap decreases the voltage pickup on an adjacent IR wire, the strap increases the flux through nearby loops. (WARNING – the scaled values for flux density are suspect – see p. 4-1.) Finally, note that the top curve (no strap) of Figure 4-1 provides measured IR data for Station 75 in Figure 3-2.

Tests to determine the details of current pickup in coaxial cables were performed in the forward bay. A test line (coax with shield [type RG-58] or without shield [simulated by 24 AWG wire]) was routed along the bottom left flange (22-ply graphite/epoxy) in the FEB (Figure 3-1). The test circuit consisted of the line (loaded fore and aft with loads R_L and R_D, respectively) connected (at Stations 60 and 98) in parallel with the flange (resistance $R_F \ll R_L + R_D$). The line current was determined from voltage waveforms observed across the diagnostic resistance (R_D) and was expressed as V_o/R_D, where V_o is the voltage peak (Table 4-2).

Three basic coupling mechanisms were theorized to produce contributions to the line current – an injected diffusion current (due to the IR voltage down the flange), a diffusion flux current (due to the voltage induced in the loop formed between the line and flange), and a current due to the distributed capacitance between the line and flange. Since the diffusion flux was effectively shielded by the coax shield, it was not examined, although it would affect the bare wire tests. The analysis of test results, therefore, focused on the effect of distributed capacitance.

The voltage source for the distributed capacitance is the IR voltage (V) down the flange, so the line current component (I_C) due to this coupling mechanism should have a dV/dt waveform. Since V is a driving point current (I) type waveform, I_C should therefore be a di/dt type waveform which will contain higher frequencies than the line current IR component (Figure 5-3).
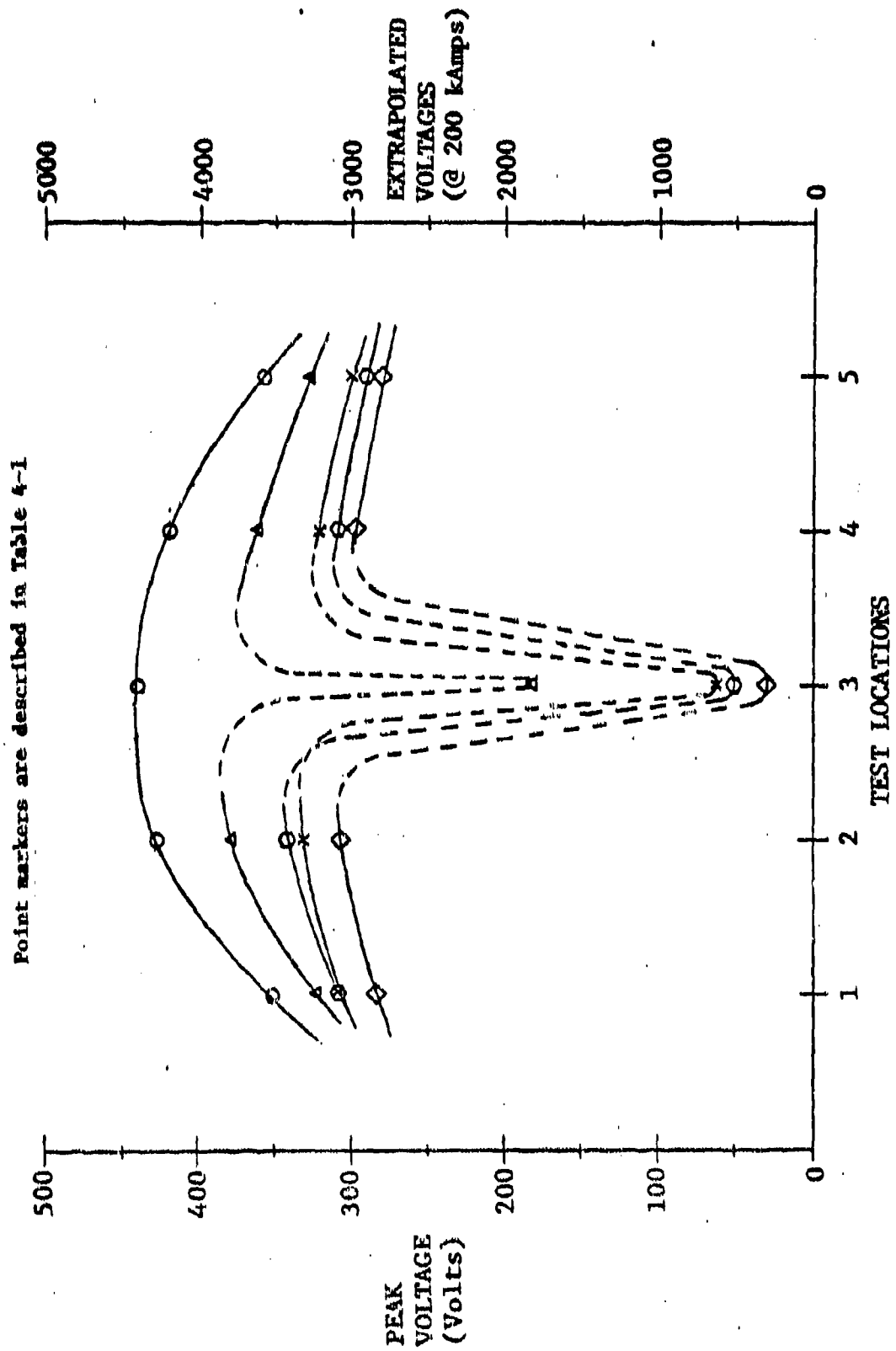
B-23

Figure 4-1. Plot of IR Voltage Drops Near a Grounding Strap in the Forward Bay
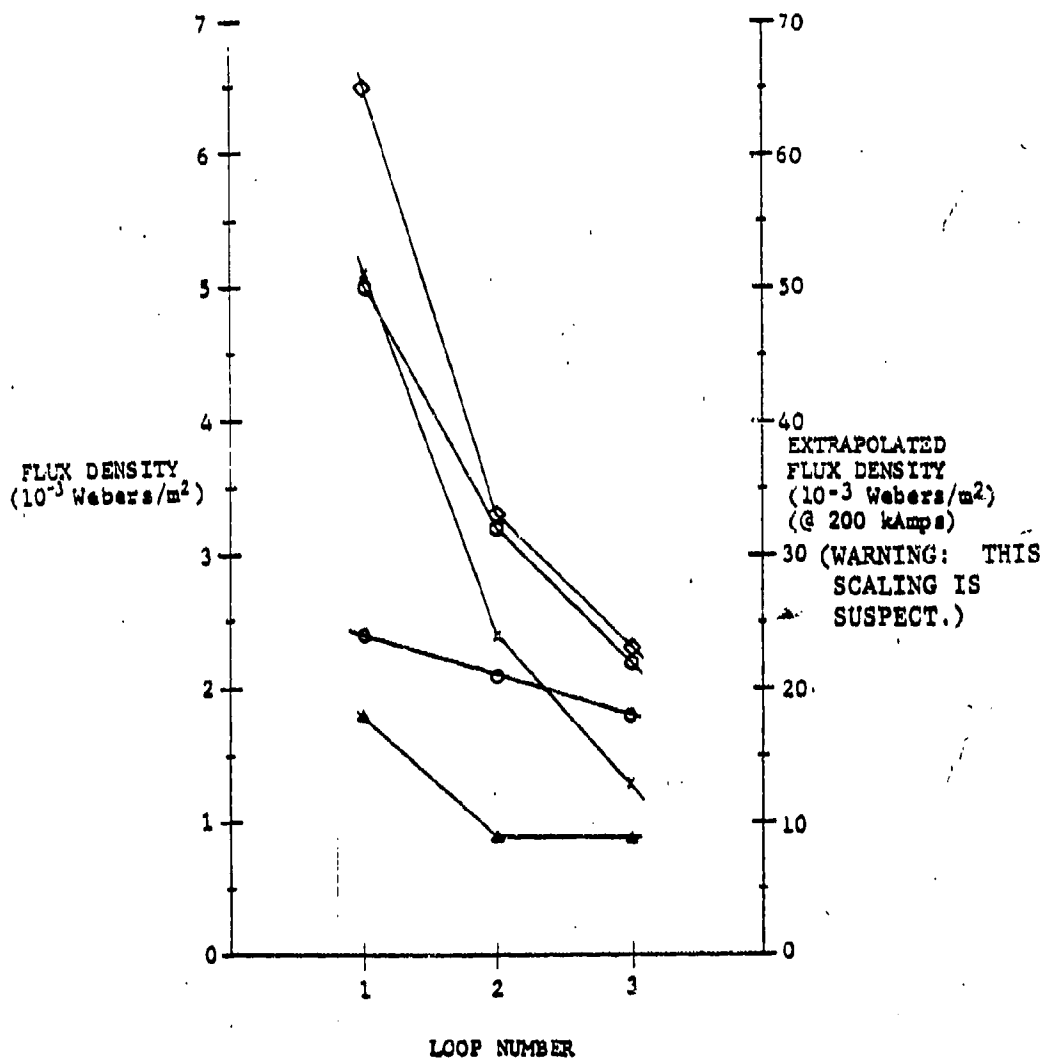
Point Markers are described in Table 4-1

Figure 4-2. Flux Density Calculations from Three (2 x 4 inch)
Loops Near a Grounding Strap in the Forward Bay

Table 4-2. Data From Coaxial Cable Tests in the Forward Bay

TEST NO.	LOAD RESISTOR (Ω) R_L	R_D	COAX SHIELD YES	COAX SHIELD NO	PEAK LINE CURRENT * CURRENT (mA) 20kA	200kA	TIME (μs) PEAK	50%	MISCELLANEOUS
1	0	50		X	4.1K	41K	4.0	9	24 AWG bare wire
2	100	97		X	649	6490	4.5	10	
3	10K	84.6		X	9.9	99	5.0	12	
4	0	50	X		300	3000	~6	--	
5	100	97	X		88	880	5.5	13.0	
6	10K	33.3	X		5.5	55	4.5	10.5	
7	OPEN	1100		X	1.7	17	0.8	--	dV/dt waveform
8	OPEN	100		X	1.7	17	0.8	--	dV/dt waveform
9	OPEN	100	X		NEGL	NEGL	--	--	
10	OPEN	100	X		.3	3	0.8	--	Shield open at forward end.
11	0	95		X	2.9K	29K	3.2	10	Cable rerouted to center.
12	0	95	X		242	2.4K	5.3	28	
13	0	95	X		2.9K	29K	3.2	9.7	Shield open at aft end.

* Equivalent current thru the diagnostic load, R_D.

1. Groundpoints for shield and load termination were the metal ring members at stations 60 and 98.
2. Shields were grounded at both ends unless specified.
3. Measured peak currents given for a 20kA and 200kA source current (i.e. 10:1 scaling factor.)

B-26

The waveforms observed in Tests 1 through 6 were driving current-type waveforms, with HF components much lower than LF components. For R_L open, however, Tests 7 and 8 produced a dV/dt (i.e., di/dt) waveform (and greater HF components) indicating capacitive coupling. This was to be expected, since opening R_L should maximize the capacitance between line and flange. The peak line current was also independent of the value of R_D in Tests 7 and 8 (also to be expected) and was totally due to capacitive coupling. Note that the coaxial cable shield reduces the capacitive coupling to a negligible amount in Test 9. In any case, the maximum HF voltage observed across R_D had a value less than 0.1V (46 MHz), indicating minimal HF problem for coaxial cables.

Tests on shielded/unshielded twisted pairs with 100Ω loading at each end were primarily conducted in the forward bay. Initial testing with the RG-22 cable instrumentation indicated the measured signals were mostly due to spurious noise and loop pickup at the twisted pair interface. Switching to the fiber optic system (Subsection 2.2) yielded voltages across the instrumentation load of less than 1V peak. However, it was found that a majority of this data could be accounted for by diffusion flux coupling through the single loop formed between the twisted pair and the instrumentation interface.

From the unshielded twisted pair data, it was adduced that little actual LF pickup occurred in the line (excluding spurious pickup at the ends). Capacitive coupling was assumed to account for the HF pickup.

For the shielded/twisted pair, the most representative data was obtained during aircraft system testing. Actual F-111 vintage avionic equipment was installed in the graphite/epoxy forward fuselage and system reaction was observed while the generator current was incrementally increased to 125 kA. Included in the system was a multiplex (MUX) digital data system with transmitter/receiver boxes placed in the FEB and aft section. The interconnecting MUX bus line was a shielded/twisted pair as used on F-16 aircraft, which produced a closed-loop system.

Fiber optic diagnostics were connected across the twisted pair in the FEB MUX box with measurements taken on both sides of a line isolation transformer. A voltage waveform was measured across an equivalent 36Ω series resistance on the primary side of the transformer, and showed diffusion flux coupling with a predominant 4 MHz component. This component would correspond to a peak of ~2V when scaled to a 200 kA driving point current level, but this should not produce circuit damage in data systems, which normally operate at ±12V maximum. At worst, an error bit might be injected, but continuous system recycling would preclude any resulting hazard. A 20 kA level produced only five intermittent errors in an external bit comparator, out of 33 shots to the fuselage. Finally, a post-test functional check showed that current levels up to 125 kA did not damage the MUX system.

SECTION 5

DRIVING POINT WAVEFORM AND INDUCED VOLTAGE MECHANISMS - THEORY AND PREDICTION

5.1 DRIVING POINT WAVEFORM

The total test circuit, including capacitor discharge pulse generator, forward fuselage test article, and return conductor, can be modeled (for low frequencies) by a simple RLC series circuit (Figure 5-1). The system input is a voltage step (magnitude V_o), and the output is the driving point waveform $i(t)$. From Kirchhoff's laws, the differential equation for the system is:
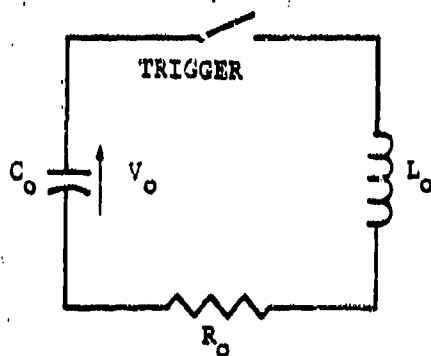
$$\frac{d^2 i}{dt^2} + 2\gamma\omega_o \frac{di}{dt} + \omega_o^2 i = \omega_o^2 \frac{C_o \, dv}{dt} \tag{1}$$

where $v(t)$ is the input voltage waveform, and

$$\gamma = \frac{R_o}{2}\sqrt{\frac{C_o}{L_o}} = \frac{R_o}{R_c}$$

$$\omega_o = \frac{1}{\sqrt{L_o C_o}} = 2\pi f_o \tag{2}$$

f_o = the natural frequency

C_o = Bank capacitance

L_o = Total series inductance of bank, load assembly,, resistor, etc.

R_o = Total effective series resistance

Figure 5-1. Lightning Generator Equivalent Circuit

The solution of Equation 1 for a voltage step input is simply*:

$$i(t) = (A/w_d) e^{-bt} \sinh w_d t \qquad \text{(OVERDAMPED for } R_o > R_c)$$

$$= (A/\omega_d) e^{-bt} \sin \omega_d t \qquad \text{(UNDERDAMPED for } R_o < R_c) \qquad (3)$$

$$= At\, e^{-bt} \qquad \text{(CRITICALLY DAMPED for } R_o = R_c)$$

where:

$$A = C_o V_o \omega_o^2 = \frac{V_o}{L_o}$$

$$w_d = \omega_o \sqrt{\gamma^2 - 1} = j\omega_d = \frac{1}{\sqrt{L_o C_o}} \sqrt{\frac{R_o^2 C_o}{4\, L_o} - 1} \qquad (4)$$

$$b = \gamma\omega_o = \frac{R_o}{2\, L_o}$$

Note that we may also write the solution in the form

$$i(t) = B(e^{-\alpha t} - e^{-\beta t}) \qquad (5)$$

where:

$$B = \frac{A}{2w_d}$$

$$\alpha = b - w_d = b\left(1 - \frac{w_d}{b}\right) = \frac{R_o}{2\, L_o}\left(1 - \sqrt{1 - \frac{4\, L_o}{R_o^2 C_o}}\right) = b - j\omega_d \qquad (6)$$

$$\beta = b + w_d = b\left(1 + \frac{w_d}{b}\right) = \frac{R_o}{2\, L_o}\left(1 + \sqrt{1 - \frac{4\, L_o}{R_o^2 C_o}}\right) = b + j\omega_d$$

*All functions in this section are assumed to be zero for $t < 0$. The expressions shown hold for $t \geq 0$.

B-30

Also note that for the overdamped solution we have $0 < \alpha < \beta < 2b$ (from Equation 6, so that $\exp(-\alpha t) > \exp(-\beta t)$, for $t > 0$, and $i(t)$ is a unipolar pulse with no overshoot (Figure 5-2a).

From Equation 3 we also have

$$\frac{di}{dt}(t) = \alpha B \left(\frac{\beta}{\alpha} e^{-\beta t} - e^{-\alpha t} \right) \tag{7}$$

which, since $\alpha < \beta$, starts positive. But as $t \to \infty$, $e^{-\alpha t}$ dominates, so that di/dt goes to zero from the negative direction (Figure 5-2b). (The details of aperture coupling are discussed in Subsection 5.7.)

The spectral densities of the overdamped i and di/dt (calculated as the absolute square of the Fourier transform) are shown in log-log scale in Figure 5-3. The 40 dB/decade attenuation is a direct result of the system behavior as a second-order low-pass linear filter.

$$\Phi_i(\omega) = |\mathcal{F}(i)|^2 = \frac{A^2}{4\pi^2} \frac{1}{(\omega^2 + \alpha^2)(\omega^2 + \beta^2)} \to \frac{A^2}{4\pi^2} \omega^{-4} \text{ (as } \omega \to \infty)$$

$$\tag{8}$$

$$\Phi_{\frac{di}{dt}}(\omega) = \omega^2 |\mathcal{F}(i)|^2 = \underline{\hspace{4cm}} \to \frac{A^2}{4\pi^2} \omega^{-2} \text{ (as } \omega \to \infty)$$

Using the preceding equations, we can calculate various waveform parameters. The maximum current is

$$\hat{I} = (A/\omega_0)k_1 = V_0 k_1 \sqrt{\frac{C_0}{L_0}} = \frac{V_0}{\sqrt{\alpha\beta}} k_1 \tag{9}$$

(A)

APERTURE COUPLED
INDUCED VOLTAGE
$(\propto \frac{di}{dt})$ DERIVED FROM
CURRENT WAVEFORM
IN (A)

OFTEN ACCOMPANIED BY H.F. SIGNALS FROM
CABLE, AIRFRAME RESONANCES OR $\frac{dE}{dt}$

(B)

CURRENT PULSE AND APERTURE COUPLED INDUCED VOLTAGE
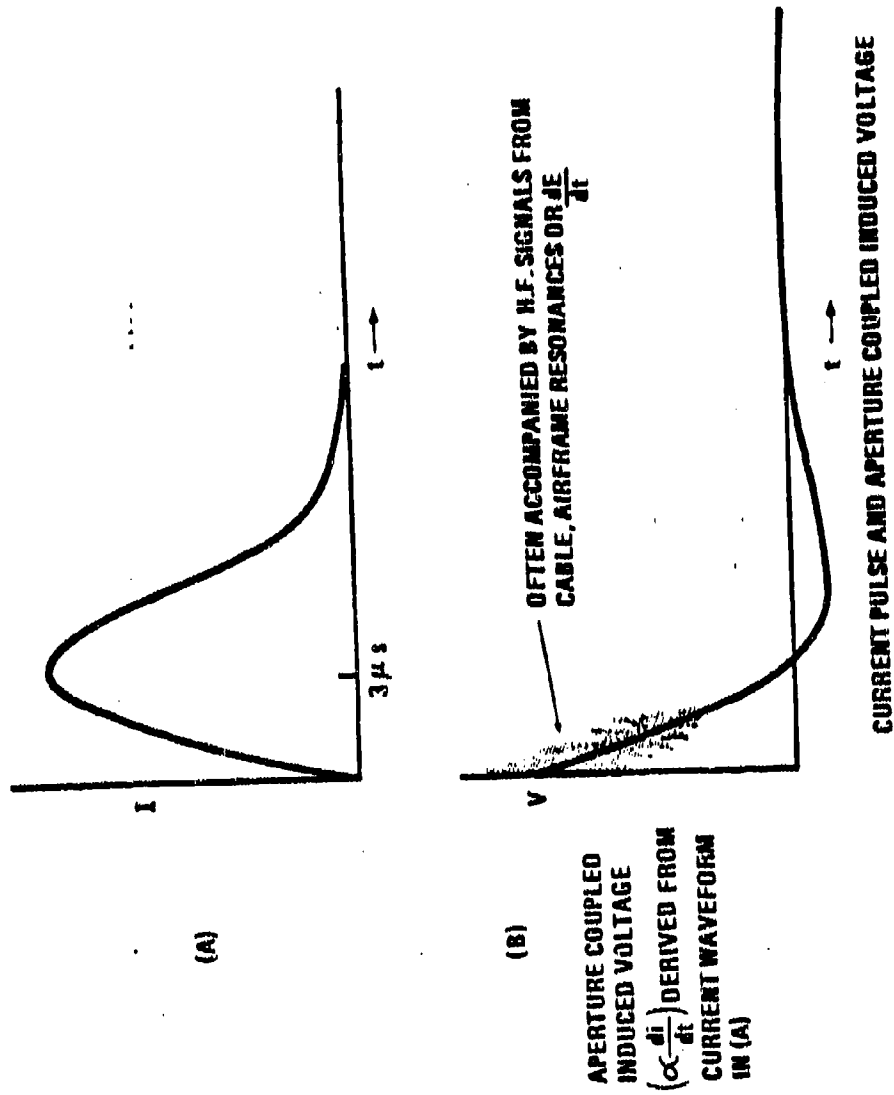
Figure 5-2. Current Pulse and Aperture Coupled Induced Voltages

Figure 5-3. Theoretical and Practical Spectra of I and di/dt for Current Pulse (shown inset)
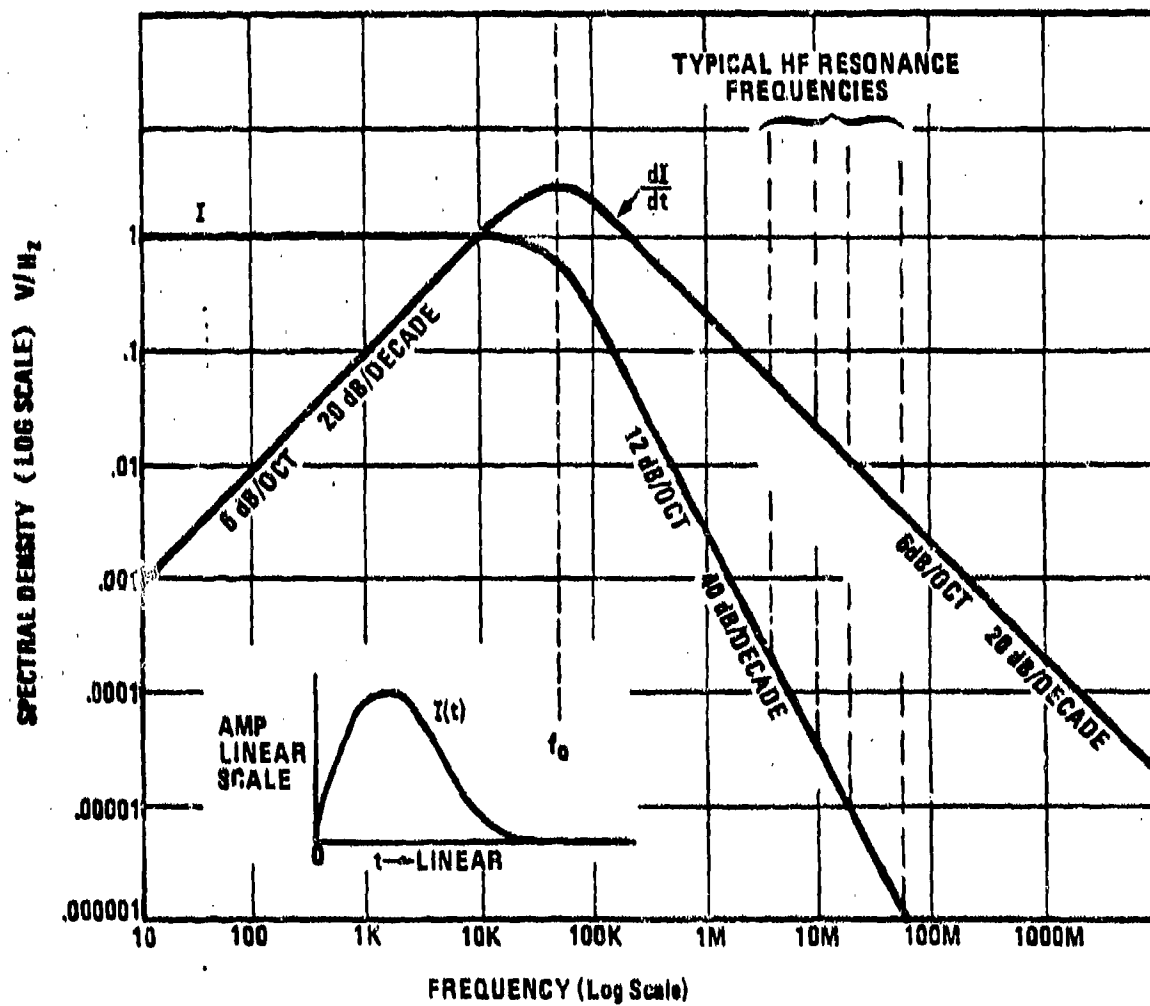
Practical spectra have the additional effect of HF resonances.

B-33

where:

$$k_1 = exp^{(-bt_{max})} \geq 1 \qquad (10)$$

$$t_{max} = \frac{1}{w_d} \text{arctanh} (w_d/b) \qquad \text{(OVERDAMPED)}$$

$$= \frac{1}{\omega_d} \text{arctan} (\omega_d/b) \qquad \text{(UNDERDAMPED)} \qquad (11)$$

$$= 1/b \qquad \text{(CRITICALLY DAMPED)}$$

Independently of R_0, the maximum rate of change $\hat{di}/dt$ is given by

$$\frac{\hat{di}}{dt} = \frac{V_o}{L_o} \qquad (12)$$

Given the values of the first five parameters for a typical test waveform in Figure 5-4, we can now calculate the others. (Exception – This reviewer could not determine how the "Action Integral" was calculated. In fact, action has units of joule-seconds, not $(ampere)^2$-seconds.) The calculated resistance and inductance agree closely with independent test circuit measurements, thus validating the RLC model for this level of $\hat{I}$ and $\hat{di}/dt$.

5.2 RESISTIVE/DIFFUSION VOLTAGES IN HOMOGENEOUS TUBES

In order to estimate theoretically the effect of fuselage material on resistive/diffusion voltages, the fuselage was modeled by a long cylindrical tube, diameter D, of homogeneous resistive material, resistivity ρ, and wall thickness h (<<D). Assume that a current is applied to this tube at one end and has an external and remote return at the other. Then the following information about output voltages V_R (measured between longitudinally spaced points on the interior surface of the tube) can be found:
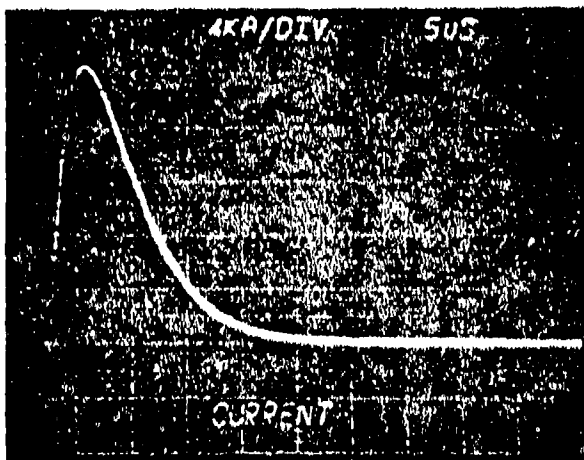
Vertical: 4 kAmps/ Div.

Horizontal: 5 usec/ Div.
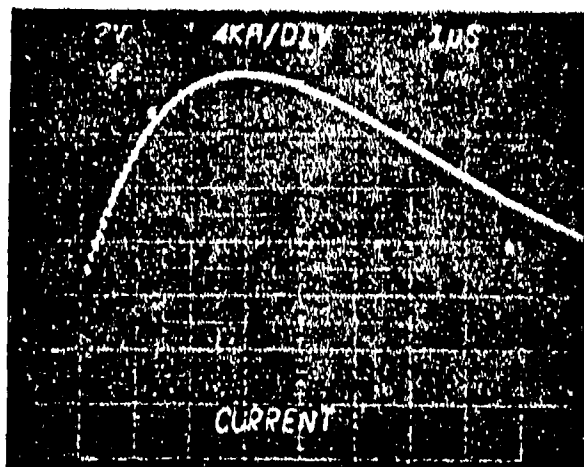
Vertical: 4 kAmps/ Div.

Horizontal: 1 usec/ Div.

Capacitance	=	4.0 uF
Voltage	=	45 kV
Current Maximum	=	20 kAmps
dI/dt Maximum	=	17.2 kAmps/usec
Peak Time	=	3.2 usec
Natural Frequency	=	49.2 kHz
Charge Transfer	=	0.18 Coulombs
Action Integral	=	2.4×10^3 A^2 sec
Total Resistance	=	1.67 Ohms

Figure 5-4. Driving Point Waveform - Overdamped

For a dc input current, I, by Ohm's law:

$$V_R = \frac{I\rho}{\pi Dh} = IR \qquad V/m \qquad (13)$$

where R is the dc resistance per unit length.

For a step function pulse, magnitude $\bar{I}$, it can be shown that

$$V_R(t) = \frac{\bar{I}\rho}{\pi Dh} \left\{ 1 + 2 \sum_{n=1}^{\infty} (-1)^n \exp\left(\frac{-n^2 t}{T_M}\right) \right\} \qquad V/m \qquad (14)$$

where:

$$T_M = \frac{\mu_o h^2}{\pi^2 \rho} = \frac{(4\pi \times 10^{-7} \, n/A^2) \, h^2}{\pi^2 \rho} = \frac{0.127 \, h^2}{\rho} \qquad \mu s \qquad (15)$$

is the characteristic diffusion time (the relative permeability of the material is assumed to be $\mu_r = 1$). Now the bracketed term in Equation 14 can be summed numerically and graphed as a function of t/T_M. From this graph (Figure 5-5) it can be seen that the system has a dead time (i.e., function = 0) of $1/2 \, T_M$, and a 10% - 90% rise time $t_r = 2.35 \, T_M$.

In the frequency domain, we can approximate the bandwidth to the -3 dB point, f_c, by the following relation (exact for the unit step function response of a first-order low-pass linear filter):

$$f_c \cong \frac{0.35}{t_r} = \frac{0.35}{2.35 \, T_M} \qquad Hz$$

$$= \frac{1.17\rho}{h^2} \qquad MHz \qquad (16)$$

where the latter equalities hold for the present system and $\mu_r = 1$.
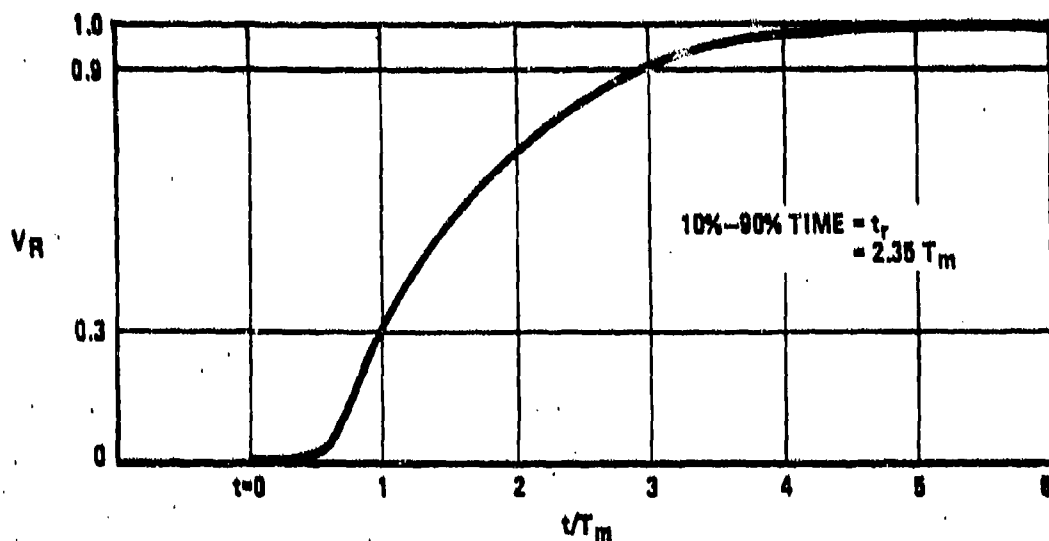
B-36

Figure 5-5. Graph of $1 + 2 \sum_{n=1}^{\infty} (-1)^n \exp\left(\frac{-n^2 t}{T_M}\right)$

Finally, assuming our system to be linear and time invariant, we note that the unit step response is simply the time integral of the unit impulse response, which in turn defines the system, so that once we have Equation 14, we can calculate the system response to any input.

For the unipolar simulation current pulse (Equation 5), which is input to the forward fuselage test article, it is a straightforward task to show

$$V_R(t) = 2RB \sum_{n=1}^{\infty} (-1)^{n-1} \left\{ \frac{\exp(-\alpha t) - \exp\left(-\frac{n^2 t}{T_M}\right)}{\left(1 - \frac{T_M \alpha}{n^2}\right)} - \frac{\exp(-\beta t) - \exp\left(-\frac{n^2 t}{T_M}\right)}{\left(1 - \frac{T_M \beta}{n^2}\right)} \right\}$$

(17)

Armed with the above general information on the voltage response of the tube to various inputs, we can examine in detail the effect of different resistivities for aluminum alloy ($\rho_{Al} \cong 4 \times 10^{-8}$ Ω-m) and graphite/epoxy ($\rho_{Gr/Ep} \cong 4000 \times 10^{-8}$ Ω-m). Note that $\rho_{Gr/Ep}$ takes into account the effect of lower resistance strakes, flanges, etc. in the YF-16 forward fuselage test article. Assume h = 2 mm. From Equation 15,

$$T_M(Al) = 12.7 \ \mu s \quad ; \quad T_M(Gr/Ep) = 12.7 \ ns \quad (18)$$

Also, using Equation 6 and data from Figure 5-4, we have

$$0 < \alpha < \beta < 2b = 418 \times 10^{-3} \quad s^{-1} \quad (19)$$

So, from Equations 18 and 19,

$$T_M\alpha, \ T_M\beta \ < \ \begin{cases} 5.31 & \text{(aluminum)} \\ 5.31 \times 10^{-3} & \text{(graphite/epoxy)} \end{cases} \quad (20)$$

We can see from Equations 17 and 20 that, in the graphite/epoxy case, all T_M terms are negligible, and we are left with (after a little calculation)

$$V_R(t) = Ri(t) \quad (Gr/Ep) \quad (21)$$

where i(t) is, as before, the driving point current waveform of Equation 5.

Unfortunately, in the aluminum case, we cannot neglect the T_M terms in Equation 17. However, the amplitude of V_R should be more or less proportional to R, while the peak should occur at later times for larger T_M Figure 5-6).

In the frequency domain (Figure 5-3), we have from Equations 16 and 18

$$f_c(Al) = 12 \ kHz \quad ; \quad f_c(Gr/Ep) = 12 \ MHz \quad (22)$$

I AS IN FIGURE 5-2a

TYPICAL VOLTAGE/m DEVELOPED BY 20KA
FLOWING ALONG A 32cm DIAMETER, 2mm
THICK TUBE OF AL. ALLOY ($\rho = 4 \times 10^{-8}$ Ω m)

V ~ 0.1V

3 μs

(a) All-Metal Structures

TYPICAL VOLTAGE/m DEVELOPED BY 20KA
FLOWING THROUGH A 32cm DIAMETER, 2mm
THICK TUBE OF GRAPHITE-EPOXY ($\rho = 4000 \times 10^{-8}$ Ω m)

400V

V

3 μs
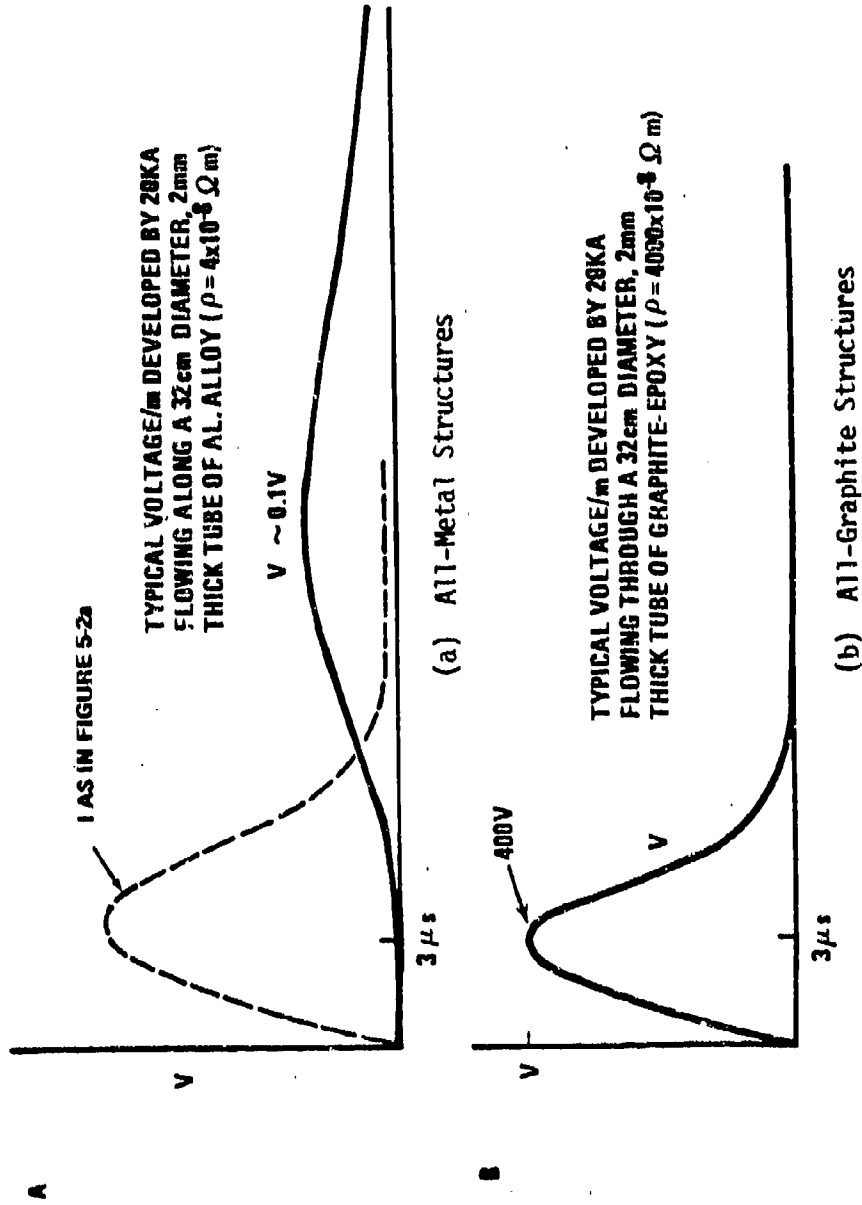
(b) All-Graphite Structures

Figure 5-6. IR Voltage in All-Metal and All-Graphite Structures

so the aluminum tube severely attenuates all components of the simulated lightning pulse above 12 kHz, while the graphite/epoxy tube attenuates only those frequencies above 12 MHz and so given a very accurate voltage proportional to the current pulse waveform (compare Equation 21 and Figure 5-6).

5.3 RESISTIVE/DIFFUSION VOLTAGES IN COMPLEX ELECTRICAL GEOMETRY

Now we use results of Subsection 5.2 to examine the general case of a cylinder made of materials with two different resistivities, ρ_1 and ρ_2 (Figure 5-7). The analysis centers on the total potential drops around the interior surface paths ABCD and ABC'D'. If the narrow center strip is graphite/epoxy and the remainder aluminum (i.e., $\rho_2 = 1000 \times \rho_1$), then from Equation 15, $T_{M1} = 1000 \times T_{M2}$. Assuming a step function input current, Equation 14 and the following discussion determine three important regimes:

1) $t < \frac{1}{2} T_{M2}$ (dead-time case)

2) $t \to \infty$ (dc case)

3) $\frac{1}{2} T_{M2} < t < T_{M1}$ (intermediate case)

(There is also a long period intermediate case, involving current diffusion into the metal, which is not important in this description.)

In Case 1, all potential drops are zero, because the time is within the dead-time for both materials. While in the dc case, $V_{AB} = V_{DC} = V_{D'C'} \neq 0$ and the two closed-path potential drops are again zero, because the current sharing is resistively controlled.

In the intermediate case (which commences in nanosecond times for graphite and extends for tens of microseconds, typically), current redistribution occurs (from the inductive sharing Case 1, to the dc Case 2) and the potential drop balance around the closed paths ABCD and ABC'D' must be maintained by a diffusion flux which links the paths. Hence, by Faraday's law,
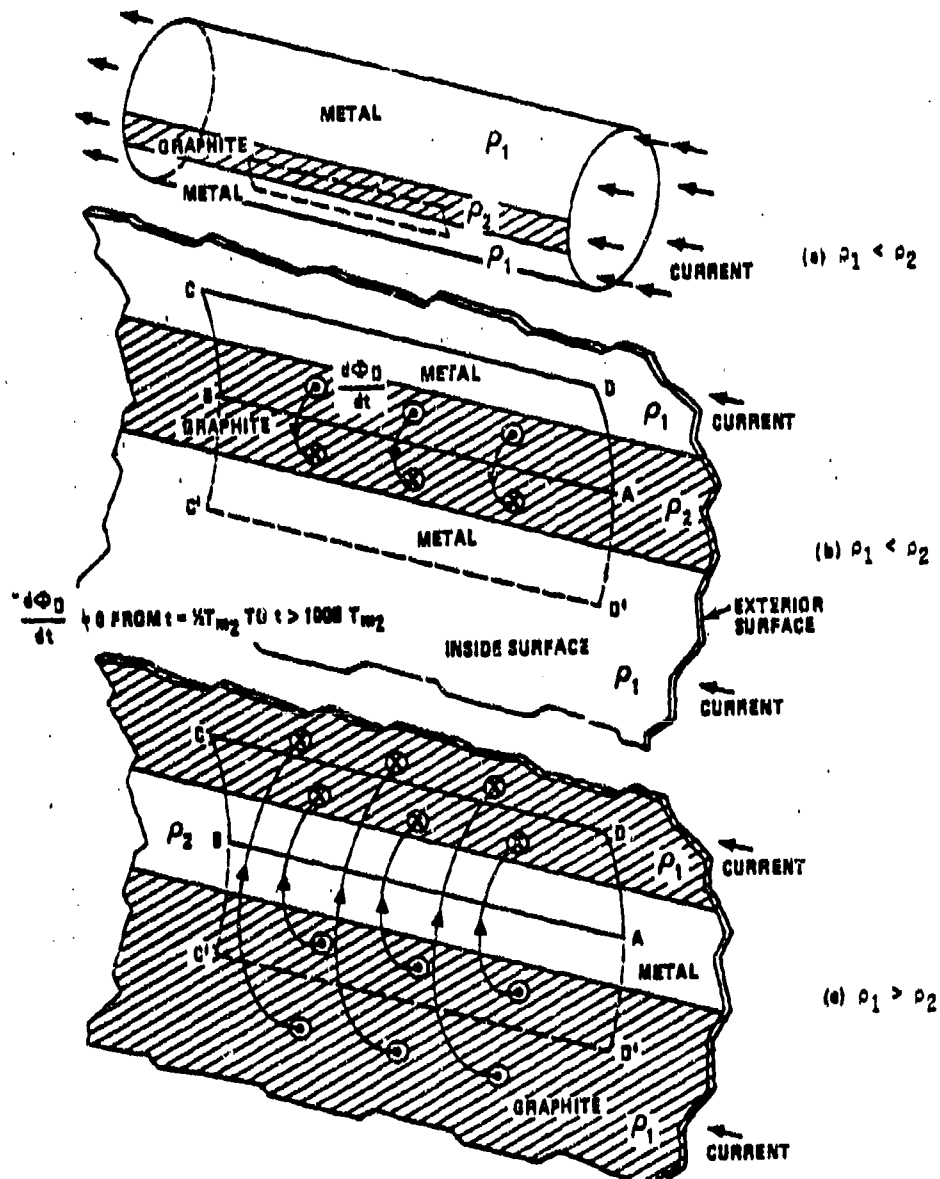
Figure 5-7. Interior Flux Distributions for a Cylindrical Model

$$V_{AB} - V_{DC} = \frac{d\,\phi_D}{dt} \qquad\qquad (23)$$

where ϕ_D is the diffusion flux. In Case 3, $V_{DC} \approx 0$, because the system is still within the dead-time for aluminum, and the diffusion flux must enter and leave the interior through the graphite/epoxy, thus linking both paths equally as in Figure 5-7(b). Thus, the diffusion flux appears as soon as V_{AB} departs from zero (i.e., from V_{DC}). (In the case of a homogeneous tube, $V_{AB} = V_{DC}$ always, so by Equation 23 there is no diffusion flux effect.)

The pattern of the diffusion flux within the tube is quite similar to the aperture flux which would occur in the tube if the graphite/epoxy strip were removed. However, this diffusion flux is not related in time to the external flux. Even so, this similarity of flux patterns makes it possible to calculate diffusion flux voltages (see Subsection 5.6). Note that if we reverse the resistivities in Figure 5-7(b), we obtain a flux pattern reminiscent of that around a straight current-carrying wire.

5.3.1 Induced Voltage Corollaries

If we assume that ρ_1 is so small that $V_{DC} \approx 0$ for all times, then, from Equation 23 and noting that V_{AB} is just the resistively produced voltage in the graphite/epoxy due to the injected current, we have:

Corollary 1

Diffusion flux voltages have the same form and spectrum
as the dominant resistive voltage within an enclosure
(but see Subsection 5.3.2).

Since $V_{DC} = 0$, but "V_{DC}" (through the path DABC) $= V_{AB} \neq 0$,

Corollary 2

It is the circuit route which determines the induced
voltage, not the reference points at the end.

Finally, since diffusion flux patterns are geometrically similar to those produced by apertures, and so are strongest near the graphite/epoxy surface (where $d\phi_D/dt = V_{AB}(t)$),

Corollary 3

Diffusion flux induced voltages within an enclosure, induced in single loops, are always less than or, in the limit, equal to the largest resistive potential drop which occurs on the surface of the enclosure, and will be smaller with increasing distance from that surface.
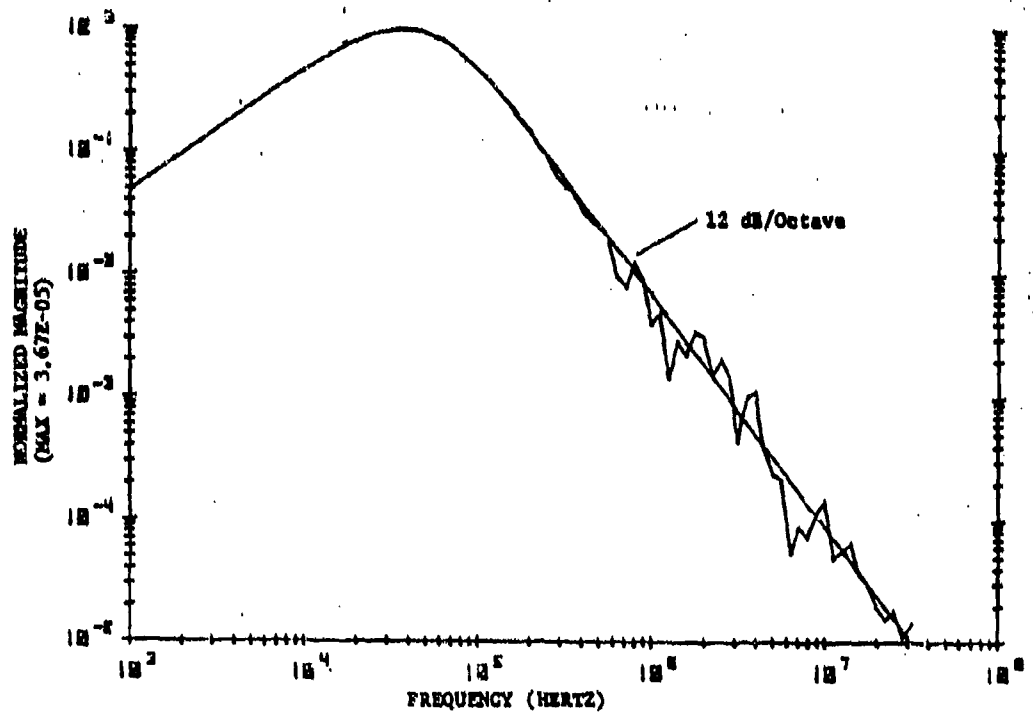
5.3.2 Diffusion Flux Voltage Waveform

In practice, Corollary 1 holds in the time range from nanosecond to microsecond times. For a typical driving point waveform (Figure 5-4), this includes most of the unipolar pulse, including the peak, so that comparison of the initial shape of the induced voltage waveform with that of the driving point waveform should be able to distinguish diffusion flux coupling ($\propto I$, Figure 5-8a)* from aperture flux coupling ($\propto di/dt$, Figure 5-2b). A key parameter here is induced voltage zero crossing time, which is equal to the driving point current peak time for a di/dt waveform, but is much earlier (first crossover, Figure 5-8a) or much later (second crossover) for a diffusion flux voltage. The second crossover and resultant bipolar pulse are necessary, even in diffusion flux coupling, to conserve total flux. Because of this distinction, the low frequency component of the diffusion flux spectrum (Figure 5-8b) will be somewhat degraded from that of the driving point waveform (Figure 5-3), although the 12 dB/octave falloff is evident.

---

*Figure 5-8a comes from a loop in the central aft bay while Figure 5-8b is the Fourier transform of a digitized forward bay waveform. However, Figure 5-8 still gives the general character of diffusion coupled voltage waveforms and spectra. (The high frequency "hash" in Figure 5-8b is due to digitizer limitations and was therefore fit with a straight line.)
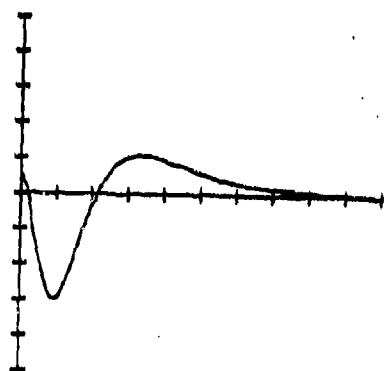
LOOP VOLTAGE PLOT
VERT: 2.00E+00   V/DIV
HORZ: 5.00E-06   S/DIV

(a) Voltage Waveform

12 dB/Octave

NORMALIZED MAGNITUDE
(MAX = 3.67E-05)

FREQUENCY (HERTZ)

(b) Fourier Transform Plot of a Voltage Waveform

Figure 5-8. Diffusion Flux Induced Voltage

5.4 POTENT COMPUTER PROGRAM

All the voltage pickup predictions in the report start with output from the POTENT program. POTENT solves Laplace's equation in two dimensions, taking as input the shape of the cross section of an arbitrary cylinder, which is assumed to be an equipotential surface. Calculations are performed on a 50 x 50 mesh, with variable mesh spacing to improve accuracy in regions of high curvature. For the magnetic case, tabulations at each mesh point provide values of magnetic flux, H_x, H_y, and $|H|$. Data can be processed by a graph plotting routine to produce mappings of magnetic flux contours (field lines) and $|H|$, as used in the report. The input surface is the whole fuselage cross-section for surface current, exterior flux, and aperture flux calculations, but consists of only the high-current regions for diffusion flux calculations (Figure 5-9).

5.5 SURFACE IR VOLTAGES

In fuselage regions without apertures, (e.g., the forward equipment bay [FEB]), resistively produced voltages, which may be observed between longitudinally spaced sensing wires on the interior surface of the aircraft skin are predicted as follows:

1. The exterior surface current density, J (i.e., current per unit width for longitudinal current), is obtained from the POTENT values for $|H|$ at that surface. Since (H_x, H_y) must be tangent to the surface (an equipotential), we have $J = |H|$. (Figure 5-9a.)

2. From Ohm's law applied to a resistive cylinder,

$$V_R = \frac{J \rho_{eff} \ell}{h} \qquad V \qquad (24)$$

where ℓ is the distance over which the voltage is measured, h is the thickness of the fuselage at that cross section (h << cross sectional dimensions) and $\rho_{eff} = 3750 \times 10^{-8}$ Ω-m. Note that $\rho_{eff} < 10^{-4}$ Ω-m (a standard value in the literature), but this takes into account the effect of lower resistance strakes, flanges, etc., in the YF-16 forward fuselage test article.

B-45
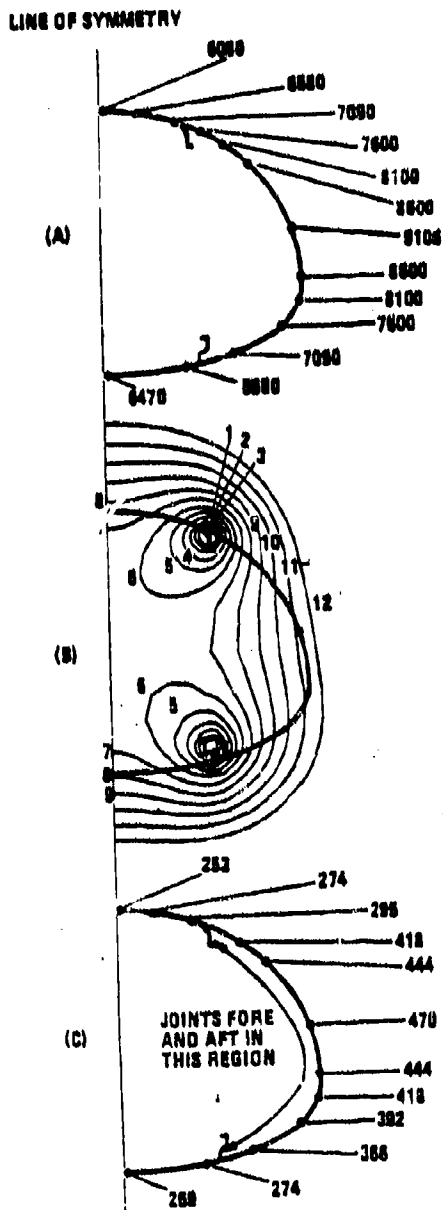
Figure 5-9. Station 75 - Calculated Flux and H Values

3. In regions containing graphite/epoxy access panels,
    a voltage drop due to screw joints must be added:

$$V_J \cong J \times 10^{-2} \qquad V \qquad\qquad (25)$$

where we have assumed two joints per panel (fore
and aft) with a "resistance" of about 5 mΩ-m per
joint.

For example, starting with J, specified in Figure 5-9a, and using
$\ell = 0.965$ m (38 in.) and $h = 0.84 \times 10^{-3}$ m (the thickness of 6-ply graphite/
epoxy in the forward bay), we should obtain the voltages in Figure 5-9c. This
is the claim made in General Dynamics' report; actually, these voltages corre-
spond to a slightly different value of ρ_{eff}/h in Equation 24.

5.6 DIFFUSION FLUX INDUCED VOLTAGES

In fuselage areas containing both graphite/epoxy and highly conduct-
ing regions (e.g., the forward bay), diffusion flux induces voltages on wire
loops which can be estimated as follows.

The POTENT program is run with a boundary surface consisting only of
the highly conducting regions (e.g., metal, strakes, and built-up flanges -
see Figure 5-9b). Effectively, the graphite/epoxy surface areas are replaced
by apertures, which should give the same flux patterns (Subsection 5.3). The
effect of the graphite/epoxy is more or less to uniformly attenuate the basic
aperture fluxes. The interior flux lines are obtained from POTENT with flux
values ϕ normalized by taking $\phi = 0$ at the boundary surface (which here is not
the whole fuselage surface), and $\phi = 1$ at the flux line corresponding to the
position of the return conductor (at about twice the fuselage radius).

For a longitudinal, rectangular loop with one side a return path in
a highly conducting fuselage region (i.e., where the voltage drop is zero), we
have

$$V = \frac{d\phi}{dt} \cong k(t)\,\phi \qquad\qquad (26)$$

where:

V   =   voltage induced in the loop

       =   voltage drop in the off-surface side of the loop

ϕ =   flux value of the flux contour at the off-surface side of the loop (i.e., the flux linked by the loop)

$k(t)$ =   time dependence of $d\phi/dt$ (assumed to be the same at all flux contours)

Now, since we have the same flux contours (but different scaled fluxes) in the aperture and graphite/epoxy cases we have from Equation 26

$$\frac{V_B}{V_A} = \frac{\phi_B}{\phi_A} = \frac{V_1}{V_S} = \frac{\phi_1}{\phi_S} \tag{27}$$

where the voltage drops and fluxes are at the wires indicated in Figure 5-10. (Only the off-surface sides of the loops are shown and should be intersected by the corresponding flux lines.) Therefore,

$$V_1 = V_S \times \frac{\phi_B}{\phi_A} \tag{28}$$

Note that ϕ_A and ϕ_B are obtained from the POTENT aperture calculation, and V_S is just the surface IR voltage which can be obtained as in Subsection 5.5.
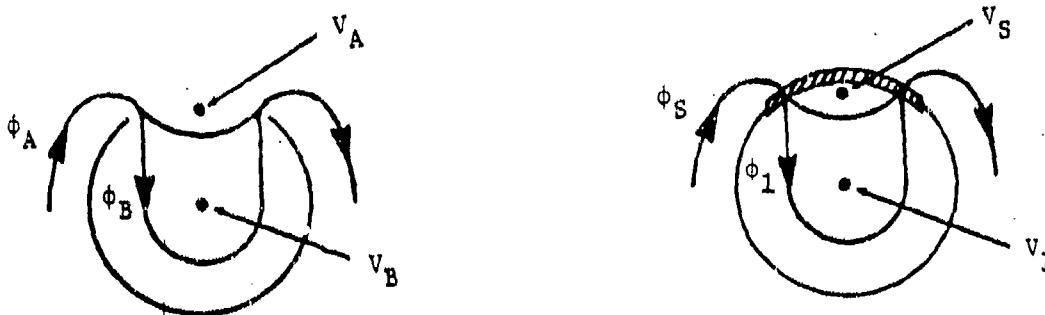

Figure 5-10. Flux Contours and Induced Voltages - Aperture versus Graphite/Epoxy

B-48

Finally, a longitudinal rectangular loop entirely interior to the fuselage (i.e., with no current return in the fuselage surface) may be viewed as a combination of two loops with fuselage current return. We obtain from Equation 28

$$\frac{V_{loop}}{V_s} = \frac{(V_1 - V_2)}{V_s} = \frac{\phi_1 - \phi_2}{\phi_s} = \frac{\phi_B - \phi_C}{\phi_A} \tag{29}$$

where 1 (B) and 2 (C) denote the nearer (to the surface) and farther ends of the loop, respectively. (Imagine a third wire and flux line below ϕ_B and ϕ_1 in Figure 5-10.)

5.7 APERTURE COUPLED VOLTAGES

Within an aperture created by an electrically transparent opening (e.g., within the cockpit or within bays having glass fiber, Kevlar, or other insulating covers), direct coupling of magnetic flux occurs to wiring and circuits. We may visualize the situation as a two-loop system, consisting of the test loop under consideration and the fuselage-return conductor loop, so

$$V = \ell M_{TF} \frac{di}{dt} \tag{30}$$

where:

di/dt = rate of change of the fuselage test current

ℓ = longitudinal length of test loop (assumed to be a planar rectangle, longitudinal in orientation)

M_{TF} = fast flux transfer inductance (per unit length)

The flux linkage of the system can be examined to determine M_{TF} from

$$\frac{\phi}{\phi_T} = \frac{\ell M_{TF} \, i}{\ell L' i} = \frac{M_{TF}}{L'} \tag{31}$$

where:

ϕ = flux linking the test loop

ϕ_T = total flux between fuselage and return conductor

L' = self-inductance (per unit length) of fuselage-return conductor loop

Further,

$$\phi_T = \phi + \phi_M \qquad (32)$$

where:

$\phi_M = \ell M i$ = flux linked by test loop due to fuselage-return conductor loop

M = mutual inductance (per unit length) between the two loops

so, from Equations 31 and 32, we have

$$M_{TF} = L' \frac{\phi}{\phi_T} = \frac{L' (\phi_T - \phi_M)}{\phi_T} = L' - \frac{L' \phi_M}{\phi_T} = L' - M \qquad (33)$$

where the last equality comes from an analogue of Equation 31, applied to ϕ_M and M.

Electric field coupling ($\propto$ dE/dt) may also occur in some circuits within apertures and will also be more apparent at higher frequencies. However, quantitative statistics are not available for dE/dt of natural lightning, and no attempt was made to simulate it in the test.